Universitat Politècnica de València
Departamento de Máquinas y Motores Térmicos

UNIVERSITAT
POLITÈCNICA
DE VALÈNCIA

Doctoral Thesis

ASSESSMENT OF DETAILED COMBUSTION AND SOOT MODELS FOR HIGH-FIDELITY AERO-ENGINE SIMULATIONS

Presented by:
Iván Olmeda Ramiro

Supervised by:
Prof. Jesús Vicente Benajes Calvo
Dr. José Manuel Pastor Enguídanos

in fulfillment of the requirements for the degree of
Doctor of Philosophy

Valencia, November 2023

Ph.D. Thesis

ASSESSMENT OF DETAILED COMBUSTION AND SOOT MODELS FOR HIGH-FIDELITY AERO-ENGINE SIMULATIONS

Written by:	Mr. Iván Olmeda Ramiro
Supervised by:	Prof. Jesús Vicente Benajes Calvo
	Dr. José Manuel Pastor Enguídanos

Examination committee:

Chairman:	Prof. Ricardo Novella Rosa
Secretary:	Prof. Juan José Hernández Adrover
Member:	Prof. Lambertus Marinus Theodorus Somers

Reviewing board:

Prof. Tommaso Lucchini
Prof. Jacobo Porteiro Fresco
Prof. Lambertus Marinus Theodorus Somers

Valencia, November 2023

Abstract

In recent years, interest in the development of efficient and clean aviation powerplants has increased due to the detrimental impact on health and the environment caused by conventional combustion systems. In this context, the research community has increasingly focused its efforts on the study of turbulent combustion and the generation of pollutant emissions such as soot particulates. With recent advances in computational power, high-fidelity simulations emerge as a valuable alternative to reproduce and analyze these phenomena. Specifically, Large Eddy Simulations (LES) are considered as one of the most promising numerical tools to provide further insight into the complex dynamic processes that characterize reactive turbulent flows and predict soot emissions in aeronautical applications.

In the present work, turbulent combustion and soot production is studied and analyzed in gas turbine engine applications by means of high-fidelity LES. Combustion modelling is addressed by a flexible tabulated chemistry method based on the flamelet concept, which is able to represent complex chemical phenomena with an affordable computational cost. In addition, an Eulerian-Lagrangian description is employed for the gas phase and droplets in order to correctly represent the multiphase flow in spray flames. A recently developed approach based on the sectional method and coupled to the tabulated chemistry framework is considered for soot prediction in computationally efficient simulations.

This numerical modelling framework is used in this work to analyze the combustion process and evaluate its capabilities to predict soot and flame characteristics in representative gas turbine burners. First, an atmospheric non-swirled spray flame is studied in terms of two-phase flow combustion. This burner shows a double reaction front structure and local extinction occurs in the inner layer due to both droplet-flame and turbulence-flame interactions, which is properly characterized by LES. Subsequently, combustion and soot production is investigated in a pressurized swirled model combustor which includes secondary dilution jets inside the combustion chamber. The assessment of the reacting flow field and soot is addressed for burner configurations with and without secondary air, showing excellent predictive capabilities in both cases. The present modelling approach accurately reproduce the complex swirled flow field, flame structure and soot dynamics and is able to provide different particle size distributions depending on the variations of the soot formation and oxidation processes.

In summary, the different practical cases studied allow to consolidate and validate the computational methodology followed in the present thesis. The

proposed tabulated modelling strategy is sufficiently valid and suitable for reproducing complex combustion and soot formation phenomena, in view of the consistency of the analysis, the accurate predictions and the satisfactory agreement with the experimental measurements.

Resumen

En los últimos años, el interés por el desarrollo de motores de aviación limpios y eficientes se ha incrementado debido al impacto perjudicial sobre la salud y el medio ambiente ocasionado por los sistemas de combustión convencionales. En este contexto, la comunidad científica ha ido centrando cada vez más sus esfuerzos en el estudio de la combustión turbulenta y la generación de emisiones contaminantes como las partículas de hollín. Con los recientes avances en lo que respecta a potencia de cálculo, las simulaciones de alta fidelidad emergen como una valiosa alternativa para reproducir y analizar estos fenómenos. En concreto, las simulaciones basadas en el modelado de la turbulencia LES son consideradas como una de las herramientas numéricas más prometedoras a la hora de profundizar en la comprensión sobre los complejos procesos dinámicos que caracterizan el flujo reactivo turbulento y predecir emisiones de hollín en aplicaciones aeronáuticas.

En el presente trabajo, se estudia y analiza la combustión turbulenta y producción de hollín en aplicaciones de turbina de gas mediante LES de alta fidelidad. El modelado de la combustión se aborda a través de un método flexible de química tabulada basado en el concepto *flamelet*, el cual es capaz de representar fenómenos químicos complejos con un coste computacional asequible. Además, se emplea una aproximación Euleriana-Lagrangiana para la descripción de la fase gaseosa y las gotas, de forma que se represente correctamente el flujo reactivo multifásico. Para la predicción de hollín en simulaciones computacionalmente eficientes, se emplea un novedoso enfoque de modelado basada en el método seccional y acoplada al modelo de combustión de química tabulada.

Esta estrategia de modelado numérica es utilizada en este trabajo para analizar el proceso de combustión y evaluar sus capacidades para predecir hollín y las características de la llama en quemadores de turbina de gas representativos. En primer lugar, se estudia la combustión de flujo bifásico en una llama atmosférica sin torbellinador con inyección líquida de combustible. Este quemador presenta una estructura doble del frente reactivo y las simulaciones numéricas son capaces de capturar adecuadamente los fenómenos de extinción local que tienen lugar en la zona interna de la llama debido a la interacción de las gotas y la turbulencia con el frente reactivo. Posteriormente, se investiga la combustión y producción de hollín en un quemador presurizado con torbellinador que incluye aire secundario de dilución en el interior de la cámara de combustión. La validación del flujo reactivo y hollín se lleva a cabo tanto en la configuración del quemador con aire secundario como sin el mismo, mostrando unas excelentes capacidades predictivas en ambos casos.

La presente estrategia de modelado reproduce de forma precisa el complejo patrón de flujo, la estructura de la llama y la dinámica de generación de hollín, además de que es capaz de proporcionar diferentes distribuciones de tamaño de partícula dependiendo de las variaciones en los procesos de formación y oxidación del hollín.

En resumen, los diferentes casos prácticos estudiados permiten consolidar y validar la metodología computacional seguida en la presente tesis. La estrategia de modelado basada en química tabulada propuesta demuestra ser lo suficientemente válida y adecuada para reproducir los complejos fenómenos de la combustión y la formación de hollín, en vista de la consistencia del análisis, las precisas predicciones y la concordancia satisfactoria con las medidas experimentales.

Resum

En els últims anys, l'interés pel desenvolupament de motors d'aviació nets i eficients s'ha incrementat a causa de l'impacte perjudicial sobre la salut i el medi ambient ocasionat pels sistemes de combustió convencionals. En aquest context, la comunitat científica ha anat centrant cada vegada més els seus esforços en l'estudi de la combustió turbulenta i la generació d'emissions contaminants com les partícules de sutge. Amb els recents avanços pel que fa a potència de càlcul, les simulacions d'alta fidelitat emergeixen com una valuosa alternativa per a reproduir i analitzar aquests fenòmens. En concret, les simulacions basades en el modelatge de la turbulència LES són considerades com una de les eines numèriques més prometedores a l'hora d'aprofundir en la comprensió sobre els complexos processos dinàmics que caracteritzen el flux reactiu turbulent i predir emissions de sutge en aplicacions aeronàutiques.

En el present treball, s'estudia i analitza la combustió turbulenta i la producció de sutge en aplicacions de turbina de gas mitjançant LES d'alta fidelitat. El modelatge de la combustió s'aborda a través d'un mètode flexible de química tabulada basat en el concepte *flamelet*, el qual és capaç de representar fenòmens químics complexos amb un cost computacional assequible. A més, s'empra una aproximació Euleriana-Lagrangiana per a la descripció de la fase gasosa i les gotes, de manera que es represente correctament el flux reactiu multifàsic. Per a la predicció de sutge en simulacions computacionalment eficients, s'empra un nou plantejament de modelatge basat en el mètode seccional i acoblat al model de combustió de química tabulada.

Aquesta estratègia de modelatge numèrica és utilitzada en aquest treball per a analitzar el procés de combustió en cremadors de turbina de gas representatius, i avaluar les seues capacitats per a predir sutge i les característiques de la flama. En primer lloc, s'estudia la combustió de flux bifàsic en una flama atmosfèrica sense remolinador amb injecció líquida de combustible. Aquest cremador presenta una estructura doble del front reactiu i les simulacions numèriques són capaces de capturar adequadament els fenòmens d'extinció local que tenen lloc en la zona interna de la flama a causa de la interacció de les gotes i la turbulència amb el front reactiu. Posteriorment, s'investiga la combustió i producció de sutge en un cremador pressuritzat amb remolinador que inclou aire secundari de dilució a l'interior de la cambra de combustió. La validació del flux reactiu i sutge es duu a terme tant en la configuració del cremador amb aire secundari com sense aquest, mostrant unes estupendes capacitats predictives en tots dos casos. La present estratègia de modelatge reprodueix de manera precisa el complex patró de flux, l'estructura de la flama i la dinàmica de generació de sutge, a més de que és capaç de proporcionar

diferents distribucions de grandària de partícula depenent de les variacions en els processos de formació i oxidació del sutge.

En resum, els diferents casos pràctics estudiats permeten consolidar i validar la metodologia computacional seguida en la present tesi. L'estratègia de modelatge basada en química tabulada proposada demostra ser prou vàlida i adequada per a reproduir els complexos fenòmens de la combustió i la formació de sutge, en vista de la consistència de l'anàlisi, les precises prediccions i la concordança satisfactòria amb les mesures experimentals.

List of publications

Following the work performed in the framework of this doctoral thesis and its associated projects, the following journal and conference papers have been published in chronological order:

- "*Large Eddy Simulations of advanced gas turbine burners*". J. Benajes, J.M. García-Olvier, J.M. Pastor, I. Olmeda. (2019). HPCCOMB2019 - 2nd Edition of the HPC Spanish Combustion Workshop 2019.

- "*LES Eulerian diffuse-interface modeling of fuel dense sprays near-and far-field*". J.M. Desantes, J.M. García-Olvier, J.M. Pastor, I. Olmeda, A. Pandal, B. Naud. (2020). International Journal of Multiphase Flow, 127. DOI: https://doi.org/10.1016/j.ijmultiphaseflow.2020.103272

- "*Large Eddy Simulations of a n-heptane spray flame with local extinction*". J. Benajes, J.M. García-Olvier, J.M. Pastor, I. Olmeda, A. Both, D. Mira. (2021). HPCCOMB2021 - 3rd Edition of the HPC Spanish Combustion Workshop 2021.

- "*Analysis of local extinction of a n-heptane spray flame using large-eddy simulation with tabulated chemistry*". J. Benajes, J.M. García-Olvier, J.M. Pastor, I. Olmeda, A. Both, D. Mira. (2022). Combustion and Flame, 235. DOI: https://doi.org/10.1016/j.combustflame.2021.111730

- "*Combustion modelling in a pressurized gas turbine burner using Large Eddy Simulations*". J.M. García-Olvier, J.M. Pastor, I. Olmeda, A. Both, D. Mira. (2022). 12CNIT - XII National and III International Conference on Engineering Thermodynamics.

- "*LES of a pressurized sooting RQL-like combustor with a computationally efficient discrete method coupled to tabulated chemistry*". J.M. García-Olvier, J.M. Pastor, I. Olmeda, A. Kalbhor, D. Mira, J.A. van Oijen. (2023). 11th European Combustion Meeting ECM2023.

- "*LES of a pressurized sooting aero-engine model burner using a computationally efficient discrete sectional method coupled to tabulated chemistry*". J.M. García-Olvier, J.M. Pastor, I. Olmeda, A. Kalbhor, D. Mira, J.A. van Oijen. Under review in Combustion and Flame.

"The most important step a man can take. It's not the first one, is it?
It's the next one. Always the next step"
Dalinar Kholin

A veces parece que una tesis doctoral tiene un único autor, la persona que firma en el documento y que acaba defendiendo ante un tribunal, pero nada más lejos de la realidad. El trabajo que he realizado durante estos últimos 5 años no habría sido posible sin una cantidad importante de personas y quisiera aprovechar este momento para agradecer por su apoyo y contribución. En parte, esto les pertenece.

En primer lugar, me gustaría agradecer al Instituto Universitario de Investigación CMT - Motores Térmicos, a su director el Prof. J. M. Desantes y en general a todo el equipo de dirección por darme la oportunidad de cursar el Programa de Doctorado y de trabajar en esta línea de investigación. Quiero expresar mi gratitud por todo el valioso conocimiento que me ha proporcionado este prestigioso centro y por garantizarme los recursos necesarios para llevar a cabo esta tesis.

Me gustaría agradecer en especial a mis directores de tesis: el Prof. Jesús Benajes y el Dr. José Manuel Pastor, por depositar su confianza en mí y supervisar de forma excelente mi trabajo. No puedo estar más agradecido a José Manuel, quien ha sido además mi tutor durante estos años, por su paciencia, sus consejos y por todo lo que me ha enseñado. Ha sido como un compañero más, con una profesionalidad y forma de ser que transmite confianza y genera un entorno de trabajo muy cómodo. Simplemente, mi más sincera admiración por la persona que más ha contribuido a este trabajo. Por otro lado, nunca podré olvidar la ayuda y apoyo de José María García y Ricardo Novella, profesores del grupo de combustión que han sido piezas clave en mi aprendizaje en este campo de investigación.

De igual manera, me gustaría mencionar a algunos compañeros que han compartido mi experiencia y me han acompañado en este viaje. Agradecer a los doctores Ibrahim Barbery y Cassio Spohr, los que han sido durante casi todo este periodo mis compañeros de despacho, por compartir las experiencias del camino, por su compañía y por hacer más ameno todo el proceso. Me gustaría agradecer también al Dr. Mario Belmar, por todo lo que heredé de él y por ser una de las personas que más me ayudó en el inicio de esta línea de investigación. Finalmente, me gustaría dedicar unas líneas a una de las personas que más me ha apoyado tanto en lo profesional como en lo personal: Carlos Moreno. Qué decir que no sepas ya. Compartimos el viaje que fue la carrera y he tenido la suerte de poder compartir contigo también este camino. Nos hemos ayudado con problemas específicos de cada uno de nuestros temas de investigación, nos hemos desahogado en los peores momentos, hemos desconectado en nuestros almuerzos diarios, nos hemos reído... En fin, gracias, no solo por ser un gran compañero, sino por ser un buen amigo.

No me gustaría dejarme a otra serie de personas del Instituto CMT cuyo trabajo y apoyo no es tan visible o directo, pero resulta imprescindible. Mi más sincero agradecimiento al conjunto de técnicos y al personal de administración. En particular, me gustaría agradecer a Amparo Cutillas, por una gestión y administración impecables y por tu infinita paciencia.

Por otro lado, durante todo el desarrollo de la tesis he tenido la suerte de contar con compañeros de otros centros de investigación, sin los cuales todo este trabajo no habría sido posible. Me gustaría agradecer a la gente del Centro de Supercomputación de Barcelona. En especial, me gustaría expresar mi admiración y gratitud al Dr. Daniel Mira, por su colaboración, sus valiosos consejos, su iniciativa y positividad. También, me gustaría agradecer a Ambrus Both por su increíble trabajo, indispensable para la consecución de mi proyecto de tesis.

Asímismo, debo agradecer también al Prof. Jeroen van Oijen y a Abhijit Kalbhor, dos de las personas que más contribuyeron durante mi estancia en la Eindhoven University of Technology, y de las que más he aprendido. Gracias al Prof. van Oijen, por acogerme y supervisar mi trabajo, y mi más sincera gratitud a Abhijit, por su colaboración, su excepcional trabajo y su simpatía.

Por último, y no menos importante, quiero dar las gracias a todas esas personas que, aunque no hayan contribuido desde el punto de vista profesional, han sido siempre un pilar importante de mi vida y me han apoyado durante toda esta etapa. Infinitas gracias a mis padres: Carmen y Víctor. Siempre habéis estado ahí y una parte de todo lo que consiga en esta vida os pertenece, ya lo sabéis. He tenido la suerte de contar con una familia que siempre ha mostrado un apoyo incondicional y que no ha fallado nunca. Por otro lado, como se suele decir, la familia que eliges: mis amigos. Por vuestra lealtad, vuestros buenos consejos, por ayudarme a desconectar y hacerme pasar varios de los mejores momentos de mi vida. Aunque muchos no entendáis ni la mitad de lo que pone en este documento, es en parte gracias a vosotros.

El desarrollo de la presente tesis ha sido posible gracias a una ayuda para la Formación de Profesorado Universitario (FPU 18/03065) perteneciente al Subprograma Estatal de Formación del Ministerio de Ciencia, Innovación y Universidades de España. Además, el trabajo desarrollado está enmarcado en el proyecto ESTiMatE (Emissions SooT ModEl), que ha sido financiado por el consorcio Clean Sky 2 bajo el programa de investigación e innovación Horizonte 2020 de la Unión Europea (acuerdo No. 821418). Las actividades de simulación numérica han sido posibles gracias a la Red Española de Supercomputación y al Centro de Supercomputación de Barcelona por los recursos computacionales proporcionados en MareNostrum, además del grupo PRACE por conceder el acceso a HAWK (GCS, HLRS, Alemania) a través del proyecto SootAero.

Contents

List of Figures

List of Tables

Nomenclature

Acronyms

ACARE	Advisory Council for Aviation Research and Innovation in Europe.
ASC	Axially Staged Combustor.
BPR	Bypass Ratio.
CARS	Coherent Anti-Stokes Raman scattering spectroscopy.
CC	Combustion Chamber.
CDSM	Clustered Discrete Sectional Method.
CFD	Computational Fluid Dynamics.
CMC, DCMC	(Double) Conditional Moment Closure.
CO_2	Carbon dioxide.
CO	Carbon monoxide.
CRSB	CORIA-Rouen Spray Burner.
CRZ	Corner Recirculation Zone.
CSP	Computational Singular Perturbation method.
DAC	Double Annular Combustor.
DNS	Direct Numerical Simulation.
DQMOM	Discrete Quadrature Method of Moments.
DSM	Discrete Sectional Method.
EEA	European Environment Agency.
F-TACLES	Filtered Tabulated Chemistry LES.
FDF	Filtered Density Function.
FGM	Flamelet Generated Manifold.

FoV	Field of View treatment.
FPI	Flamelet Prolongation of ILDM.
FPV	Flamelet Progress Variable.
GHG	Greenhouse gases.
HACA	Hydrogen-Abstraction-C_2H_2-Addition mechanism.
HPC	High-Performance Computing.
ICAO	International Civil Aviation Organization.
IEA	International Energy Agency.
ILDM	Intrinsic Low-Dimensional Manifold.
IPCC	Intergovernmental Panel on Climate Change.
IRZ	Inner Reaction/Recirculation Zone.
ISAT	In Situ Adaptative Tabulation.
KH	Kelvin-Helmholtz instability breakup model.
LBG	Lean-Burned Gas.
LDI	Lean Direct Injection concept.
LEC	Low-Emissions Combustor.
LEM	Linear Eddy Mixing model.
LES	Large-Eddy Simulation.
LE	Leading Edge.
LII	Planar Laser-Induced Incandescence.
LISA	Linearized Instability Sheet Atomization model.
LPP	Lean Premixed Prevaporised concept.
LPT	Lagrangian Particle Tracking method.
MEF	Mesoscopic Eulerian Formalism.
MOM	Method of Moments.
NDF	Number Density Function.
NO_x	Nitrogen oxides.
ODE	Ordinary Differential Equation.
OPR	Overall Pressure Ratio.
ORZ	Outer Reaction Zone.
PAH	Polycyclic Aromatic Hydrocarbon.
PBE, GPBE	(General) Population Balance Equation.
PDA	Phase Doppler Anemometry.
PDF	Probability Density Function.

PE	Partial Equilibrium method.
PIV	Particle Image Velocimetry.
PLIF	Planar Laser Induced Fluorescence.
PRISM	Picewise Reusable Implementation of Solution Mapping.
PSD	Particle Size Distribution.
QSS	Quasi-Steady State method.
RANS	Reynolds-Averaged Navier-Stokes.
RBG	Rich-Burned Gas.
RMS	Root Mean Square.
RQL	Rich-burn Quick-quench Lean-burn concept.
RT	Rayleigh-Taylor instability breakup model.
SAC	Single Annular Combustor.
SGS	Sub-Grid Scale.
SMD	Sauter Mean Diameter.
SoC	Sum of Correlation treatment.
SVF	Soot Volume Fraction.
TAB	Taylor Analogy Breakup model.
TAPS	Twin Annular Premixing Swirler combustor.
TARES	Tabulated Average Representative Evaporation State model.
TCS	Turbulent Combustion Sprays workshop.
TIT	Turbine Inlet Temperature.
TRL	Technology Readiness Level.
UFPV	Unsteady Flamelet Progress Variable.
UHC	Unburned hydrocarbons.
VOF	Volume-of-Fluid method.
WALE	Wall-Adapting Local Eddy-Viscosity model.

Latin

$\boldsymbol{\mathcal{F}}$	Vector of external forces.
$\boldsymbol{\mathcal{Q}}$	Heat source term.
$\boldsymbol{f_k}$	Volume forces on species k.
$\boldsymbol{I}$	Identity matrix.
$\boldsymbol{q}$	Heat flux vector.
$\boldsymbol{S(u)}$	Strain rate tensor.

$\boldsymbol{u}$	Velocity vector.
$\boldsymbol{V_k}$	Diffusive velocity of species k.
$\boldsymbol{v_T}$	Thermophoretic velocity.
$\boldsymbol{x}$	Position vector.
$\Delta h^o_{f,k}$	Enthalpy of formation of species k.
$\dot{Q}$	Rate of soot volume fraction.
$\mathcal{H}$	Scaled enthalpy factor.
$\mathcal{S}_C$	Segregation factor of scaled progress variable.
$\mathcal{S}_Z$	Segregation factor of mixture fraction.
$\mathcal{U}$	Pseudo-random numbers.
a	Global strain rate.
a_k	Coefficient of species k in the progress variable definition.
b_i	NASA c_p coefficients.
B_M	Spalding number.
C	Scaled progress variable.
c	Constant of Vreman model.
C_D	Drag coefficient.
C_l	Modelling constant for the subgrid turbulent kinetic energy.
c_p	Specific heat capacity at constant pressure.
C_s	Constant of Smagorinsky model.
C_v	Scaled progress variable variance.
C_w	Constant of WALE model.
C_χ	Modelling constant for the subgrid part of the scalar dissipation rate.
d, d_p	In general, diameter. Refers to both droplet and soot particle diameters.
D_k	Mass diffusion coefficient of species k.
D_s	Diffusion coefficient of soot.
D_t	Thermal diffusion coefficient.
D_{10}	Arithmetic mean of the droplet size distribution.
D_{32}	Sauter Mean Diameter.
Da, Da_t, Da_η	Damköhler numbers.
f_{rad}, Q_{rad}	Radiative factor used in non-adiabatic flamelets.

G	Depending on the context, filter function of LES, generic scalar field or flame stretch in counterflow diffusion flames.
GI_Z	Flame index.
h	Enthalpy.
h_s	Sensible enthalpy.
k, k_{res}, k_{sgs}	Turbulent kinetic energy (total, resolved and subgrid).
K_{RR}	Cumulative density function of the Rosin-Rammler distribution.
Ka	Karlovitz number.
l, ℓ	Characteristic length.
L_v	Lower heating value.
L_{ij}	Leonard stress.
Le	Lewis number.
m	Mass.
N	Soot number density.
n	Continuous particle size distribution.
N_A	Avogadro number.
n_c	In the context of the CDSM model, number of soot clusters.
n_{sec}	In the context of the DSM model, number of soot sections.
Nu	Nusselt number.
p	Pressure.
P, P_Z, P_C, $P_{\mathcal{H}}$	Probability density functions.
Pr, Pr_t	Prandtl numbers.
Q	Soot volume fraction.
q	Soot volume fraction density.
R	Radial coordinate.
Re, Re_t	Reynolds numbers.
S_c	Surface of the control volume.
S_L	Laminar flame speed.
S_T	Turbulent flame speed.
S_Z	Evaporation source term.
$s_{\chi_{Y_c}}$	Subgrid part of the scalar dissipation rate of progress variable.
s_{χ_Z}	Subgrid part of the scalar dissipation rate of mixture fraction.

Sc, Sc_t	Schmidt numbers.
Sh	Sherwood number.
T	Temperature.
t	Time.
v, V	Volume.
V_c	Control volume.
V_{max}, V_{min}	Maximum and minimum soot particle volume.
W_k	Molecular weight of species k.
x, y, z	In general, coordinates of the Cartesian system. Usually, z refers to the burner axis.
Y_c	Progress variable.
Y_k	Mass fraction of species k.
Y_s	Soot mass fraction.
$Y_{c,v}$	Progress variable variance.
Z	Mixture fraction.
Z_v	Mixture fraction variance.

Greek

α_{acc}	Accommodation coefficient for the thermophoretic velocity.
α_{ij}	Velocity gradient tensor.
β_{ij}, $\beta_{i,j}$	Depending on the context, tensor used in the Vreman model or collision frequency factor in the DSM model.
$\boldsymbol{\sigma}$	Total stress tensor.
$\boldsymbol{\tau}$	Viscous stress tensor.
χ	Scalar dissipation rate.
Δx	LES filter size.
δ_{diff}	Diffusive flame thickness.
$\dot{\omega}_k$	Chemical source term of species k.
$\dot{\omega}_s$	Soot source term.
$\dot{\omega}_{Y_c}$	Progress variable source term.
η	Kolmogorov scale.
γ	Liquid volume fraction.
κ	Planck mean absorption coefficient.
λ	Thermal conductivity.
μ	Dynamic viscosity.

μ_t	Turbulent dynamic viscosity.
ν	Cinematic viscosity.
ν_t	Turbulent cinematic viscosity.
$\overline{\tau}$	In general, unresolved momentum or scalar fluxes.
ϕ, ψ	Generic magnitude or scalar variable. ϕ also denotes the equivalence ratio.
ρ	Density.
ρ_s	Soot density.
Σ	Depending on the context, flame surface density or density of interfacial area.
σ	Stefan-Boltzmann constant.
τ	In general, refers to any characteristic time.
θ	Spray half angle.
ε	Turbulent dissipation.
ζ_Z	Volume-weighted flame index.

Superscripts

$+$	Positive part of a given variable.
$-$	Negative part of a given variable.
c	Referred to clustered sections.
d	Deviatoric part of a tensor.
ext	Referred to extinction conditions.
tab	Referred to tabulated variable.

Subscripts

η	Referred to the Kolmogorov scale.
avg	Referred to the temporal average.
f	Referred to the fuel conditions.
i	Index generally used for soot sections.
j	Index generally used for soot clusters.
k	Index generally used for species.
m	Referred to the mean state of the gas phase material properties.
ox	Referred to the oxidizer conditions.
p	Referred to droplet or particle.

rms	Referred to the Root Mean Square.
st	Referred to stoichiometric conditions.
std	Referred to the standard deviation.
t	Related to a turbulent parameter.

Symbols, operators and functions

$'$	Fluctuating component.
$''$	Fluctuating component for Favre filtering.
δ	Dirac function.
δ_{ij}	Kronecker symbol.
$\langle\rangle$	Temporal average.
∇	Nabla operator.
$\overline{}$	Reynolds average or filtering.
^{T}	Transpose of a matrix.
$\mathrm{Tr}(\cdot)$	Trace operator.
$\widetilde{}$	Favre average or filtering.
D/Dt	Material derivative.

Chapter 1

Introduction

Nowadays, mankind is in a process of change in terms of energy production. Going back to the 1960s, only 6% of primary energy consumption came from low-carbon sources, while this percentage increased to around 16% in 2019, according to the data based on BP Statistical Review of World Energy [1]. These new energy sources are the sum of nuclear energy and renewable energies such as hydropower, wind, solar and others, which are positioned as an alternative to face the climate and energy crisis of recent years. Even so, and according to information published by the International Energy Agency (IEA), fossil fuels still account for more than 80% of the global energy supply, as it is illustrated in Fig. 1.1 from the last IEA World Energy Statistics report in 2021 [2]. Moreover, the specific case of the transportation sector presents the highest reliance on this energy source, accounting for up to 65% of total oil consumption, as can be observed in Fig 1.2 from the IEA report. Therefore, combustion processes and the efficient burning of these fuels remain a particularly important issue in the development of propulsion plants for this sector.

Unfortunately, combustion systems in transportation are accompanied by the generation of several products and pollutant emissions, whose effects on health and the environment can be very harmful. In fact, the detrimental health effects of air pollution are one of the main causes of disease and premature death, making it one of the most significant environmental health risks in Europe [3]. According to the European Environment Agency (EEA) estimation in 2019, up to 307,000 premature deaths were attributed to fine particulate matter ($PM_{2.5}$) emissions while around 40,000 were due to the multiple

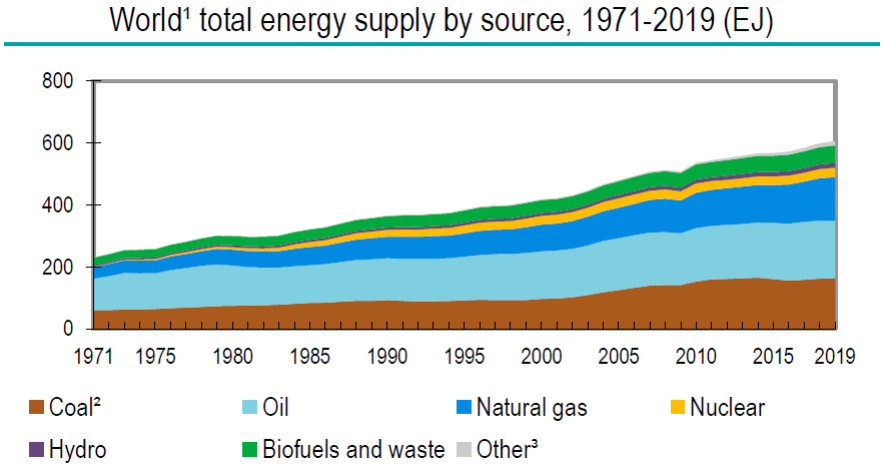

Figure 1.1: Total energy supply by fuel type ("Other" refers to geothermal, solar, wind, tide/wave/ocean, heat and other sources). [2]

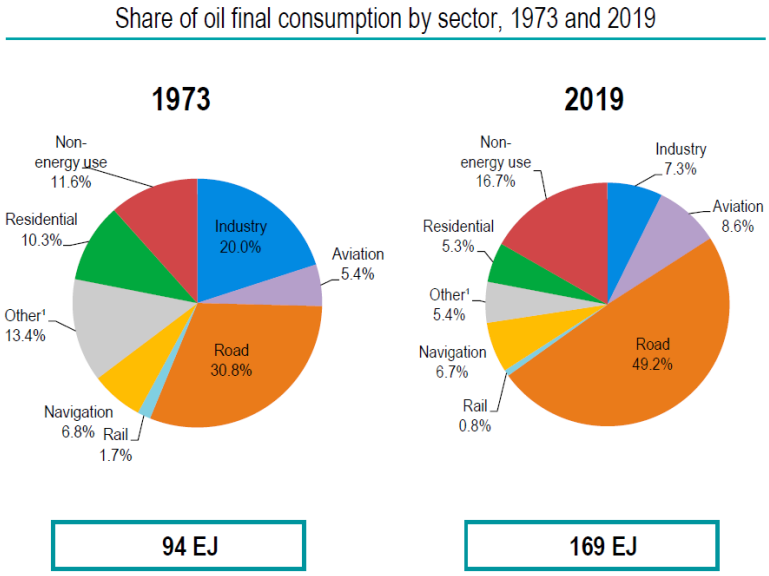

Figure 1.2: Oil consumption by sector (comparison between 1973 and 2020). [2]

adverse health effects of nitrogen dioxide (NO_2). For instance, the generation of nitrogen oxides (NO_x) is the cause of many problems such as irritation of eyes, nose and throat, breathing problems, asthma, reduced lung function or impacts on liver, spleen and blood. Similarly, fine particulate matter emissions

can cause central nervous system disturbances, chronic obstructive pulmonary disease, lung cancer or cardiovascular disorders [4]. Fig. 1.3 shows a summary of how different pollutant emissions from combustion processes can affect a multitude of organs and systems in the human body.

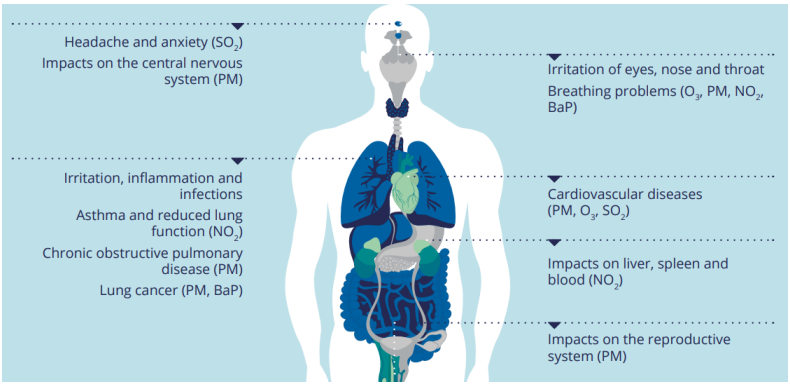

Figure 1.3: Potential impact on human health of the main sources of ambient air pollution. [4]

On the other hand, some of the products of combustion systems are part of the well-known greenhouse gases (GHG), which are responsible for the global warming, the rise in sea level and, in general, climate change. According to the most recent report published by the Intergovernmental Panel on Climate Change (IPCC) [5], the Earth's global temperature has increased on average by about 1.1°C since the pre-industrial age, largely due to the emission of greenhouse gases such as carbon dioxide (CO_2). Although there was a decrease in 2020 due to the pandemic restrictions, CO_2 emissions have rebounded in 2021 (see Fig. 1.4) and the target for the Net Zero Scenario proposed by the IEA assumes a reduction of up to 20% in CO_2 levels [6]. Consequently, the interest in reducing greenhouse emissions in the transport sector and developing cleaner and more environmentally friendly engines has increased from industry and regulators.

Concerning the particular situation of the aviation sector, air traffic generates between 2 and 3% of total CO_2 emissions, representing around 14% of the emissions of the entire transport sector and ranking as the second largest source of GHG emissions from transportation [8, 9] On top of that, aircraft engines are a major source of non-CO_2 emissions, including water vapour, SO_2, nitrogen oxides and soot particles. Although the number of flights decreased during the 2020 COVID-19 situation, air traffic is recovering in the years since, and forecasts for 2050 predict an increase of up to 5% over pre-pandemic levels [10] In this context, the reduction in GHG emissions proposed

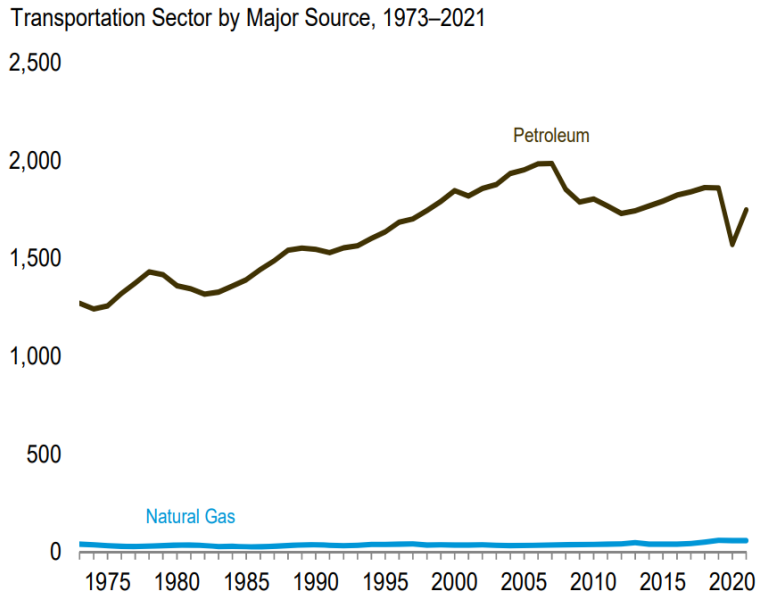

Figure 1.4: CO_2 emissions from transportation sector by major source (Million Metric Tons of CO_2). [7]

in the Paris Agreement [11], as well as the goals established by organisations such as ICAO-CAEP or the Advisory Council for Aviation Research and Innovation in Europe (ACARE), present a very challenging scenario for aviation. Fig. 1.5 summarises the main goals proposed by ACARE for 2020 and 2050, with a strong focus on CO_2, NO_x and noise reduction, but without neglecting concerns about other pollutants such as CO, unburned hydrocarbons and soot particles [12].

In general, the reduction of emissions in aero-engines can be achieved by increasing the engine thermal efficiency and the propulsive efficiency [14]. The historical increase in Overall Pressure Ratio (OPR) and Turbine Inlet Temperature (TIT) have been in the direction of increasing thermal efficiency and therefore reducing fuel consumption. However, for a given combustor technology, this has led to an increase in NO_x emissions [15], justifying the interest in the development of new burner technologies and combustion strategies. On the other hand, the increase in the Bypass Ratio (BPR) in order to benefit propulsive efficiency also entails an increase in TIT to achieve the required engine thrust. This combination of requirements results in high BPR engine designs combined with lean burn combustors. In this scenario, the research of efficient aeronautical combustion systems capable of meeting pollutant emis-

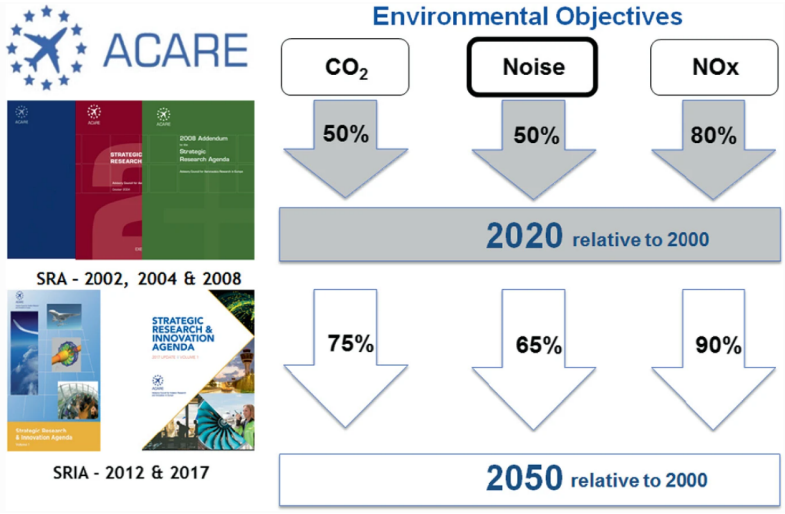

Figure 1.5: Summary of the main goals proposed by ACARE for 2020 and 2050 in terms of emission reduction. [13]

sion requirements has been and continues to be a topic of special relevance for the aviation industry. The following subsection aims to give an overview of the evolution of gas turbine burner concepts and combustion technologies in recent years, in the direction of developing efficient and environmentally friendly propulsion plants.

1.1 Current and future technologies of clean aeroengines

The interest and concern for developing low-emission combustor concepts for aircraft engines dates back to the mid-1970s, following the first regulations regarding pollutant emissions. Around this time, the Single Annular Combustor (SAC) was the standard technology for aero-engines and the Low-Emissions Combustor (LEC) concept [16–18] emerged as an alternative to conventional burners, thanks to the improvements in fuel injection systems and the combustion process in general. This combustor architecture was soon followed by what is known as Double Annular Combustor (DAC), in order to satisfy the following ICAO regulations on NO_x emissions [19]. However, the single annular technology was not abandoned and new versions of this type of burner emerged introducing lean partially premixed combustion (with the Twin Annular Premixing Swirler combustor, or TAPS) and developing advanced rich

burn technologies. In general, the whole period between the 1990s and around 2015 is marked by the coexistence of new burner designs based on the single and double annular technologies, in order to comply with the increasingly stringent CAEP regulations [20]. In the following years, the demand for engines with higher OPR (for improved fuel efficiency) that are capable of maintaining even lower NO_x levels has put some of the existing burner concepts at risk and has resulted in the development of newer technologies (such as the Lean Direct Injection concept), which are currently at a lower Technology Readiness Level (TRL).

Starting with one of the most defining technologies for aeronautical burners, the Rich-Burn Quick-Mix Lean-Burn (RQL) concept was employed in many of the modern aero-engines. The RQL concept dates back to 1980 [21] and has been the most representative combustion technology for advanced rich burn combustors. In this system, the combustion process is divided into three parts: the combustion of a rich fuel-air mixture in the primary zone, a quick quench or quick mixing region with secondary injected air and a final combustion under lean conditions due to the additional dilution air. A schematic of this type of burner can be seen on the left side of Fig. 1.6. The first region allows for improved combustion stability due to the generation of high concentrations of energetic hydrogen and hydrocarbon radical species. In addition, the reduced flame temperature and oxygen concentration due to the rich conditions prevents NO_x production. However, the products of this first combustion zone contain high amounts of CO, UHC and soot [22], so the quench section located downstream is necessary to oxidize CO and other intermediate species. The transition to the lean region involves passing through stoichiometric mixing conditions, where the temperature increases and favorable conditions for the formation of NO_x are satisfied. Therefore, it is necessary a very quick mixture with the secondary air to minimise the generation of thermal NO_x. The graphic on the right side of Fig. 1.6 illustrates the described NO_x formation path inside a RQL combustor. Finally, the lean burn section is employed to completely consume CO, soot and unburned hydrocarbons. The RQL technology proved to be a very promising alternative to conventional burners due to its advantages in terms of ignition, combustion stability and emission reduction. In fact, in its early years, due to its overall performance and safety considerations, the RQL was preferred over lean premixed options in aero-engine applications [23]. Nevertheless, while the concept has room for improvement, soot generated by RQL combustors can be high if the airflow distribution is not well optimized and its capability to reduce NO_x is limited [24], especially taking into account the very high OPR levels of recent years.

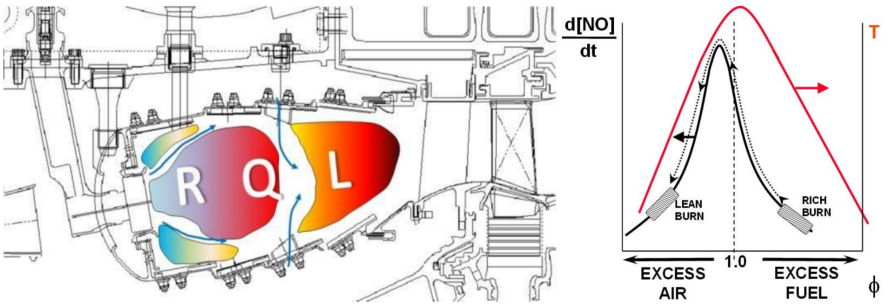

Figure 1.6: Left: Schematic of the RQL concept [25], right: NO_x path inside the RQL burner [23]. ϕ, equivalence ratio.

As an introduction to lean combustion in aircraft propulsion plants, burner concepts with a fuel-staging strategy were conceived almost contemporaneously to the RQL technology. So that, the Double Annular Combustor (DAC) [26] and the Axially Staged Combustor (ASC) [17] concepts emerged with a combustion chamber operating at lower equivalence ratios (between 0.6 and 0.8) in order to further decrease NO_x emissions. Overall, the working principle of both systems is quite similar: the fuel-air mixture level, combustion stoichiometry and the temperature reached in the combustion chamber are controlled in a staged way, by injecting fuel in different locations. Therefore, the injectors in the region usually named as pilot zone operate at low power settings and the main zone is fueled and ignited at higher power requirements. While the DAC system distributes the different fuel injection regions in two concentric annuluses, the SAC system uses an axial distribution and the main stage is placed downstream the combustor. The objective of achieving lean operating conditions resulted in significant NO_x and soot reductions in these concepts, however, other problems related to design complexities, difficulties in control systems and low combustion efficiency in the mid power range were encountered [24].

One of the first concepts to incorporate a partially premixed combustion system was the Twin Annular Premixing Swirler (TAPS). It is a system that pretends to solve the difficulties posed by double annular and fuel-staged burner concepts by investigating new approaches to the single annular combustor [27]. In fact, the configuration of the TAPS technology is very similar at first sight to conventional SAC concept and the main difference lies in the fuel injection system. The key to TAPS concept is the incorporation of partially premixed combustion with a internally staged injection technology. Ignition and flame stability at low power is maintained by a pilot only mode composed of a simplex atomiser which interacts with the surrounding swirled air

streams and atomises the fuel spray. The main stage is mounted concentrically to the pilot stage and the primary partially premixed flame is stabilised in the mixing layer between pilot and main stages [24]. This technology has been awarded ultra-low NO_x status due to the capability of premixed combustion to reduce these emissions over the long term. In addition, it features several improvements over previous concepts, such as better temperature distribution at the burner exit, which increases turbine life. In Fig. 1.7, it is possible to observe an schematic of the concepts previously described, as well as a brief comparison of their characteristics. From this combustor technology, GE Aviation continued the line of research and developed the TAPS II concept, with the aim of improving burner characteristics, further reducing emissions and extending the system to smaller engine designs [28].

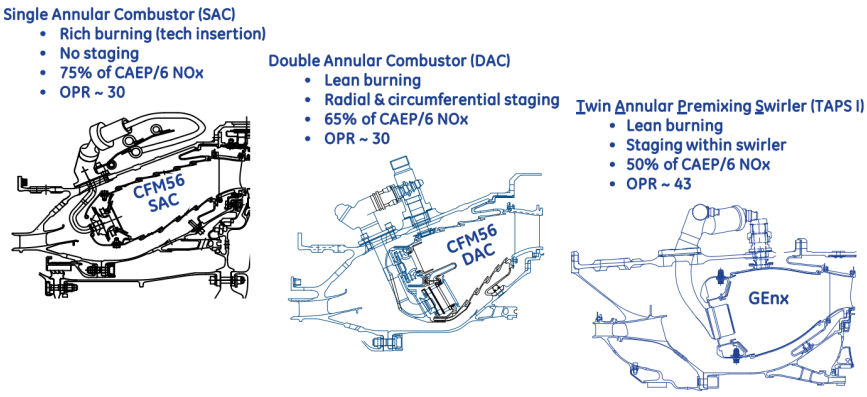

Figure 1.7: Schematics and comparison between SAC, DAC and TAPS systems from GE combustors [27].

Within this ultra-low NO_x category it is also possible to find the Lean Direct Injection (LDI) [29] and Lean Premixed Prevaporised (LPP) [30] technologies (schematics in Fig. 1.8). Although they were conceived shortly after the previous ones (in fact, the TAPS concept has occasionally been referred to as LDI or LPP [31, 32]), their development is more modern and they have remained at a slightly lower TRL. The LDI system is based on the injection of fuel directly into the combustion chamber. A large fraction of air is swirled upstream and a rapid fuel-air mixing in the near injection region is intended, reaching a low equivalence ratio. Therefore, the LDI concept needs to achieve an efficient mixing of air and fuel before completing combustion and to deal with possible instabilities of the reaction process, since they operate close to the extinction limit [33]. This strategy is expected to perform stably and to generate very low NO_x emissions over a wide range of operating conditions,

especially at high temperature and pressure [15]. On the other hand, the LPP concept is probably the most promising in terms of nitrogen oxide production. In this case, fuel is evaporated and mixed with the air stream before entering the combustion chamber, creating a homogeneous mixture at low equivalence ratio which is close to the lean blowout limit. One of the key factors of this system is to achieve a uniform lean mixture so that local hot rich-burn spots are eliminated. Consequently, in addition to reducing NO_x emissions, there are no emissions of soot particles. As is generally the case with combustors based on premixed combustion, the main design challenge is to prevent auto-ignition, flashback and blowout risk, which poses very demanding limitations on the application for modern aero-engines with high OPR.

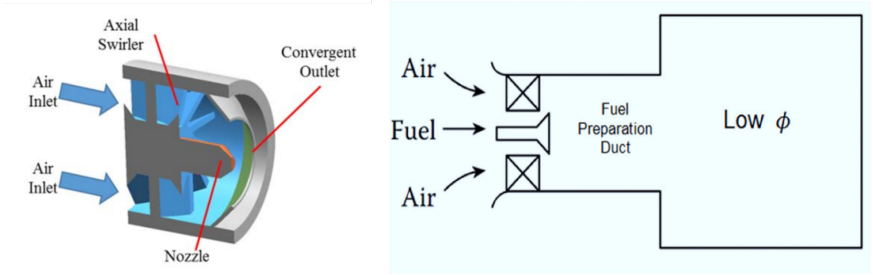

Figure 1.8: LDI injection module [34] and schematic of LPP combustor concept [15].

In view of the many different concepts described above (and many other more complex or specific ones that have been omitted) that marked the evolution of combustors in gas turbine engines, the interest in developing cleaner burner technologies and in understanding in depth the physic-chemical processes that take place in combustion chambers seems justified. However, due to the complexity of this kind of applications, it is not easy to find tools that allow the analysis of combustion and emissions production at an affordable cost.

1.2 Thesis objective

Based on the above mentioned context, the present thesis is focused on the study and analysis of combustion and soot production in representative gas turbine engine applications from a numerical modelling framework. Soot formation appears to be important only in RQL technologies, however, it is also relevant in lean burner concepts. Although no soot is expected in the main operating condition, the switch from pilot to main operation mode may lead

to smoke generation and, therefore, an accurate estimation of soot particulates may be necessary. From the different technologies described in the previous section, many researchers have developed combustors with simplified geometries to experimentally study the physico-chemical phenomena that take place in these applications [35–39]. However, even these academic rigs are very expensive to manufacture, test and measure, so other tools have appeared to complement the experiments in the recent years.

This is the case of Computational Fluid Dynamics (CFD), which has recently become a fundamental design tool [40, 41] and has made important contributions to increasing efficiency, reducing pollutant emissions and using alternative fuels in a wide range of practical applications [42]. In particular for the study of turbulent flames, most numerical simulations in industrial applications have been considering RANS (Reynolds-Average Navier-Stokes) models, but during the last few years the increase in computational power has allowed the transition to Large-Eddy Simulations (LES). The development and evolution of High-Performance Computing (HPC) systems [43, 44] has led to high-fidelity simulations on complex geometries where the uncertainty of the models has been reduced and the reliability of the numerical predictions has increased [45–49]. In this sense, the main objective of this thesis is *the study and analysis of the reactive flow in gas turbine applications, as well as the validation of numerical models for combustion and soot predictions, by means of high-fidelity CFD simulations.*

In addition, in order to achieve the primary objective, a set of partial or specific objectives are defined below, which will define the content of the research work:

- Define a solid working methodology for the performance of high-fidelity LES in representative aeronautical burner applications, from the numerical model approach and pre-processing to the development of tools for post-processing and analysis of the results.
  - Set-up different study cases of aeronautical applications and solve multiple simulations with a HPC research code, checking the numerical stability and evaluating the computational cost to achieve computationally efficient calculations.
  - Develop post-processing tools and algorithms for the evaluation of results. Validate the models employed by comparing the numerical predictions with experimental measurements available in the literature for the different cases.

- Study of the liquid fuel injection and the combustion process in spray flames. This is the first application case where a tabulated chemistry approach and a Lagrangian spray model will be used to characterize the reacting flow. For this purpose, an atmospheric reference flame, based on a LDI aeronautical burner is selected for the analysis.
  - Characterize the carrier and dispersed phase and evaluate the numerical predictions in terms of gas and droplet velocities.
  - Illustrate the flame structure and topology, distinguishing between the different regions of the flame, analysing the distribution of chemical species and evaluating the lift-off length.
  - Analyze the results focusing on the interaction between droplets and the flame front. Demonstrate the capability of the considered modelling framework of reproducing the different extinction phenomena that appear in this application.
- Analysis of the reacting flow and soot formation and oxidation phenomena in a gas turbine model combustor. In this second application, the previously mentioned combustion model based on tabulated chemistry will be coupled to a computationally efficient detailed soot model for emissions prediction. A sooting RQL-like pressurized burner is considered for this study.
  - Characterize the flow pattern inside the combustor and identify the different recirculation zones and turbulent structures.
  - Analyze the soot formation and oxidation process and discuss the capability of the soot modelling approach to reproduce soot distribution and quantity, as well as particle size distributions.
  - Evaluate the effect of including secondary dilution air in terms of the reacting flow field characterization and soot production.

The present research has been carried out within the frame of the *CMT-Motores Térmicos* institute at *Universitat Politècnica de València* (Spain), which has acquired over the years a great deal of experience in thermal engine research and the automotive sector, but has also recently entered the aviation industry. Indeed, this thesis has been supported by the national CHEST project funded by the Spanish Ministerio de Economía y Competitividad and by the European project Emissions SooT ModEl (ESTiMatE),

of which the CMT institute is a partner together with the Barcelona Supercomputing Center (BSC), Technischen Universität Berlin (TUB), Technische Universiteit Eindhoven (TUE), Technische Universität Darmstadt (TUD), Karlsruher Institut für Technologie (KIT) and the Institute of Combustion Technology for Aerospace Engineering (IVLR) at Stuttgart University. The ESTiMatE project aims to address the issue of soot formation for kerosene-type fuels and to contribute to the characterization and prediction of the combustion process and emissions by using advanced numerical simulation validated with reference experiments.

1.3 Thesis outline

After introducing the present research work with the appropriate context (**Chapter 1**), the structure and content of the thesis document, consisting of a total of six chapters, is described below.

Chapter 2 contains a literature review on the fundamentals of numerical modelling in gas turbine applications. Since this research has a numerical focus, the chapter aims to describe the most relevant physical processes present in these systems and to review the modelling strategies that have been employed in recent years. Therefore, combustion and turbulence theory will be briefly described, as well as the different models available to characterise turbulent reactive flow, liquid fuel injection and predict soot emissions.

In **Chapter 3**, the methodology followed for performing the CFD simulations and the numerical tools used are presented. This chapter is mainly focused on the detailed description of the models used for the prediction of reactive flow, liquid fuel injection and soot particle production. In addition, some generalities of the multi-physics HPC code and numerical methods used will be mentioned.

Chapter 4 includes the study carried out on the first application case described in the thesis objectives. The combustion process will be studied and the accuracy of the CFD models used will be evaluated in an atmospheric reference flame with n-heptane injection. The idea of this chapter is to provide insight on the reacting flow with liquid fuel injection and to assess the different numerical models for combustion and spray characterization in an aero-burner application. In addition, droplet-flame interaction phenomena are analyzed and the capabilities of the modelling framework for reproducing flame local extinction are evaluated.

The structure of **Chapter 5** is very similar to the previous one and is intended to illustrate the study of the reactive flow and soot emissions on a gas turbine combustor. In this case, a pressurized swirl-stabilized burner is considered with a usual RQL-like architecture, due to the higher soot production of the mentioned concept. The results for both gaseous and solid phases are presented and compared with experimental measurements for the model validation. Furthermore, the effect of the dilution air inside the combustion chamber in terms of soot production is evaluated and discussed.

Finally, **Chapter 6** summarizes the main conclusions of the thesis, concerning general findings about numerical modelling on gas turbine applications and more specific aspects of combustion and soot modelling. Moreover, some indications are given about possible future works or investigations based on the knowledge acquired during this thesis.

References

[1] BP. *Statistical Review of World Energy*. 2020.

[2] International Energy Agency. *Key World Energy Statistics 2021*. 2021.

[3] European Environment Agency. *Air pollution: how it affects our health*. 2021.

[4] European Environment Agency. *EEA Report: Healthy environment, healthy lives: how the environment influences health and well-being in Europe*. 2020.

[5] Intergovernmental Panel on Climate Change. *Climate Change 2021 The Physical Science Basis*. 2021.

[6] International Energy Agency. *Transport – analysis*. 2022.

[7] U.S. Energy Information Administration. *September 2022 Monthly Energy Review*. 2022.

[8] International Energy Agency. *CO2 Emissions in 2022*. 2021.

[9] Lee, David S et al. "The contribution of global aviation to anthropogenic climate forcing for 2000 to 2018". In: *Atmospheric Environment* 244 (2021), p. 117834.

[10] EASA. *European Aviation Environmental Report 2022*. 2022.

[11] United Nations Framework Convention on Climate Change. *Paris Agreement: UN Climate Conference*. 2015.

[12] ACARE. *Strategic Research and Innovation Agenda, The goals of Flightpath 2050*. 2017.

[13] Kors, Eugene and Collin, Dominique. "Perspective on 25 Years of European Aircraft Noise Reduction Technology Efforts and Shift Towards Global Research Aimed at Quieter Air Transport". In: *Aviation Noise Impact Management: Technologies, Regulations, and Societal Well-being in Europe*. Springer International Publishing Cham, 2022, pp. 57–116.

[14] Yin, Feijia and Rao, A Gangoli. "Performance analysis of an aero engine with inter-stage turbine burner". In: *The Aeronautical Journal* 121.1245 (2017), pp. 1605–1626.

[15] Lefebvre, Arthur H and Ballal, Dilip R. *Gas turbine combustion: alternative fuels and emissions*. CRC press, 2010.

[16] Roberts, R, Peduzzi, A, and Vitti, GE. *Experimental clean combustor program, phase 1.* Tech. rep. 1975.

[17] Bruce, TW, Davis, FG, Kuhn, TE, and Mongia, HC. *Pollution Reduction Technology Program for Small Jet Aircraft Engines, Phase 2.* Tech. rep. 1978.

[18] Anderson, RD, Herman, AS, Tomlinson, JG, Vaught, JM, and Verdouw, AJ. *Pollution Reduction Technology Program, Turboprop Engines, Phase 1.* Tech. rep. 1976.

[19] Mongia, HC and Dodds, WGAE. "Low emissions propulsion engine combustor technology evolution past, present and future". In: *24th Congress of International Council of the Aeronautical Sciences, Yokohama, Japan, Aug.* 2004, pp. 2004–609.

[20] Madden, Paul. "CAEP combustion technology review process and CAEP NOx goals". In: *CAEP Publication: Fergus Falls, MN, USA* (2014).

[21] Mosier, SA and Pierce, RM. "Advanced Combustor Systems for Stationary Gas Turbine Engines, Phase I. Review and Preliminary Evaluation, Volume I". In: *contract* (1980), pp. 68–02.

[22] Samuelsen, GS, Brouwer, J, Vardakas, MA, and Holdeman, JD. "Experimental and modeling investigation of the effect of air preheat on the formation of NO x in an RQL combustor". In: *Heat and Mass Transfer* 49 (2013), pp. 219–231.

[23] Samuelsen, Scott. "Rich burn, quick-mix, lean burn (RQL) combustor". In: *The Gas Turbine Handbook* (2006), pp. 227–233.

[24] Liu, Yize et al. "Review of modern low emissions combustion technologies for aero gas turbine engines". In: *Progress in Aerospace Sciences* 94 (2017), pp. 12–45.

[25] Guellouh, Noureddine, Szamosi, Zoltán, and Siménfalvi, Zoltán. "Combustors with low emission levels for aero gas turbine engines". In: *International Journal of Engineering and Management Sciences* 4.1 (2019), pp. 503–514.

[26] Bahr, DWand and Gleason, CC. *Experimental clean combustor program, phase 1.* Tech. rep. 1975.

[27] Foust, Michael, Thomsen, Doug, Stickles, Richard, Cooper, Clayton, and Dodds, Will. "Development of the GE aviation low emissions TAPS combustor for next generation aircraft engines". In: *50th AIAA aerospace sciences meeting including the new horizons forum and aerospace exposition*. 2012, p. 936.

[28] Stickles, R and Barrett, J. *TAPS II combustor final report*. Tech. rep. 2013.

[29] Alkabie, HS, Andrews, GE, and Ahmad, NT. "Lean low NOx primary zones using radial swirlers". In: *Turbo Expo: Power for Land, Sea, and Air*. Vol. 79207. American Society of Mechanical Engineers. 1988, V003T06A027.

[30] Rusell, P., Beal, G., and Hinton, B. "Low NOx heavy fuel combustor concept program". In: *NASA Technical Report* (1981).

[31] Kuentzmann, Paul. *Report of the independent experts to CAEP/8 on the second NOx review and the establishment of medium and long term technology goals for NOx*. Vol. 9953. International Civil Aviation Organization, 2010.

[32] Dhanuka, Sulabh K, Temme, Jacob E, and Driscoll, James F. "Unsteady aspects of lean premixed prevaporized gas turbine combustors: flame-flame interactions". In: *Journal of Propulsion and Power* 27.3 (2011), pp. 631–641.

[33] Belmar Gil, Mario. "Computational study on the non-reacting flow in Lean Direct Injection gas turbine combustors through Eulerian-Lagrangian Large-Eddy Simulations". PhD thesis. Universitat Politècnica de València, 2021.

[34] Yu, Han, Zhu, Pengfei, Suo, Jianqin, and Zheng, Longxi. "Investigation of discharge coefficients for single element lean direct injection modules". In: *Energies* 11.6 (2018), p. 1603.

[35] Weigand, Peter, Meier, Wolfgang, Duan, Xu Ru, Stricker, Winfried, and Aigner, Manfred. "Investigations of swirl flames in a gas turbine model combustor: I. Flow field, structures, temperature, and species distributions". In: *Combustion and flame* 144.1-2 (2006), pp. 205–224.

[36] Janus, B, Dreizler, A, and Janicka, J. "Experiments on swirl stabilized non-premixed natural gas flames in a model gasturbine combustor". In: *Proceedings of the Combustion Institute* 31.2 (2007), pp. 3091–3098.

[37] Linassier, Guillaume et al. "Application of numerical simulations to predict aircraft combustor ignition". In: *Comptes Rendus Mécanique* 341.1-2 (2013), pp. 201–210.

[38] Barré, David et al. “Flame propagation in aeronautical swirled multi-burners: Experimental and numerical investigation”. In: *Combustion and Flame* 161.9 (2014), pp. 2387–2405.

[39] Geigle, Klaus Peter, Zerbs, Jochen, Köhler, Markus, Stöhr, Michael, and Meier, Wolfgang. “Experimental analysis of soot formation and oxidation in a gas turbine model combustor using laser diagnostics”. In: *Journal of engineering for gas turbines and power* 133.12 (2011).

[40] Versteeg, Henk Kaarle and Malalasekera, Weeratunge. *An introduction to computational fluid dynamics: the finite volume method*. Pearson education, 2007.

[41] Slotnick, Jeffrey P et al. *CFD vision 2030 study: a path to revolutionary computational aerosciences*. Tech. rep. 2014.

[42] Veynante, Denis and Vervisch, Luc. “Turbulent combustion modeling”. In: *Progress in energy and combustion science* 28.3 (2002), pp. 193–266.

[43] Jeffers, James and Reinders, James. *Intel Xeon Phi coprocessor high performance programming*. Newnes, 2013.

[44] Saini, Subhash et al. “Early multi-node performance evaluation of a knights corner (KNC) based NASA supercomputer”. In: *2015 IEEE International Parallel and Distributed Processing Symposium Workshop*. IEEE. 2015, pp. 57–67.

[45] Gövert, Simon, Mira, Daniel, Kok, Jacobus BW, Vázquez, Mariano, and Houzeaux, Guillaume. “Turbulent combustion modelling of a confined premixed methane/air jet flame using tabulated chemistry”. In: *Energy procedia* 66 (2015), pp. 313–316.

[46] Hasse, Christian. “Scale-resolving simulations in engine combustion process design based on a systematic approach for model development”. In: *International Journal of Engine Research* 17.1 (2016), pp. 44–62.

[47] Donini, A, M. Bastiaans, RJ, Van Oijen, JA, and H. de Goey, LP. “A 5-D implementation of FGM for the large eddy simulation of a stratified swirled flame with heat loss in a gas turbine combustor”. In: *Flow, turbulence and combustion* 98 (2017), pp. 887–922.

[48] Gövert, Simon, Mira, Daniel, Kok, Jim BW, Vázquez, Mariano, and Houzeaux, Guillaume. “The effect of partial premixing and heat loss on the reacting flow field prediction of a swirl stabilized gas turbine model combustor”. In: *Flow, turbulence and combustion* 100 (2018), pp. 503–534.

[49] Mira, Daniel, Pérez-Sánchez, Eduardo J, Borrell, Ricard, and Houzeaux, Guillaume. "HPC-enabling technologies for high-fidelity combustion simulations". In: *Proceedings of the Combustion Institute* (2022).

Chapter 2

Fundamentals of numerical modelling in gas turbine burners

In most aeronautical burner applications (and, in general, in most engineering applications) combustion is turbulent in nature. On the one hand, most naturally occurring flows are turbulent and, in addition, the combustion process releases heat and generates certain instabilities in the flow by buoyancy and gas expansion, which favours the transition to this flow regime. On the other hand, turbulence accelerates mixing processes and thus improves combustion. In other words, combustion and turbulent flow are two physical (or physico-chemical) phenomena that are highly synergistic and benefit from each other for most industrial applications. However, turbulent combustion is an extremely complex phenomenon even today, as its study and understanding involves a large number of disciplines. Generally speaking, just the study of turbulence or combustion itself presents an obvious challenge, as these are complex phenomena if treated independently. But the number of associated and coupled physical and chemical processes makes the study of turbulent combustion a great challenge for the research community even today.

In relation to the above, there are several fundamental aspects that are worth understanding and studying with regard to the analysis of the reactive flow in a general combustion system:

- One of the fundamental elements of a combustion system is the fuel itself, which may be present in different states of matter depending on the particular application (e.g. coal, gasoline, natural gas...). In many cases, such as in aviation engines, the fuel is in a liquid state and its injection into the combustion chamber and its atomisation are very relevant processes, the study of which is already a considerable challenge. In addition, combustion takes place at the molecular level, so it is necessary to evaporate the liquid fuel droplets and to achieve a suitable air-fuel mixture in a reasonable time and space.

- Achieving a fast mixing process between gaseous air and fuel requires high velocities induced by turbulent flow, as mentioned above. Although it is a discipline that has been extensively studied for several years, there is still a significant lack of knowledge about the nature of turbulence. It is a scientific field that has presented many difficulties due to its chaotic nature and many of the conclusions drawn from particular cases are not yet extensible to general flow or any other type of application.

- The combustion process in essence (from the point of view of the set of reactions and chemical species that take place and that participate in the oxidation of the fuel) is another great challenge as far as the study of turbulent reactive flow is concerned. From a chemical point of view, combustion can be described by a very large number of reactions (in the order of thousands) and involves about several hundred chemical species. Therefore, it is practically impossible to include all the chemical steps describing the process in a numerical model and it is necessary to develop and employ different strategies to discard the reactions and chemical species that are less relevant or that affect the results to a lesser extent.

- Related to the previous point, the generation of pollutants such as NO_x, CO or soot is another process that occurs at the molecular level and depends on many chemical and physical factors. For instance, the soot formation process from the nucleation of the first particles to their growth into larger particles depends on several chemical species originated during the fuel oxidation. In addition, and more specifically in turbulent flames, soot production is strongly coupled to the flow and flame dynamics and thus becomes a very complex problem due to the large number of multi-physical interactions. To this day, there are some questions that remain open, such as the pathways leading to the formation of the first soot precursor molecules or the transition from these to the incipient particles [1].

- Since combustion releases a considerable amount of energy, heat transfer, heat loss to the walls and radiation effects are other topics of interest with regard to combustion systems. From a more technological approach, it is necessary to have control of how much of the heat released during combustion is transferred to the different elements of an engine to ensure that they do not overheat. On the other hand, heat losses to the walls, including radiation, are of great importance for NO_x production, as they greatly affect the flame temperature and thus influence the formation mechanism of this pollutant.

The points listed here are only intended to summarise some of the most important aspects of turbulent flames and to highlight the complexity of the problem from a phenomenological point of view. From the point of view of numerical modelling, this whole set of coupled phenomena with different characteristic time and length scales is one of the major difficulties in predicting the reactive flow in combustion systems [2]. Ultimately, most modelling strategies involve establishing a balance between what part of the physical process is solved directly and what part is modelled according to certain more or less restrictive hypotheses. In the context of numerical models, there is a trade-off between the degree of simplification of the physical phenomenon (in terms of sub-processes solved, modelled or even not included in the model) and the computational cost of the calculation. In many cases, using very detailed models in terms of the physics solved does not compensate for the disproportionate increase in computational resources, which can even become impractical in realistic applications or practical devices.

This thesis document comprises a research work on numerical modelling of turbulent combustion in gas turbine burners and, therefore, this chapter aims to review the most relevant physical and chemical fundamentals in these applications, as well as the most widely used modelling frameworks for the prediction of each of the important processes in the field of turbulent reactive flow. First, to start from the basis of the problem, the fundamental equations of fluid mechanics are described. After this, the most important concepts of turbulence theory, combustion, soot formation and oxidation and sprays are briefly presented. In each section, the theoretical foundations of each of these disciplines are described on the one hand and the most relevant ideas and strategies concerning numerical modelling are presented on the other hand. Emphasis is placed on aeronautical combustor applications as well as on the concepts that contextualise the work to be presented in the following chapters. It is important to mention that the content of this chapter is no more than a condensed summary of the vast theoretical framework behind disciplines such

as fluid mechanics or turbulent combustion and any interested reader can find more detailed information on these topics in the multitude of books available [3–6].

2.1 Equations of fluid mechanics

To introduce the fundamentals of turbulent combustion, it is important to first review the governing equations of fluid mechanics. These equations are usually presented in a variety of forms, however, they all arise from the application of the fundamental laws of physics (i.e. conservation of mass, Newton's laws and thermodynamics) to a fluid volume. When these laws are applied directly to a fluid volume that follows the trajectory of a fluid particle, what is known as a Lagrangian formulation is obtained. Nevertheless, it is common to consider this volume in a fixed position in space, thus an Eulerian formulation is employed. In this way, the concept of control volume (V_c) is first defined as an open system that allows mass flow, together with the surface that delimits it or control surface (S_c). The set of conservation equations is complemented by initial and boundary conditions, as well as constitutive relations that define other processes at the molecular level such as reactions, molecular diffusion or equations of state.

Before expressing the different equations, it is useful to define two concepts that serve to understand and deduce the conservation equations. On the one hand, the material derivative represents the rate of change of a certain physical quantity ϕ due to it is subjected to a fluid field with a certain velocity:

$$\frac{D\phi}{Dt} = \frac{\partial \phi}{\partial t} + \boldsymbol{u} \cdot \nabla \phi. \tag{2.1}$$

The first term on the right hand side (RHS) of Eq. 2.1 is the temporal derivative of the physical magnitude and the second represents the convective term, which is defined by the scalar product of the velocity vector $\boldsymbol{u}$ and the gradient (expressed by the operator ∇) of ϕ.

On the other hand, the Reynolds transport theorem helps to drive the fundamental conservation laws that will be described later. The general form of the Reynolds theorem is as follows:

$$\frac{d}{dt}\int_{V_c} \phi \, dV = \int_{V_c} \frac{\partial \phi}{\partial t} \, dV + \int_{S_c} \phi \boldsymbol{u} \, d\boldsymbol{S}. \tag{2.2}$$

Thus, the variation over time of an extensive quantity attached to a given fluid volume (term on the left hand side of the equation 2.2) is equal to the sum of the variation of the associated intensive quantity ϕ (specific property or per unit mass) in the control volume and the convective flux of that quantity across the surface of the control volume.

The first conservation equation is derived by applying this theorem to the mass property. So that, the continuity equation in its conservative form (this formulation is followed along this text) read as follows:

$$\frac{\partial \rho}{\partial t} + \boldsymbol{\nabla} \cdot (\rho \boldsymbol{u}) = 0. \tag{2.3}$$

In this equation, ρ is the density and $\boldsymbol{u}$ is the velocity vector.

For a general combustion problem, multiple species are involved through multiple chemical reactions. Therefore, it is convenient to formulate the transport equation for species mass conservation (for N_s species):

$$\frac{D\rho Y_k}{Dt} = \frac{\partial \rho Y_k}{\partial t} + \boldsymbol{\nabla} \cdot (\rho \boldsymbol{u} Y_k) = \boldsymbol{\nabla} \cdot (-\rho \boldsymbol{V_k} Y_k) + \dot{\omega}_k, \quad k = 1, ..., N_s, \tag{2.4}$$

where Y_k is the mass fraction, $\boldsymbol{V_k}$ is the diffusive velocity and $\dot{\omega}_k$ is the chemical source term of the kth species.

The diffusive mass flux $\rho \boldsymbol{V_k} Y_k$ represents the transport of species apart from their transport due to the flow velocity $\boldsymbol{u}$. The expression for species diffusion may be obtained by solving a linear system of equations of size N_s^2 in each direction at each point and at each instant for non-stationary flows [3], which is computationally very expensive [7] and simplifications are commonly used. Many approximations adopt Fick's law, which allows the diffusive flux to be expressed as follows:

$$\rho \boldsymbol{V_k} Y_k = -\rho D_k \boldsymbol{\nabla} Y_k, \quad k = 1, ..., N_s. \tag{2.5}$$

In Eq. 2.5, D_k is the mass diffusion coefficient for species k. Several approaches are based on a mixture-averaged mass diffusion coefficient [8] while other more complex strategies consider a multi-component formulation [9].

By the application of the theorem described by Eq.2.2 to the linear momentum, together with Newton's second law, the conservation of momentum may be expressed with the following equation:

$$\frac{D\rho\boldsymbol{u}}{Dt} = \frac{\partial\rho\boldsymbol{u}}{\partial t} + \boldsymbol{\nabla}\cdot(\rho\boldsymbol{u}\boldsymbol{u}) = \boldsymbol{\nabla}\cdot\boldsymbol{\sigma} + \boldsymbol{\mathcal{F}}. \tag{2.6}$$

In this expression, $\boldsymbol{\sigma}$ is the total stress tensor and $\boldsymbol{\mathcal{F}}$ is the vector of external forces.

The total stress that affects and deforms a certain fluid volume is composed of a part that depends on the hydrostatic pressure (and acts in the normal direction) and by the viscous stresses, such that:

$$\boldsymbol{\sigma} = -p\boldsymbol{I} + \boldsymbol{\tau}, \tag{2.7}$$

where p is the pressure, $\boldsymbol{I}$ is the identity matrix and $\boldsymbol{\tau}$ is the viscous stress tensor. For Newtonian fluids and gas-phase flows applications, the viscous stress tensor may be described by the following expression:

$$\boldsymbol{\tau} = \mu\left[(\boldsymbol{\nabla}\boldsymbol{u}) + (\boldsymbol{\nabla}\boldsymbol{u})^T - \frac{2}{3}(\boldsymbol{\nabla}\cdot\boldsymbol{u})\,\boldsymbol{I}\right]. \tag{2.8}$$

In this relation, μ is the dynamic viscosity and the bulk viscosity is supposed to be zero [10]. It is interesting to also define the kinematic viscosity ν, given by $\nu = \mu/\rho$.

Regarding the energy equation, special attention is required as it can take different forms depending on whether it is formulated for the internal energy, enthalpy (and/or its different chemical and sensible contributions) or even temperature. More details on this distinction can be found in the book by Poinsot and Veynante [3]. For this text, enthalpy (chemical and sensible) has been considered when formulating the energy equation, which read as follows:

$$\frac{D\rho h}{Dt} = \frac{\partial\rho h}{\partial t} + \boldsymbol{\nabla}(\rho\boldsymbol{u}h) = \frac{Dp}{Dt} - \boldsymbol{\nabla}\cdot\boldsymbol{q} + \boldsymbol{\tau}\cdot\boldsymbol{\nabla}\boldsymbol{u} + \boldsymbol{\mathcal{Q}} + \rho\sum_{k=1}^{N_s} Y_k\boldsymbol{f_k}\cdot\boldsymbol{V_k}, \tag{2.9}$$

where $\boldsymbol{\mathcal{Q}}$ is the heat source term and $\rho\sum_{k=1}^{N_s} Y_k\boldsymbol{f_k}\cdot\boldsymbol{V_k}$ is the power produced by volume forces $\boldsymbol{f_k}$ on species k.

It is worth to highlight that the expression is written for the enthalpy considering the sensible and chemical contribution. Thus, h takes the form:

$$h = h_s + \sum_{k=1}^{N_s} \Delta h^o_{f,k} Y_k = \int_{T_0}^{T} c_p \, dT + \sum_{k=1}^{N_s} \Delta h^o_{f,k} Y_k, \tag{2.10}$$

with h_s being the sensible enthalpy, $\Delta h^o_{f,k}$ the enthalpy of formation of species k at standard temperature, T_0 a reference temperature and c_p the mass heat capacity at constant pressure.

The heat flux vector $\boldsymbol{q}$ includes contributions from different types of heat transfer. A general form including the heat flux given by Fourier's law and a second term due to species diffusion with different enthalpies may be expressed as follows:

$$\boldsymbol{q} = -\lambda \boldsymbol{\nabla} T + \rho \sum_{k=1}^{N_s} h_k Y_k \boldsymbol{V_k}, \tag{2.11}$$

where λ is the mixture thermal conductivity and h_k the enthalpy of species k. It is useful to define the thermal diffusion coefficient D_t with the relation $D_t = \lambda / (\rho c_p)$.

The term $\Phi = \boldsymbol{\tau} \cdot \boldsymbol{\nabla u}$ in Eq. 2.9 takes special relevance when it comes to characterize dissipation in turbulent flows. It is the viscous heating source term and describes the energy transfer from the kinetic energy of the flow and the thermal energy due to viscous friction.

Finally, it is important to define several dimensionless numbers in order to measure the diffusion contribution of different phenomena:

$$Pr = \frac{\nu}{D_t}, \tag{2.12}$$

$$Sc_k = \frac{\nu}{D_k}, \tag{2.13}$$

$$Le_k = \frac{\alpha}{D_k}. \tag{2.14}$$

In the above relations, Pr is Prandtl number and Sc_k and Le_k are Schmidt and Lewis numbers of species k, respectively. They describe the relation between viscous, molecular mass and thermal diffusion rates and have an important role in analyzing the behavior of fluids.

2.2 Turbulence theory

Most flows in nature are turbulent and, although the problem of turbulence has been studied for more than a century, there is still no general solution to this type of flow. In essence, turbulence is three-dimensional, non-stationary, rotational and intermittent. In fact, its randomness makes it impossible to study it from deterministic approximations and statistical methods have to be used for this purpose. However, from the point of view of many industrial applications, turbulent flow has a great advantage: its diffusivity causes an increase in momentum, mass and energy transfer rates. From a reactive flow point of view, this characteristic is very beneficial for accelerating the mixing process and obtaining optimal air-fuel ratio conditions for efficient combustion.

In many textbooks, turbulence is described as a phenomenon with fractal structure. In fact, turbulent flows are composed of a repetition of vortexes or eddies at different scales, i.e. with different characteristic lengths. The term *eddy* is intended to identify a region of the flow of size ℓ that is at least moderately coherent. It is important to define at this point the local Reynolds number for a certain eddy of size ℓ:

$$Re(\ell) = \frac{\ell\, U(\ell)}{\nu}. \tag{2.15}$$

This size introduces the concept of the energy cascade, first described by Richardson in 1922 [11]. Fig. 2.1 shows a schematic of this concept, representing the energy content as a function of length scale.

The energy cascade aims to characterise the production, distribution and transfer of energy between the different scales of the turbulent flow, as well as to determine which scales are the most relevant of the flow. The main idea behind this concept is that there are three broad ranges of length scales.

- The largest eddies are characterised by a length ℓ_0, which is comparable to the flow scale, and their characteristic velocity is comparable to the mean flow velocity. In this case, the Reynolds number $Re(\ell_0) = \ell U(\ell)/\nu$ is therefore very high and the direct effects of viscosity are negligible. This is the scale range where the turbulent kinetic energy is produced and contains most of energetic contribution. These large eddies are very unstable and break up, transferring this energy to smaller eddies.

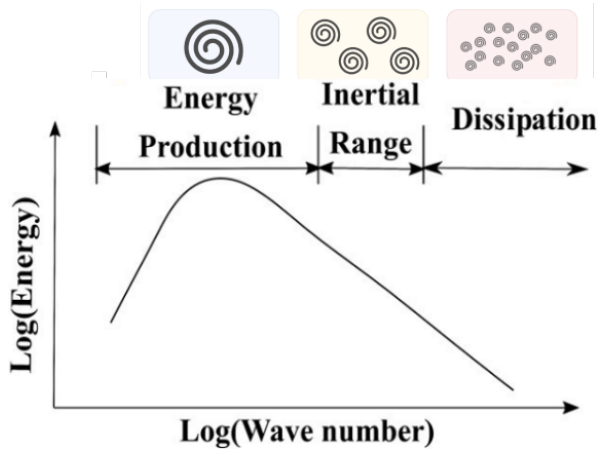

Figure 2.1: Schematic of the energy cascade. Represents the energy content as function of the wave number.

- The intermediate scale range known as the inertial range is characterised by the transfer of energy from larger to smaller eddies by non-viscous mechanisms.
- Eventually, the energy transfer continues until the Reynolds number is small enough that the motion of the eddies is stable and the viscosity is able to dissipate the kinetic energy in the form of heat. This is known as the dissipation range.

It is important to note that, throughout the energy transfer process, dissipation is at the end of the cascade. However, the dissipation rate ε is determined in the first step of the process, from the energy transferred from the larger eddies.

Although the concept of the energy cascade allows a qualitative characterisation of the length scale ranges of turbulence, several questions remain to be answered, such as what is the length of the smallest eddies responsible for the energy dissipation or how to quantify the limits of each of the above-mentioned ranges. All these questions were answered by Kolmogorov in 1941 [12, 13], as well as more fundamental aspects about the nature of turbulence. Basically, the set of hypotheses determine the anisotropic behavior of the smallest eddies and their exclusive dependence on viscosity ν and dissipation ε, establishing what is known as the universal equilibrium range (containing the inertial and dissipation ranges described above). From this, the length of the smallest eddies η, which is called the Kolmogorov scale, is determined by:

$$\eta = \left(\frac{\nu^3}{\varepsilon}\right)^{1/4}. \tag{2.16}$$

For more details on these hypotheses, their implications and the characterisation of the different scale ranges, any interested reader may consult the wide range of textbooks on the subject [5, 14]. It is worth mentioning that the implications derived from the universal character of eddies with smaller size (universal equilibrium range) are the basis for some of the models that try to describe turbulent flow.

With this brief introduction, necessary to define the fundamentals and characteristics of turbulence, the following subsection aims to introduce the different frameworks regarding the simulation of turbulent flows. Special emphasis will be placed on Large-Eddy Simulations, since it is the approach defined for this thesis, as well as on the most commonly used turbulence models in gas turbine applications.

2.2.1 Overview of turbulence modelling frameworks

Over the years, different frameworks for modelling turbulent flows have been developed and studied. Broadly speaking, these strategies address the turbulence problem by modifying the governing equations and solving them using different numerical methods. The idea of overcoming the limitations of solving all time and length scales has led to the development of different types of modelling strategies, although one of the most widespread classifications is associated with model adaptivity [15]. This class of models modifies the different magnitudes to be solved, and therefore the equations themselves, to a reduced order or dimension, or to a statistical formulation, so as to simplify the multiscale problem. Within this type of models, three main frameworks can be distinguished for the modelling of turbulent flows: Direct Numerical Simulation (DNS), Reynolds-Averaged Navier-Stokes (RANS) and Large-Eddy Simulation (LES).

Before describing each of these frameworks, some generalities are given to understand the most relevant differences and their applicability. Fig. 2.2 illustrates the results for a certain turbulent flow problem using the three mentioned strategies, as well as the relation to the energy cascade and turbulence scales described in the previous section. In essence, one of the main differences between these different frameworks lies in the amount of length scales that are

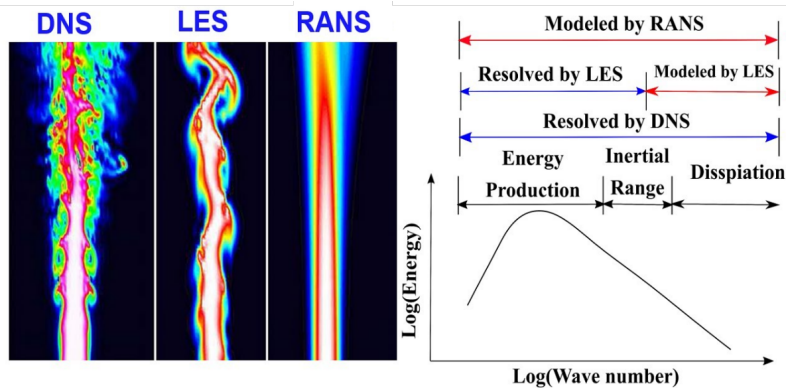

Figure 2.2: Left: turbulent flow solved by means of DNS, LES and RANS approaches. Right: plot of the energy cascade with the differences between frameworks in terms of resolved and modelled turbulence scales. Image from [16].

modelled or solved. Thus, the DNS approach resolves all scales of turbulence, from the largest eddies in the energy production range to the Kolmogorov scale eddies responsible for dissipation. In contrast, RANS simulations do not resolve any of the scales and all of them are modelled by solving the equations for the mean flow. The LES framework falls somewhere in between. LES perform a spatial filtering of the Navier-Stokes equations so that only the larger scales are solved, while small-scale turbulence is modelled by means of subgrid-scale (SGS) models. In view of the contours of Fig. 2.2, RANS allow to obtain time-averaged fields or quantities of interest, LES give access to the temporal and spatial evolution of the quantities representative of the spatial filtering of the governing equations and DNS provides the exact spatial and temporal evolution from the direct solution of the equations. Obviously, there is a trade-off between the number of scales solved and the complexity and computational cost of the simulations, with DNS being extremely computationally expensive and RANS being the most affordable approach in that respect. In gas turbine applications, the RANS framework has been extensively used due to the relatively low computational cost and applicability to complex and larger geometries. However, advancements in computing technologies and massively parallel architectures have made it possible to extend the study of turbulent reacting flow in aeronautical burners to the LES and even DNS approaches. This work is focused on LES, therefore, the following paragraphs are intended to briefly describe the fundamentals and mathematical aspects of this turbulence modelling approach. For additional information on the RANS and DNS approaches, the reader is referred to any of the usual turbulent combustion books [3, 5, 15].

2.2.2 Large-Eddy Simulation

As mentioned before, one of the main issues of turbulent flow modelling is the multi-scale nature of turbulence. In particular, the resolution of the smallest scales (Kolmogorov eddies) demands really fine discretizations in order to correctly capture them, which is unfeasible in realistic applications. Large-Eddy Simulations (LES) arise as an alternative turbulence modelling framework based on the resolution of the larger flow scales and the modelling of the smaller ones. In order to distinguish between the resolved and modelled scales, a filtering operation is performed in LES which basically implies that the scales smaller than the filter size are modelled, while the rest are resolved. The mathematical implications of this operation derive in a system of filtered governing equations, based on the general fluid mechanics equations described in Section 2.1. The unresolved contribution of flow magnitudes (which corresponds to the unresolved or sub-grid scales) appears in the form of unclosed terms in the transport equations, and appropriate sub-grid scale models are required for their closure. All of these particularities of the LES approach are addressed in this subsection.

LES filtering

The LES filtering operation aims for the distinction between resolved and unresolved scales. The application of spatial filters to the set of governing equations implies that only the resolved part of the different magnitudes will be treated as the unknown of the problem and additional terms will appear representing the interaction between resolved and unresolved scales.

Several filtering strategies may be considered, usually classified in explicit and implicit approaches. The explicit approach introduces the filter explicitly, applying it to the transport equations and discretizing the problem. In the implicit approach, it is presumed that a filtering operation exists, corresponding to the discretization, but the exact filter effect is unknown [17]. In general, the spatial filter is assumed to be characterized by a length proportional to the computational grid size Δx. Therefore, the filtered quantity $\overline{\phi}$ of any variable is mathematically described by the convolution product between its instantaneous value $\phi(\boldsymbol{x'}, t)$ and the normalized filter G with a characteristic length Δx:

$$\overline{\phi}(\boldsymbol{x}, t) = \int \phi(\boldsymbol{x'}, t) G(\boldsymbol{x} - \boldsymbol{x'}) d\boldsymbol{x'}. \tag{2.17}$$

Therefore, in the LES decomposition, the instantaneous field of any variable ϕ is obtained as the sum of the filtered field and the unresolved part:

$$\phi = \overline{\phi} + \phi', \tag{2.18}$$

where ϕ' is the sub-grid component of ϕ. In variable density flows where the density shows a fluctuating behaviour, issues regarding the mathematical description are often avoided by using Favre or density-weighted filters. The Favre-filtering of a certain field read as:

$$\widetilde{\phi} = \frac{\overline{\rho\phi}}{\overline{\rho}}, \tag{2.19}$$

where ρ is the unfiltered density. Considering the Favre-filtering of a given field, the LES decomposition may be rewritten as:

$$\phi = \widetilde{\phi} + \phi''. \tag{2.20}$$

where ϕ'' is the Favre-filtered sub-grid fluctuation of ϕ. The described filtering operation can then be applied to the general governing equations and it results in the filtered LES equations, which are presented in the following lines.

Filtered governing equations

In the LES formalism, the filtering operation is applied directly to the governing equations. A new set of equations is then obtained, where the unknowns are the filtered quantities, and can be solved numerically in the computational grid. The full system of filtered governing equations (derived from the generic equations of continuity, species, momentum and energy conservation: Eqs. 2.3, 2.4, 2.6 and 2.9, respectively) in the LES context read as:

$$\frac{\partial \overline{\rho}}{\partial t} + \boldsymbol{\nabla} \cdot (\overline{\rho} \widetilde{\boldsymbol{u}}) = 0, \tag{2.21}$$

$$\frac{\partial \overline{\rho} \widetilde{Y_k}}{\partial t} + \boldsymbol{\nabla} \cdot \left(\overline{\rho} \widetilde{\boldsymbol{u}} \widetilde{Y_k}\right) = -\boldsymbol{\nabla} \cdot \left[\overline{\rho} \widetilde{\boldsymbol{V_k} Y_k} + \overline{\rho} \left(\widetilde{\boldsymbol{u} Y_k} - \widetilde{\boldsymbol{u}} \widetilde{Y_k}\right)\right] + \overline{\dot{\omega}_k}, \quad k = 1, ..., N_s, \tag{2.22}$$

$$\frac{\partial \overline{\rho} \widetilde{\boldsymbol{u}}}{\partial t} + \boldsymbol{\nabla} \cdot (\overline{\rho} \widetilde{\boldsymbol{u}} \widetilde{\boldsymbol{u}}) = -\boldsymbol{\nabla} \overline{p} + \boldsymbol{\nabla} \cdot [\overline{\boldsymbol{\tau}} - \overline{\rho} (\widetilde{\boldsymbol{u}\boldsymbol{u}} - \widetilde{\boldsymbol{u}} \widetilde{\boldsymbol{u}})] + \overline{\boldsymbol{\mathcal{F}}}, \tag{2.23}$$

$$\frac{\partial \overline{\rho} \widetilde{h}}{\partial t} + \boldsymbol{\nabla} \cdot \left(\overline{\rho} \widetilde{\boldsymbol{u}} \widetilde{h}\right) = \frac{\overline{Dp}}{Dt} - \boldsymbol{\nabla} \cdot \left[\overline{\boldsymbol{q}} + \overline{\rho} \left(\widetilde{\boldsymbol{u} h} - \widetilde{\boldsymbol{u}} \widetilde{h}\right)\right] + \boldsymbol{\nabla} \cdot (\overline{\boldsymbol{\tau}} \overline{\boldsymbol{u}}) + \overline{\boldsymbol{\mathcal{Q}}} + \overline{\rho} \sum_{k=1}^{N_s} \left(\widetilde{Y_k \boldsymbol{f_k} \boldsymbol{u}} + \widetilde{Y_k \boldsymbol{f_k} \boldsymbol{V_k}}\right), \tag{2.24}$$

where all magnitudes are defined by the same symbols as in Section 2.1, but using filtered quantities. The total derivative of pressure $\overline{Dp/Dt}$ is usually neglected under the low Mach number approximation. In addition, the viscous heating effects $\boldsymbol{\nabla} \cdot (\overline{\boldsymbol{\tau}} \overline{\boldsymbol{u}})$ are considered to be small and are typically neglected in the enthalpy equation. The filtered laminar viscous stress tensor $\overline{\boldsymbol{\tau}}$ in the momentum equation is modelled using the Stoke's assumption:

$$\overline{\boldsymbol{\tau}} = \widetilde{\mu} \left[(\boldsymbol{\nabla} \widetilde{\boldsymbol{u}}) + (\boldsymbol{\nabla} \widetilde{\boldsymbol{u}})^T - \frac{2}{3} (\boldsymbol{\nabla} \cdot \widetilde{\boldsymbol{u}}) \boldsymbol{I}\right], \tag{2.25}$$

while the filtered heat flux is given by:

$$\overline{\boldsymbol{q}} = -\frac{\overline{\lambda}}{c_p} \boldsymbol{\nabla} \widetilde{h} = -\overline{\rho} \widetilde{D} \boldsymbol{\nabla} \widetilde{h}. \tag{2.26}$$

As observed, additional unclosed terms appear in the governing equations, given by: $\overline{\rho} \left(\widetilde{\boldsymbol{u} Y_k} - \widetilde{\boldsymbol{u}} \widetilde{Y_k}\right)$, $\overline{\rho} (\widetilde{\boldsymbol{u}\boldsymbol{u}} - \widetilde{\boldsymbol{u}} \widetilde{\boldsymbol{u}})$ and $\overline{\rho} \left(\widetilde{\boldsymbol{u} h} - \widetilde{\boldsymbol{u}} \widetilde{h}\right)$. They appear when rewritting the convective terms of the filtered equations and correspond to the sub-grid scale (SGS) Reynolds stresses (term in the momentum equation) and SGS scalar fluxes (terms in the species and enthalpy equations). The modelling of these terms is addressed below.

Sub-grid scale models

The first closure problem corresponds to the modelling of the sub-grid scale Reynolds stresses, i.e., the term $\overline{\rho} (\widetilde{\boldsymbol{u}\boldsymbol{u}} - \widetilde{\boldsymbol{u}} \widetilde{\boldsymbol{u}})$ in the previously presented gov-

erning equations. The most popular models for this purpose are the well-known eddy-viscosity models. They are based on the Boussinesq assumption [3], in which the momentum fluxes are linearly dependent to the velocity gradients (or the strain rate tensor) of the large scales:

$$\overline{\rho}\left(\widetilde{\boldsymbol{u}\boldsymbol{u}}-\widetilde{\boldsymbol{u}}\widetilde{\boldsymbol{u}}\right)=-\mu_t\left[\left(\boldsymbol{\nabla}\widetilde{\boldsymbol{u}}\right)+\left(\boldsymbol{\nabla}\widetilde{\boldsymbol{u}}\right)^T-\frac{2}{3}\left(\boldsymbol{\nabla}\cdot\widetilde{\boldsymbol{u}}\right)\boldsymbol{I}\right]. \tag{2.27}$$

In the expression above, μ_t is known as eddy viscosity or turbulent viscosity and the different eddy-viscosity approaches aim to provide a model for this variable.

The first and simplest eddy-viscosity model was proposed by Smagorinsky in 1963 [18]. In this approach, the turbulent viscosity is estimated using a characteristic length scale Δx and the filtered strain rate $\boldsymbol{S}(\widetilde{\boldsymbol{u}})=\frac{1}{2}\left(\nabla\widetilde{\boldsymbol{u}}+\nabla^T\widetilde{\boldsymbol{u}}\right)$:

$$\mu_t=\overline{\rho}\left(C_S\Delta x\right)^2\left|\boldsymbol{S}(\widetilde{\boldsymbol{u}})\right|, \tag{2.28}$$

where C_S is a modelling constant which ranges from 0 (in laminar flows) to 0.2. The advantages and weaknesses of the Smagorinsky SGS model are well known. Although it is a simple and robust approach, it is not suitable for transitioning flows or to treat wall turbulence. In addition, it tends to overpredict the turbulent diffusivity and to cause artificial re-laminarization in low-turbulence regions.

In view of the limitations of the classical Smagorinsky model, several approaches have been proposed in order to improve the model behaviour. Included in the same family of eddy-viscosity models, the Wall-Adapting Local Eddy-viscosity (WALE) model [19] estimates the turbulent viscosity using a combined expression of the filtered strain rate tensor and its deviatoric component, $\boldsymbol{S^d}(\widetilde{\boldsymbol{u}})=\frac{1}{2}\left(\nabla\widetilde{\boldsymbol{u}}+\nabla^T\widetilde{\boldsymbol{u}}\right)-\frac{1}{3}\left(\nabla\cdot\widetilde{\boldsymbol{u}}\right)\boldsymbol{I}$, as follows:

$$\mu_t=\overline{\rho}\left(C_w\Delta x\right)^2\frac{\left(\boldsymbol{S^d}(\widetilde{\boldsymbol{u}})\boldsymbol{S^d}(\widetilde{\boldsymbol{u}})\right)^{3/2}}{\left(\boldsymbol{S}(\widetilde{\boldsymbol{u}})\boldsymbol{S}(\widetilde{\boldsymbol{u}})\right)^{5/2}+\left(\boldsymbol{S^d}(\widetilde{\boldsymbol{u}})\boldsymbol{S^d}(\widetilde{\boldsymbol{u}})\right)^{5/4}}. \tag{2.29}$$

The WALE model has the property of eddy-viscosity vanishing near solid surfaces in plane shear and the damping for μ_t is not required in the near-wall region. Following a similar approach, Vreman proposed a sub-grid scale

model [20] which also deals with the usual limitations of the Smagorinsky model, leading to a better prediction of the kinetic energy dissipation and to the vanishing of the turbulent viscosity in laminar flow conditions and wall bounded flows. The Vreman SGS model is used in the applications studied in this thesis and is further detailed in Chapter 3. A more recent approach concerning the eddy-viscosity models is given by the Sigma model [21]. In this case, the turbulent viscosity is related to the singular values of the resolved velocity gradient tensor. The Sigma model leads to the vanishing of the eddy-viscosity in two-dimensional and two-component flows as well as in axisymmetric or isotropic contraction/expansion cases. In addition, μ_t damping is also not necessary due to its behaviour near solid walls.

Eddy-viscosity models have demonstrate to provide realistic results and are characterized by their robustness, ease of implementation and reduced computational cost. However, they present limitations and the values of the model constants are expected to vary depending on the flow conditions and geometry. From another perspective, dynamic closures are developed in order to deal with these limitations of the conventional eddy-viscosity approaches. Dynamic closures are based on the Germano identity [22], which introduces the concept of a test-filter scale (usually denoted as $\alpha\Delta x$) for the dynamic formulation, and have been developed for multiple SGS models. For instance, the dynamic procedure was applied to the original Smagorinsky approach resulting in the well-known Dynamic Smagorinsky SGS model [23]. In this regard, the coefficients of the SGS model are adjusted actively based on the instantaneous filtered solutions:

$$C_S \Delta x^2 = \frac{1}{2} \frac{\langle L_{ij} M_{ij} \rangle}{\langle M_{ij} M_{ij} \rangle}, \tag{2.30}$$

where L_{ij} is called the resolved stress or Leonard stress, M_{ij} is expressed by the test-filter scale and the strain rate tensor and $\langle \cdot \rangle$ denotes the spatial average over the homogeneous flow direction. Dynamic approaches have been also applied to the WALE eddy-viscosity model (resulting in a Dynamic WALE) [24] and to determine the constant of the Vreman proposal [25]. Moreover, dynamic models have also been developed for scalar fluxes [23], sub-grid scalar variance [26] and one-equation models where the sub-grid stress tensor is related to the sub-grid turbulent kinetic energy and an additional transport equation is solved (Dynamic Structure model [27]).

Bardina et al. [28] introduced an alternative SGS Reynolds stress model that relies on the similarity hypothesis between the resolved field and a test

scale. It is based on the fact that the exchange between the large and small scales takes place between the smallest resolved scales and the largest unresolved scales. Therefore, the SGS stresses are determined by the scale of the test-filter (as introduced previously with the dynamic models). Derived from the similarity based closure, the so-called non-linear, Clark or tensor diffusivity model [29] emerged from evaluating the test-filtering analytically. In addition, mixed models, such as the Smagorinsky-Bardina approach [30, 31], combined the eddy-viscosity term from the original Smagorinsky formulation with the similarity expressions.

Other SGS velocity models have been proposed, such as de-convolution methods [32], models which solve one or multiple additional transport equations for the full SGS stress tensor [33] or the probability density function [34], or approaches that explicitly construct the sub-grid velocity field based on small-scale vortices [35], fractals [36] or one-dimensional turbulence models [37]. They have been successfully employed in different cases, however, the simplicity, reliability and low computational cost of the eddy-viscosity model family has extended their use in most practical applications.

On the other hand, the modelling of unresolved scalar fluxes, $\overline{\rho}\left(\widetilde{\boldsymbol{u}Y_k} - \widetilde{\boldsymbol{u}}\widetilde{Y_k}\right)$ and $\overline{\rho}\left(\widetilde{\boldsymbol{u}h} - \widetilde{\boldsymbol{u}}\widetilde{h}\right)$, is usually addressed following the classical gradient diffusion assumption. This approach is closely related to the eddy viscosity models for the SGS Reynolds stress modelling since it is also based on the Boussinesq hypothesis and uses the turbulent Schmidt or Prandtl numbers. Alternatives to this approach have been proposed for species and temperature turbulent mixing and they are mainly reduced to the Linear Eddy Mixing (LEM) model [38] or transported FDF approaches [39, 40], but their detailed description and applicability is out of the scope of this work.

2.3 Combustion theory

This section is dedicated to the introduction of combustion fundamentals and modelling approaches. In general, combustion comprises all the physicochemical processes that take place during the ignition of a fuel in a fluid medium. Despite the simple definition of the concept, the combustion process could be considerably complex and it is not only governed by turbulence or the flow motion, but it also depends on the fuel and oxidizer mixing. Different combustion modes or regimes are possible depending on the flow configuration, type of fuel and injection system present in the combustion system [41]. Laminar flames is usually the starting point to understand the process and the

different combustion regimes and a brief theoretical review is addressed first in this section. Subsequently, turbulent combustion is the next step to approach real applications and the interaction between turbulence and the chemical process is commonly described by turbulent combustion diagrams. In the end, understanding the combustion regime and the degree of turbulence-chemistry interaction is the key to choose the appropriate turbulent combustion model for a particular application. An overview of the most commonly used combustion modelling frameworks in the context of numerical simulations of aeronautical burners is given at the end of this section.

2.3.1 Laminar combustion

Laminar flames are the keystone to understand the basics of the combustion process and combustion regimes. In this subsection, a brief description of the fundamentals of premixed and non-premixed combustion is presented. It is worth to mention that the modelling approach used in the present work is focused on non-premixed flames, however, premixed combustion is also introduced for completeness and its relevance in partially premixed combustion regimes.

Premixed combustion

In premixed flames, fuel and oxidizer are completely mixed before reacting. Therefore, two regions are perfectly distinguished: the unburnt premixed gases and the fully burnt reactants, separated by the flame or reacting front.

Due to the fact that reactants are already mixed before combustion, chemistry is the controlling process in laminar premixed flames. In the context of combustion, it is important to introduce the Damköhler number, which relates a characteristic physical time $\tau_{physical}$ and a characteristic chemical time $\tau_{chemical}$:

$$Da = \frac{\tau_{physical}}{\tau_{chemical}}. \tag{2.31}$$

This dimensionless number is useful for general combustion cases in order to determine the relevance of physical (e.g. mixing) and chemical processes. In the case of premixed flames where mixing is not important, this number is close to 0.

The presence of a flame front that clearly separates two zones of the flow with different species concentration and energy content implies a diffusive

flow of species and heat from the fully burnt to unburnt gases in the premixed flames. This results in a propagation or advance of the flame front through the unburnt reactant mixture and introduces the concept of laminar flame speed S_L. This laminar flame speed is the relative velocity at which the flame front propagates normal to itself with respect to the mean flow.

In view of this concept, laminar premixed flames may be understood as a transient process where a reacting front is initiated and advances through a homogeneous mixture of fuel and oxidizer until it is completely consumed. A representative application of this case is the combustion process in a classical spark-ignition engine, where a spark initiates a flame front which propagates through a given fuel-air mixture inside the combustion chamber. The alternative to this process is the premixed flame produced in a Bunsen burner type application. In this case, a steady flame front is stabilized at some point, separating the region of burning gases from a zone characterized by the continuous supply of a fuel-oxidizer mixture at a certain velocity v_u. Therefore, this combustion system reaches the equilibrium when the velocity of the reactants supply equals the laminar flame speed (or the velocity at which the reactants are being consumed due to the chemical process). The stability of the flame front is then controlled by the relation between v_u and S_L. On the one hand, if $S_L \ll v_u$ the reacting front starts to be lifted and it could eventually lead to flame blow-off. On the other hand, flashback conditions may be achieved if $S_L \gg v_u$, where the flame front propagates through the reactants mixture supply line.

In essence, the laminar flame speed is a key parameter in premixed flames, it is required for the solution of a given premixed combustion problem and its estimation is therefore crucial. The concept was first introduced by Mallard and Le Chatelier [42] finding a proportional relationship between the laminar flame speed and the thermal diffusivity and a characteristic reaction rate. Further investigations [43] led to theories based on the asymptotic behaviour of the flame front to identify different regions of the premixed flame and solutions and analytical expressions for temperature and laminar flame speed were found.

Non-premixed combustion

Non-premixed flames are characterized by the separation of the fuel and oxidizer streams. In this case, combustion occurs in the diffusive region where transport phenomena allow mixing of the two reactants prior to the combustion process. In non-premixed combustion systems, there is no danger of

flashback due to the fact that no homogeneous reactive mixture is provided by the fuel supply line. Mixing is the controlling process in this type of flames and its characteristic time is usually slower than the chemical reaction, which evidences higher characteristic Damköhler numbers for non-premixed combustion. Since diffusive fluxes govern the mixing process, non-premixed flames are commonly called diffusion flames.

A wide variety of non-premixed flame configurations are available. If fuel and oxidizer streams move in the same direction, it is possible to found reactive mixing layers or gaseous reacting sprays. On the contrary, counterflow flame configurations are characterized by opposite streams, where fuel and oxidizer are advected towards the reaction zone situated in the middle of the domain. In contrast to premixed flames, a characteristic velocity is not present in diffusion flames. However, they can be strained and characterized by a certain strain level, which controls the diffusion effects and the thickness of diffusion and reaction layers.

In the context of the non-premixed combustion, it is important to define the mixture fraction concept. The mixture fraction Z is a quantity which describes the mixing process. It can be defined for each element and represents the total mass of that element in a given mixture. If a combination of the elements composing the fuel is used, the fuel mixture fraction is obtained, representing the mass coming from the fuel for any mixture. A generalized definition for arbitrary hydrocarbon fuel and oxidizer was provided by Bilger, defining a factor for the characterization of a given gas mixture:

$$b = 2\frac{Y_C}{W_C} + 0.5\frac{Y_H}{W_H} - \frac{Y_O}{W_O}, \tag{2.32}$$

where Y_k and W_k are the elemental mass fraction and molecular weights of carbon, hydrogen and oxygen. The mixture fraction Z is defined after a scaling, in order to obtain a bounded value between 0 and 1:

$$Z = \frac{b - b_o}{b_f - b_o}, \tag{2.33}$$

where b_o and b_f are evaluated at conditions of pure oxidizer and fuel, respectively. This definition leads to $Z = 1$ in the fuel stream and $Z = 0$ in the oxidizer one.

With the introduction of this concept and assuming that any reactive scalar only depends on time and the Z coordinate [3], it is usual to rewrite the transport equations in the mixture fraction space for non-premixed flame

configurations. For instance, the transport equation for species mass fraction (assuming unity Lewis) read as:

$$\rho\frac{\partial Y_k}{\partial t} = \frac{1}{2}\rho\chi\frac{\partial^2 Y_k}{\partial^2 Z} + \dot{\omega}_k, \tag{2.34}$$

where χ is introduced as the scalar dissipation rate, defined by:

$$\chi = 2D\frac{\partial Z}{\partial x}\frac{\partial Z}{\partial x}. \tag{2.35}$$

The scalar dissipation rate and Eq. 2.35 establish the relation between the mixture fraction space and physical space. It represents the strength of convection and diffusion and it is directly linked to the strain rate a to which the flame is subjected. Once a closed expression for χ is determined, Eq. 2.34 (and the analogous equation for temperature) can be entirely solved in the mixture fraction space, providing the flame structure. These equations (transport equations for temperature and species mass fraction in the Z space) are usually called the flamelet equations. They introduce the flamelet concept and are the key element in many diffusion flame theories and combustion modelling approaches.

If several diffusion flames at different strain rates are considered, it is possible to found a relationship between temperature and the scalar dissipation rate at the stoichiometric conditions χ_{st}. This dependency is also illustrated in terms of the strain rate a itself (due to the linear dependency with χ_{st}), or even the Damköhler number (due to its proportionality to χ_{st}^{-1}). The mentioned relation leads to a characteristic curve known as the S-curve. An illustration of this curve is shown in Fig. 2.3.

Different branches are identified in the S-curve. At low strain, it is defined a region where the flame evolves from the inert conditions to the stable burning branch. This is the auto-ignition range and is limited by the ignition point at Da_{ign}. The increase of the strain rate (or decrease of the Damköhler number) at a given point of the stable burning branch implies higher diffusion and the eventual flame quenching at the extinction point (for a given strain a_{ext} or Damköhler numer Da_{ext}). A region characterized by re-ignition and flame extinction is comprised then between the ignition and extinction points. The intermediate unstable burning branch is found in this range which is characterized by high sensitivity to small strain perturbations. Small strain variations may lead to the re-ignition to the stable burning branch or the extinction to the weakly reacting branch (also known as lower branch). For even higher strain rates, the flame does not present chemical activity. The S-curve

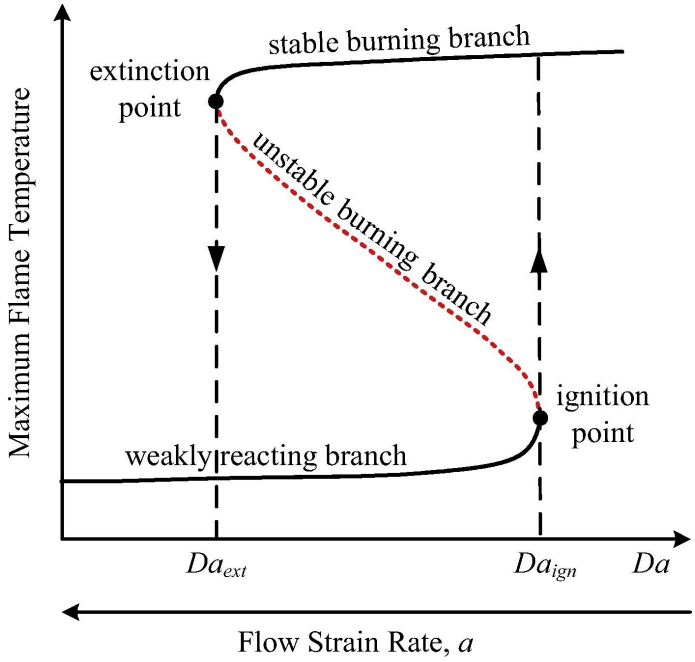

Figure 2.3: Example of the S-curve illustrating the temperature as a function of the Damköhler number (or the inverse of the strain rate or stoichiometric scalar dissipation rate). Image from [44].

can be generally used to characterize the evolution of a diffusion flame subject to varying flow conditions, such as ignition, extinction or flame instability.

2.3.2 Turbulent combustion

Previous to the introduction of the usual combustion modelling approaches, it is necessary to give some notions of turbulent combustion. One of the most important ideas that a turbulent combustion model must describe is how turbulence and chemistry affect each other in the context of a turbulent flame. An overview of this interaction is usually given by the typical turbulent combustion diagrams, which are briefly introduced in this subsection. A summary of the combustion and turbulence-chemistry interaction scales is given in the following paragraphs, which define the basis of the turbulent combustion models used for the most studied combustion applications.

Premixed combustion

Diagrams for the definition of turbulent premixed combustion regimes were introduced by Borghi [45], Peters [4], Abdel-Gayed and Bradley [46], and other authors. The usual diagrams are based on the comparison of characteristic length scales (ratio between the characteristic turbulence integral scale l_t and the characteristic diffusive flame thickness δ_{diff}) and the comparison of characteristic velocities (ratio between the characteristic velocity of the turbulence integral scale u' and the laminar flame speed S_L). Therefore, it is important to first define some estimations of the combustion scales and some additional dimensionless numbers. Assuming unity Lewis and Schmidt numbers, characteristic flame thickness and time based on the thermal diffusivity D_t can be defined according to Peters [4]:

$$\delta_{diff} = \frac{D_t}{S_L}, \tag{2.36}$$

$$\tau_{diff} = \frac{D_t}{S_L^2}. \tag{2.37}$$

With these assumptions, the turbulence Reynolds and Damköhler numbers can be expressed as:

$$Re_t = \frac{u' l_t}{S_L \delta_{diff}}, \tag{2.38}$$

$$Da = \frac{l_t S_L}{u' \delta_{diff}}. \tag{2.39}$$

Additionally, the Karlovitz number relates the flame scales with the Kolmogorov scales, as follows:

$$Ka = \frac{\tau_{diff}}{\tau_\eta} = \frac{\delta_{diff}^2}{\eta^2}. \tag{2.40}$$

The different turbulent premixed combustion regimes can be classified in a diagram similar to that shown in Fig. 2.4.

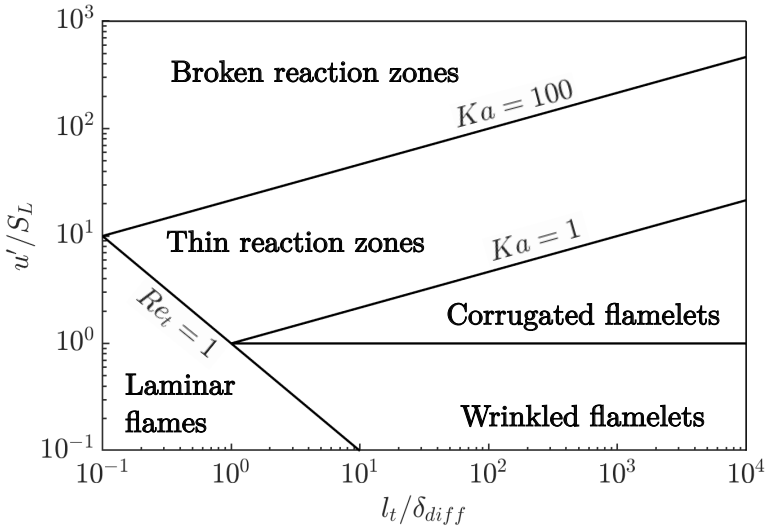

Figure 2.4: Regimes of turbulent premixed combustion assuming unity Schmidt number.

Four regions or regimes of turbulent premixed combustion are identified in this diagram, apart from the laminar regime situated at $Re_t < 1$:

- The wrinkled flamelets regime is not of much interest due to the low turbulence level. In this region, $u' < S_L$ and the laminar flame propagation dominates over the flame front corrugations due to turbulence.
- The corrugated flamelets regime is characterized by $Re > 1$, $Ka < 1$ and, therefore, $\delta_{diff} < \eta$. The reacting front is not affected by turbulence perturbations and the flame structure remains laminar and quasi-steady.
- Thin reaction zones are defined by $1 < Ka < 100$. Eddies of the size of the Kolmogorov scale can enter and perturb the preheat region but the reaction zone is not disturbed by turbulence.
- Broken reaction zones, delimited by $Ka > 100$, are characterized by the perturbation of the reaction layer due to turbulence. In this case, eddies can penetrate the reaction zone and even extinguish the flame.

Non-premixed combustion

In contrast to turbulent premixed combustion, there is no clear consensus on the regime diagrams and characteristic scales of turbulent non-premixed

flames due to the absence of a well defined characteristic velocity. For the estimation of the characteristic flame thickness, Peters [4] provided some definitions based on the diffusivity, analogously to the estimation of the diffusive flame thickness in premixed flames. It is possible to evaluate the expression using the thermal diffusivity in the oxidizer or alternatively in the stoichiometric mixture:

$$\delta_{diff} = \sqrt{\frac{2D_{t,ox}}{a}}, \tag{2.41}$$

$$\delta_{diff,st} = \sqrt{\frac{2D_{t,st}}{a}}. \tag{2.42}$$

Alternative estimations were provided by other authors, such as the definition based on the definition of the scalar dissipation rate introduced by Poinsot and Veynante [3], but they are not included here for simplicity.

Regarding time scales, different definitions and estimations are also available in the literature. On the one hand, the rate of mixing may be characterized by a mixing time scale according to [47]:

$$\tau_m = \frac{Z_{st}^2}{\chi_{st}}. \tag{2.43}$$

In this case, only mixing is considered and no information about chemistry is considered. On the other hand, Peters provided a definition for the chemical time scale using the conditions at the extinction point, expressed as:

$$\tau_c^{ext,\chi} = \frac{Z_{st}^2\left(1 - Z_{st}^2\right)}{\chi_{st}^{ext}}. \tag{2.44}$$

This time scale at the extinction point becomes similar to the mixing time scale τ_m if Z_{st} is low, denoting the limit where the dissipation of radicals due to diffusive mixing overcomes the production due to chemistry. An alternative estimation of the time scale was given by Ihme and Pitsch [47] using the concept of progress variable. The expression of the chemical time scale follows:

$$\tau_c^{\dot{\omega}} = \frac{\rho_{st}^{max} Y_{c,st}^{max} - \rho_{st}^{min} Y_{c,st}^{min}}{\max(\dot{\omega}_{Y_{c,st}})}, \tag{2.45}$$

where Y_c and $\dot{\omega}_{Y_c}$ are the progress variable and its source term and the time scale is computed using their unsteady evolution at the stoichiometric point.

Among the variety of alternatives for the regime diagram of non-premixed combustion, the proposal of Williams [6] is presented in Fig. 2.5. The diagram is characterized by the turbulence Reynolds number Re_t and turbulence Damköhler numbers based on the turbulence integral scale and the Kolmogorov scale:

$$Da_t = \frac{\tau_t}{\tau_c}, \tag{2.46}$$

$$Da_\eta = \frac{\tau_\eta}{\tau_c} = \frac{1}{Ka}. \tag{2.47}$$

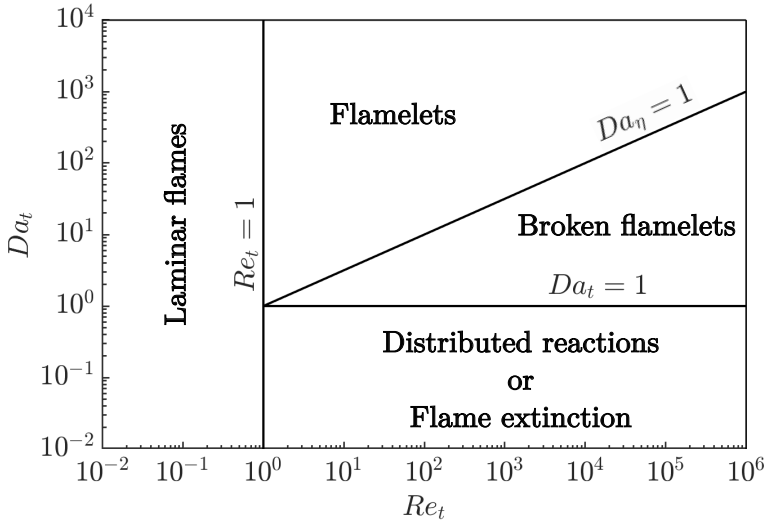

Figure 2.5: Regimes of turbulent non-premixed combustion assuming unity Schmidt number.

Three main regions are present in this turbulent non-premixed diagram:

- The flamelet regime is defined by the condition of $Da_\eta > 1$. In this case, the Kolmogorov time scale is larger than the combustion characteristic time. Therefore, even the smallest eddies do not affect the reaction zone and it behaves like a thin sheet deformed by the turbulent flow, but maintaining a laminar flame structure.

- The broken flamelets region, delimited by $Da_\eta < 1$ and $Da_t > 1$, features a flame front partially affected by turbulence. The turbulence integral scales do not penetrate and disturb the reaction zone, but it is perturbed by the smallest eddies, causing local extinctions in the flame.
- In the distributed reactions regime ($Da_t < 1$) the reacting front is totally affected by all the turbulence scales. The reaction zone widens due to the high turbulent mixing and it is possible to achieve the complete flame extinction if turbulence is able to quickly deplete the radical production.

Partially premixed combustion

After reviewing the main combustion modes and regimes, it is worth to highlight some details about partially premixed combustion. Partial premixing is the name given to all regimes that are neither fully premixed nor purely non-premixed. It is a combustion regime characteristic of gas turbines applications and is indeed the least understood. In these cases, fuel and air are typically injected separately but a rapid mixing is achieved (often due to the usual swirled injection systems) before ignition and the combustion process occurs in a stratified mixture. Partially premixed regimes govern auto-ignition problems, the characterization of the lift-off length and flame stabilization in the near nozzle region of burners, local extinction events or re-ignition mechanisms. The usual turbulent combustion models developed for purely premixed or diffusion flames can still perform well in these applications (sometimes one better than the other, depending on the premixing level) [48], however, they should be used with caution. In general, combustion models that are valid for both premixed and non-premixed modes or that consider multi-regime conditions are more adequate for partially premixed combustion systems. Other classical models may be revisited or extended in order to properly reproduce the flame structure in these cases.

2.3.3 Combustion modelling

The combustion regimes previously introduced serve as a starting point when selecting an appropriate turbulent combustion model depending on the physical processes that dominate the flame [15, 41]. Most of the turbulent combustion models present in the literature are based on the scale separation concept, which states that one of the scales is much greater than the others and, therefore, the reacting flow is governed by certain phenomena and may be characterized by one of the described combustion regimes. In the general

LES framework, turbulent combustion models usually derive naturally to filtered laminar flames in low-turbulence regions and they assume that a large part of the flame structure is preserved [49].

In this subsection, an overview of the different approaches for combustion modelling in the LES context is provided. It is not intended to give an extensive understanding or mathematical description of each of the approaches, instead, only some notions and characteristics of the models are described in order to remark their advantages and applicability. The classification is based on the reviews by [15, 41, 49] and the reader is referred to these works for further information.

Chemical description

Chemistry in the combustion process addresses the phenomena that occur at atomic level. The complex group of chemical reactions that take place during the process is characterised by very different time scales, depending on how fast or slow the reactions are. Therefore, a strategy is needed for solving this complex system and for integrating it together with the rest of transport phenomena. Different methods have been developed for addressing the chemistry problem and a summary is given in the following lines. Note that some of these approaches are applied to the chemical scheme, prior to the calculation of the reacting flow.

- Constitutive relations. It consists on the description of the chemical and atomic processes as a continuum by means of Arrhenius laws.
- Chemical mechanism reduction. The number of species and reactions required is decreased by the identification of the most relevant chemical processes for an adequate representation of the original mechanism. Some of the different methods for chemistry reduction are the Quasi-steady state (QSS), Partial Equilibrium (PE), Computational Singular Perturbation (CSP) [50] and Intrinsic Low-dimensional Manifold (ILDM) [51, 52].
- Stiff chemistry integrators. The stiffness in the system of ordinary or partial differential equations needed for the chemistry description in the presence of transport is removed with different techniques [53, 54].
- Storage chemistry approaches. Pre-computed laminar or turbulent flames are tabulated in a given database. During the CFD computation,

the chemical integration is accelerated and the thermochemical state is determined by the pre-tabulated simplified flames. Most of these approaches are based on the previously mentioned flamelet concept, i.e., the flame front is composed of one-dimensional steady/unsteady premixed or non-premixed flames and the chemical description is provided by the pre-computation and tabulation of these flames. The Flamelet Generated Manifold (FGM) [55, 56], the Flamelet Progress Variable (FPV) [57] or Flamelet Prolongation of ILDM (FPI) [58] are some of the usual methods following this strategy. Additional approaches have been developed considering the on-the-fly adaptation of the thermochemical tables, such as the In Situ Adaptative Tabulation (ISAT) [59], the Picewise Reusable Implementation of Solution Mapping (PRISM) [60] or Artificial Neural Networks [61].

All of these strategies for chemistry reduction and simplification are not considered combustion models themselves and serve as a methodology to reduce the computational cost of computing complex chemistry. However, most of these methods are directly linked to turbulent combustion models and often share their assumptions and limitations, reducing the range of applicability [49].

Turbulent combustion models

Turbulent combustion models in the LES framework are usually extensions of models developed in RANS, which is justified by the fact that the combustion process usually takes place at unresolved scales below the LES filter. This poses a complicated situation from a modelling point of view. For example, in gas turbine applications, a correct description of both rapidly evolving species in a thin flame front highly affected by turbulence and slow chemical reactions taking place in low-turbulence regions is needed. In these cases, highly energetic fast-consuming species such as kerosene coexist with the slow chemical processes of species such as NO or CO.

In this context, a variety of LES turbulent combustion models arise based on the fundamental combustion regimes described during this section. For premixed flames, it is usual to apply the progress variable concept, which characterizes the state of reaction. The progress variable c is commonly scaled (it becomes equal to one in fully burnt gases and equal to zero in the fresh mixture) and subjected to a transport equation which describes the propagation of the flame front. In non-premixed cases, the previously introduced

mixture fraction is also transported in order to represent the local mixing state within the flame. Following these main ideas, many turbulent combustion have been developed during the last years and they are briefly described in the subsequent paragraphs following the classification of [41, 49].

In geometrical approaches, the flame front is described as a geometrical entity. These models rely on the assumption of a sufficiently thin flame front, representing an interface between fresh and burnt gases in premixed flames or between fuel and oxidizer in non-premixed cases. Different models have been proposed following this description:

- G-field equation. This method is based on the reformulation of the transport equation of progress variable in its propagating form, where the laminar flame speed S_L appears explicitly and characterizes the propagation of premixed flame elements. It is applicable to premixed flames. A scalar field variable G is used with an arbitrary definition and an iso-surface of G is fixed using a chosen value G_0. The level set of the scalar at G_0 is considered to represent the spatial location of the flame [62]. This model may be extended to turbulent flames considering the filtered scalar field $\widetilde{G}$ and the unresolved flux, which leads to a turbulent flame speed S_T. This approach becomes a good option for numerical simulation of large systems where it is not required to know the internal structure of the flame [63] but it is necessary to provide an adequate model for S_T.

- Flame surface density. The flame is identified as a surface and the concept of flame surface density Σ is introduced, which represents the available flame area per unit volume. In this approach, the mean burning rate of species i is modelled following $\dot{\omega}_i = \dot{\Omega}_i \Sigma$ and the local burning rate per unit of flame area $\dot{\Omega}_i$ is estimated from a more or less complex laminar flame. This formulation allows for the decoupling of the chemical description ($\dot{\Omega}_i$) and the flame-turbulence interaction (Σ). The flame surface density can be estimated using algebraic relations or as a solution of a balance equation. Different formulations of balance equations for Σ have been proposed both for non-premixed turbulent combustion [64] and premixed flames [65], but in the end, the usual modelling issues emerge and appropriate closures are required for the unresolved terms of the Σ equation.

- Flame wrinkling [66, 67]. It is an extension of the previously described method. In this case, a flame wrinkling factor Ξ is introduced which is

related to the ratio of the flame surface end its projection in the direction of flame propagation. More complex transport equations may be also derived and closed for Ξ, compared to the equations for Σ, but this approach is more convenient for initial and boundary conditions [41].

- Thickened flame. The thickened flame method was originally conceived as an interesting solution to propagate a premixed flame on coarse grids [68]. It is based on the scaling of the thermal diffusivity and the characteristic reaction rate following the fundamental definitions of the laminar flame speed and flame thickness [6, 10]. If the thermal diffusivity is increased by a certain factor and the reaction rate is decreased by the same value, the flame thickness is multiplied and an artificially thickened flame is created, maintaining the combustion velocity. Depending on the scaling value, it could be possible to resolve the thickened flame front on LES computational grids. Due to this flame front thickening, the interaction between turbulence and chemistry is modified and further investigation is required in order to account for this effect. For this purpose, the use of efficiency functions has been extended [69, 70]. This approach seems to be promising especially in combustion instabilities, where the flow scales are larger than the laminar flame thickness [3].

Although the G-field and flame surface density approaches require some statistical treatments, they are initially conceived as a purely geometrical description of the flame. In the statistical approaches, this assumption is relaxed and special attention is given to the statistical properties of the intermediate states of the flame front. The sub-grid terms of the LES description are typically derived using Probability Density Functions (PDF) or Filtered Density Functions (FDF) [71]. Several numerical models have emerged based on this strategy and some of them are summarized below:

- Presumed probability density functions. The probability density function of a given quantity ξ, $\widetilde{P}(\xi, x, t)$, measures the probability to find, for a given location x and instant t, the variable ξ within a certain range. It can be used to provide a sub-grid closure to any quantity ϕ (which could be species mass fraction, chemical source terms, etc.). Given a set of space variables ξ_N, the filtered quantity $\widetilde{\phi}$ can be obtained by the integration of the joint PDF:

$$\widetilde{\phi} = \int_{\xi_1} \dots \int_{\xi_N} \phi(\xi_1, \dots, \xi_N) \widetilde{P}(\xi_1, \dots, \xi_N) d\xi_1 \dots \xi_N. \tag{2.48}$$

The simplest way to address this problem is to presume a function for the PDF. The PDF shape has been usually described by delta, beta, Gaussian or Log-Normal mathematical functions. In this approach, the filtered quantities and the PDF is parametrized as function of the mean $\widetilde{\xi}$ and variance $\widetilde{\xi''^2}$ of the space variables and additional balance equations for solving them are required in order to close the problem.

- Transported probability density functions. Instead of presuming a shape for the PDF, the alternative strategy involves the resolution of transport equations of joint PDFs for velocity and reactive scalars [5, 72, 73]. The main advantage of this approach is the availability to deal with chemistry: all the chemical source terms appear in a closed form and modelling is not required. However, additional diffusive terms (usually named as micromixing) are present and remain unclosed [41]. In addition, the resolution of transport equations for the PDFs implies a prohibitive computational cost in industrial applications.

- Conditional moment closure [74–76]. The Conditional Moment Closure (CMC) approach was conceived as a model for non-premixed combustion. However, it is currently applicable also to premixed flames and even for multi-regime conditions. In this approach, transport equations for conditional filtered terms are solved and then they can be integrated using presumed PDFs to estimate the sub-grid unknowns. Therefore, in the case of non-premixed combustion, reactive scalars conditioned to a specific value of mixture fraction Z are solved: $\widetilde{Y_k|Z}$. It is extended to premixed flames by conditioning to the progress variable c: $\widetilde{Y_k|c}$, or even for both combustion modes using the combined conditioning: $\widetilde{Y_k|Z,c}$. Since transport equations for each combination of species and mixture fraction and/or progress variable values are solved, the computational cost of this model is quite expensive.

- Linear Eddy Model [15, 38]. The Linear Eddy Model (LEM) is usually classified as a pseudo-statistical approach. It can be applied to both premixed and non-premixed flames. This model solves a first set of one-dimensional equations accounting for molecular mixing at scales not solved in the simulations. Subsequently, this first solution is mapped onto a triple-map structure which represents the outcome of an individual eddy motion. This method allows for an efficient parallel implementation [15] but it is still computationally expensive. However, it has been succesfully applied in some diverse appliactions [77, 78].

There are many other strategies for turbulent combustion modelling, but they have not been included here for simplicity. This section aims to provide an overview of combustion modelling and the different major groups of approaches that exist and have been applied for modelling combustion systems (in gas turbines and many other applications) in the LES context. For further information on turbulent combustion modelling, any interested reader is referred to the classical numerical combustion books or any other extensive review on combustion modelling [3, 4, 15, 41].

2.4 Soot modelling

Due to the harmful effects of particulate matter on health and environment, a thorough understanding of the soot formation processes in combustion systems is crucial. Soot is a solid carbonaceous substance which results from fuel pyrolysis at rich conditions and high temperature. However, some details about the physical and chemical processes that lead to soot formation are still unknown. This is why the development of predictive tools remains a challenge and new discoveries are continuously emerging that lead to the implementation of increasingly accurate and computationally efficient soot models.

In this section, an overview of the current understanding of the different processes involved in soot production is presented. In addition, a brief description of the numerical modelling approaches for describing these processes is provided below.

2.4.1 Fundamentals of soot production

A description of the different processes leading to soot production is presented here. The complete set of phenomena may be classified in soot precursor formation, physical processes (which involve nucleation and collisional phenomena) and chemical processes (such as growth and oxidation due to surface chemical reactions).

Gas precursors formation

Unsaturated hydrocarbons (such as acetylene) are produced as a result of the pyrolysis process, which involves the substantial decomposition and rearrangement of fuel molecules and takes place in high-temperature fuel-rich environments. The creation of polycyclic aromatic hydrocarbons (PAHs), which are

well-known as precursors to soot formation [79], depends heavily on the products generated during fuel pyrolysis. The formation of the first aromatic ring and its growth to larger PAHs is still an unknown topic today. According to Wang and Chung [80], the main pathway to the formation of the first benzene ring may be related to a variety of processes including acetylene addition to butatrienyl radical (n-C_4H_3), propargyl (C_3H_3) recombination, reaction between cyclopentadienyl (c-C_5H_5) and methyl radical (CH_3), among others. Similar to the formation of the first ring, several paths have been proposed during the last years to describe the growth of PAHs from a single aromatic ring. However, the best-known pathway for PAH growth is described by the two-step Hydrogen-Abstraction-C_2H_2-Addition (HACA) mechanism [81]. The HACA mechanism consists of a set of alternating reactions combining the radical formation through the loss of hydrogen atoms from stable molecules and the acetylene addition, leading to the growth of aromatic molecules. Although there are some other proposals, they all end up converging to an acetylene-addition pathway [79].

Physical phenomena

The physical phenomena involved in soot formation consist of, on the one hand, the transition from gaseous soot precursors to the first solid particles (known as soot nucleation) and, on the other hand, the associated collisional processes. A schematic of the different processes can be observed in Fig. 2.6.

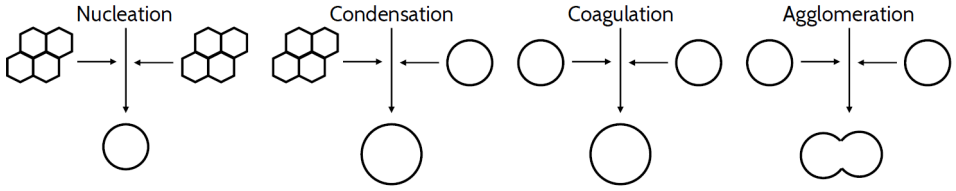

Figure 2.6: Physical phenomena in soot formation. Image from [82].

Nucleation remains one of the least understood processes in soot formation. This process involves the formation of the first soot particles (nuclei) from the gaseous precursors and, even today, a unique soot precursor has not been identified and no mechanism defining the nucleation process has been established. Nevertheless, it is widely accepted that soot nuclei is generated by the collision and physical coalescence of large PAH molecules [83]. In

particular, pyrene dimerization has been extensively used to characterize the nucleation process [84–87].

Once the first soot particles are formed, collisional processes may take place. The collisional phenomena include PAH-soot interactions and soot-soot interactions. The interaction between gaseous precursors (mostly PAHs) and solid soot particles is referred as condensation, and contribute to the increase of the soot mass [88]. On the other hand, coagulation corresponds to the collision and combination of soot particles which leads to a larger solid particle. If the coagulation takes place between two small particles, it results in coalescence and a bigger particle with a nearly spherical shape is obtained. However, the continuous soot-soot interactions eventually form more complex structures of aggregated particles [79]. The latter process is commonly called agglomeration. Coagulation and agglomeration affect significantly the soot number density and may influence the morphology of soot particles.

Chemical phenomena

The total soot mass produced is strongly affected by chemical processes that occur in the surface of soot particles. These chemical phenomena include surface growth and soot oxidation processes. They do not influence essentially the soot number density, i.e., they are related to the increase or decrease of soot particle size without affecting the particle number. Fig. 2.7 illustrates the chemical processes in soot formation.

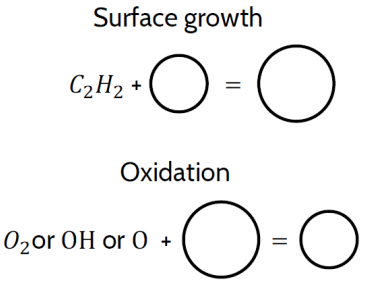

Figure 2.7: Chemical phenomena in soot formation. Image from [82].

Particle surface growth is the process of mass addition through heterogeneous surface reactions with gas phase species. In this regard, acetylene is widely accepted as the main contributor in these chemical process [89–91]. Soot surface growth is usually described using the HACA mechanism [81, 83],

in a similar way to the formation of gaseous PAHs. The chemical $C-H$ bonds present in the surface of soot particles are subjected to the abstraction of hydrogen atoms, which leads to the formation of radicals that end up reacting with acetylene and increasing the particle size. Despite the wide use of this mechanism, particle surface growth is not fully understood. Some extensions of the HACA mechanism have been proposed in the literature [92–95] and several experimental studies on sooting flames have been carried out [89, 96] in order to accurately describe and provide further insight on this process.

Finally, soot oxidation is a chemical reaction process that starts as soon as the first soot particles appear, although it is usually placed at the end of the soot formation chain. It is the only process that reduces the total amount of soot generated through surface reactions with oxidizing species. There is a general consensus that the soot oxidation is mainly caused by chemical reactions with molecules such as O_2, radicals like OH and, with less contribution, O atoms. H_2O, CO_2, NO, N_2O and NO_2 have been also reported as important oxidants in lean environments [97, 98]. Furthermore, oxidation-induced fragmentation is a minor derived process that may affect the soot particle size and number density through the physical division of soot aggregates [99].

2.4.2 Numerical prediction

In a context characterised by a number of not completely understood processes, the development of numerical prediction tools for soot formation faces a challenging scenario. Furthermore, the development of predictive models not only provides a tool to contribute to the design of cleaner propulsion systems, but also allows a deeper understanding of the previously mentioned phenomena. This situation evidences the growing interest during the last years in the study and implementation of accurate and computationally efficient techniques to describe the processes governing soot formation. Depending on the capability of the modelling approach to describe the number density and particle size distribution (PSD) of soot particles, the different strategies are usually classified in empirical or semi-empirical models and detailed models.

The empirical models are based on the use of experimental correlations to describe the soot formation processes [100, 101]. These approaches are very easy to implement and lead to calculations characterized by a considerably low computational cost. However, the empirical parameters are usually not sufficient to describe in detail all the physical and chemical processes taking place and are often conditional on specific operating conditions. As an extension to

these models, the semi-empirical approaches try to include additional subprocesses beyond the simplified formulation of the usual empirical methods. It is possible to find in this group the well-known two-equation models, which describe the evolution of soot mass fraction and number density assuming a mono-disperse soot population [102, 103]. They are easily integrated into turbulent models and are able to maintain a reasonable computational cost for complex applications. Although it is possible to obtain good predictions of soot volume fraction magnitude and number density with semi-empirical models, they still rely on fitting empirical correlations and do not provide information on the PSD. In an intermediate step between semi-empirical and detailed models, some proposals emerge, such as the three-equation model developed by Franzelli et al. [104], which aims to recover the PSD while maintaining the computational cost. Nevertheless, it does not explicitly provide information about the particle distribution, and its reconstruction method requires further validation.

Detailed soot models consider aerosol dynamics in order to predict the particle size distribution. The dynamics of a polydisperse particulate system is represented by the Population Balance Equation (PBE), which is directly or indirectly solved in the detailed approaches. Monte Carlo methods are the basis of most of the stochastic models that accurately predict the evolution of soot particle dynamics [105, 106]. In these models, soot is represented by discrete particles and the PSD shape or soot morphology is not assumed. Therefore, in order to obtain converged statistics for the particle size distribution, a large amount of soot particles needs to be transported, leading to a high computational cost. Although new methods are emerging to apply these models to 3D cases, their use is still limited to 0D configurations and one-dimensional laminar flames.

An alternative approach is provided by the Method of Moments (MOM) based models, which arise as a computationally efficient option for describing the PBE [107, 108]. In this case, the statistical moments of the particle size distribution or number density function are transported and used for the reconstruction of the PSD. In addition, soot main magnitudes, such as volume fraction or number density, are represented by a finite number of moments and it is possible to obtain information on soot morphology through volume-surface descriptions. MOM-based models have been successfully applied in laminar [81, 83] and turbulent [109, 110] flame simulations for the prediction of soot particle dynamics with an affordable computational cost. The main limitation of this approach is related to the reconstruction of the PSD. It does not provide directly the PSD and complex mathematical methods are required for the closure of high unknown moments needed for the reconstruction.

From another perspective, other detailed models are based on the discretization of the PBE in a finite number of groups. The Discrete Sectional Method (DSM) [111, 112] is one of the most representative models in this family. In this approach, the continuous soot particle size distribution is divided into a finite number of sections. Transport equations are solved for the soot mass fraction of each section and the particle size distribution is recovered from the sectional soot mass. A good accuracy on the representation of the PSD requires a large number of soot sections (up to 100), which usually leads to an increased computational cost. Additional extensions of DSM models have been proposed in order to provide information on soot morphology [113], but they are even more computationally expensive since require an additional transport equation per section for the particle number density. These methods were mainly applied in RANS frameworks, but have recently been extended to LES for the study of turbulent flames thanks to the development of more efficient approaches [114, 115].

The aforementioned models constitute the most usual strategies for soot modelling, however, a wide variety of alternatives has been proposed. For example, kinetic models [1, 116] are based on the same principle as the discrete sectional method (discretization of the PBE in bins) and facilitate the coupling between gas and soot phases, but remain computationally expensive due to the requirement of detailed mechanism and a large number of bins. On the other hand, Lagrangian approaches have demonstrated good capabilities for soot prediction [117–119], however, are limited due to the CPU cost. In general, the different options for soot modelling are based on the trade-off between the level of detail in the description of the processes (which conditions the accuracy of the predictions) and the associated computational cost for more or less complex applications.

Furthermore, it is important to highlight that the modelling approach employed for the chemistry description of the combustion process has a significant impact on soot prediction. For instance, a reliable prediction of the PAH chemistry may lead to an accurate prediction of soot. Nonetheless, the correct chemical description of large PAHs involves very complex chemical kinetic schemes which include hundreds of species and thousands of reactions [120]. Detailed chemical mechanisms are usually employed in 1D calculations of canonical configurations but its computational cost is prohibitive in 3D flames. Kinetic reduction techniques such as those described in Section 2.3.3 have also been employed in the context of soot prediction in flames, but even with reduced mechanisms the computational cost is unfeasible, especially if detailed models are used in realistic applications. The tabulated flamelet-based combustion models are more commonly used for sooting flame calculations

[110, 114, 121, 122], due to their reduced computational requirements. However, particular attention must be paid to the validity of the fast chemistry assumption when predicting the slow soot evolution and the gas-solid phase coupling in flamelet-based methods require further investigation [123].

2.5 Spray modelling

During the last few years, multiphase flows and sprays have been extensively studied from a theoretical point of view, by means of numerical simulations and in a multitude of experimental tests [124]. A large part of the combustion systems used in vehicle propulsion, such as gas turbines, internal combustion engines or liquid-fueled rockets, use liquid fuel for their operation, which is usually injected inside the combustion chamber as a turbulent spray. Therefore, understanding the phenomena that control fuel injection, droplet evaporation and combustion, and the interaction of the spray with the flame is of particular relevance in terms of developing efficient propulsion systems.

Compared to the gas-phase combustion, turbulent spray combustion adds a further degree of complexity to the problem. Fig. 2.8 illustrates an scheme with the main interactions that occur in spray combustion, which were described in detail by Jenny et al. [125]. The processes characterizing gas-phase combustion may be observed on the left side, with arrows 1-5. In this case, flow turbulence lead to gas dispersion or macro-mixing (arrow 1) and molecular diffusion or micro-mixing determines the local structure of the flow field (2), which indeed depends on the length scales of turbulence and the local scalar gradients (3). A two-way interaction then occurs, where combustion is controlled by the resulting distribution of species and temperature and the chemical reactions enhance micro-mixing (4). Finally, flow field statistics are also affected by the heat release and expansion due to the combustion process (5). When considering two-phase flow, dispersed and continuous phases are strongly coupled, starting by the momentum exchange at the droplet boundaries (9). Droplets are dispersed due to droplet turbulence (6) and evaporation controls the gaseous fuel supply in the domain (7). Droplet evaporation greatly depends on the other processes and is influenced by gas dispersion (11), micro-mixing (13) and on the vapor boundary layer thickness, which is related to the local velocity difference (8 and 10). Furthermore, evaporation is enhanced by radiative heat transfer from the reaction layers (14) and micro-mixing is also influenced by the scalar gradients in the vapor layers around evaporating droplets (12 and 13). Note that the set of phenomena mentioned above constitutes a very complex and challenging scenario, even without considering other very important processes related to the spray dynamics such as atomization or droplet collisions.

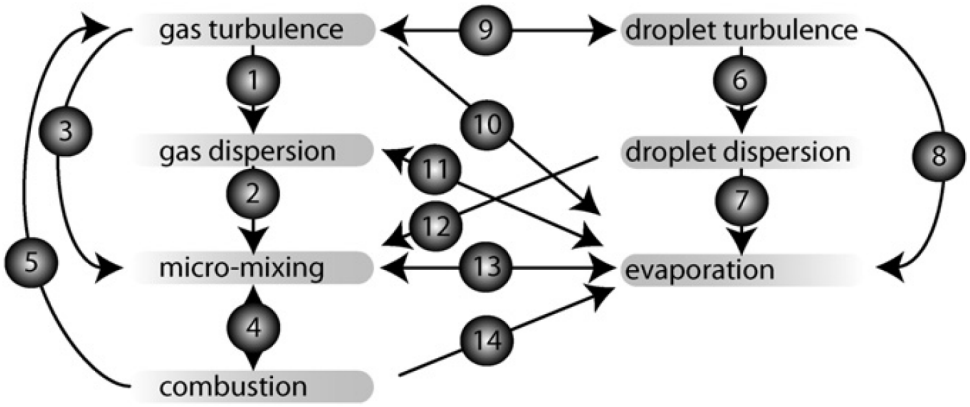

Figure 2.8: Scheme illustrating different phenomena and interactions in spray combustion. Image from [125].

In view of all the coupled processes described above, it can be deduced that spray combustion modelling presents a huge challenge. In the first instance, the modelling of the atomization process could be considered as a separate subject of study, and historically the decomposition of a liquid jet into ligaments and droplets in order to obtain an accurate description of the droplet size distribution has been addressed using different approaches such as the Linearized Instability Sheet Atomization (LISA) [126], the Taylor Analogy Breakup (TAB) [127], Kelvin-Helmholtz (KH) [128] and Rayleigh-Taylor (RT) [129] instability breakup models for the primary and/or secondary atomization. In addition, some phenomena which take place at droplet level (such as the dynamic interaction between the droplet and the surrounding gas or droplet evaporation) are usually very expensive to solve directly with the basic equations. The general modelling frameworks for spray combustion typically consider point droplet approximations and make use of the so-called small scale models [125]. Since this thesis is not exclusively dedicated to spray combustion, the details about these models are not specified here. Any interested reader may found additional information about droplet dispersion, momentum transfer and drag models in [130–132]. Moreover, the modelling of droplet evaporation, mass and heat transfer have been extensively studied by some authors and detailed analysis are addressed in [133, 134].

In this section, a brief description and summary of the modelling frameworks employed for spray combustion is provided. The reader is referred to the usual spray combustion modelling books and reviews for further information about the topic [125, 135–137].

2.5.1 Modelling frameworks for sprays

There are two main modelling frameworks that are employed for the representation of two-phase spray flows in CFD: the Eulerian approach and the Lagrangian approach. The spray models are typically characterized by the flow regime based on the volume fraction occupied by the liquid phase. On the one hand, in Eulerian methods the liquid and gas are treated as a single continuum with variable properties which can be discontinuous across the phase interface. These models have been usually applied to dense sprays, i.e., the flow regime dominated by the atomization phenomena. On the other hand, Lagrangian approaches are based on the individual particle tracking of droplet trajectories through the domain and are considered in the diluted or very diluted regimes, where the primary atomization is completed, droplet collisions are commonly neglected and the liquid volume fraction is lower than $1e^{-3}$.

In the following paragraphs, the Eulerian and Lagrangian approaches for spray combustion are briefly reviewed, focusing on the general characteristics and the different methods employed in each formulation.

Eulerian approach

Normally, the complete spray flow is composed of a dense spray core surrounded by a dispersed flow region, which eventually becomes a dilute spray [138, 139]. In order to properly describe the dense regime, Euler-Euler models have been historically used [137], where both phases are represented in an Eulerian reference system. The Eulerian formulation is used uniquely for both gas and liquid phases and the interface is also considered, where variations of density and viscosity are present. The formulation of the governing equations using the single-fluid Eulerian approach within the LES framework leads to a system of filtered transport equations very similar to the one presented in Section 2.2.2 (see Eqs. 2.21 and 2.23 for the filtered governing mass and momentum equations). These equations do not distinguish between both phases, there are no interphase exchange terms and the main difference lies in the presence of an additional term in the momentum equation, which represents the source of momentum due to surface tension and acts only at the gas-liquid interface. Therefore, the location of the surface interface between gas and liquid is usually reconstructed by means of either the Volume-of-Fluid (VOF) [140] or level-set [141] methods.

In the VOF method, the gas-liquid interface is recovered using the liquid volume fraction γ, ranging from zero to unity depending on the volume covered

by the liquid ($\gamma = 1$ indicates the liquid and $\gamma = 0$ the gaseous phase). A transport equation is then solved for the volume fraction, that reads:

$$\frac{\partial \gamma}{\partial t} + \nabla \cdot (\gamma \boldsymbol{u}) = 0. \tag{2.49}$$

Although this methodology requires fewer assumptions on primary breakup, it is important to properly resolve the interface and approximate the momentum source term in order to avoid numerical issues at the interface [135].

Another approach to track the interface between gas and liquid is the level-set method [141]. It is based on the definition of a scalar field $G(\boldsymbol{x}, t)|_\Gamma$ where Γ represents the interface between two inviscid fluids. The location and dynamics of the interface is solved by the level set equation:

$$\frac{\partial G(\boldsymbol{x}, t)}{\partial t} + \boldsymbol{u} \nabla G(\boldsymbol{x}, t) = 0. \tag{2.50}$$

This modelling approach has demonstrated to present several numerical issues in regions of high curvature of G, which have been attempted to be solved using numerical methods proposed by different authors [142, 143].

The previously described methods are based on the reconstruction of the gas-liquid interface, however, other approaches based on the diffuse-interface concept have been developed and applied in the recent years. For instance, the $\Sigma - Y$ approach [144] employs two modelling concepts to address the two-phase flow description: the density of interfacial area (Σ) and the liquid fraction (Y), and the unresolved interface features are modeled instead of being tracked. This approach has been successfully employed for reacting sprays under high Reynolds and Weber number conditions [145].

Even though the Eulerian treatment is suitable for the dense spray regime, the necessity to reproduce the behaviour of the interface makes high resolution simulations very demanding compared to other modelling approaches. Furthermore, the single-fluid Eulerian models are generally not feasible for the dilute (or very dilute) regime unless sub-grid models are included for the correct prediction of the secondary breakup, wider mesh spacing and droplet evaporation. In this regard, the Mesoscopic Eulerian Formalism (MEF) [146, 147] and multi-fluid Eulerian formulations are a viable alternative under these conditions, where multiple sets of Navier-Stokes equations are solved for the

gas phase and the different droplet size groups [148] or even different liquid components [149, 150]. Nevertheless, as far as the dilute regime is concerned, Lagrangian approaches are still the state of the art to date.

Lagrangian approach

The Eulerian-Lagrangian method is the most widely used modelling framework in the combustion of dilute sprays [125]. In the Euler-Lagrange formulation, the dispersed phase is described by Lagrangian equations while the gas phase is represented in an Eulerian reference system. Although it is possible to consider resolved droplets within the Eulerian-Lagrangian framework (specially in extremely expensive DNS of very simplified cases [151–153]), the point droplet approximation is broadly extended, where droplets are represented by point particles, evolve following Lagrangian equations and the evaporation rate, change of enthalpy and coupling forces are modelled. Using the generic formulation of the governing equations for the gas phase (see Section 2.1), the mass, species, momentum and energy conservation equations in the Eulerian-Lagrangian approach may be written as:

$$\frac{\partial \rho}{\partial t} + \boldsymbol{\nabla} \cdot (\rho \boldsymbol{u}) = S_C, \tag{2.51}$$

$$\frac{\partial \rho Y_k}{\partial t} + \boldsymbol{\nabla} \cdot (\rho \boldsymbol{u} Y_k) = \boldsymbol{\nabla} \cdot (-\rho \boldsymbol{V_k} Y_k) + \dot{\omega}_k + \delta_{k,F} S_C, \quad k = 1, ..., N_s, \tag{2.52}$$

$$\frac{\partial \rho \boldsymbol{u}}{\partial t} + \boldsymbol{\nabla} \cdot (\rho \boldsymbol{u}\boldsymbol{u}) = -\boldsymbol{\nabla} p + \boldsymbol{\nabla} \cdot \boldsymbol{\tau} + \boldsymbol{\mathcal{F}} + S_M, \tag{2.53}$$

$$\frac{\partial \rho h}{\partial t} + \boldsymbol{\nabla} (\rho \boldsymbol{u} h) = \frac{Dp}{Dt} - \boldsymbol{\nabla} \cdot \boldsymbol{q} + \boldsymbol{\tau} \cdot \boldsymbol{\nabla} \boldsymbol{u} + \boldsymbol{\mathcal{Q}} + \rho \sum_{k=1}^{N_s} Y_k \boldsymbol{f_k} \cdot \boldsymbol{V_k} + S_H, \tag{2.54}$$

where S_C, S_M and S_H are the mass, momentum and enthalpy source terms corresponding to the interaction with the liquid spray. These phase exchange terms are usually computed using the droplet heating, evaporation and motion models, resulting in a strongly coupled equation system for the description of the two-phase flow. In addition, the computation of the source terms requires a proper specification of the distribution of droplets in the spray, which may be achieved through several approaches.

One of the most established strategies for determining droplet distributions is the use of discrete droplet models [154], in which several discrete droplet size classes are specified. This approach is specially useful to account for droplet

size distribution coming from experimental measurements [155, 156], since experimental techniques such as Particle Image Velocimetry (PIV) or Phase Doppler Particle Analyzer (PDPA) provide discrete droplet distributions. On the other hand, it is not easy to determine the appropriate number of size classes to sufficiently represent the spray in discrete models. Ultimately, there is a trade-off between the correct description of the polydispersity of sprays and the associated computational cost [137]. Besides the usual discrete models, sectional approaches [157] have been also developed, which also assume a discrete droplet size distribution and have been extended to Eulerian multi-fluid models [158, 159].

From another perspective, probability density function (PDF) methods [6] constitute another group of strategies for describing the spray within the Eulerian-Lagrangian formulation. They assume a continuous droplet size distribution given by a distribution function which is a function of the different droplet parameters (such as droplet position, velocity, radius, temperature...) and time. The temporal evolution of this function is obtained from the so-called spray equation, providing the probable number of droplets per unit volume at a given position and time. The numerical solution of the spray equation is particularly challenging in dense spray computations and more novel strategies have emerged in order to address this issue. The Discrete Quadrature Method of Moments (DQMOM) [160, 161], for instance, does not evaluate the PDF of the spray distribution itself and only a few moments of the PDF are considered.

To sum up, the Eulerian-Lagrangian approach (in particular, Euler-Lagrange models using the point droplet approximation and discrete methods for droplet distribution) has been the reference framework for spray modelling for the last few years. They have demonstrate to reproduce well the spray characteristics from the secondary breakup to the very dilute regime, however, their predictive capabilities for spray breakup (specially for the primary atomization) are questionable and not all physics are captured accurately [135]. Moreover, although Eulerian-Lagrangian models provide reasonably good predictions of droplet distributions in the domain, they require an unrealistic amount of droplets in order to correctly capture the distribution of droplet number densities [162], which may be solved by means of alternative modelling descriptions such as fully Lagrangian approaches [163].

References

[1] Richter, Henning and Howard, Jack B. "Formation of polycyclic aromatic hydrocarbons and their growth to soot—a review of chemical reaction pathways". In: *Progress in Energy and Combustion science* 26.4-6 (2000), pp. 565–608.

[2] Peters, N. "Multiscale combustion and turbulence". In: *Proceedings of the Combustion Institute* 32.1 (2009), pp. 1–25.

[3] Poinsot, Thierry and Veynante, Denis. *Theoretical and numerical combustion*. RT Edwards, Inc., 2005.

[4] Peters, Norbert. *Turbulent combustion*. Cambridge university press, 2000.

[5] Pope, Stephen B. *Turbulent flows*. Cambridge university press, 2000.

[6] Williams, Forman A. *Combustion Theory: The fundamental theory of chemically reacting flow systems*. CRC Press, 1965.

[7] Ern, Alexandre and Giovangigli, Vincent. *Multicomponent transport algorithms*. Vol. 24. Springer Science & Business Media, 1994.

[8] Smooke, Mitchell D. *Reduced kinetic mechanisms and asymptotic approximations for methane-air flames: a topical volume*. Springer, 1991.

[9] Kee, Robert J, Dixon-Lewis, Graham, Warnatz, Jürgen, Coltrin, Michael E, and Miller, James A. "A Fortran computer code package for the evaluation of gas-phase multicomponent transport properties". In: *Sandia National Laboratories Report SAND86-8246* 13 (1986), pp. 80401–1887.

[10] Kuo, Kenneth K. "Principles of combustion". In: (1986).

[11] Richardson, Lewis F. *Weather prediction by numerical process*. University Press, 1922.

[12] Kolmogorov, Andrei Nikolaevich, Levin, V., Hunt, Julian Charles Roland, Phillips, Owen Martin, and Williams, David. "The local structure of turbulence in incompressible viscous fluid for very large Reynolds numbers". In: *Proceedings of the Royal Society of London. Series A: Mathematical and Physical Sciences* 434.1890 (1991), pp. 9–13. DOI: 10.1098/rspa.1991.0075.

[13] Kolmogorov, Andrei Nikolaevich, Levin, V., Hunt, Julian Charles Roland, Phillips, Owen Martin, and Williams, David. "Dissipation of energy in the locally isotropic turbulence". In: *Proceedings of the Royal Society of London. Series A: Mathematical and Physical Sciences* 434.1890 (1991), pp. 15–17. DOI: 10.1098/rspa.1991.0076.

[14] Tennekes, Hendrik and Lumley, John L. *A first course in turbulence*. The MIT Press, 1972.

[15] Echekki, Tarek and Mastorakos, Epaminondas. "Turbulent combustion modeling: Advances, new trends and perspectives". In: (2010).

[16] Applied Computational Fluid Dynamics. *DNS, LES and URANS*. Youtube. 2020. URL: https://www.youtube.com/watch?v=6wEgC5H9yLg&ab_channel=AppliedComputationalFluidDynamics.

[17] Germano, Massimo. "Turbulence: the filtering approach". In: *Journal of Fluid Mechanics* 238 (1992), pp. 325–336.

[18] Smagorinsky, Joseph. "General circulation experiments with the primitive equations: I. The basic experiment". In: *Monthly weather review* 91.3 (1963), pp. 99–164.

[19] Nicoud, Franck and Ducros, Frédéric. "Subgrid-scale stress modelling based on the square of the velocity gradient tensor". In: *Flow, turbulence and Combustion* 62.3 (1999), pp. 183–200.

[20] Vreman, AW. "An eddy-viscosity subgrid-scale model for turbulent shear flow: Algebraic theory and applications". In: *Physics of fluids* 16.10 (2004), pp. 3670–3681.

[21] Nicoud, Franck, Toda, Hubert Baya, Cabrit, Olivier, Bose, Sanjeeb, and Lee, Jungil. "Using singular values to build a subgrid-scale model for large eddy simulations". In: *Physics of fluids* 23.8 (2011).

[22] Germano, Massimo, Piomelli, Ugo, Moin, Parviz, and Cabot, William H. "A dynamic subgrid-scale eddy viscosity model". In: *Physics of Fluids A: Fluid Dynamics* 3.7 (1991), pp. 1760–1765.

[23] Moin, Parviz, Squires, Kyle, Cabot, W, and Lee, Sangsan. "A dynamic subgrid-scale model for compressible turbulence and scalar transport". In: *Physics of Fluids A: Fluid Dynamics* 3.11 (1991), pp. 2746–2757.

[24] Toda, H Baya, Truffin, Karine, and Nicoud, Franck. "Is the dynamic procedure appropriate for all SGS models". In: *V european conference on computational fluid dynamics, ECCOMAS, Lisbon, Portugal*. 2010, pp. 14–17.

[25] You, Donghyun and Moin, Parviz. "A dynamic global-coefficient subgrid-scale eddy-viscosity model for large-eddy simulation in complex geometries". In: *Physics of Fluids* 19.6 (2007).

[26] Pierce, Charles D and Moin, Parviz. "A dynamic model for subgrid-scale variance and dissipation rate of a conserved scalar". In: *Physics of Fluids* 10.12 (1998), pp. 3041–3044.

[27] Pomraning, Eric and Rutland, Christopher J. "Dynamic one-equation nonviscosity large-eddy simulation model". In: *AIAA journal* 40.4 (2002), pp. 689–701.

[28] Bardina, Jorge, Ferziger, J, and Reynolds, WC. "Improved subgrid-scale models for large-eddy simulation". In: *13th fluid and plasmadynamics conference*. 1980, p. 1357.

[29] Clark, Robert A, Ferziger, Joel H, and Reynolds, William Craig. "Evaluation of subgrid-scale models using an accurately simulated turbulent flow". In: *Journal of fluid mechanics* 91.1 (1979), pp. 1–16.

[30] Zang, Yan, Street, Robert L, and Koseff, Jeffrey R. "A dynamic mixed subgrid-scale model and its application to turbulent recirculating flows". In: *Physics of Fluids A: Fluid Dynamics* 5.12 (1993), pp. 3186–3196.

[31] Lodato, Guido, Domingo, Pascale, and Vervisch, Luc. "Three-dimensional boundary conditions for direct and large-eddy simulation of compressible viscous flows". In: *Journal of computational physics* 227.10 (2008), pp. 5105–5143.

[32] Adams, Nikolaus A and Soltz, S. "Deconvolution methods for subgrid-scale approximation in large-eddy simulation". In: *Modern simulation strategies for turbulent flow*. RT Edwards, Inc, 2001.

[33] Deardorff, JW. "The use of subgrid transport equations in a three-dimensional model of atmospheric turbulence". In: (1973).

[34] Gicquel, Laurent YM, Givi, P, Jaberi, FA, and Pope, SB. "Velocity filtered density function for large eddy simulation of turbulent flows". In: *Physics of Fluids* 14.3 (2002), pp. 1196–1213.

[35] Misra, Ashish and Pullin, Dale I. "A vortex-based subgrid stress model for large-eddy simulation". In: *Physics of Fluids* 9.8 (1997), pp. 2443–2454.

[36] Scotti, Alberto and Meneveau, Charles. "Fractal model for coarse-grained nonlinear partial differential equations". In: *Physical review letters* 78.5 (1997), p. 867.

[37] Kerstein, Alan R. "One-dimensional turbulence: A new approach to high-fidelity subgrid closure of turbulent flow simulations". In: *Computer Physics Communications* 148.1 (2002), pp. 1–16.

[38] Kerstein, Alan R. "A Linear- Eddy Model of Turbulent Scalar Transport and Mixing". In: *Combustion Science and Technology* 60.4-6 (1988), pp. 391–421. DOI: 10.1080/00102208808923995.

[39] Sheikhi, MRH, Drozda, TG, Givi, P, Jaberi, FA, and Pope, SB. "Large eddy simulation of a turbulent nonpremixed piloted methane jet flame (Sandia Flame D)". In: *Proceedings of the Combustion Institute* 30.1 (2005), pp. 549–556.

[40] Sheikhi, MRH, Givi, P, and Pope, SB. "Velocity-scalar filtered mass density function for large eddy simulation of turbulent reacting flows". In: *Physics of fluids* 19.9 (2007).

[41] Veynante, Denis and Vervisch, Luc. "Turbulent combustion modeling". In: *Progress in energy and combustion science* 28.3 (2002), pp. 193–266.

[42] Mallard, ELCH and Le Chatelier, H. "Combustion of explosive gas mixtures". In: *Ann Mine* 8 (1883), p. 274.

[43] Sernenov, N. "Thermal theory of combustion and explosion. III. Theory of normal flame propagation". In: *Prog. Phys, Sci., USSR* 24 (1940), pp. 433–486.

[44] Huo, Hongfa, Wang, Xingjian, and Yang, Vigor. "A general study of counterflow diffusion flames at subcritical and supercritical conditions: Oxygen/hydrogen mixtures". In: *Combustion and flame* 161.12 (2014), pp. 3040–3050.

[45] Borghi, R. "On the structure and morphology of turbulent premixed flames". In: *Recent Advances in the Aerospace Sciences: In Honor of Luigi Crocco on His Seventy-fifth Birthday*. Springer, 1985, pp. 117–138.

[46] Abdel-Gayed, RG, Bradley, Derek, and Lung, FK-K. "Combustion regimes and the straining of turbulent premixed flames". In: *Combustion and Flame* 76.2 (1989), pp. 213–218.

[47] Ihme, Matthias and Pitsch, Heinz. "Prediction of extinction and reignition in nonpremixed turbulent flames using a flamelet/progress variable model. 2. Application in LES of Sandia flames D and E". In: *Combustion and Flame* 155.1-2 (2008), pp. 90–107. DOI: 10.1016/j.combustflame.2008.04.015.

[48] Illana, Enric, Mira, Daniel, and Mura, Arnaud. "An extended flame index partitioning for partially premixed combustion". In: *Combustion Theory and Modelling* 25.1 (2021), pp. 121–157.

[49] Gicquel, L.Y.M., Staffelbach, G., and Poinsot, T. "Large Eddy Simulations of gaseous flames in gas turbine combustion chambers". In: *Progress in Energy and Combustion Science* 38.6 (2012), pp. 782–817. DOI: https://doi.org/10.1016/j.pecs.2012.04.004.

[50] Lam, Sau-Hai and Goussis, Dimitris A. "Understanding complex chemical kinetics with computational singular perturbation". In: *Symposium (International) on Combustion*. Vol. 22. 1. Elsevier. 1989, pp. 931–941.

[51] Maas, Ulrich and Pope, Stephen B. "Implementation of simplified chemical kinetics based on intrinsic low-dimensional manifolds". In: *Symposium (International) on Combustion*. Vol. 24. 1. Elsevier. 1992, pp. 103–112.

[52] Maas, Ulrich and Pope, Stephen B. "Simplifying chemical kinetics: intrinsic low-dimensional manifolds in composition space". In: *Combustion and flame* 88.3-4 (1992), pp. 239–264.

[53] Brown, Peter N, Byrne, George D, and Hindmarsh, Alan C. "VODE: A variable-coefficient ODE solver". In: *SIAM journal on scientific and statistical computing* 10.5 (1989), pp. 1038–1051.

[54] Petzold, Linda R. *Description of DASSL: a differential/algebraic system solver*. Tech. rep. Sandia National Labs., Livermore, CA (USA), 1982.

[55] Oijen, J.A. Van and Goey, L.P.H. De. "Modelling of Premixed Laminar Flames using Flamelet-Generated Manifolds". In: *Combustion Science and Technology* 161.1 (2000), pp. 113–137. DOI: 10.1080/00102200008935814.

[56] Goey, LPH de, Oijen, JA van, Bongers, H, and Groot, GRA. "New flamelet based reduction methods: the bridge between chemical reduction techniques and flamelet methods". In: *European Combustion Meeting, Orléans (France)*. 2003.

[57] Pierce, Charles D. and Moin, Parviz. "Progress-variable approach for large-eddy simulation of non-premixed turbulent combustion". In: *Journal of Fluid Mechanics* 504.504 (2004), pp. 73–97. DOI: 10.1017/S0022112004008213.

[58] Fiorina, Benoit et al. "Modelling non-adiabatic partially premixed flames using flame-prolongation of ILDM". In: *Combustion Theory and Modelling* 7.3 (2003), p. 449.

[59] Pope, Stephen B. “Computationally efficient implementation of combustion chemistry using in situ adaptive tabulation”. In: (1997).

[60] Tonse, Shaheen R, Moriarty, Nigel W, Brown, Nancy J, and Frenklach, Michael. “PRISM: Piecewise reusable implementation of solution mapping. An economical strategy for chemical kinetics”. In: *Israel Journal of Chemistry* 39.1 (1999), pp. 97–106.

[61] Christo, Farid C, Masri, Assaad R, Nebot, Eduardo Mario, and Pope, Stephen B. “An integrated PDF/neural network approach for simulating turbulent reacting systems”. In: *Symposium (International) on Combustion*. Vol. 26. 1. Elsevier. 1996, pp. 43–48.

[62] Buckmaster, John D. *The mathematics of combustion*. SIAM, 1985.

[63] Smiljanovski, V, Moser, V, and Klein, Rupert. “A capturing-tracking hybrid scheme for deflagration discontinuities”. In: *Combustion Theory and Modelling* 1.2 (1997), p. 183.

[64] Marble, FE and Broadwell, JE. “The coherent flame model of nonpremixed turbulent combustion”. In: *Project Squid TRW-9-PU, Project Squid Headquarters, Chaffee Hall, Purdue University* (1977).

[65] Pope, SB. “The evolution of surfaces in turbulence”. In: *International journal of engineering science* 26.5 (1988), pp. 445–469.

[66] Weller, H.G., Marooney, C.J., and Gosman, A.D. “A new spectral method for calculation of the time-varying area of a laminar flame in homogeneous turbulence”. In: *Symposium (International) on Combustion* 23.1 (1991). Twenty-Third Symposium (International) on Combustion, pp. 629–636. DOI: https://doi.org/10.1016/S0082-0784(06)80310-3.

[67] Weller, Henry G. “The Development of a New Flame Area Combustion Model Using Conditional Averaging”. In: 1993.

[68] Butler, T.D. and O’Rourke, P.J. “A numerical method for two dimensional unsteady reacting flows”. In: *Symposium (International) on Combustion* 16.1 (1977), pp. 1503–1515. DOI: https://doi.org/10.1016/S0082-0784(77)80432-3.

[69] Angelberger, Christian, Veynante, Denis P., Egolfopoulos, Fokion N., and Poinsot, Thierry. “Large eddy simulations of combustion instabilities in premixed flames”. In: 1999.

[70] Colin, O., Ducros, F., Veynante, D., and Poinsot, T. "A thickened flame model for large eddy simulations of turbulent premixed combustion". In: *Physics of Fluids* 12.7 (2000), pp. 1843–1863. DOI: 10.1063/1.870436.

[71] Gao, Feng and O'Brien, Edward E. "A large-eddy simulation scheme for turbulent reacting flows". In: *Physics of Fluids A: Fluid Dynamics* 5.6 (1993), pp. 1282–1284. DOI: 10.1063/1.858617.

[72] Pope, S.B. "PDF methods for turbulent reactive flows". In: *Progress in Energy and Combustion Science* 11.2 (1985), pp. 119–192. DOI: https://doi.org/10.1016/0360-1285(85)90002-4.

[73] O'Brien, E. E. "The probability density function (pdf) approach to reacting turbulent flows". In: *Turbulent Reacting Flows*. Ed. by Paul A. Libby and Forman A. Williams. Berlin, Heidelberg: Springer Berlin Heidelberg, 1980, pp. 185–218. DOI: 10.1007/3540101926_11.

[74] Klimenko, A Yu. "Multicomponent diffusion of various admixtures in turbulent flow". In: *Fluid dynamics*. 25.3 (1990), pp. 327–334. DOI: 10.1007/BF01049811.

[75] Bilger, R. W. "Conditional moment closure for turbulent reacting flow". In: *Physics of Fluids A: Fluid Dynamics* 5.2 (1993), pp. 436–444. DOI: 10.1063/1.858867.

[76] Klimenko, A.Y. and Bilger, R.W. "Conditional moment closure for turbulent combustion". In: *Progress in Energy and Combustion Science* 25.6 (1999), pp. 595–687. DOI: https://doi.org/10.1016/S0360-1285(99)00006-4.

[77] Smith, Thomas and Menon, Suresh. "Model simulations of freely propagating turbulent premixed flames". In: *Symposium (International) on Combustion* 26.1 (1996), pp. 299–306. DOI: https://doi.org/10.1016/S0082-0784(96)80229-3.

[78] McMurthy, Patrick A., Menon, Suresh, and Kerstein, Alan R. "A linear eddy sub-grid model for turbulent reacting flows: Application to hydrogen-AIR combustion". In: *Symposium (International) on Combustion* 24.1 (1992). Twenty-Fourth Symposium on Combustion, pp. 271–278. DOI: https://doi.org/10.1016/S0082-0784(06)80036-6.

[79] Frenklach, Michael. "Reaction mechanism of soot formation in flames". In: *Phys. Chem. Chem. Phys.* 4 (2002). DOI: 10.1039/B110045A.

[80] Wang, Yu and Chung, Suk Ho. "Soot formation in laminar counterflow flames". In: *Progress in Energy and Combustion Science* 74 (2019), pp. 152–238. DOI: https://doi.org/10.1016/j.pecs.2019.05.003.

[81] Frenklach, Michael and Wang, Hai. "Detailed Mechanism and Modeling of Soot Particle Formation". In: *Soot Formation in Combustion: Mechanisms and Models*. Ed. by Henning Bockhorn. Berlin, Heidelberg: Springer Berlin Heidelberg, 1994, pp. 165–192. DOI: 10.1007/978-3-642-85167-4_10.

[82] Marchal, Caroline. "Modelisation de La Formation et de l'oxydation Des Suies Dans Un Moteur Automobile". PhD thesis. Université d'Orléans, 2008.

[83] Frenklach, Michael and Wang, Hai. "Detailed modeling of soot particle nucleation and growth". In: *Symposium (International) on Combustion*. Vol. 23. 1. Elsevier. 1991, pp. 1559–1566.

[84] Schuetz, Charles A. and Frenklach, Michael. "Nucleation of soot: Molecular dynamics simulations of pyrene dimerization". In: *Proceedings of the Combustion Institute* 29.2 (2002), pp. 2307–2314. DOI: https://doi.org/10.1016/S1540-7489(02)80281-4.

[85] Aubagnac-Karkar, Damien, El Bakali, Abderrahman, and Desgroux, Pascale. "Soot particles inception and PAH condensation modelling applied in a soot model utilizing a sectional method". In: *Combustion and Flame* 189 (2018), pp. 190–206. DOI: https://doi.org/10.1016/j.combustflame.2017.10.027.

[86] Wang, Hu et al. "A comparison study on the combustion and sooting characteristics of base engine oil and n-dodecane in laminar diffusion flames". In: *Applied Thermal Engineering* 158 (2019), p. 113812. DOI: https://doi.org/10.1016/j.applthermaleng.2019.113812.

[87] Mitra, Tirthankar, Zhang, Tongfeng, Sediako, Anton D., and Thomson, Murray J. "Understanding the formation and growth of polycyclic aromatic hydrocarbons (PAHs) and young soot from n-dodecane in a sooting laminar coflow diffusion flame". In: *Combustion and Flame* 202 (2019), pp. 33–42. DOI: https://doi.org/10.1016/j.combustflame.2018.12.010.

[88] Eaves, Nick A., Dworkin, Seth B., and Thomson, Murray J. "Assessing relative contributions of PAHs to soot mass by reversible heterogeneous nucleation and condensation". In: *Proceedings of the Combustion Institute* 36.1 (2017), pp. 935–945. DOI: https://doi.org/10.1016/j.proci.2016.06.051.

[89] Haynes, B.S. and Wagner, H.Gg. "Soot formation". In: *Progress in Energy and Combustion Science* 7.4 (1981), pp. 229–273. DOI: https://doi.org/10.1016/0360-1285(81)90001-0.

[90] Calcote, H.F. "Mechanisms of soot nucleation in flames—A critical review". In: *Combustion and Flame* 42 (1981), pp. 215–242. DOI: https://doi.org/10.1016/0010-2180(81)90159-0.

[91] Harris, Stephen J. and Weiner, Anita M. "Surface Growth of Soot Particles in Premixed Ethylene/Air Flames". In: *Combustion Science and Technology* 31.3-4 (1983), pp. 155–167. DOI: 10.1080/00102208308923637.

[92] Mauss, Fabian, Schäfer, Thomas, and Bockhorn, Henning. "Inception and growth of soot particles in dependence on the surrounding gas phase". In: *Combustion and Flame* 99.3 (1994). 25th Symposium (International) on Combustion Papers, pp. 697–705. DOI: https://doi.org/10.1016/0010-2180(94)90064-7.

[93] Hwang, J.Y. and Chung, S.H. "Growth of soot particles in counterflow diffusion flames of ethylene". In: *Combustion and Flame* 125.1 (2001), pp. 752–762. DOI: https://doi.org/10.1016/S0010-2180(00)00234-0.

[94] Blanquart, G. and Pitsch, H. "Analyzing the effects of temperature on soot formation with a joint volume-surface-hydrogen model". In: *Combustion and Flame* 156.8 (2009), pp. 1614–1626. DOI: https://doi.org/10.1016/j.combustflame.2009.04.010.

[95] Wang, Yu, Raj, Abhijeet, and Chung, Suk Ho. "Soot modeling of counterflow diffusion flames of ethylene-based binary mixture fuels". In: *Combustion and Flame* 162.3 (2015), pp. 586–596. DOI: https://doi.org/10.1016/j.combustflame.2014.08.016.

[96] Homann, K.H. and Wagner, H.Gg. "Some new aspects of the mechanism of carbon formation in premixed flames". In: *Symposium (International) on Combustion* 11.1 (1967), pp. 371–379. DOI: https://doi.org/10.1016/S0082-0784(67)80161-9.

[97] Roth, P., Brandt, O., and Von Gersum, S. "High temperature oxidation of suspended soot particles verified by CO and CO2 measurements". In: *Symposium (International) on Combustion* 23.1 (1991). Twenty-Third Symposium (International) on Combustion, pp. 1485–1491. DOI: https://doi.org/10.1016/S0082-0784(06)80417-0.

[98] Matarrese, R., Castoldi, L., and Lietti, L. "Oxidation of model soot by NO2 and O2 in the presence of water vapor". In: *Chemical Engineering Science* 173 (2017), pp. 560–569. DOI: https://doi.org/10.1016/j.ces.2017.08.017.

[99] Sirignano, Mariano, Kent, John, and D'Anna, Andrea. "Further experimental and modelling evidences of soot fragmentation in flames". In: *Proceedings of the Combustion Institute* 35.2 (2015), pp. 1779–1786. DOI: https://doi.org/10.1016/j.proci.2014.05.010.

[100] Moss, J.B., Stewart, C.D., and Syed, K.J. "Flowfield modelling of soot formation at elevated pressure". In: *Symposium (International) on Combustion* 22.1 (1989), pp. 413–423. DOI: https://doi.org/10.1016/S0082-0784(89)80048-7.

[101] Kennedy, Ian M., Kollmann, Wolfgang, and Chen, J.-Y. "A model for soot formation in a laminar diffusion flame". In: *Combustion and Flame* 81.1 (1990), pp. 73–85. DOI: https://doi.org/10.1016/0010-2180(90)90071-X.

[102] Leung, K.M., Lindstedt, R.P., and Jones, W.P. "A simplified reaction mechanism for soot formation in nonpremixed flames". In: *Combustion and Flame* 87.3 (1991), pp. 289–305. DOI: https://doi.org/10.1016/0010-2180(91)90114-Q.

[103] Lindstedt, Peter R. "Simplified Soot Nucleation and Surface Growth Steps for Non-Premixed Flames". In: *Soot Formation in Combustion: Mechanisms and Models*. Ed. by Henning Bockhorn. Berlin, Heidelberg: Springer Berlin Heidelberg, 1994, pp. 417–441. DOI: 10.1007/978-3-642-85167-4_24.

[104] Franzelli, B., Vié, A., and Darabiha, N. "A three-equation model for the prediction of soot emissions in LES of gas turbines". In: *Proceedings of the Combustion Institute* (2018). DOI: 10.1016/J.PROCI.2018.05.061.

[105] Singh, Jasdeep, Balthasar, Michael, Kraft, Markus, and Wagner, Wolfgang. "Stochastic modeling of soot particle size and age distributions in laminar premixed flames". In: *Proceedings of the Combustion Institute* 30.1 (2005), pp. 1457–1465. DOI: https://doi.org/10.1016/j.proci.2004.08.120.

[106] Balthasar, M and Kraft, M. "A stochastic approach to calculate the particle size distribution function of soot particles in laminar premixed flames". In: *Combustion and Flame* 133.3 (2003), pp. 289–298. DOI: https://doi.org/10.1016/S0010-2180(03)00003-8.

[107] Frenklach, Michael and Harris, Stephen J. "Aerosol dynamics modeling using the method of moments". In: *Journal of Colloid and Interface Science* 118.1 (1987), pp. 252–261. DOI: https://doi.org/10.1016/0021-9797(87)90454-1.

[108] Frenklach, Michael. "Method of moments with interpolative closure". In: *Chemical Engineering Science* 57.12 (2002). Population balance modelling of particulate systems, pp. 2229–2239. DOI: https://doi.org/10.1016/S0009-2509(02)00113-6.

[109] Mueller, M.E., Blanquart, G., and Pitsch, H. "Hybrid Method of Moments for modeling soot formation and growth". In: *Combustion and Flame* 156.6 (2009), pp. 1143–1155. DOI: https://doi.org/10.1016/j.combustflame.2009.01.025.

[110] Mueller, Michael E. and Pitsch, Heinz. "LES model for sooting turbulent nonpremixed flames". In: *Combustion and Flame* 159.6 (2012), pp. 2166–2180. DOI: https://doi.org/10.1016/j.combustflame.2012.02.001.

[111] Netzell, Karl, Lehtiniemi, Harry, and Mauss, Fabian. "Calculating the soot particle size distribution function in turbulent diffusion flames using a sectional method". In: *Proceedings of the Combustion Institute* 31.1 (2007), pp. 667–674.

[112] Gelbard, Fred, Tambour, Yoram, and Seinfeld, John H. "Sectional representations for simulating aerosol dynamics". In: *Journal of Colloid and Interface Science* 76.2 (1980), pp. 541–556.

[113] Zhang, Qingan. "Detailed modeling of soot formation/oxidation in laminar coflow diffusion flames". PhD thesis. University of Toronto, 2009.

[114] Rodrigues, P., Franzelli, B., Vicquelin, R., Gicquel, O., and Darabiha, N. "Coupling an LES approach and a soot sectional model for the study of sooting turbulent non-premixed flames". In: *Combustion and Flame* 190 (2018), pp. 477–499.

[115] Kalbhor, Abhijit. "Model development and numerical investigation of soot formation in combustion". PhD thesis. Eindhoven University of Technology, 2023.

[116] D'Anna, A. and Kent, J.H. "A model of particulate and species formation applied to laminar, nonpremixed flames for three aliphatic-hydrocarbon fuels". In: *Combustion and Flame* 152.4 (2008), pp. 573–587. DOI: https://doi.org/10.1016/j.combustflame.2007.08.003.

[117] Ong, Jiun Cai, Pang, Kar Mun, Walther, Jens Honore, Ho, Jee-Hou, and Ng, Hoon Kiat. "Evaluation of a Lagrangian Soot Tracking Method for the prediction of primary soot particle size under engine-like conditions". In: *Journal of Aerosol Science* 115 (2018), pp. 70–95. DOI: https://doi.org/10.1016/j.jaerosci.2017.10.013.

[118] Dellinger, Nicolas, Bertier, Nicolas, Dupoirieux, Francis, and Legros, Guillaume. "Hybrid Eulerian-Lagrangian method for soot modelling applied to ethylene-air premixed flames". In: *Energy* 194 (2020), p. 116858. DOI: https://doi.org/10.1016/j.energy.2019.116858.

[119] Gallen, Lucien, Felden, Anne, Riber, Eleonore, and Cuenot, Bénédicte. "Lagrangian tracking of soot particles in LES of gas turbines". In: *Proceedings of the Combustion Institute* 37.4 (2019), pp. 5429–5436. DOI: https://doi.org/10.1016/j.proci.2018.06.013.

[120] Saggese, Chiara et al. "Kinetic modeling of particle size distribution of soot in a premixed burner-stabilized stagnation ethylene flame". In: *Combustion and Flame* 162.9 (2015), pp. 3356–3369. DOI: https://doi.org/10.1016/j.combustflame.2015.06.002.

[121] Yang, Suo, Lew, Jeffry K., and Mueller, Michael E. "Large Eddy Simulation of soot evolution in turbulent reacting flows: Presumed subfilter PDF model for soot–turbulence–chemistry interactions". In: *Combustion and Flame* 209 (2019), pp. 200–213. DOI: https://doi.org/10.1016/j.combustflame.2019.07.040.

[122] Xuan, Y. and Blanquart, G. "Effects of aromatic chemistry-turbulence interactions on soot formation in a turbulent non-premixed flame". In: *Proceedings of the Combustion Institute* 35.2 (2015), pp. 1911–1919. DOI: https://doi.org/10.1016/j.proci.2014.06.138.

[123] Attili, Antonio, Bisetti, Fabrizio, Mueller, Michael E., and Pitsch, Heinz. "Damköhler number effects on soot formation and growth in turbulent nonpremixed flames". In: *Proceedings of the Combustion Institute* 35.2 (2015), pp. 1215–1223. DOI: https://doi.org/10.1016/j.proci.2014.05.084.

[124] Lefebvre, Arthur H and McDonell, Vincent G. *Atomization and sprays*. CRC press, 2017.

[125] Jenny, Patrick, Roekaerts, Dirk, and Beishuizen, Nijso. "Modeling of turbulent dilute spray combustion". In: *Progress in Energy and Combustion Science* 38.6 (2012), pp. 846–887.

[126] Schmidt, David P et al. "Pressure-swirl atomization in the near field". In: *SAE transactions* (1999), pp. 471–484.

[127] O'Rourke, Peter J and Amsden, Anthony A. *The TAB method for numerical calculation of spray droplet breakup*. Tech. rep. SAE technical paper, 1987.

[128] Reitz, Rolf D. "Mechanism of breakup of round liquid jets". In: *Encyclopedia of fluid mechanics* 10 (1986).

[129] Patterson, Mark A and Reitz, Rolf D. "Modeling the effects of fuel spray characteristics on diesel engine combustion and emission". In: *SAE transactions* (1998), pp. 27–43.

[130] Schiller, Links. "A drag coefficient correlation". In: *Zeit. Ver. Deutsch. Ing.* 77 (1933), pp. 318–320.

[131] Eisenklam, Paul, Arunachalam, SA, and Weston, JA. "Evaporation rates and drag resistance of burning drops". In: *Symposium (International) on combustion*. Vol. 11. 1. Elsevier. 1967, pp. 715–728.

[132] Chiang, CH, Raju, MS, and Sirignano, WA. "Numerical analysis of convecting, vaporizing fuel droplet with variable properties". In: *International journal of heat and mass transfer* 35.5 (1992), pp. 1307–1324.

[133] Sazhin, Sergei S. "Modelling of fuel droplet heating and evaporation: Recent results and unsolved problems". In: *Fuel* 196 (2017), pp. 69–101.

[134] Both, Ambrus. "High-fidelity numerical simulations of reacting flows with tabulated chemistry". PhD thesis. Universitat Politècnica de Catalunya, 2023.

[135] Kronenburg, A. "Spray Combustion–A Fresh Perspective". In: *Proc. Aust. Combust. Symp., Sydney: University of Sydney*. 2007.

[136] Jiang, Xi, Siamas, GA, Jagus, K, and Karayiannis, TG. "Physical modelling and advanced simulations of gas–liquid two-phase jet flows in atomization and sprays". In: *Progress in energy and combustion science* 36.2 (2010), pp. 131–167.

[137] Merci, Bart, Roekaerts, Dirk, and Sadiki, Amsini. *Experiments and numerical simulations of diluted spray turbulent combustion*. Springer, 2011.

[138] Tseng, L-K, Ruff, GA, and Faeth, Gerard M. "Effects of gas density on the structure of liquid jets in still gases". In: *AIAA journal* 30.6 (1992), pp. 1537–1544.

[139] Faeth, GM. "Spray combustion phenomena". In: *Symposium (international) on combustion*. Vol. 26. 1. Elsevier. 1996, pp. 1593–1612.

[140] De Villiers, E, Gosman, AD, and Weller, HG. "Large eddy simulation of primary diesel spray atomization". In: *SAE transactions* (2004), pp. 193–206.

[141] Herrmann, Marcus. "A Eulerian level set/vortex sheet method for two-phase interface dynamics". In: *Journal of Computational Physics* 203.2 (2005), pp. 539–571.

[142] Sussman, Mark and Fatemi, Emad. "An efficient, interface-preserving level set redistancing algorithm and its application to interfacial incompressible fluid flow". In: *SIAM Journal on scientific computing* 20.4 (1999), pp. 1165–1191.

[143] Enright, Douglas, Fedkiw, Ronald, Ferziger, Joel, and Mitchell, Ian. "A hybrid particle level set method for improved interface capturing". In: *Journal of Computational physics* 183.1 (2002), pp. 83–116.

[144] Vallet, Ariane, Burluka, AA, and Borghi, R. "Development of a eulerian model for the" atomization" of a liquid jet". In: *Atomization and sprays* 11.6 (2001), pp. 619–642.

[145] Desantes, JM et al. "LES Eulerian diffuse-interface modeling of fuel dense sprays near-and far-field". In: *International Journal of Multiphase Flow* 127 (2020), p. 103272.

[146] Sanjosé, M et al. "Fuel injection model for Euler–Euler and Euler–Lagrange large-eddy simulations of an evaporating spray inside an aeronautical combustor". In: *International Journal of Multiphase Flow* 37.5 (2011), pp. 514–529.

[147] Vié, Aymeric, Jay, Stéphane, Cuenot, Bénédicte, and Massot, Marc. "Accounting for polydispersion in the eulerian large eddy simulation of the two-phase flow in an aeronautical-type burner". In: *Flow, turbulence and combustion* 90 (2013), pp. 545–581.

[148] Bayoro, F, Habachi, C, and Daniel, E. "Numerical and physical basis of an Eulerian multi-phase flow model for the simulation of the liquid injection in internal combustion engines". In: *Proceedings of the ILASS Europe Conference, Paper*. 2008, pp. 2–5.

[149] Vujanović, Milan, Edelbauer, Wilfried, Berg, Eberhard von, Tatschl, Reinhard, and Duić, Neven. "Enhancement and validation of an Eulerian-Eulerian approach for diesel sprays". In: *Proceedings of the ILASS Europe Conference, Paper*. 2008, pp. 2–4.

[150] Drew, Donald A and Passman, Stephen L. *Theory of multicomponent fluids*. Vol. 135. Springer Science & Business Media, 2006.

[151] Bagchi, Prosenjit and Balachandar, S. "Response of the wake of an isolated particle to an isotropic turbulent flow". In: *Journal of Fluid Mechanics* 518 (2004), pp. 95–123.

[152] Burton, Tristan M and Eaton, John K. "Fully resolved simulations of particle-turbulence interaction". In: *Journal of Fluid Mechanics* 545 (2005), pp. 67–111.

[153] Zoby, MRG, Navarro-Martinez, S, Kronenburg, A, and Marquis, AJ. "Evaporation rates of droplet arrays in turbulent reacting flows". In: *Proceedings of the Combustion Institute* 33.2 (2011), pp. 2117–2125.

[154] Dukowicz, John K. "A particle-fluid numerical model for liquid sprays". In: *Journal of computational Physics* 35.2 (1980), pp. 229–253.

[155] McDonell, V. G. and Samuelsen, G. S. "An Experimental Data Base for the Computational Fluid Dynamics of Reacting and Nonreacting Methanol Sprays". In: *Journal of Fluids Engineering* 117.1 (1995), pp. 145–153. DOI: 10.1115/1.2816804.

[156] Ge, Haiwen et al. "Laser-Based Experimental and Monte Carlo PDF Numerical Investigation of an Ethanol/Air Spray Flame". In: *Combustion Science and Technology - COMBUST SCI TECHNOL* 180 (2008), pp. 1529–1547. DOI: 10.1080/00102200802125693.

[157] Tambour, Yoram. "A Lagrangian sectional approach for simulating droplet size distribution of vaporizing fuel sprays in a turbulent jet". In: *Combustion and Flame* 60.1 (1985), pp. 15–28. DOI: https://doi.org/10.1016/0010-2180(85)90115-4.

[158] Laurent, Frédérique and Massot, Marc. "Multi-fluid Modeling of Laminar Poly-dispersed Spray Flames: Origin, Assumptions and Comparison of the Sectional and Sampling Methods". In: *Combustion Theory and Modelling* 5 (2001). DOI: 10.1088/1364-7830/5/4/303.

[159] Laurent, Frédérique, Massot, Marc, and Villedieu, Philippe. "Eulerian multi-fluid modeling for the numerical simulation of coalescence in polydisperse dense liquid sprays". In: *Journal of Computational Physics* 194.2 (2004), pp. 505–543. DOI: https://doi.org/10.1016/j.jcp.2003.08.026.

[160] Marchisio, Daniele L. and Fox, Rodney O. "Solution of population balance equations using the direct quadrature method of moments". In: *Journal of Aerosol Science* 36.1 (2005), pp. 43–73. DOI: https://doi.org/10.1016/j.jaerosci.2004.07.009.

[161] Fox, R.O., Laurent, F., and Massot, M. "Numerical simulation of spray coalescence in an Eulerian framework: Direct quadrature method of moments and multi-fluid method". In: *Journal of Computational Physics* 227.6 (2008), pp. 3058–3088. DOI: https://doi.org/10.1016/j.jcp.2007.10.028.

[162] Sazhin, S S, Shchepakina, E, and Sobolev, V. "Modelling of sprays: recent results and future challenges". In: *Journal of Physics: Conference Series* 1096.1 (2018), p. 012052. DOI: 10.1088/1742-6596/1096/1/012052.

[163] Healy, DP and Young, JB. "Full Lagrangian methods for calculating particle concentration fields in dilute gas-particle flows". In: *Proceedings of the Royal Society A: Mathematical, Physical and Engineering Sciences* 461.2059 (2005), pp. 2197–2225.

Chapter 3

Computational methodology

This chapter is focused on the description of the general modelling framework employed in this work. As derived from the fundamentals review addressed in Chapter 2, the combustion process in gas turbine applications features a complex physico-chemical behaviour and the pathway leading to the production of soot or, in general, any other pollutant is characterised by a large set of multi-phase and multi-scale phenomena. Therefore, the strategy used for modelling the relevant processes studied in this work is described here in terms of turbulent reacting flows, sprays for liquid fuel injection and soot production.

The simulation code employed in the present thesis is Alya [1], developed by the Barcelona Supercomputing Center. It is a computational code prepared to solve very complex multi-physics, multi-scale and multi-domain coupled problems. Alya is designed for high-performance computing (HPC) and provides an infrastructure for solving massively parallel calculations. The code has been extensively used for many different applications [2–6] and is under continuous development and optimization [7–12]. For turbulent combustion simulations in Alya, a flexible tabulated chemistry model is implemented within the LES framework. As mentioned in Chapter 2, tabulated chemistry methods have been extensively investigated and Alya provides a state of the art tabulated combustion model which allows for the use of different reference flamelets, complex table structures and even the consideration of heat loss effects. The present tabulated modelling framework has been successfully applied in several combustion problems [13–18]. An Eulerian-Lagrangian two-

way coupling is developed in order to account for dispersion and evaporation of liquid fuel sprays. Lagrangian particle transport is addressed in Alya to model evaporating droplets and semi-empirical models for droplet dynamics, heat and mass transfer and evaporation are adapted for the proper coupling with the Eulerian tabulated chemistry methods. The full implementation of the tabulated combustion model and the Eulerian-Lagrangian coupling within the LES framework in Alya has been performed by Ambrus Both [19] and any interested reader is referred to his work for further details. Recently, an efficient integration of the discrete sectional method for soot prediction has been implemented in the Alya code by Abhijit Kalbhor and Daniel Mira [20, 21]. For the application of the detailed sectional soot model in LES, additional transport equations for the mass fraction of clustered sections are solved and the source terms accounting for soot formation and oxidation processes can be tabulated in the manifold. The described strategy allows for a computationally efficient implementation and has been evaluated and proved its consistency in laminar flames [20] and has been applied to turbulent combustion cases [21, 22].

In this work, Alya is employed for turbulent reacting flow simulations in aero-engine combustors, accounting for multi-phase flows and soot production. Therefore, the above mentioned modelling framework is used and evaluated here and requires an adequate description, which is addressed in this chapter. The general LES framework is introduced first followed by the turbulent combustion modelling approach. In Section 3.3, the modelling strategy for soot prediction is explained while Section 3.4 presents the Lagrangian spray model. Finally, a summary of the methodology and modelling approach is given in Section 3.5.

3.1 Large-eddy simulation framework

As previously introduced in Chapter 2, large-eddy simulations address the multi-scale problem of turbulent flows by separating the turbulence large scales (large eddies) to be resolved and the small scales (small eddies) to be modelled, using a filtering cut-off length. The idea behind this approach is the universality of small scales, which can be modelled using universal models. Therefore, any field ϕ is decomposed in a resolved part and a sub-grid component, where the resolved field represents an instantaneous spatial average in a control volume defined by the filter size.

This section is focused on the description of the turbulence modelling framework. First, the LES governing equations are presented with the dif-

ferent assumptions considered. After that, the sub-grid scale model employed in this work for the LES closure is described. Finally, a summary of the numerical methods employed is outlined. For further information and details about the LES framework implemented in Alya, the dissertation of Both [19] is recommended.

3.1.1 Governing equations

The equations describing the gas phase correspond to the low-Mach number approximation of the Navier-Stokes equations with the energy equation represented by the total enthalpy. A Favre-filtered description of the governing equations is followed to avoid the modelling of terms including density fluctuations. The Favre-filtering of any quantity ϕ is given by:

$$\widetilde{\phi} = \frac{\overline{\rho\phi}}{\overline{\rho}}, \tag{3.1}$$

where ρ is the unfiltered density field. Therefore, in the mathematical expressions of the following lines, the tilde ($\widetilde{\phi}$) denotes the Favre-filtering, while Reynolds-filtering is given by the overline ($\overline{\phi}$).

The filtered governing equations for LES correspond to the continuity, momentum and enthalpy and read as:

$$\frac{\partial \bar{\rho}}{\partial t} + \boldsymbol{\nabla} \cdot (\bar{\rho}\tilde{\boldsymbol{u}}) = \bar{S}_C, \tag{3.2}$$

$$\frac{\partial \bar{\rho}\tilde{\boldsymbol{u}}}{\partial t} + \boldsymbol{\nabla} \cdot (\bar{\rho}\tilde{\boldsymbol{u}}\tilde{\boldsymbol{u}}) = -\boldsymbol{\nabla} \cdot \overline{\tau}_M - \boldsymbol{\nabla}\bar{p} + \boldsymbol{\nabla} \cdot (\bar{\mu}\boldsymbol{\nabla}\tilde{\boldsymbol{u}}) + \bar{S}_M, \tag{3.3}$$

$$\frac{\partial \overline{\rho}\tilde{h}}{\partial t} + \boldsymbol{\nabla} \cdot \left(\bar{\rho}\tilde{\boldsymbol{u}}\tilde{h}\right) = -\boldsymbol{\nabla} \cdot \overline{\tau}_h + \boldsymbol{\nabla} \cdot \left(\bar{\rho}\bar{D}\boldsymbol{\nabla}\tilde{h}\right) + \bar{S}_H, \tag{3.4}$$

where standard notation is used for all the quantities with $\bar{\rho}$, $\tilde{\boldsymbol{u}}$, $\tilde{h}$, $\tilde{D}$, $\bar{p}$ and $\bar{\mu}$ represent the density, velocity vector, total enthalpy (sensible and chemical), diffusivity, pressure and dynamic viscosity using filtered quantities. The bulk viscosity effects are neglected following the Stokes assumption. To simplify the scalar transport in the governing equations, a unity Lewis number assumption is considered. Therefore, the thermal diffusivity is used in the transport of all scalar fields, described by $D = \frac{\lambda}{\rho c_p}$.

The τ term stands for the unresolved or sub-grid terms related to the filtering operation. It applies to the unresolved momentum flux $\overline{\tau}_M$ and the unresolved enthalpy flux $\overline{\tau}_h$, which can be expressed as follows:

$$\overline{\tau}_M = \left(\overline{\rho}\widetilde{\boldsymbol{u}\boldsymbol{u}} - \overline{\rho}\widetilde{\boldsymbol{u}}\widetilde{\boldsymbol{u}}\right), \tag{3.5}$$

$$\overline{\tau}_h = \left(\overline{\rho}\widetilde{h\boldsymbol{u}} - \overline{\rho}\widetilde{h}\widetilde{\boldsymbol{u}}\right). \tag{3.6}$$

These are the unclosed terms of the filtered LES equations and need to be modelled accordingly. The closure of the unresolved fluxes is addressed in the following subsection.

The generic form of the LES equations contain additional terms related to the coupling between the disperse phase and the gas phase. They correspond to the source terms associated to the mass, momentum and energy exchange ($\bar{S}_C$, $\bar{S}_M$, and $\bar{S}_H$) between the droplets and the gas. The closure for these terms is obtained by the integration of Eqs. (3.62), (3.65) and (3.66) [23], which will be described in Section 3.4.

3.1.2 LES sub-grid closure

The aforementioned unresolved fluxes $\overline{\tau}_M$ and $\overline{\tau}_h$ of the filtered LES equations require an adequate closure and this subsection aims to describe the models used for this purpose.

Eddy-viscosity model

In this work, the sub-grid scale stress tensor $\overline{\tau}_M$ is determined by an eddy-viscosity model. As introduced in the previous chapter, in eddy-viscosity models the unresolved momentum fluxes are modeled according to the Boussinesq approximation [24]:

$$\overline{\tau}_M - \frac{1}{3}\,\mathrm{Tr}(\overline{\tau}_M) = -2\overline{\rho}\nu_t\left(\boldsymbol{S}(\widetilde{\boldsymbol{u}}) - \frac{1}{3}\,\mathrm{Tr}(\boldsymbol{S}(\widetilde{\boldsymbol{u}}))\right), \tag{3.7}$$

where $\mathrm{Tr}(\cdot)$ is the trace operator, $\boldsymbol{S}(\widetilde{\boldsymbol{u}})$ the resolved strain rate tensor and ν_t the turbulent or sub-grid viscosity. Note that Eq. 3.7 corresponds to the adapted equation for variable density flows, using Favre-filtered quantities and the deviatoric part of the strain rate tensor. The isotropic contribution of the sub-grid stress tensor $\frac{1}{3}\,\mathrm{Tr}(\overline{\tau}_M)$ is not directly included in the governing equations and it is absorbed into the filtered pressure.

In order to determine ν_t, the Vreman sub-grid model [25] is used in the present work. It is a derivation of the well-known Smagorinsky sub-grid model

[26] which deals with the overprediction of the kinetic energy dissipation estimated by the Smagorinsky model in low-turbulence regions. The sub-grid viscosity in the Vreman model is expressed as:

$$\nu_t = c\left(\frac{\beta_{11}\beta_{22} - \beta_{12}^2 + \beta_{11}\beta_{33} - \beta_{13}^2 + \beta_{22}\beta_{33} - \beta_{23}^2}{\alpha_{ij}\alpha_{ij}}\right), \tag{3.8}$$

where c is a modelling constant and α_{ij} and β_{ij} are defined using the Einstein summation convention by:

$$\alpha_{ij} = \frac{\partial \widetilde{u}_j}{\partial x_i}, \tag{3.9}$$

$$\beta_{ij} = \Delta_m^2 \alpha_{mi}\alpha_{mj}, \tag{3.10}$$

where Δ_m is the filter size in the m dimension. In this work, an isotropic filter is assumed, equal to the mean element size and given by $\Delta_m = \Delta x = \sqrt[3]{V_{elem}}$, where V_{elem} is the element volume.

The modelling constant c is related to the Smagorinsky constant C_S by $c \approx 2.5C_S^2$. Using the theoretical value for homogeneous isotropic turbulence $C_S = 0.17$ [27] leads to $c = 0.07$. However, higher values of C_S are useful to obtain robust simulations in complex cases and Vreman's recommendation of $c = 0.1$ (which corresponds to $C_S = 0.2$) is used here. The same single-value constant has been used in previous studies where satisfactory results were obtained [15, 28]. Like the Smagorinsky model, Vreman's proposal only requires the local filter size and the derivatives of the resolved velocity field thus it is quite simple and easy to compute in actual LES. In addition, it correctly reproduces the vanishing of the sub-grid viscosity in laminar flow configurations, as demonstrated by the author [25].

Unresolved scalar fluxes

The sub-grid fluxes of scalar quantities are commonly closed using the gradient diffusion approach [29]. In this regard, the unresolved scalar flux $\overline{\tau}_\zeta$ of a given scalar ζ is modelled as:

$$\overline{\tau}_\zeta = \left(\overline{\rho}\widetilde{\zeta\boldsymbol{u}} - \overline{\rho}\widetilde{\zeta}\widetilde{\boldsymbol{u}}\right) = -\frac{\overline{\rho}\nu_t}{Sc_t}\boldsymbol{\nabla}\widetilde{\zeta}, \tag{3.11}$$

where Sc_t is the turbulent or sub-grid Schmidt number and ν_t is estimated from the previously described eddy-viscosity model. It is worth mentioning

that Eq. 3.11 corresponds to the model for any generic scalar, which will be useful for the transport equations of the scalars involved in the combustion model. In the particular case of thermal transport, the unresolved enthalpy flux $\overline{\tau}_h$ introduced with Eq. 3.6 is modelled analogously with the expression:

$$\overline{\tau}_h = -\frac{\overline{\rho}\nu_t}{Pr_t}\boldsymbol{\nabla}\widetilde{h}. \tag{3.12}$$

In this case, Pr_t is the turbulent or sub-grid Prandtl number. Both the turbulent Schmidt and Prandtl numbers are model parameters and a constant value of 0.7 is commonly used in several reacting flow calculations [30–33]. In this work, the same value for both dimensionless numbers, $Sc_t = Pr_t = 0.7$, is retained in order to avoid preferential sub-grid transport between different scalars [19].

3.1.3 Numerical methods

A brief description of the numerical methods used for solving the aforementioned equations is given in this subsection. For more details the reader is referred to [19]. The discretization strategy is based on a conservative finite element scheme, where stabilisation is only introduced for the continuity equation by means of a non-incremental fractional-step method, modified in order to account for variable density flows [28]. The final scheme preserves momentum and angular momentum for variable density flows. The error of kinetic energy conservation is of order $O\left(dt \cdot h^{k+1}\right)$ (with h and k being the element size and order, respectively), thus dissipation is limited. Standard stabilized finite elements are used for the scalars, while the time integration is carried out by means of an explicit third order Runge-Kutta scheme for momentum and scalars. The chosen low dissipation FE scheme presents good accuracy compared to other low dissipation finite volume and finite difference methods with the advantage of being able to increase the order of accuracy at will without breaking the fundamental symmetry properties of the discrete operators.

3.2 Turbulent combustion model

The flamelet-based tabulated chemistry framework implemented in the Alya code is used in this work for combustion modelling. Flamelet methods were

already presented in Chapter 2 as one of the extensively used options for turbulent flame simulations. The tabulated methods present in the literature offer different strategies in terms of the flamelet configuration used, the combination of steady and unsteady flames or the parametrization of the flamelet database, among other features. In this work, an approach based on the Flamelet Generated Manifold (FGM) method [34] is employed and the characteristics of the combustion model are described in this section.

First, the flamelet method is presented, focusing on the flamelet configurations and combinations employed and the different controlling variables considered for tabulation. Subsequently, the strategy used for the integration of tabulated properties to account for turbulence-chemistry interactions is described. Finally, the tabulation process and the final table structure is summarized. Again, the reader is referred to [19] for a more detailed description of the turbulent combustion model.

3.2.1 Flamelet method

The thermo-chemical state of the flame in this configuration is described by the flamelet method [35]. A scale separation between the flow and the chemistry is assumed, so that the flame structure can be defined by a composition of one-dimensional (1D) flames. Among the many canonical flame configurations, counterflow diffusion flamelets are used for all the applications studied in this work. This case is characterized by the inlet conditions of two opposed streams (temperature and composition of fuel and oxidizer) and the global strain rate a, defined in the far field of the oxidizer flow. A schematic of the counterflow flame configuration can be observed in Fig. 3.1. The equations system of the one-dimensional problem for this configuration [36] is presented here for completeness:

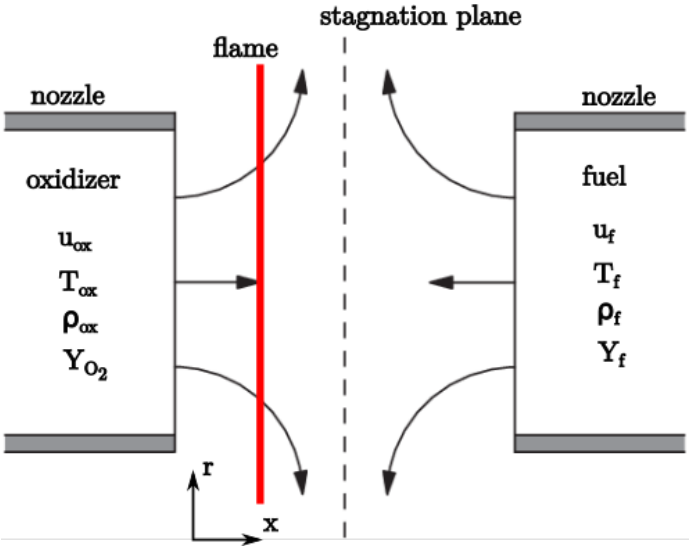

Figure 3.1: Scheme of a generic counterflow diffusion flame configuration. Adapted from [37].

$$\frac{\partial \rho}{\partial t} + \frac{\partial \rho u}{\partial x} = -\rho G, \tag{3.13}$$

$$\frac{\partial \rho Y_k}{\partial t} + \frac{\partial \rho u Y_k}{\partial x} = \frac{\partial}{\partial x}\left(\frac{\lambda}{Le_k c_p}\frac{\partial Y_k}{\partial x}\right) + \dot{\omega}_k - \rho Y_k G, \tag{3.14}$$

$$\frac{\partial \rho h}{\partial t} + \frac{\partial \rho u h}{\partial x} = \frac{\partial}{\partial x}\left[\frac{\lambda}{c_p}\frac{\partial h}{\partial x} + \frac{\lambda}{c_p}\sum_{k=1}^{N_s}\left(\frac{1}{Le_k} - 1\right) h_k \frac{\partial Y_k}{\partial x}\right] - \rho h G + S_h^{rad}, \tag{3.15}$$

$$\rho\frac{\partial G}{\partial t} + \rho u\frac{\partial G}{\partial x} = \frac{\partial}{\partial x}\left(\mu\frac{\partial G}{\partial x}\right) + \rho_{ox}a^2 - \rho G^2, \tag{3.16}$$

Basically, the equations are derived from the generic conservation equations (see Eqs. 2.3, 2.4, 2.6, 2.9). G is the local flame stretch defined as $G = \frac{\partial v}{\partial y}$ where v is the velocity component in y. The stretch transport equation is derived from the momentum equation, together with the assumption of potential flow conditions on the far field. In the present work, these equations are solved using detailed chemistry with Chem1D [38], assuming a unity Lewis number approach. The chemical mechanism used is specified for each particular application in the corresponding chapter.

In order to include heat loss effects in counterflow diffusion flamelets, the enthalpy level in this configuration is decreased using an additional source term in Eq. 3.15, S_h^{rad}. In Chem1D, this term is calculated following an optically thin radiative model. Therefore, the radiative source term is computed using the following expression:

$$S_h^{rad} = -4Q_{rad}\kappa\sigma\left(T^4 - T_{ff}^4\right), \tag{3.17}$$

where κ is the Planck mean absorption coefficient of the gas mixture, σ is the Stefan-Boltzmann constant and T and T_{ff} are the local and far field temperatures, respectively. Q_{rad} is a modelling constant which is equal to 1 for cases with physically meaningful radiation. Higher Q_{rad} values induce artificial radiation and are used here to reach lower enthalpy states.

For the generation of the flamelet database, laminar diffusion flamelets at different strain rates are tabulated in order to account for strain effects on the thermodiffusive behaviour of the reacting layer. Therefore, the entire stable branch is recovered with the steady-state solutions until the extinction point. An extinguishing flamelet initiated from the last stable instance (extinction point) is used as a natural continuation of this two-dimensional manifold [39], conducting an unsteady calculation to account for the transient development to the mixing state. Fig. 3.2 shows a representation of the manifold considering the mentioned approach. Note that only the solution for one enthalpy level ($Q_{rad} = 0$) is represented.

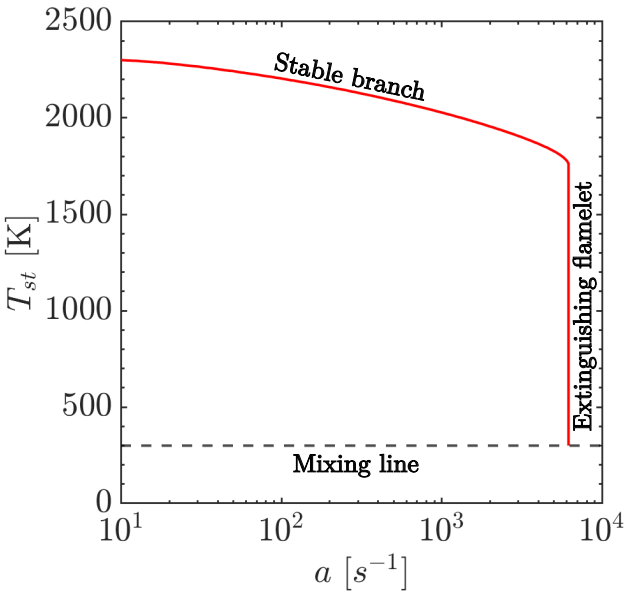

Figure 3.2: Illustration of the flamelet composition of the manifold represented by the stoichiometric temperature T_{st} in function of the strain rate a. It corresponds to ethylene-air counterflow flames at ambient conditions and with $Q_{rad} = 0$.

Controlling variables

Three controlling variables are used to characterize the thermochemical state of the flamelets composing the manifold: mixture fraction Z, progress variable Y_c, and scaled enthalpy $\mathcal{H}$. The mixture fraction is determined by Bilger's formula, while the progress variable Y_c in this study is defined as:

$$Y_c = \sum_{k=1}^{N} \frac{a_k}{W_k} Y_k. \tag{3.18}$$

In view of the wide variety of progress variable definitions used in the literature, the selection of an appropriate progress variable which provides an adequate parametrization of the flamelet states is not evident. For instance, the use of both adiabatic and non-adiabatic flamelets makes it difficult to find a single definition that ensures the monotonic behaviour of the progress variable for all conditions. In this work, different definitions are used for the different studied cases, which are described in the corresponding sections. To

facilitate the flamelet manifold tabulation, retrieval and integration, a scaled progress variable C is defined as:

$$C = \frac{Y_c - Y_{c,min}(Z)}{Y_{c,max}(Z) - Y_{c,min}(Z)}, \tag{3.19}$$

where $Y_{c,max}(Z)$ and $Y_{c,min}(Z)$ are the maximum and minimum progress variable profiles which correspond to $C = 0$ in the mixing line and $C = 1$ in the stable solution of the lowest strain flamelet. Note that, in this way, the dependency of the strain rate is accounted in the manifold by the use of the normalized progress variable, which varies between 0 and 1 depending on the strain level.

The different enthalpy levels reached with the previously described method are accounted in the manifold by means of a scaled enthalpy factor $\mathcal{H}$. It is calculated using the following expression:

$$\mathcal{H} = \frac{h - h_{min}(Z, C)}{h_{max}(Z, C) - h_{min}(Z, C)}. \tag{3.20}$$

For a particular value of the total enthalpy h, the scaled enthalpy $\mathcal{H}$ is defined by the maximum and minimum enthalpy levels, $h_{max}(Z, C)$ and $h_{min}(Z, C)$, given in the low-dimensional manifold for every mixture fraction and progress variable. Therefore, $\mathcal{H} = 1$ corresponds to the maximum enthalpy level (or adiabatic conditions) and the minimum level is defined by $\mathcal{H} = 0$ (given by the maximum radiation factor considered during the flamelet calculations).

Flamelet calculations are the first stage of this turbulent combustion modelling approach and a three-dimensional database is obtained when considering the procedure and controlling variables presented here. Any magnitude ψ that describes the thermo-chemical state can be tabulated in this three-dimensional table as function of the mixture fraction, scaled progress variable and enthalpy factor: $\psi(Z, C, \mathcal{H})$.

Tabulated chemistry in the LES framework

In order to describe the chemical evolution of the reacting flow, additional transport equations for the filtered controlling variables within the LES framework are needed. The normalized enthalpy is obtained directly from the filtered enthalpy solved in Eq. 3.4. However, additional transport equations are

required for the filtered mixture fraction and progress variable, which follow the generic form of a scalar transport equation:

$$\frac{\partial \overline{\rho}\widetilde{Z}}{\partial t} + \boldsymbol{\nabla}\cdot\left(\overline{\rho}\widetilde{\boldsymbol{u}}\widetilde{Z}\right) = -\boldsymbol{\nabla}\cdot\overline{\tau}_Z + \boldsymbol{\nabla}\cdot\left(\bar{\rho}\bar{D}\boldsymbol{\nabla}\widetilde{Z}\right) + \bar{S}_Z, \tag{3.21}$$

$$\frac{\partial \overline{\rho}\widetilde{Y_c}}{\partial t} + \boldsymbol{\nabla}\cdot\left(\overline{\rho}\widetilde{\boldsymbol{u}}\widetilde{Y_c}\right) = -\boldsymbol{\nabla}\cdot\overline{\tau}_{Y_c} + \boldsymbol{\nabla}\cdot\left(\bar{\rho}\bar{D}\boldsymbol{\nabla}\widetilde{Y_c}\right) + \overline{\dot{\omega}}_{Y_c}. \tag{3.22}$$

Note that all magnitudes are analogous to those described in Section 3.1.1 (see Eqs. 3.2 to 3.4). The source term $\bar{S}_Z$ in the $\widetilde{Z}$ equation refers to the mass generated by droplet evaporation, while $\overline{\dot{\omega}}_{Y_c}$ is the filtered progress variable source term. The unresolved terms appearing after the LES filtering $\overline{\tau}_Z$ and $\overline{\tau}_{Y_c}$ are closed using the gradient diffusion approach for sub-grid scalar fluxes (see Eq. 3.11):

$$\overline{\tau}_Z = -\frac{\overline{\rho}\nu_t}{Sc_t}\boldsymbol{\nabla}\widetilde{Z}, \tag{3.23}$$

$$\overline{\tau}_{Y_c} = -\frac{\overline{\rho}\nu_t}{Sc_t}\boldsymbol{\nabla}\widetilde{Y}_c. \tag{3.24}$$

3.2.2 Turbulence-chemistry interaction

In this work, the presumed probability density function approach is used to account for turbulence/chemistry interactions at the sub-grid scale. The tabulated properties ψ from the manifold are integrated with a presumed-shape probability density function (PDF) that describes the statistical effect of turbulence on the flame structure [29]. Therefore, for any tabulated variable ψ this three-dimensional manifold $\psi = \psi(Z, C, \mathcal{H})$ must be integrated with a filtered joint-PDF $\widetilde{P}(Z, C, \mathcal{H})$. Any Favre-filtered tabulated quantity $\widetilde{\psi}$ is given by:

$$\widetilde{\psi} = \int_0^1\int_0^1\int_0^1 \psi(Z, C, \mathcal{H})\widetilde{P}(Z, C, \mathcal{H})dZdCd\mathcal{H}, \tag{3.25}$$

while the non-density-weighted filtered magnitudes are obtained from:

$$\overline{\psi} = \overline{\rho}\int_0^1\int_0^1\int_0^1 \frac{\psi(Z, C, \mathcal{H})}{\rho(Z, C, \mathcal{H})}\widetilde{P}(Z, C, \mathcal{H})dZdCd\mathcal{H}. \tag{3.26}$$

The filtered density $\overline{\rho}$ is obtained from the Favre-filtered specific volume $\widetilde{1/\rho}$ by:

$$\overline{\rho} = \frac{1}{\widetilde{1/\rho}} = \frac{1}{\int_0^1 \int_0^1 \int_0^1 \frac{1}{\rho(Z,C,\mathcal{H})} \widetilde{P}(Z,C,\mathcal{H}) dZ dC d\mathcal{H}}. \tag{3.27}$$

The joint-PDF $\widetilde{P}(Z,C,\mathcal{H})$ of three independent variables is prohibitively complex for most modelling strategies, thus the joint-PDF is treated as a product of statistically independent PDFs of each degree of freedom [40]:

$$\widetilde{P}(Z,C,\mathcal{H}) \approx \widetilde{P}_Z(Z)\widetilde{P}_C(C)\widetilde{P}_{\mathcal{H}}(\mathcal{H}). \tag{3.28}$$

In general, β or δ functions are commonly used for the presumed-shape PDF of each control variable. Usually, a δ function is used in the modelling of scaled enthalpy in non-adiabatic cases due to the fact that sub-grid enthalpy variations are not linked to different sub-grid levels of $\mathcal{H}$ [19]. Mixture fraction is normally modelled using a β-PDF but the sub-grid contribution of the scaled progress variable depends on the particular case. In the applications studied in the present thesis, different approaches are used regarding the presumed shape PDFs for each control variable and the description is given in the dedicated chapters. However, the most general approach is described here, which corresponds to β functions for both mixture fraction and progress variable and a δ function for the scaled enthalpy. In this case, the distributions of mixture fraction and progress variable are defined by the filtered values $\widetilde{Z}$, $\widetilde{Y_c}$ and sub-grid variances $Z_v = \widetilde{ZZ} - \widetilde{Z}\widetilde{Z}$, $Y_{c,v} = \widetilde{Y_c Y_c} - \widetilde{Y_c}\widetilde{Y_c}$ of Z and Y_c, respectively.

A closure for the sub-grid scale variances Z_v, $Y_{c,v}$ is then required to recover the tabulated quantities, so transport equations for Z_v and $Y_{c,v}$ are solved [41] on top of Eqs. 3.21 and 3.22. The transport equations for the mixture fraction and progress variable sub-grid variances are given by:

$$\frac{\partial \overline{\rho} Z_v}{\partial t} + \boldsymbol{\nabla} \cdot (\overline{\rho}\tilde{\boldsymbol{u}} Z_v) = -\boldsymbol{\nabla} \cdot \overline{\tau}_{Z_v} + \boldsymbol{\nabla} \cdot \left(\bar{\rho}\bar{D}\boldsymbol{\nabla} Z_v\right) - 2\overline{\tau}_Z \cdot \boldsymbol{\nabla}\tilde{Z} - \overline{s}_{\chi_Z}, \tag{3.29}$$

$$\frac{\partial \overline{\rho} Y_{c,v}}{\partial t} + \boldsymbol{\nabla} \cdot (\overline{\rho}\tilde{\boldsymbol{u}} Y_{c,v}) = -\boldsymbol{\nabla} \cdot \overline{\tau}_{Y_{c,v}} + \boldsymbol{\nabla} \cdot \left(\bar{\rho}\bar{D}\boldsymbol{\nabla} Y_{c,v}\right) - 2\overline{\tau}_{Y_c} \cdot \boldsymbol{\nabla}\tilde{Y}_c - \overline{s}_{\chi_{Y_c}} + 2\left(\overline{Y_c \dot{\omega}}_{Y_c} - \tilde{Y}_c \overline{\dot{\omega}}_{Y_c}\right). \tag{3.30}$$

The unresolved fluxes of mixture fraction and progress variable variances, $\overline{\tau}_{Z_v}$ and $\overline{\tau}_{Y_{c,v}}$, are closed using the gradient diffusion approach (see Eq. 3.11):

$$\overline{\tau}_{Z_v} = -\frac{\overline{\rho}\nu_t}{Sc_t}\boldsymbol{\nabla} Z_v, \tag{3.31}$$

$$\overline{\tau}_{Y_{c,v}} = -\frac{\overline{\rho}\nu_t}{Sc_t}\boldsymbol{\nabla} Y_{c,v}, \tag{3.32}$$

The terms $\overline{s}_{\chi Z}$ and $\overline{s}_{\chi Y_c}$ correspond to the unresolved part of the scalar dissipation rate of mixture fraction and progress variable, respectively. They are modelled assuming a linear relaxation of the variance within the sub-grid [29] and are given by:

$$\overline{s}_{\chi Z} = \overline{\rho} C_\chi \frac{Z_v}{\tau_{SGS}}, \tag{3.33}$$

$$\overline{s}_{\chi Y_c} = \overline{\rho} C_\chi \frac{Y_{c,v}}{\tau_{SGS}}. \tag{3.34}$$

where $C_\chi = 2$ is a modelling constant [42] and τ_{SGS} is a sub-grid time scale [28]. The chemical state of the turbulent flame in the LES framework is ultimately described by the five control variables: $\widetilde{Z}$, Z_v, $\widetilde{Y_c}$, $Y_{c,v}$ and $\widetilde{h}$.

3.2.3 Tabulation strategy

The present tabulated chemistry model is intended to provide the required magnitudes for the closure of the governing equations: Eqs. 3.2, 3.3, 3.4, 3.21, 3.22, 3.29 and 3.30. In view of the equations system, the filtered mixture properties $\overline{\rho}$, $\overline{\mu}$ and $\overline{D}$ are required. Therefore, the final manifold contains the following tabulated properties: the thermal conductivity $\overline{\lambda}$, dynamic viscosity $\overline{\mu}$, molecular weight $\overline{W}$ and the mean NASA c_p coefficients $\widetilde{b_i}$ of the mixture. During the CFD calculation, the enthalpy equation is solved and the temperature is recalculated using the NASA polynomials: $\widetilde{T} = T(\widetilde{h}, \widetilde{b_i})$. After that, the filtered density $\overline{\rho}$ is computed with the ideal gas law using the calculated temperature, the tabulated molecular weight $\overline{W}$ and the specified thermodynamic pressure. During the evaluation of $\widetilde{T}$, the specific heat is also obtained as $\widetilde{c_p} = c_p(\widetilde{h}, \widetilde{b_i})$ and it is used together with the density and the tabulated thermal conductivity $\overline{\lambda}$ to compute $\overline{D}$. Finally, the progress variable source term $\overline{\dot{\omega}}_{Y_c}$ and the first term in the progress variable variance source $\overline{Y_c\dot{\omega}}_{Y_c}$ are also tabulated in order to solve Eqs. 3.22 and 3.30.

3.3 Soot modelling

In the present dissertation, soot modelling is addressed by means of an efficient implementation of the sectional method within the LES framework and it is integrated with the tabulated chemistry model for combustion in Alya. The soot aerosol dynamics are described by the Population Balance Equation (PBE) of the particle Number Density Function (NDF). Solving the PBE is not feasible in turbulent flows, and the method of moments (MoM) [43] and the discrete sectional method (DSM) [44] have been proposed to model the NDF. The particle distribution is approximated in MoM by solving transport equations for the low-order moments, while the continuous distribution is discretized by a finite amount of sections for the DSM. The sectional method is selected in this work due to its capability to predict different distribution shapes. However, it could be computationally demanding when the number of sections is increased to improve accuracy. In this regard, the efficient implementation employed here aims to take advantage of these qualities of the sectional modelling approach while maintaining an affordable computational cost for use in a practical application.

The following subsections are focused on the description of the soot modelling approach. In the first subsection, the basis and fundamental principles of the discrete soot sectional method are described. Subsequently, the efficient implementation of the sectional model within the LES-FGM framework is introduced. The soot sectional approach used in this work is based on the work of Hoerle and Pereira [45] and the efficient coupling with the FGM model has been carried out by Kalbhor and Mira [20, 21]. Any reader is referred to these works for further information and details of the modelling approach.

3.3.1 Sectional soot method

The soot modeling approach is based on the discrete sectional method (DSM) [44, 46]. In the DSM-based models, the problem of solving the General Population Balance Equation (GPBE) that characterizes the continuous Particle Size Distribution (PSD) is addressed by dividing the PSD into a finite number of sections n_{sec}. Particle sizes within a range between a minimum V_{min} and maximum V_{max} volume can be resolved, depending on the number of sections considered. Fig. 3.3 shows an illustration of the section discretization principle.

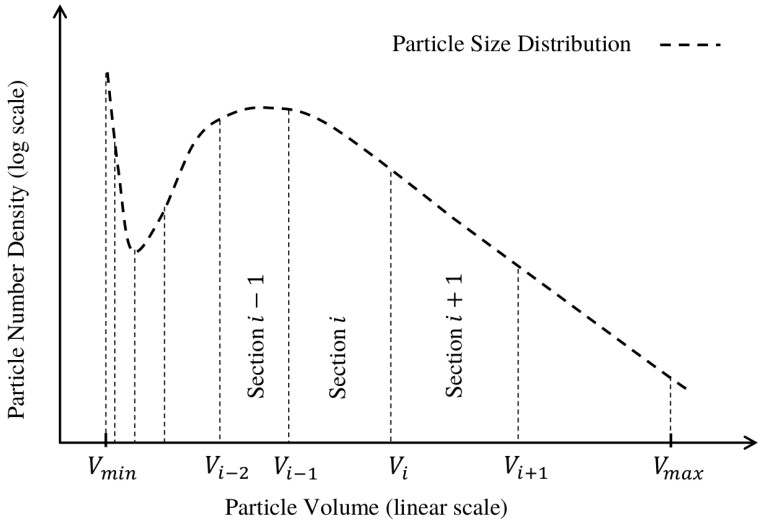

Figure 3.3: Schematic of the PSD discretization into a finite number of sections in the DSM. Image from [21].

Transport equation for soot sections

For each representative soot size (section i), the governing equation for the soot mass fraction $Y_{s,i}$ is solved by considering flow convection, diffusion, thermophoresis, and soot sources. The sectional soot transport equation can be formulated as:

$$\frac{\partial\left(\rho Y_{s,i}\right)}{\partial t}+\nabla\cdot\left(\rho\left[\boldsymbol{u}+\boldsymbol{v_T}\right]Y_{s,i}\right)=\nabla\cdot\left(\rho D_{s,i}\nabla Y_{s,i}\right)+\dot{\omega}_{s,i}\quad\forall\quad i\in[1,n_{sec}] \tag{3.35}$$

Assuming the soot volume negligible compared to the total gas volume, the soot volume fraction of section i can be calculated from the soot mass fraction $Y_{s,i}$ as:

$$Q_i=\frac{\rho}{\rho_s}Y_{s,i}, \tag{3.36}$$

where ρ_s is the density of soot particles. In Eq. 3.35, $\dot{\omega}_{s,i}$ is the sectional source term, which can be expressed as function of the rate of soot volume fraction as $\dot{\omega}_{s,i}=\rho_s\dot{Q}_i$. The thermophoretic velocity $\boldsymbol{v_T}$ is calculated with Frienlander's expression [47] as:

$$\boldsymbol{v_T} = -\frac{3}{4}\left(1 + \frac{\pi\alpha_{acc}}{8}\right)^{-1}\frac{\nu}{T}\nabla T, \tag{3.37}$$

where ν is the kinematic viscosity, T is the local temperature and α_{acc} is the accommodation coefficient taken as 0.9. $D_{s,i}$ in Eq. 3.35 is the diffusion coefficient of soot section i and it is assumed to be $\sim 1\%$ of the average gas diffusivity to ensure the numerical stability.

Sectional discretization

The discretization of soot particles with respect to their volume into different sections is performed in this work assuming a linear growth of particle size in logarithmic scale [46]. Therefore, the limit in terms of particle volume of a given section i is determined by:

$$V_i = V_{min}\left(\frac{V_{max}}{V_{min}}\right)^{i/n_{sec}}, \quad i = 1, 2, ..., n_{sec} \tag{3.38}$$

Assuming this discretization, the lower boundary of section i is V_{i-1}, the upper boundary corresponds to V_i and the biggest particle of section $i-1$ is the same as the smallest particle of section i, as illustrated in Fig. 3.3. The volume of the smallest particle V_{min} is defined by the carbon-equivalent volume of the number of carbon atoms of two soot precursor molecules. In this work, pyrene ($C_{16}H_{10}$) is selected as the aromatic precursor [48], thus, $V_{min} = 3.428 \cdot 10^{-28}$ m^3. The biggest particle size V_{max} defines the limit of the PSD and the range of the largest modelled particle. It is chosen as an unattainable soot particle volume such that the particles no longer accumulate in the last section. In the present model, $V_{max} = 5.236 \cdot 10^{-16}$ m^3.

The soot distribution inside a section is characterized by the soot volume fraction density q_i, which is assumed to be a constant distribution within each section:

$$q_i = \frac{Q_i}{V_i - V_{i-1}}, \tag{3.39}$$

where Q_i is the soot volume fraction of section i. The particle size distribution within each section n_i is defined from the soot volume fraction density as follows:

$$n_i(v) = \frac{q_i}{v}, \tag{3.40}$$

where v is the volume between section boundaries. This formulation leads to the calculation of soot number density in section i, N_i, by the integration of the continuous particle size distribution:

$$N_i = \int_{V_{i-1}}^{V_i} n_i(v)dv. \tag{3.41}$$

Assuming the constant profile of the section size distribution (Eq. 3.39), the number density becomes:

$$N_i = \frac{Q_i}{V_i - V_{i-1}} \ln\left(\frac{V_i}{V_{i-1}}\right). \tag{3.42}$$

Finally, the total soot volume fraction (SVF) and total soot number density (N_T) are calculated with the following expressions:

$$SVF = \sum_{i=1}^{n_{sec}} Q_i, \tag{3.43}$$

$$N_T = \sum_{i=1}^{n_{sec}} N_i. \tag{3.44}$$

Soot source terms

The source terms for soot chemistry are evaluated by including the contributions of soot kinetics (nucleation, PAH condensation, surface growth, oxidation) and soot particle dynamics (coagulation) sub-processes. An schematic of the different processes involved in soot formation is illustrated in Fig. 3.4.

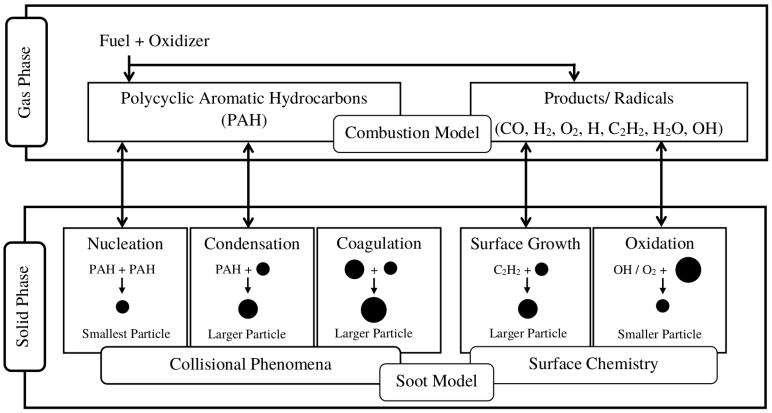

Figure 3.4: Subprocesses controlling soot formation and oxidation and respective involved gaseous species. Image from [21].

Considering these processes, the total soot mass fraction source term in Eq. 3.35 can be written as:

$$\dot{\omega}_{s,i} = \rho_s \dot{Q}_i = \rho_s \left(\dot{Q}_{nuc,i} + \dot{Q}_{cond,i} + \dot{Q}_{coag,i} + \dot{Q}_{sg,i} + \dot{Q}_{ox,i} \right), \tag{3.45}$$

where $\dot{Q}_{nuc,i}$, $\dot{Q}_{cond,i}$, $\dot{Q}_{coag,i}$, $\dot{Q}_{sg,i}$ and $\dot{Q}_{ox,i}$ are the rates of soot volume fraction for section i due to nucleation, condensation, coagulation, surface growth and oxidation.

Soot is assumed to nucleate through the dimerization of PAH, taken as pyrene (A4) in the current model. This step contributes only to the first section and it is modelled using an expression analogous to the Smoluchowski's equation [49]. Therefore, the rate of change in soot volume fraction due to nucleation is given by:

$$\dot{Q}_{nuc,1} = 2 v_{PAH} \beta_{PAH,PAH} N_{PAH}^2, \tag{3.46}$$

where v_{PAH} is the volume, $\beta_{PAH,PAH}$ is the collision frequency factor (estimated for the free molecular regime using an amplification factor due to van der Waals interactions [48]) and N_{PAH} is the number density of PAH molecules (in this case, $N_{PAH} = N_{A4} = [A4]\, N_A$).

The condensation process is modelled as the coalescence of a PAH molecule on the surface of soot particles and the source term is computed according to [48]. Assuming a unity condensation probability and considering Eq. 3.39, the total volume growth rate due to condensation is:

$$\Delta\dot{Q}_{cond,i} = v_{PAH}\beta_{i,PAH}N_{PAH}\frac{Q_i}{V_i - V_{i-1}}\ln\left(\frac{V_i}{V_{i-1}}\right). \tag{3.47}$$

The coagulation process of soot particles is described by following the model proposed by Kumar and Ramkrishna [50]. The morphological description of soot particles is not considered for simplicity. By using Eq. 3.41, the source term for coagulation read as:

$$\dot{Q}_{coag,i} = \frac{dN_i}{dt}\frac{(V_i - V_{i-1})}{\ln\left(\frac{V_i}{V_{i-1}}\right)}, \tag{3.48}$$

where $\frac{dN_i}{dt}$ is the soot coagulation source term for section i derived by [50].

The growth and oxidation of soot particles by surface reactions are modeled through the standard hydrogen-abstraction-C_2H_2-addition (HACA) mechanism [51, 52]. The strategy introduced by Hoerlle and Pereira [45] is used to account for the conservation of surface radicals during acetylene addition. The full set of chemical reactions and some of the mathematical expressions are omitted here for brevity. The final expressions for the change in soot volume fraction due to surface growth, O_2 and OH oxidation are given by:

$$\Delta\dot{Q}_{sg,i} = 2v_C k_{sg}\left[C_2H_2\right]\left[C^*_{soot,n}\right]_i N_A, \tag{3.49}$$

$$\Delta\dot{Q}_{ox_{O_2},i} = -2v_C k_{ox_{O_2}}\left[O_2\right]\left[C^*_{soot,n}\right]_i N_A, \tag{3.50}$$

$$\Delta\dot{Q}_{ox_{OH},i} = -\gamma_{OH}v_C\beta_{i,OH}\left[OH\right]N_A\frac{Q_i}{V_i - V_{i-1}}\ln\left(\frac{V_i}{V_{i-1}}\right), \tag{3.51}$$

where v_C is the volume of one carbon atom, k_{sg} and $k_{ox_{O_2}}$ are the chemical reaction rates of the corresponding HACA mechanism reactions, $C^*_{soot,n}$ are the dehydrogenated carbon atoms, γ_{OH} is the corresponding reaction probability and N_A is the Avogadro number. Note that the total oxidation source term is finally obatined by:

$$\Delta\dot{Q}_{ox,i} = \Delta\dot{Q}_{ox_{O_2},i} + \Delta\dot{Q}_{ox_{OH},i}. \tag{3.52}$$

Inter-sectional dynamics

The growth or reduction of particle size due to the aforementioned processes leads to an eventual movement of particles to higher or lower sections. These

movements are crucial for determining the exact source term for a particular section. These inter-sectional dynamics are already included in the coagulation mode, however, a special treatment is required when it comes to condensation, surface growth and oxidation processes. The total rate of change in soot volume fraction $\Delta\dot{Q}_i$ for section i is defined by:

$$\Delta\dot{Q}_i = \Delta\dot{Q}_i^{in} + \Delta\dot{Q}_i^{out}, \tag{3.53}$$

where $\Delta\dot{Q}_i^{in}$ is the source term due to particles that remain in the same section while $\Delta\dot{Q}_i^{out}$ is the source term due to particles that move out of the neighboring section and enter in the current one. The relation between these terms is determined based on the conservation of volume and number density along with the assumption of an even distribution of $\Delta\dot{Q}_i$ across the section. Therefore, the decrease of number density in a given section i due to condensation or surface growth is the same of section $i+1$, $-\Delta N_i = \Delta N_{i+1}$. The relationship is analogous in the case of the oxidation process, considering the opposite direction: $-\Delta N_i = \Delta N_{i-1}$. Taking this into account, the final condensation $\dot{Q}_{cond,i}$, surface growth $\dot{Q}_{sg,i}$ and oxidation $\dot{Q}_{ox,i}$ source terms can be derived from the different $\Delta\dot{Q}_i^{in}$ and $\Delta\dot{Q}_i^{out}$ depending on the section considered. Note that there are some sections that require a special treatment (first and last) due to the fact that there is no soot entering into the first section from lower sections and no soot particle grows beyond the maximum size of the last section, in the particular case of soot growth. The full description of inter-sectional dynamics requires much detail and it is omitted here for brevity. Any interested reader is referred to [21] for the complete description and particularization for each subprocess.

3.3.2 Description of the FGM-CDSM formalism for LES

In the present FGM-DSM approach, the detailed chemistry-based solutions of steady and unsteady counterflow diffusion flamelets are used for the creation of the manifold. During flamelet generation, transport equations for soot mass fractions in n_{sec} sections are also solved, as described in the previous subsection. However, for the application of the discrete sectional method in LES, the number of sections n_{sec} are combined into a limited group of clusters n_c for the transport of soot in the CFD simulation. This approach of clustered sections within the FGM chemistry framework is referred to as FGM-CDSM [20]. By assuming the preservation of soot PSD within the clustered section, the soot mass fraction in a clustered section ($\widetilde{Y}_{s,j}^c$) is given by:

$$\widetilde{Y}^c_{s,j} = \sum\nolimits_{i=i_j^{\min}}^{i_j^{\max}} \widetilde{Y}_{s,i}, \tag{3.54}$$

where $i_j^{\min}$ and $i_j^{\max}$ are, respectively, the lower and upper limit of the sections i that are clustered in j. In this work, a uniform clustering of sections is employed and Fig. 3.5 illustrates an schematic of the clustering process.

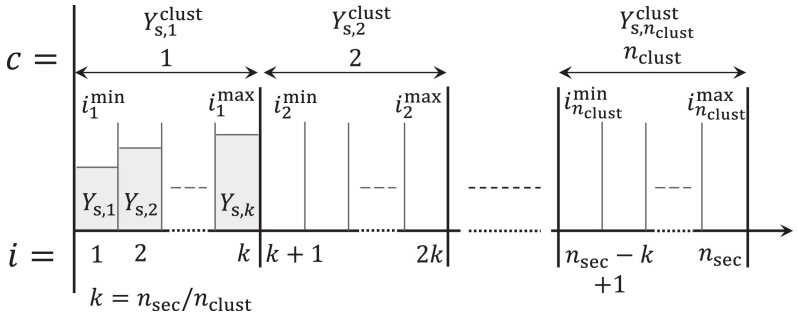

Figure 3.5: Methodology for uniform clustering in the FGM-CDSM modelling approach. Image from [21].

Therefore, filtered transport equations are solved during the CFD calculation for the soot mass fraction in a few n_c clustered sections instead n_{sec} as:

$$\frac{\partial \overline{\rho}\widetilde{Y}^c_{s,j}}{\partial t} + \boldsymbol{\nabla}\cdot\left(\overline{\rho}\left[\widetilde{\boldsymbol{u}} + \widetilde{\boldsymbol{v}}_T\right]\widetilde{Y}^c_{s,j}\right) = -\overline{\tau}_{Y^c_{s,j}} + \boldsymbol{\nabla}\cdot\left(\overline{\rho}\overline{D}_s\boldsymbol{\nabla}\widetilde{Y}^c_{s,j}\right) + \overline{\dot{\omega}}^c_{s,j}, \qquad \forall\ j\ \in [1, n_c] \tag{3.55}$$

where $\overline{\tau}_{Y^c_{s,j}}$ is the unresolved scalar flux, which is modelled considering the gradient diffusion approach (see Eq. 3.11):

$$\overline{\tau}_{Y^c_{s,j}} = -\frac{\overline{\rho}\nu_t}{Sc_t}\boldsymbol{\nabla}\widetilde{Y}^c_{s,j}. \tag{3.56}$$

The thermophoretic velocity $\widetilde{\boldsymbol{v}}_T$ in Eq. 3.55 is modeled following [53]:

$$\widetilde{\boldsymbol{v}}_T = -0.554\overline{\nu}\frac{\nabla\widetilde{T}}{\widetilde{T}}. \tag{3.57}$$

In the current modelling approach, soot source terms are tabulated in the manifold. Hence, the non-linear dependence of different soot subprocesses with sectional soot mass fractions is not explicitly solved in the CFD, but included in the flamelet computations . The inter-sectional dependence of soot particles is implicitly accounted for in the flamelet stage, where a full description of the gas phase and soot sectional equations are solved fully coupled [54]. Therefore, the resulting flamelet calculation accounts for all the soot sub-processes and the inter-sectional dependency. This method allows for a reduction in computational cost by the clustering of the soot sections, which mainly assumes that the interactions of the clustered sections with the turbulent flow field is similar to those of the individual sections [20].

The approach employed for the chemical source term treatment in the transport of slowly evolving species such as PAH and NO in other works [40, 55], is applied for soot in the proposed modelling framework [20]. Accordingly, the soot source term for the clustered section is split into production ($\dot{\omega}^{c,+}_{s,j}$) and consumption rates ($\dot{\omega}^{c,-}_{s,j}$). The consumption rate is linearized by soot mass fraction to avoid the un-physical production of soot, so the filtered soot source term for the clustered section is modeled as:

$$\overline{\dot{\omega}}^{c}_{s,j} = \overline{\dot{\omega}}^{c,+}_{s,j} + \overline{\dot{\omega}}^{c,-}_{s,j} \approx \left[\overline{\dot{\omega}}^{c,+}_{s,j}\right]^{\mathrm{tab}} + \widetilde{Y}_{s,j} \left[\frac{\dot{\omega}^{c,-}_{s,j}}{Y_{s,j}}\right]^{\mathrm{tab}} , \tag{3.58}$$

where the production term and linearized consumption term are parameterized through gas-phase thermochemical variables and tabulated (denoted by 'tab' superscript) in the manifold. For the LES application, the soot source term is convoluted with the β-PDF function in a pre-processing stage. With this approximation, turbulence-soot interaction is partially accounted for by including the effect of sub-grid scale fluctuations in mixture-fraction and progress variables on soot source terms.

After the CFD calculation of soot transport in clustered sections, the distribution of soot mass fraction within the n_{sec} sections is re-constructed ($Y^{\mathrm{re}}_{s,i}$) via the expression:

$$\widetilde{Y}^{\mathrm{re}}_{s,i} = \left[\widetilde{\mathcal{F}}_i\right]^{\mathrm{tab}} \widetilde{Y}^{c}_{s,j} \qquad \forall\ j \in (1, n_c)\ ;\ i \in (1, n_{sec})\,, \tag{3.59}$$

with $\mathcal{F}_i$ the mass fraction of section i in cluster j given by:

$$\mathcal{F}_i = \frac{Y_{s,i}}{\sum_{i=i^{\min}_j}^{i^{\max}_j} Y_{s,i}}. \tag{3.60}$$

This fraction is assumed to be a function of the control variables only and it is included in the database. Subsequently, relevant soot quantities such as total number density, average particle diameter, and PSDF can be derived from the re-constructed soot mass fractions using the appropriate relations [45].

3.4 Spray modelling

The evaporating droplet cloud is described by Lagrangian particles using a Lagrangian Particle Tracking (LPT) method. In this approach, droplets are represented by point particles which move independently in the computational domain and interact with the gaseous phase. As introduced in Chapter 2, this strategy is valid for dilute sprays where the volume fraction of the liquid phase is below a given threshold ($1e^{-3}$) [23]. To describe the state of a droplet, a tracking algorithm is used to obtain the location, velocity, temperature, and particle sizes by solving ordinary differential equations (ODEs). The first two variables are treated with a kinematic model, while the the thermodynamic conditions of the droplet are given from the heat and mass transfer models. The description of these models is addressed in this section.

The droplet kinematic behaviour is approached first and the differential equations for droplet position and velocity are presented. Then, the heat and mass transfer models are introduced, together with the different assumptions considered. Finally, the material properties required for the closure of the model equations and their tabulation within the tabulated chemistry framework are discussed.

3.4.1 Droplet kinematics

Droplets movement is governed by Newton's laws of motions. It is assumed that surface tension forces are sufficiently high so the deformation of droplets is neglected. In addition, droplets rotation is also considered to be negligible. The dominant force considered in the kinematic modelling of droplets is the drag and the governing equations describing the particle transport are given by:

$$\frac{d\boldsymbol{x}_p}{dt} = \boldsymbol{u}_p, \tag{3.61}$$

$$m_p \frac{d\boldsymbol{u}_p}{dt} = m_p \left(\boldsymbol{u}_p - \boldsymbol{u}\right) \frac{3}{4} \frac{C_D Re_p \rho_m \nu_m}{\rho_p d_p^2}, \tag{3.62}$$

where the subscript p refers to particle information, with $\boldsymbol{x}_p$, $\boldsymbol{u}_p$, m_p, ρ_p, d_p and C_D being the particle position, velocity, mass, density, diameter and drag coefficient. The particle Reynolds number Re_p is given by:

$$Re_p = \frac{d_p|\boldsymbol{u}_p - \boldsymbol{u}|}{\nu_m}. \tag{3.63}$$

The subscript m refers to adequate representative conditions of the surrounding gas, being ρ_m the density, ν_m the kinematic viscosity and $\boldsymbol{u}$ the velocity. The ODE system of location and velocity is solved by a combined Newmark/Newton-Raphson scheme [2]. The drag coefficient C_D is determined based on the Stokes flow around a sphere, considering high order Reynolds number effects with the Schiller-Naumann correction [23], following:

$$C_D = \begin{cases} \frac{24}{Re_p} + 3.6Re_p^{-0.313}, & Re_p \leq 1000, \\ 0.44, & Re_p > 1000. \end{cases} \tag{3.64}$$

The typical high Reynolds number limit for turbulent flows [56] is applied and the drag coefficient takes a constant value at high Reynolds, $C_D = 0.44$.

3.4.2 Heat and mass transfer models

The heat transfer between the droplet and the surrounding gas is described by assuming infinite conductivity on the liquid [57], where the droplet temperature T_p is given by:

$$m_p \frac{dT_p}{dt} = \frac{\pi d_p \lambda_m Nu}{c_{p,p}} (T_s - T_p) + \frac{L_v}{c_{p,p}} \frac{dm_p}{dt}, \tag{3.65}$$

where T_s is the temperature of the gas phase (denoted by the subscript s that refers to "seen" magnitudes) and λ_m is the representative conductivity of the surrounding gas. In Eq. 3.65, $c_{p,p}$ and L_v refer to the particle heat capacity and lower heating value of the fuel respectively.

Droplet evaporation is described by the Spalding mass transfer number B_M and the Sherwood number Sh as:

$$\frac{dm_p}{dt} = -\pi \rho_m d_p D_f Sh \ln(1 + B_M), \tag{3.66}$$

where D_f is the fuel diffusivity and the Spalding number B_M can be obtained from the fuel mass fraction at the interface $Y_{f,i}$ and the surrounding $Y_{f,s}$:

$$B_M = \frac{Y_{f,i} - Y_{f,s}}{1 - Y_{f,i}}. \tag{3.67}$$

The system of energy and mass ODEs is strongly coupled, and variations in evaporation rates influence droplet surface temperature. An implicit method is used to solve the heat and mass transfer after the particle velocities are updated. The Reynolds number dependence of the heat and mass transfer rates is modelled using the Ranz-Marshall correlation [58] applied on both the Nusselt Nu and Sherwood Sh numbers. Additional corrections are introduced following Abramzon and Sirignano [59] to account for Stefan flow, and the interaction between Stefan flow and the flow around the droplet.

3.4.3 Material properties and tabulated quantities

In the previously described models for heat and mass transfer of droplets, the gas phase material properties are required in order to solve the full equations system. These properties are non-constant across the film around the droplet and depend on temperature and composition. Therefore, a mean state is usually considered. In the equations described above, this mean state is represented by the subscript m.

In this work, the so called "1/3" law is employed, where the mean properties are evaluated at a virtual state characterized by a weighted average of the seen and interface composition and temperature [60]. Furthermore, the computation of these mean properties is integrated within the tabulated chemistry framework presented previously by means of the Tabulated Average Representative Evaporation State (TARES) model. It evaluates the representative properties of the gas phase using the already tabulated properties of the gas (needed for the general governing equations of the reacting flow introduced in the previous sections): the thermal conductivity ($\overline{\lambda}$), dynamic viscosity ($\overline{\mu}$), molecular weight ($\overline{W}$) and the mean NASA c_p coefficients ($\widetilde{b_i}$) of the mixture. For brevity, the full TARES model is not described here and the reader is referred to [19] for further details.

Overall, the use of the TARES approach for the calculation of the mean gas properties demands additional tabulated quantities. For completeness, in spray calculations using the TARES model the manifold is extended with

the fuel mass fraction $\widetilde{Y}_f$, fuel diffusivity $\overline{D}_f$, temperature $\widetilde{T}$ and the derivatives of thermal conductivity, dynamic viscosity and diffusivity with respect to temperature $\frac{\partial \lambda}{\partial T}$, $\frac{\partial \mu}{\partial T}$ and $\frac{\partial D}{\partial T}$, respectively.

3.5 Summary

In this chapter, a general overview of the modelling approach employed in this work has been introduced. Targeting aeronautical burner applications, combustion modelling is addressed in this work by means of tabulated chemistry (FGM) within the LES framework. For reacting flow simulations of spray flame applications, an Eulerian-Lagrangian description is used for the gaseous and disperse phases, respectively. A recently developed approach based on the Discrete Sectional Method and coupled to the LES-FGM framework (FGM-CDSM) is considered for soot prediction with a low computational cost. The balance between accuracy and computational efficiency in the present modelling strategy is achieved using a complete flamelet database, where several quantities are tabulated and retrieved during the CFD calculation. Table 3.1 contains a summary of all quantities that need to be tabulated depending on the models used. The proper description of each of these quantities and their necessity for the different models or the resolution of the transport equations have been addressed during this chapter.

It is worth mentioning that Table 3.1 contains all magnitudes that are necessary for the CFD calculation (i.e. for solving the equations or computing the different model expressions). However, additional variables are tabulated for post-processing tasks. For instance, mass fractions of species $\widetilde{Y}_k$ are computed during the manifold generation but they are not transported in the CFD. Instead, they are retrieved directly from the flamelet table using the control variables.

Fig. 3.6 shows a diagram containing the workflow followed by the present approach, as well as the coupling between the different elements and modelling parameters in the FGM-CDSM framework.

As described in the previous sections, the main element of this tabulated modelling framework is the flamelet manifold. It is generated during a preprocessing stage by the computation of different 1D flames and the integration for turbulent combustion is performed following a presumed-shape PDF approach. The manifold contains the required quantities for the full description of the thermochemical state and additional magnitudes or source terms depending on the models used (e.g. soot cluster source terms, mean gas properties for the spray model, etc.). During the CFD calculation, the Navier-Stokes

Combustion model	
Quantity	Symbol
Dynamic viscosity	$\overline{\mu}$
Thermal conductivity	$\overline{\lambda}$
Molecular weight	$\overline{W}$
c_p coefficients	$\widetilde{b}_i$
Progress variable source term	$\overline{\dot{\omega}_{Y_c}}$
$Y_{c,v}$ source term	$\overline{Y_c \dot{\omega}_{Y_c}}$

Soot model	
Quantity	Symbol
Production soot cluster source term	$\overline{\dot{\omega}}_{s,j}^{c,+}$
Consumption soot cluster source term	$\frac{\overline{\dot{\omega}_{s,j}^{c,-}}}{\overline{Y_{s,j}}}$

Spray model	
Quantity	Symbol
Fuel mass fraction	$\widetilde{Y}_f$
Fuel diffusivity	$\overline{D}_f$
Temperature	$\widetilde{T}$
Properties derivatives	$\frac{\partial \lambda}{\partial T}$ $\frac{\partial \mu}{\partial T}$ $\frac{\partial D}{\partial T}$

Table 3.1: Summary of the tabulated quantities of the present modelling framework.

equations and transport equations for the control variables and soot clusters are solved and the computational code is in constant interaction with the manifold providing the filtered values of control variables and retrieving the required magnitudes and source terms. Finally, in a post-processing stage, additional variables are computed or retrieved from the manifold such as species mass fractions or the original soot sections for the PSD reconstruction.

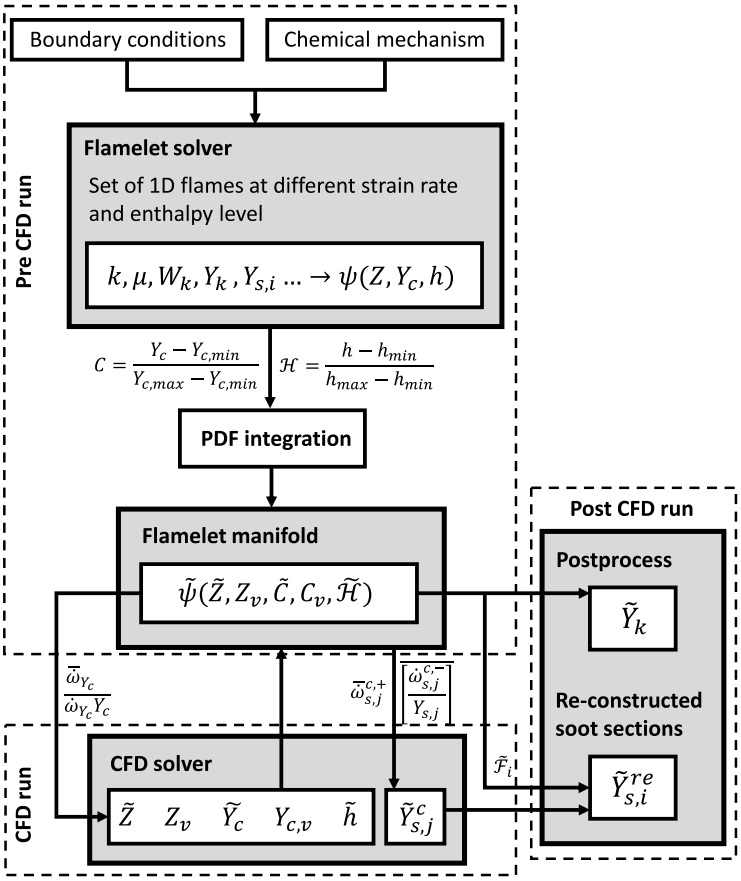

Figure 3.6: Workflow and coupling of the FGM-CDSM modelling framework.

In the following chapters, the modelling approach described here is applied to different case studies of turbulent flames in representative gas turbine applications. On the one hand, the Eulerian-Lagrangian approach for combustion of dilute sprays is evaluated in a reference spray flame. On the other hand, a gaseous aero-engine model combustor is studied in terms of combustion and soot formation and oxidation.

References

[1] Vazquez, M. et al. "Multiphysics engineering simulation toward exascale". In: *J. Comput. Sci.* 14 (2016), pp. 15–27.

[2] Houzeaux, Guillaume et al. "Dynamic load balance applied to particle transport in fluids". In: *International Journal of Computational Fluid Dynamics* 30.6 (2016), pp. 408–418.

[3] Turon, A, González, EV, Sarrado, C, Guillamet, G, and Maimí, P. "Accurate simulation of delamination under mixed-mode loading using a cohesive model with a mode-dependent penalty stiffness". In: *Composite Structures* 184 (2018), pp. 506–511.

[4] Wang, Zhinuo J et al. "Human biventricular electromechanical simulations on the progression of electrocardiographic and mechanical abnormalities in post-myocardial infarction". In: *EP Europace* 23 (2021), pp. i143–i152.

[5] Calmet, Hadrien et al. "Computational modelling of an aerosol extraction device for use in COVID-19 surgical tracheotomy". In: *Journal of Aerosol Science* 159 (2022), p. 105848.

[6] Guillamet, Gerard et al. "Application of the partial Dirichlet-Neumann contact algorithm to simulate low-velocity impact events on composite structures". In: *Composites Part A: Applied Science and Manufacturing* 167 (2023), p. 107424.

[7] Borrell, Ricard et al. "Parallel mesh partitioning based on space filling curves". In: *Computers & Fluids* 173 (2018), pp. 264–272.

[8] Banchelli, Fabio, Garcia-Gasulla, Marta, Houzeaux, Guillaume, and Mantovani, Filippo. "Benchmarking of state-of-the-art HPC Clusters with a Production CFD Code". In: *Proceedings of the Platform for Advanced Scientific Computing Conference*. 2020, pp. 1–11.

[9] Borrell, Ricard et al. "Heterogeneous CPU/GPU co-execution of CFD simulations on the POWER9 architecture: Application to airplane aerodynamics". In: *Future Generation Computer Systems* 107 (2020), pp. 31–48.

[10] Oyarzun, Guillermo, Mira, Daniel, and Houzeaux, Guillaume. "Performance assessment of cuda and openacc in large scale combustion simulations". In: *arXiv preprint arXiv:2107.11541* (2021).

[11] Banchelli, Fabio et al. “A portable coding strategy to exploit vectorization on combustion simulations”. In: *arXiv preprint arXiv:2210.11917* (2022).

[12] Houzeaux, Guillaume et al. “Dynamic resource allocation for efficient parallel CFD simulations”. In: *Computers & Fluids* 245 (2022), p. 105577.

[13] Mira, Daniel et al. “Heat transfer effects on a fully premixed methane impinging flame”. In: *Flow, Turbulence and Combustion* 97 (2016), pp. 339–361.

[14] Gövert, Simon et al. “Heat loss prediction of a confined premixed jet flame using a conjugate heat transfer approach”. In: *International Journal of Heat and Mass Transfer* 107 (2017), pp. 882–894.

[15] Mira, D et al. “Numerical characterization of a premixed hydrogen flame under conditions close to flashback”. In: *Flow, Turbulence and Combustion* 104 (2020), pp. 479–507.

[16] Mira, Daniel et al. “LES study on spray combustion with renewable fuels under ECN spray-A conditions”. In: *Internal Combustion Engine Division Fall Technical Conference*. Vol. 85512. American Society of Mechanical Engineers. 2021, V001T06A004.

[17] Both, Ambrus, Mira Martínez, Daniel, and Lehmkuhl Barba, Oriol. “Assessment of tabulated chemistry models for the les of a model aero-engine combustor”. In: *Proceedings of Global Power and Propulsion Society, GPPS Chania22, 18th-20th September, 2022*. Global Power and Propulsion Society (GPPS). 2022.

[18] Benajes, J et al. “Analysis of local extinction of a n-heptane spray flame using large-eddy simulation with tabulated chemistry”. In: *Combustion and Flame* 235 (2022), p. 111730.

[19] Both, Ambrus. “High-fidelity numerical simulations of reacting flows with tabulated chemistry”. PhD thesis. Universitat Politècnica de Catalunya, 2023.

[20] Kalbhor, Abhijit, Mira, Daniel, and Oijen, Jeroen van. “A computationally efficient approach for soot modeling with the discrete sectional method and FGM chemistry”. In: *Combustion and Flame* 255 (2023), p. 112868.

[21] Kalbhor, Abhijit. “Model development and numerical investigation of soot formation in combustion”. PhD thesis. Eindhoven University of Technology, 2023.

[22] Bao, Hesheng, Kalbhor, Abhijit, Maes, Noud, Somers, Bart, and Van Oijen, Jeroen. "Investigation of soot formation in n-dodecane spray flames using LES and a discrete sectional method". In: *Proceedings of the Combustion Institute* 39.2 (2023), pp. 2587–2597.

[23] Jenny, Patrick, Roekaerts, Dirk, and Beishuizen, Nijso. "Modeling of turbulent dilute spray combustion". In: *Progress in Energy and Combustion Science* 38.6 (2012), pp. 846–887. DOI: 10.1016/j.pecs.2012.07.001.

[24] Poinsot, Thierry and Veynante, Denis. *Theoretical and numerical combustion*. RT Edwards, Inc., 2005.

[25] Vreman, AW. "An eddy-viscosity subgrid-scale model for turbulent shear flow: Algebraic theory and applications". In: *Physics of fluids* 16.10 (2004), pp. 3670–3681.

[26] Smagorinsky, Joseph. "General circulation experiments with the primitive equations: I. The basic experiment". In: *Monthly weather review* 91.3 (1963), pp. 99–164.

[27] Lilly, Douglas K. "The representation of small-scale turbulence in numerical simulation experiments". In: *Proc. IBM Sci. Comput. Symp. on Environmental Science*. 1967, pp. 195–210.

[28] Both, Ambrus, Lehmkuhl, Oriol, Mira, D, and Ortega, Marc. "Low-dissipation finite element strategy for low Mach number reacting flows". In: *Computers & Fluids* 200 (2020), p. 104436.

[29] Domingo, P., Vervisch, L., and Veynante, D. "Large-eddy simulation of a lifted methane jet flame in a vitiated coflow". In: *Combustion and Flame* 152.3 (2008), pp. 415–432. DOI: http://dx.doi.org/10.1016/j.combustflame.2007.09.002.

[30] Tyliszczak, Artur, Cavaliere, Davide E, and Mastorakos, Epaminondas. "LES/CMC of blow-off in a liquid fueled swirl burner". In: *Flow, Turbulence and Combustion* 92 (2014), pp. 237–267.

[31] Rittler, Andreas, Proch, Fabian, and Kempf, Andreas M. "LES of the Sydney piloted spray flame series with the PFGM/ATF approach and different sub-filter models". In: *Combustion and Flame* 162.4 (2015), pp. 1575–1598.

[32] Giusti, Andrea, Kotzagianni, Maria, and Mastorakos, Epaminondas. "LES/CMC simulations of swirl-stabilised ethanol spray flames approaching blow-off". In: *Flow, turbulence and combustion* 97 (2016), pp. 1165–1184.

[33] Franzelli, B, Vié, A, Boileau, M, Fiorina, B, and Darabiha, N. "Large eddy simulation of swirled spray flame using detailed and tabulated chemical descriptions". In: *Flow, Turbulence and Combustion* 98 (2017), pp. 633–661.

[34] Oijen, J.A. Van and Goey, L.P.H. De. "Modelling of Premixed Laminar Flames using Flamelet-Generated Manifolds". In: *Combustion Science and Technology* 161.1 (2000), pp. 113–137. DOI: 10.1080/00102200008935814.

[35] Peters, N. "Laminar diffusion flamelet models in non-premixed turbulent combustion". In: *Progress in Energy and Combustion Science* 10.3 (1984), pp. 319–339. DOI: https://doi.org/10.1016/0360-1285(84)90114-X.

[36] Ramaekers, WJS. "Development of flamelet generated manifolds for partially-premixed flame simulations". PhD thesis. 2011.

[37] He, Z. Y., Zhou, Kun, Xiao, Ming, and Wei, F. "Simulation of Soot Size Distribution in a Counterflow Flame". In: *International Journal of Chemical Reactor Engineering* 13 (2015), pp. 101–95.

[38] CHEM1D. *A one dimensional flame code. Eindhoven University of Technology.* 2002.

[39] Delhaye, S., Somers, L.M.T., van Oijen, J.A., and de Goey, L.P.H. "Incorporating unsteady flow-effects beyond the extinction limit in flamelet-generated manifolds". In: *Proceedings of the Combustion Institute* 32.1 (2009), pp. 1051–1058. DOI: https://doi.org/10.1016/j.proci.2008.06.111.

[40] Ihme, Matthias and Pitsch, Heinz. "Prediction of extinction and reignition in nonpremixed turbulent flames using a flamelet/progress variable model. 2. Application in LES of Sandia flames D and E". In: *Combustion and Flame* 155.1-2 (2008), pp. 90–107. DOI: 10.1016/j.combustflame.2008.04.015.

[41] Pitsch, Heinz, Cha, Chong M., and Fedotov, Sergei. "Flamelet modelling of non-premixed turbulent combustion with local extinction and re-ignition". In: *Combustion Theory and Modelling* 7.2 (2003), pp. 317–332. DOI: 10.1088/1364-7830/7/2/306.

[42] Kemenov, Konstantin A, Wang, Haifeng, and Pope, Stephen B. "Modelling effects of subgrid-scale mixture fraction variance in LES of a piloted diffusion flame". In: *Combustion Theory and Modelling* 16.4 (2012), pp. 611–638.

[43] Frenklach, Michael. "Method of moments with interpolative closure". In: *Chemical Engineering Science* 57.12 (2002). Population balance modelling of particulate systems, pp. 2229–2239. DOI: https://doi.org/10.1016/S0009-2509(02)00113-6.

[44] Gelbard, Fred, Tambour, Yoram, and Seinfeld, John H. "Sectional representations for simulating aerosol dynamics". In: *Journal of Colloid and Interface Science* 76.2 (1980), pp. 541–556.

[45] Hoerlle, Cristian A. and Pereira, Fernando M. "Effects of CO2 addition on soot formation of ethylene non-premixed flames under oxygen enriched atmospheres". In: *Combustion and Flame* 203 (2019), pp. 407–423. DOI: 10.1016/J.COMBUSTFLAME.2019.02.016.

[46] Netzell, Karl, Lehtiniemi, Harry, and Mauss, Fabian. "Calculating the soot particle size distribution function in turbulent diffusion flames using a sectional method". In: *Proceedings of the Combustion Institute* 31.1 (2007), pp. 667–674.

[47] Friendlander, S.K. *Smoke, Dust and Haze: Fundamentals of Aerosol Dynamics*. Oxford University Press, New York, USA, 2000.

[48] Roy, Somesh Prasad. *Aerosol-dynamics-based soot modeling of flames*. The Pennsylvania State University, 2014.

[49] Frenklach, Michael and Wang, Hai. "Detailed modeling of soot particle nucleation and growth". In: *Symposium (International) on Combustion*. Vol. 23. 1. Elsevier. 1991, pp. 1559–1566.

[50] Kumar, Sanjeev and Ramkrishna, D. "On the solution of population balance equations by discretization—I. A fixed pivot technique". In: *Chemical Engineering Science* 51.8 (1996), pp. 1311–1332.

[51] Frenklach, Michael. "On surface growth mechanism of soot particles". In: *Symposium (International) on Combustion* 26.2 (1996), pp. 2285–2293. DOI: https://doi.org/10.1016/S0082-0784(96)80056-7.

[52] Appel, Jörg, Bockhorn, Henning, and Frenklach, Michael. "Kinetic modeling of soot formation with detailed chemistry and physics: laminar premixed flames of C2 hydrocarbons". In: *Combustion and Flame* 121.1-2 (2000), pp. 122–136.

[53] Rodrigues, P., Franzelli, B., Vicquelin, R., Gicquel, O., and Darabiha, N. "Coupling an LES approach and a soot sectional model for the study of sooting turbulent non-premixed flames". In: *Combustion and Flame* 190 (2018), pp. 477–499.

[54] Kalbhor, Abhijit and Oijen, Jeroen van. "An assessment of the sectional soot model and FGM tabulated chemistry coupling in laminar flame simulations". In: *Combustion and Flame* 229 (2021), p. 111381. DOI: 10.1016/j.combustflame.2021.02.027.

[55] Mueller, Michael E and Pitsch, Heinz. "LES model for sooting turbulent nonpremixed flames". In: *Combustion and Flame* 159.6 (2012), pp. 2166–2180.

[56] Schechter, Robert S. *Transport Phenomena (Bird, R. Byron; Stewart, Warren E.; Lightfoot, Edwin N.)* 1961.

[57] Ma, Likun and Roekaerts, Dirk. "Numerical study of the multi-flame structure in spray combustion". In: *Proceedings of the Combustion Institute* 36 (2017), pp. 2603–2613. DOI: 10.1016/j.proci.2016.06.015.

[58] Ranz, W E and Marshall, W R. "Evaporation from drops: Part 1". In: *Chem. eng. prog* 48.3 (1952), pp. 141–146.

[59] Abramzon, B and Sirignano, W A. "Droplet vaporization model for spray combustion calculations". In: *International journal of heat and mass transfer* 32.9 (1989), pp. 1605–1618.

[60] Yuen, M. C. and Chen, L. W. "On drag of evaporating liquid droplets". In: *Combustion Science and Technology* 14.4-6 (1976), pp. 147–154. DOI: 10.1080/00102207608547524.

Chapter 4

Combustion modelling of a spray-flame

Current and near-future propulsion technologies mainly rely on liquid-fueled combustion systems [1]. Spray combustion plays a major role in the efficiency and pollutant control in those applications, but remains challenging for both experimental diagnostics and numerical simulations [2, 3]. The complexity arises from the strong interaction between spray, turbulence and combustion chemistry. In order to get further understanding on two-phase flow combustion, dedicated experimental facilities are developed to obtain reliable measurement data during burner operation [4]. These canonical flames allow detailed diagnostics and can be used with high-fidelity models to obtain deep understanding on the flame physics.

In this context, this chapter presents the application of the modelling framework for multiphase flows described in Chapter 3 in a n-heptane spray-flame. The reference spray-flame selected is the Coria Rouen Spray Burner (CRSB) [5], which has been studied in the Workshop on Turbulent Combustion Sprays (TCS) [4] in order to get further understanding on two-phase flow combustion. According to combined experimental and numerical diagnostics [6], this burner shows a double reaction front structure, with an inner wrinkled partially-premixed flame and an outer laminar diffusion flame. A hot region is located between those inner and outer reaction zones, where droplet vaporization is enhanced and most of the vapor fuel that feeds the flame is generated, as already found in other spray-flames analysis [7]. The flame sta-

bilization height is then controlled by the available fuel vapor defined by the polydisperse spray distribution [8].

One of the main issues when addressing this case is how to describe the multimode combustion phenomena characterizing different regions of the flame. In [6] a 2-step scheme in LES using flame resolved simulations and neglecting the subgrid scale wrinkling was employed, so the modelling strategy did not include assumptions of the combustion regime inherently. The overall agreement with the experiments was satisfactory, but the lift-off length was underpredicted. Improved lift-off predictions were obtained by Filtered Tabulated Chemistry (F-TACLES) [9] calculations, where a premixed flamelet manifold was built using a 106-species and 1738-reactions detailed mechanism. This method assumes the flame structure is premixed, and the diffusion burning influencing the flame anchoring and the outer flame layer are neglected. The flame lift-off length was correctly recovered, and the agreement with the experiments was satisfactory. In [10] the Conditional Moment Closure (CMC) method was used to describe the flame structure and double-conditioning was used to account for flame propagation in the limit of negligible scalar dissipation rate of mixture fraction. This approach was also able to reproduce the burning rates and the lift-off length. The analysis of the DCMC equation terms indicated that non-premixed burning modes are prominent at the flame base. It was also shown that the spray vaporization term mainly acts in fuel-rich regions, but evaporative cooling may affect the chemical reaction balance. In this regard, flame local extinctions were investigated in [11] by means of high-speed optical diagnostics applied to the CRSB. Different mechanisms of droplet-turbulence-flame interaction and local extinction phenomena were highlighted from those experimental results, but have not been assessed so far in computations of this burner. As indicated in [2], flame blow-off transient is characterized by an increase of the degree of local extinction, so accurate modelling of these events is critical for combustor stability simulations.

Tabulated chemistry approaches, such as Flamelet Generated Manifold (FGM) [12] or Flamelet/Progress Variable (FPV) [13] models, are appealing due the possibility to include complex chemistry effects at yet affordable computational cost as described by Chatelier et al. [9]. FGM-RANS simulations were applied to the CRSB in [14], where the main flame characteristics are shown to be properly reproduced. In the present work, a similar approach based on non-adiabatic unsteady flamelet tabulation [15] in a LES framework is applied to study the combustion process in the CRSB and analyze the capabilities of the model to reproduce droplet-flame and turbulence-flame interactions leading to local quenching and re-ignition. Flamelet approaches

successfully captured extinction and re-ignition in gaseous flames [16], but additional effects have to be accounted for in spray flames [15]. The interaction between the droplets and the flame is not fully understood, and introduces complexities in the modelling approach. Based on the model predictions, further insight is provided for the mechanism governing those phenomena.

The chapter is structured as follows: first, the characteristics of the spray-flame, the numerical setup and the modelling approach are described in Section 4.1. Subsequently, Section 4.2 presents the description of the flow field and assessment of the gaseous phase. Section 4.3 contains the results related to the dispersed phase in terms of droplet size, velocity and temperature. The flame characteristics and structure are described in Section 4.4, including the comparison of the OH mass fraction field and lift-off length with the experimental measurements. Finally, the analysis of local extinction in the CRSB is addressed in Section 4.5. The content of the present chapter is published in [17, 18].

4.1 Case description

This section presents the description of the experimental and numerical setups of the spray-flame studied in this chapter. The general characteristics of the experimental test rig and available measurements are detailed at first. Afterwards, some considerations of the modelling approach employed are given, as well as defining the different parameters used in this application. Finally, the description of the computational domain and numerical grid is presented.

4.1.1 Experimental test rig

As introduced in the previous section, the case studied in this work is the n-heptane spray-flame from the CORIA Rouen Spray Burner (CRSB) [5]. The CRSB is an open burner based on the geometry of the gaseous KIAI burner [19]. It is operated with an air mass flow rate of 6 g/s at atmospheric pressure and temperature of 298 K. Air is injected in a plenum and exits to the atmosphere through an annulus-shaped duct with an inner and outer diameter of 10 and 20 mm, respectively, with a Reynolds number $\sim$14000 based on annular jet outlet conditions. In contrast to the confined burner, the injection system is characterized by a non-swirling air co-flow. The liquid n-heptane injection comes from a hollow-cone pressurized injector (8 bar injection pressure) with a 80^{o} angle and a fuel mass flow rate of 0.28 g/s. Fig. 4.1 illustrates

a schematic of the experimental burner and the details of the injection system while Table 4.1 shows the operating conditions.

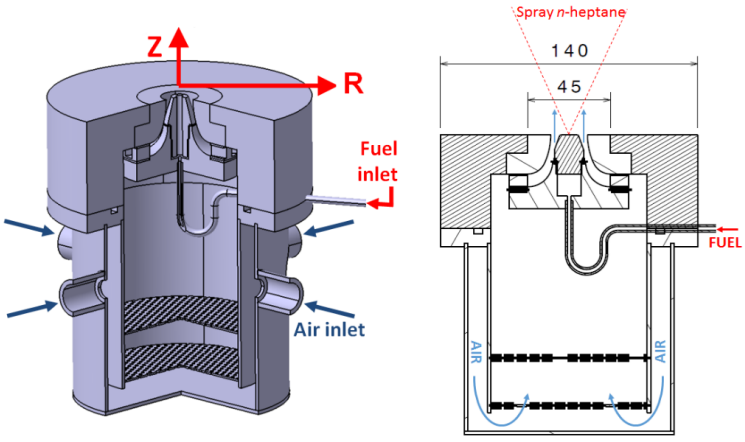

Figure 4.1: Experimental setup and schematic of the injection system in the CRSB, from [5].

	Air co-flow	Fuel (n-heptane)
Mass flow [g/s]	6	0.28
Temperature [K]	298	298

Table 4.1: Operating conditions of the CRSB.

This burner is a reference test case in the Workshop on Turbulent Combustion on Sprays (TCS) [4], with multiple experimental diagnostics available for spray and flame characterization. Droplet size and velocity are measured by Phase Doppler Anemometry (PDA), while gas-phase velocities are obtained by seeding the co-flow [6]. Flame structure is characterized by simultaneous high-speed OH Planar Laser Induced Fluorescence (PLIF) and Particle Image Velocimetry (PIV) measurements. Those techniques allowed the identification of the flame front disruptions due turbulence and droplet interaction [11].

4.1.2 Details of the modelling approach

The general modelling framework implemented in the computational code and employed in the present thesis was described in Chapter 3. In this section, the specific strategy and modelling parameters used in this case are presented. For

the analysis of combustion in this spray-flame, the FGM combustion model is used together with the LPT method for liquid fuel injection. Therefore, the following paragraphs are intended to clarify the thermochemical conditions, composition of the flamelet manifold and the parameters used for droplet injection. The characteristics omitted here are assumed to be the same as specified in Chapter 3.

Thermochemical conditions and combustion model

Regarding combustion modelling, the flamelet method outlined in Chapter 3 is used here. The CRSB is an atmospheric spray-flame where fuel and air are injected at the conditions specified in Table 4.1. Therefore, for flamelet calculations, $p = 1$ atm and $T_{air} = 298$ K. Due to the fact that fuel is injected in liquid phase, the boiling point of n-heptane at atmospheric pressure is taken as fuel temperature $T_{fuel} = 371.54$ K. The chemistry for n-heptane is given by the 188-species skeletal mechanism from Lu and Law [20], which has demonstrated a satisfactory performance in n-heptane flame numerical simulations [14].

As indicated in the previous section, the CRSB shows different burning characteristics featuring premixed and diffusion modes simultaneously in different regions of the flame. The inner layer is subjected to strong variations in mixture composition and high strain while the outer layer is laminar and dominated by diffusion. In such conditions, the use of 1D counterflow diffusion flamelets is proposed here to describe the global flame behaviour, as the flame front is controlled by the diffusion of reactants and this mechanism plays a key role in the stabilization of the flame, as pointed out by DCMC LES of this flame [10]. Chatellier et al. [9] proposed a premixed flamelet manifold for this burner, but the diffusion burning influencing the flame anchoring and the outer flame layer was neglected with this approach, as diffusion across mixture fraction lines could not be be described by the tabulation of premixed flamelets [21]. In the inner reaction zone, part of the reacting layer has premixed characteristics accompanied by a diffusion-dominated layer subjected to a highly strained flow field. According to the analysis performed by Liñan et al. [22], as the flow approaches extinction conditions the flame structure between diffusion and premixed flamelets become more similar. This similarity has been also used in [23], and supports the selection of strained diffusion flamelets in this region, which are able to describe both the influence of strain on the flame front and the extinction process.

The flamelet manifold is generated following the strategy described in Chapter 3: laminar counterflow diffusion 1D flames are tabulated at different strain rates until the extinction, where the manifold is continued by an unsteady extinguishing flamelet. A representation of the manifold is illustrated in Fig.4.2a, where the temperature profiles of the different flamelets are plotted at increased strain (from red to black). The effects of heat loss on the flamelet database are considered using the approach explained in the previous chapter. Strained diffusion flamelets are tabulated at different enthalpy levels and the local enthalpy deficit is generated through a radiative source term in the energy equation. In this way, the concept of scaled enthalpy (see Eq. 3.20) is applied as an additional control variable for the parametrization of the manifold.

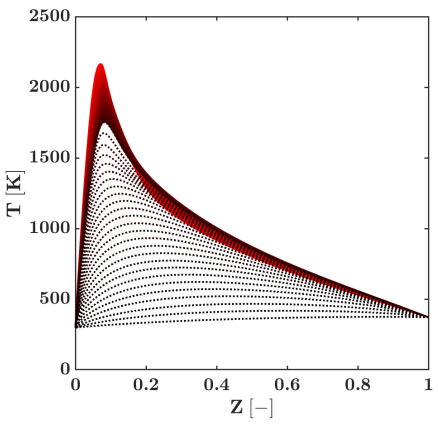

(a) Representation of the flamelet manifold. Solid lines: steady flamelets, dashed lines: extinguishing flamelets. Strain rate represented by colour from red to black as the strain rate increases.

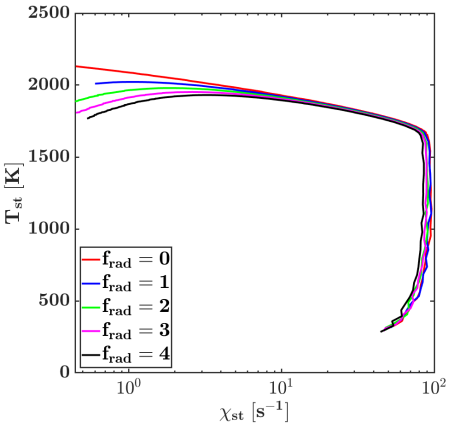

(b) S-curve of the n-heptane flame described by the stoichiometric temperature as function of the strain at different enthalpy levels (described by the scaling of the radiation term f_{rad}).

Figure 4.2: Flamelets used in the tabulation process.

The effect of the enthalpy on the thermochemical properties of the flame can be distinguished in Fig. 4.2b, where temperature at stoichiometric is plotted as function of the stoichiometric scalar dissipation rate at different enthalpy levels (represented by the scaling factor of the radiative source term f_{rad}). It shows a higher influence of the enthalpy level at low scalar dissipation rates. The effect of heat loss on the extinction and estimated time and length combustion scales is summarised in Table 4.2. The extinction point is

shifted to lower strains as the heat loss is augmented by the up-scaling of the radiative term, though the impact is minor for the operating conditions of the CRSB burner. Consequently, the increase in heat losses results in a slightly larger chemical time scale and diffusive flame thickness at extinction. The time scale of the extinction event is also provided as: $\tau_{ext} = 1/a_{ext}$, this metric agrees well with the time it takes for the unsteady flamelets to extinguish. It is approximately 0.7 ms for all considered heat-loss levels.

Scaling of radiation term	0	1	2	3	4
a_{ext} [1/s]	1496	1452	1416	1375	1335
χ_{ext} [1/s]	89.93	87.23	85.15	82.35	80.20
$T_{st,ext}$ [K]	1656	1657	1651	1651	1650
τ_{ext} [ms]	0.668	0.689	0.706	0.727	0.749
$\tau_c^{ext,\chi}$ [ms]	0.042	0.044	0.045	0.047	0.048
δ_{diff}^{ext} [mm]	0.172	0.175	0.177	0.179	0.182

Table 4.2: Extinction point with different degrees of heat loss (0 scaling is the adiabatic case), a_{ext}: strain rate at the extinction point, $T_{st,ext}$: temperature at stoichiometric composition at the extinction point, τ_{ext}: time scale of extinction.

The tabulation of flamelets at different enthalpy levels is used to account for the heat loss during droplet evaporation. As the evaporation rates are highly sensitive to small temperature variations of the surrounding gas, the addition of these thermal states into the flamelet manifold is important to ensure correct heat and mass transfer during the phase change. Furthermore, it has already been shown that dealing with enthalpy deficit in flames by radiative heat losses can be used as an alternative to other approaches [24]. Therefore, this is a reasonable option to account for heat transfer to the droplets, as the evaporation process also requires an exchange of enthalpy similarly to the heat loss in flames.

The presumed PDF integration is employed in order to account for turbulence/chemistry interaction. In this work, the distribution of mixture fraction is characterised by a β-function uniquely defined by the filtered value $\widetilde{Z}$ and subgrid variance Z_v of Z while δ-functions are applied to the scaled progress variable and enthalpy parameter. This modelling strategy assumes, that most unresolved effects are attributed to spatial mixture fraction fluctuations, and the subgrid enthalpy and progress variable variations are a consequence of the varying mixture fraction. In this case, the effect of the progress variable variance is not considered just for simplicity due to the liquid injection. Therefore,

the parametrization of the manifold is characterized by the use of four controlling variables: $\widetilde{Z}$, Z_v, $\widetilde{Y_c}$, $\widetilde{h}$. The system of governing equations relevant to this case read as follows:

$$\frac{\partial \overline{\rho}}{\partial t} + \boldsymbol{\nabla} \cdot (\overline{\rho}\tilde{\boldsymbol{u}}) = \overline{S}_C, \tag{4.1}$$

$$\frac{\partial \overline{\rho}\tilde{\boldsymbol{u}}}{\partial t} + \boldsymbol{\nabla} \cdot (\overline{\rho}\tilde{\boldsymbol{u}}\tilde{\boldsymbol{u}}) = -\boldsymbol{\nabla} \cdot \overline{\tau}_M - \boldsymbol{\nabla}\overline{p} + \boldsymbol{\nabla} \cdot (\bar{\mu}\boldsymbol{\nabla}\tilde{\boldsymbol{u}}) + \overline{S}_M, \tag{4.2}$$

$$\frac{\partial \overline{\rho}\tilde{h}}{\partial t} + \boldsymbol{\nabla} \cdot \left(\overline{\rho}\tilde{\boldsymbol{u}}\tilde{h}\right) = -\boldsymbol{\nabla} \cdot \overline{\tau}_h + \boldsymbol{\nabla} \cdot \left(\bar{\rho}\bar{D}\boldsymbol{\nabla}\tilde{h}\right) + \overline{S}_H, \tag{4.3}$$

$$\frac{\partial \overline{\rho}\tilde{Z}}{\partial t} + \boldsymbol{\nabla} \cdot \left(\overline{\rho}\tilde{\boldsymbol{u}}\tilde{Z}\right) = -\boldsymbol{\nabla} \cdot \overline{\tau}_Z + \boldsymbol{\nabla} \cdot \left(\bar{\rho}\bar{D}\boldsymbol{\nabla}\tilde{Z}\right), \tag{4.4}$$

$$\frac{\partial \overline{\rho}\tilde{Y}_c}{\partial t} + \boldsymbol{\nabla} \cdot \left(\overline{\rho}\tilde{\boldsymbol{u}}\tilde{Y}_c\right) = -\boldsymbol{\nabla} \cdot \overline{\tau}_{Y_c} + \boldsymbol{\nabla} \cdot \left(\bar{\rho}\bar{D}\boldsymbol{\nabla}\tilde{Y}_c\right) + \overline{\dot{\omega}}_{Y_c}, \tag{4.5}$$

$$\frac{\partial \overline{\rho}Z_v}{\partial t} + \boldsymbol{\nabla} \cdot (\overline{\rho}\tilde{\boldsymbol{u}}Z_v) = -\boldsymbol{\nabla} \cdot \overline{\tau}_{Z_v} + \boldsymbol{\nabla} \cdot \left(\bar{\rho}\bar{D}\boldsymbol{\nabla}Z_v\right) - 2\overline{\tau}_Z \cdot \boldsymbol{\nabla}\tilde{Z} - 2\overline{s}_{\chi_Z}. \tag{4.6}$$

The modelling assumptions and parameters considered here were already described in Chapter 3 and are not repeated here. Note that the set of equations corresponds to the previously described transport equations, accounting for the coupling between gas and dispersed phases.

The thermochemical table contains then 101x11x101x11 entries corresponding those four controlling variables (for clarity, $(n_{\widetilde{Z}}, n_{Z_v}, n_{\widetilde{C}}, n_{\widetilde{\mathcal{H}}}) = (101, 11, 101, 11)$, where n_ϕ is the number of points used for the discretization of control variable ϕ). For the progress variable discretization, a uniform spacing is used across the flame front, while the mixture fraction space is discretized with a non-uniform distribution centered at the stoichiometric mixture fraction with a growing rate of 1.1 towards the lean and rich sides. The variance of the mixture fraction is discretized with a power function with exponential $p = 3$. The enthalpy level is tabulated for 11 equidistant steps. Note, that the number of these levels is larger than the number of different radiation scalings applied, we chose this approach because the radiation scaling does not guarantee an equidistant spacing in enthalpy, thus more levels are applied in the table to represent the flamelets in sufficient detail.

In this case, the expression introduced in Eq. 3.18 is used for the progress variable definition, using four species with $Y_k = \{Y_{CO_2}, Y_{CO}, Y_{H_2}, Y_{H_2O}\}$. The coefficients proposed by Ma [25] accounting for the contribution of each species to the progress variable Y_c are considered here: $a_k = \{4.0, 1.0, 0.5, 2.0\}$.

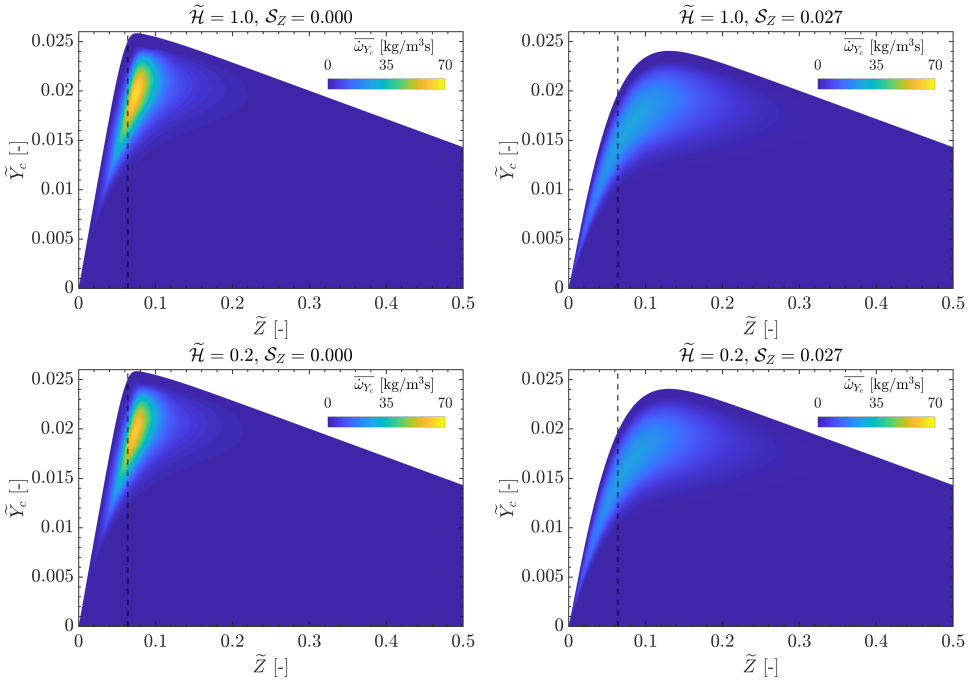

Figure 4.3: Illustration of the non-adiabatic manifold used for the CRSB simulations. Effect of scaled enthalpy $\widetilde{\mathcal{H}}$ and mixture fraction segregation factor $\mathcal{S}_Z$ on the $\widetilde{Z} - \widetilde{Y}_c$ map of the filtered progress variable source term $\overline{\dot{\omega}_{Y_c}}$. Dashed line: stoichiometric mixture fraction.

In order to illustrate the flamelet manifold and the effects of the controlling variables on it, Fig. 4.3 presents the $\widetilde{Z} - \widetilde{Y_c}$ map of the filtered progress variable source term $\overline{\dot{\omega}_{Y_c}}$ for different enthalpy levels $\widetilde{\mathcal{H}}$ and values of mixture fraction variance, which is represented here by the segregation factor: $\mathcal{S}_Z = \frac{Z_v}{\widetilde{Z}(1-\widetilde{Z})}$. The maximum scaling of the radiative factor used is relatively low, thus, the effect on the filtered progress variable source term is not too strong and only a slight decrease of $\overline{\dot{\omega}_{Y_c}}$ peak value is observed when increase heat losses. The progress variable and its source term are, on the contrary, strongly affected by the mixture fraction variance. Not only the magnitude of $\overline{\dot{\omega}_{Y_c}}$ is considerably decreased for low $\widetilde{\mathcal{H}}$ values, but also the Y_c peak is displaced to higher mixture fraction values and $\overline{\dot{\omega}_{Y_c}}$ is distributed in a wider range of $\widetilde{Z}$.

Spray modelling

The differential equations that solve the droplet dynamics, mass and temperature were presented in Chapter 3 (see Eqs. 3.61, 3.62, 3.65 and 3.66) with

the description of the Lagrangian approach used in this work. Therefore, this subsection aims to specify the strategy employed for the droplet injection and the different parameters considered.

The liquid fuel injection is modeled in a hollow cone shape in order to reproduce the conditions of the pressurized injector and droplets are injected in an annulus located 2 mm downstream the nozzle, where it is assumed that the atomization process is completed [26]. The initial droplet temperature is assumed constant following the operating conditions presented in Table 4.1. Droplet position, velocity, diameter and mass are determined stochastically. The droplet initial location inside the annulus is defined by the azimuthal angle φ and the radius r, which are computed using the following expressions:

$$\varphi = 2\pi\mathcal{U}_1, \tag{4.7}$$

$$r = \sqrt{r_{min}^2 + \mathcal{U}_2(r_{max}^2 - r_{min}^2)}. \tag{4.8}$$

In the equations above, r_{min} and r_{max} are the minimum and maximum radius of the annulus and $\mathcal{U}_1$ and $\mathcal{U}_2$ are pseudo-random numbers in the $[0, 1)$ interval. The angle determining the velocity direction θ depends on the radial coordinate along the annulus and is defined by:

$$\tan\theta = \frac{r}{r_{max}} \tan\theta_{max}. \tag{4.9}$$

Therefore, the velocity direction is parametrized by only θ_{max} and the minimum angle is determined by $\theta_{min} = \arctan\left(\frac{r_{min}}{r_{max}} \tan\theta_{max}\right)$. The tangential component of the initial droplet velocity is considered as zero and the complete velocity vector is computed by an imposed injection velocity magnitude v_{inj}.

Finally, the droplet size is characterized by a modified Rosin-Rammler distribution [15]. The expression for the initial droplet diameter read as:

$$d = d_{min} + (d_{RR} - d_{min})(-\ln(1 - \mathcal{U}_3 K_{RR}))^{1/q}, \tag{4.10}$$

where d_{min} is the minimum droplet diameter, d_{RR} is a parameter related to the mean droplet diameter of the distribution, q is the parameter which controls the distribution width and $\mathcal{U}_3$ is a pseudo-random number. The distribution is

clipped at larger diameters of d_{max} using the factor K_{RR}, which corresponds to the cumulative density function of the original distribution:

$$K_{RR} = 1 - \exp\left(-\left(\frac{d_{max} - d_{min}}{d_{RR} - d_{min}}\right)^{q}\right). \tag{4.11}$$

Considering this modified Rosin-Rammler distribution, the probability density function (PDF) of the initial droplet diameter read as follows:

$$PDF_d = \frac{q}{K_{RR}(d_{RR} - d_{min})}\left(\frac{d_{max} - d_{min}}{d_{RR} - d_{min}}\right)^{q-1} \exp\left(-\left(\frac{d_{max} - d_{min}}{d_{RR} - d_{min}}\right)^{q}\right). \tag{4.12}$$

The PDF of droplet diameter using in this work is illustrated in Fig. 4.4. It corresponds to a distribution with $d_{min} = 1$ μm, $d_{max} = 70$ μm, $d_{RR} = 26.46$ μm and $q = 2.3$. The red line is the analytical function described by Eq. 4.12 while blue bars represent the stochastic distribution of droplet sizes at the injection plane. As observed, the statistical procedure for droplet sizes fits well the analytical distribution in this case. In addition, dashed lines represent the commonly used mean diameters for the characterization of the droplet size distribution: the arithmetic mean D_{10} and the Sauter Mean Diameter (SMD) D_{32}. They are defined by:

$$D_{10} = \frac{\sum_{i=1}^{n} d_i}{n}, \tag{4.13}$$

$$D_{32} = \frac{\sum_{i=1}^{n} d_i^3}{\sum_{i=1}^{n} d_i^2}. \tag{4.14}$$

The mean diameters are computed from the stochastic data obtaining: $D_{10} = 23.54$ μm and $D_{32} = 32$ μm.

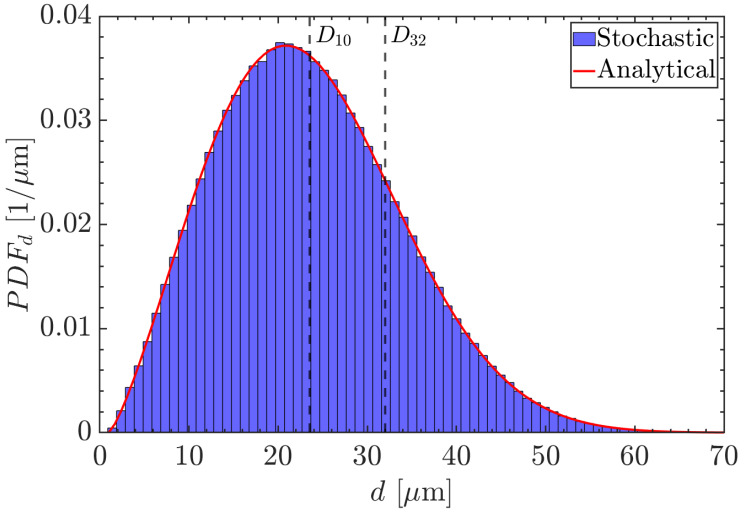

Figure 4.4: PDF of the Rosin-Rammler distribution used in the CRSB. Red line: analytical function, blue bars: stochastic distribution. Parameters: $d_{min} = 1$ μm, $d_{max} = 70$ μm, $d_{RR} = 26,46$ μm and $q = 2.3$. Mean diameters: $D_{10} = 23.54$ μm and $D_{32} = 32$ μm.

Droplets are injected following the outlined stochastic procedure in order to define their position, velocity and size. The number of droplets injected at each time step is determined by the mean flow rate specified by the operating conditions (see Table 4.1), $\dot{m}_f = 0.28$ g/s. In this work, the concept of parcels is used and each computational element of the Lagrangian approach represent a certain number of droplets of similar size and properties. The number of droplet per parcel $n_{d/p}$ is selected to satisfy a certain number of parcels injected per second: $\dot{N}_p$. The value is estimated assuming spherical droplets and taking into account the total mass flow rate:

$$n_{d/p} = \frac{\dot{m}_f / \dot{N}_p}{\frac{\pi d_{mean}^3}{6} \rho_L}, \tag{4.15}$$

where d_{mean} is a mean droplet diameter and ρ_L is the density of n-heptane. The number of parcels per second is chosen as $\dot{N}_p = 2.2{\cdot}10^6$ parcels/s to ensure a good agreement with the experimental data with a reasonable computational time, according to [27]. Taking into account all the parameters specified above, $n_{d/p} = 19$ droplet/parcel is considered for this case.

As a summary, Table 4.3 contains all the parameters used for droplet injection in the CRSB. Regarding the injection velocity, a dependency on the droplet size is used in order to determine the magnitude of the injection velocity vector v_{inj}, following: $v_{inj} = 33$ m/s for droplets with $d < 10$ μm decreasing linearly with diameter to $v_{inj} = 25$ m/s for droplets with $d > 55$ μm, according to [14]. In general, all the parameters for the droplet injection and size distribution are chosen to ensure the numerical feasibility and to reproduce the experimental data at the closest axial positions.

Injection location parameters	
r_{min}	1.4885 mm
r_{max}	2.5335 mm
Injection velocity	
θ_{min}	35°
θ_{max}	50°
$v_{inj} = f(d)$	$[25, 33]$ m/s
Droplet size distribution parameters	
d_{min}	1 μm
d_{max}	70 μm
d_{RR}	26.46 μm
q	2.3
D_{10}	23.54 μm
D_{32}	32 μm

Table 4.3: Summary of the injection parameters used in the CRSB.

4.1.3 Numerical setup

The computational domain used for the CRSB calculations is based on the experimental test rig described in previous subsections. An schematic of the numerical domain is presented in Fig. 4.5 (left). The domain includes a cylindrical volume of 200 mm in radius and 500 mm in height to account for the environment of the flame. A constant air mass flow rate at 298K is prescribed as inlet condition and non-slip adiabatic walls are used as boundary conditions.

The mesh used for this geometry results in a total of 20M elements using a hybrid mesh with tetrahedrons, prisms and pyramids. It is refined to a

minimum filter size of $\Delta x = 0.2$ mm inside the air duct, in the injection region and in the near field of the flame, as shown in Fig. 4.5 (right). Layers of prisms are applied in the air duct in order to better resolve the boundary layer.

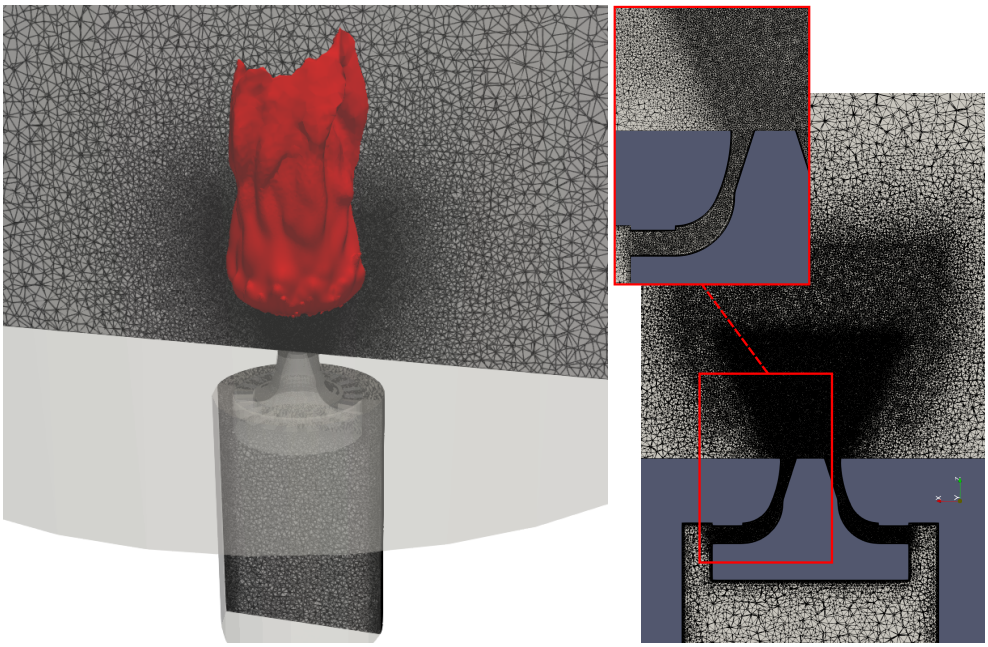

Figure 4.5: Left: computational domain and overview of the mesh (stoichiometric mixture fraction iso-surface of the flame represented in red colour). Right: detailed view of the mesh in the injection region.

In view of the estimated diffusive length scale presented in Table 4.2, the filter size is comparable to the diffusive thickness in the near region of the flame ($\Delta x \sim 1.16\delta^{ext}_{diff}$). Even in the outer flame zone, where the filter size becomes coarser ($\Delta x \sim 0.34$ mm), length scales of $\sim 2\delta^{ext}_{diff}$ are resolved. Note that the definition employed considers the thermal diffusivity of the oxidizer (see Eq. 2.41 in Chapter 2) thus the resulting length scale is the most restrictive one (the lowest) in terms of flame front resolution. In the present modelling approach, it is not strictly necessary to resolve the reacting front, however, it is interesting to have a notion of the $\Delta x/\delta^{ext}_{diff}$ ratio. Furthermore, the estimation of Kolmogorov scales η at different locations of the burner evidences a minimum value of $\eta \sim 0.023$ mm close to the exit of the injection nozzle. This corresponds to $\Delta x/\eta \sim 8.7$, which suggest a really good resolution in terms of the ratio between the filter size and Kolmogorov scale. The grid

quality is also evaluated by using Pope's criterion [28]. In this regard, resolved and sub-grid parts of the turbulent kinetic energy are computed, following the approximation of Yoshizawa [29] for the estimation of the sub-grid component. The expression of the total turbulent kinetic energy read as:

$$k = k_{res} + k_{sgs} \approx \frac{1}{2}\mathbf{u}_{rms}^2 + 2C_l\Delta x^2 \mathbf{S}(\tilde{\mathbf{u}}) : \mathbf{S}(\tilde{\mathbf{u}}), \tag{4.16}$$

where $\mathbf{u}_{rms}$ is the Root Mean Square of velocity field, $\mathbf{S}(\tilde{\mathbf{u}})$ is the strain rate tensor and C_l is a modelling constant taken as $C_l = 0.0886$ [29]. According to Pope's criterion, at least 80% of the turbulent kinetic energy should be resolved for an adequate LES calculation, i.e., $k_{res} \geqslant 0.8k$. Fig. 4.6 shows the contour of k_{res}/k in a vertical cut plane of the CRSB. As observed, k_{res}/k is very close to 1 in the central location of the main jet, in the flame position and even in the region close to the air inlet. Therefore, almost all the turbulent kinetic energy is solved in the region of interest and only a few regions present a k ratio below 0.8, such as the vicinity of the burner walls or the plenum, where no turbulent fluctuations are expected.

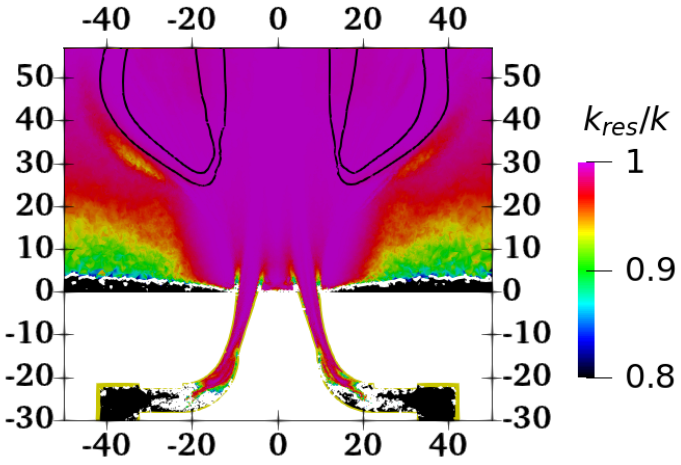

Figure 4.6: Ratio between resolved turbulent kinetic energy k_{res} and total turbulent kinetic energy k in a vertical cut plane of the CRSB. White line: $k_{res}/k = 0.8$. Black line: iso-line of OH mass fraction to illustrate the flame position. Spatial units in mm.

In addition, further refinement to 79M element mesh was performed in order to check grid convergence, however, it did not exhibit different dynamics

or affected significantly the results, so the 20M element mesh was retained for the analysis. (For any interested reader, the comparison between both meshes in terms of velocity field is included in Appendix A).

In this work, time-averages for both gas phase and droplets statistics are collected over about 100 ms, which correspond to approximately 30 flow-through times. The flow-through is estimated by the averaged axial velocity integrated over a volume enclosing the flame and its surrounding.

4.2 Flow field description

This section includes a description of the flow field characteristics and the gas-phase results of the CRSB using the modelling approach previously presented. In this section (and also in the following), the numerical results are compared with the experimental data at radial stations located at different axial positions. Fig. 4.7 shows a schematic of the stations considered for the comparison with experiments.

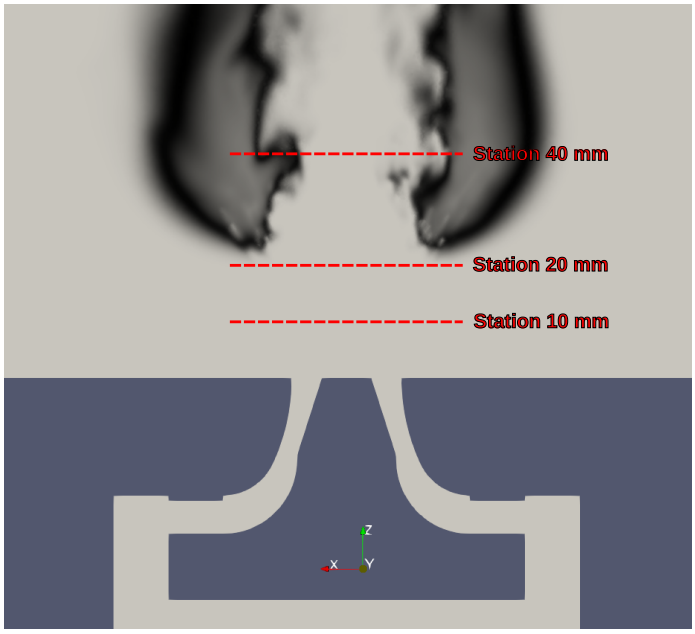

Figure 4.7: Sketch of the radial stations where LES results are compared with the experimental data. Stations are represented on a vertical central plane colored by temperature in order to visualize the position of the flame.

In order to understand the behaviour of the flow field in the CRSB, the instantaneous and mean velocity magnitude in the vertical plane of the burner is shown in Fig. 4.8. The burner exhibits a flow pattern similar to that of an annular jet [30]. The air coming from the plenum enters the nozzle and accelerates, reaching the atmosphere with a velocity of 25 m/s, approximately. It is possible to appreciate a small recirculation zone near the position of the injector. In addition, the local increase of the velocity due to the droplet injection is visible, specially in the instantaneous contours of the left picture. Downstream, mixing decelerates the gas jet and it widens at an axial position of 25 mm due to the presence of the flame, as it is shown in the contour plot of mean axial velocity (right side of Fig. 4.8).

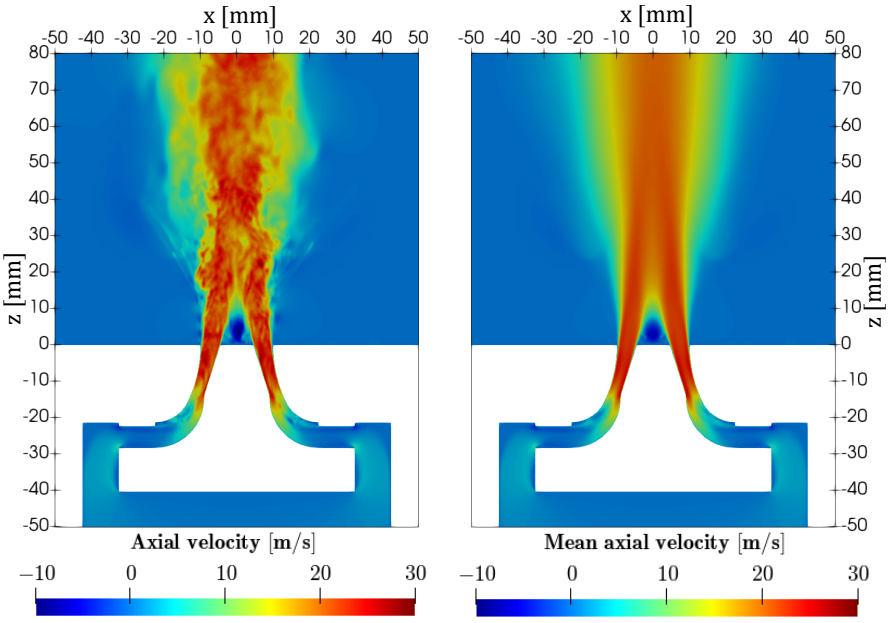

Figure 4.8: Fields of axial velocity on a vertical central plane. Left: instantaneous values, right: time-averaged values.

Fig. 4.9 shows the results obtained for the axial gas velocity. Mean and root mean square (RMS) values are compared with the experimental measurements at three different radial stations. In view of the results, only a slight underprediction of the axial velocity fluctuation is obtained, but the overall agreement is quite good. LES is able to accurately capture the axial velocity mean and fluctuating profiles and to reproduce the widening of the air jet.

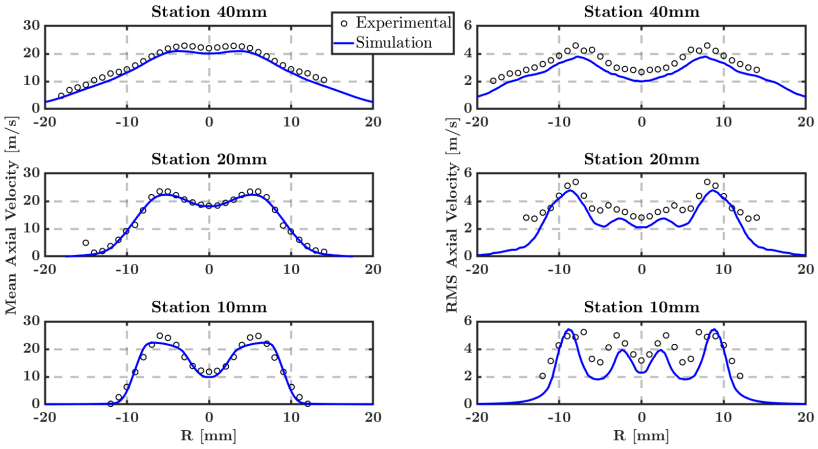

Figure 4.9: Comparison of axial velocity profiles at different radial stations for the gas phase. Left: mean values, right: RMS values. Blue lines: LES results, circles: experiments.

The radial velocity component is shown in Fig. 4.10. In the same way as the previous plots, mean radial velocity and RMS are well predicted by the simulation. The only remarkable difference is observed at the 40 mm station, where the peak value of mean radial velocity is underestimated. However, the agreement between the simulation and the PDA measurements is satisfactory and ensure the correct aerodynamic stabilization of the flame.

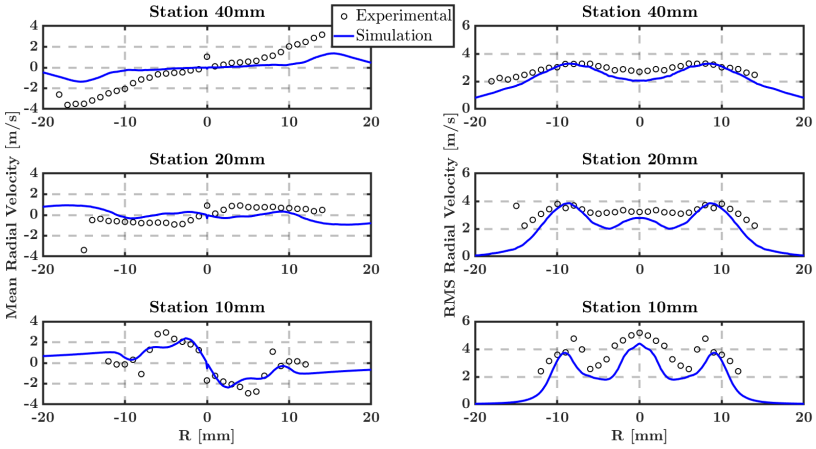

Figure 4.10: Comparison of radial velocity profiles at different radial stations for the gas phase. Left: mean values, right: RMS values. Blue lines: LES results, circles: experiments.

4.3 Spray assessment

The results related to the dispersed phase are shown in this section. Fig. 4.11 shows an illustration of the spray in which droplets are colored by diameter (left) and axial velocity (right). As already described in previous works [6], this burner features the largest and inertial droplets at higher radial positions, as shown in Fig. 4.11 left. The largest droplet diameters are found matching the hollow-cone shape of the spray, while the smallest ones (with lower Stokes number) are located near the centerline. In terms of droplet velocity, it can be seen that these low inertial droplets, which follow the air stream coming from the annular nozzle, present a velocity closer to the gas phase at the axis. So that, in the right picture of Fig. 4.11, droplet axial velocity reaches values higher than 20 m/s in the central region, which is comparable with the values already seen in Fig. 4.9.

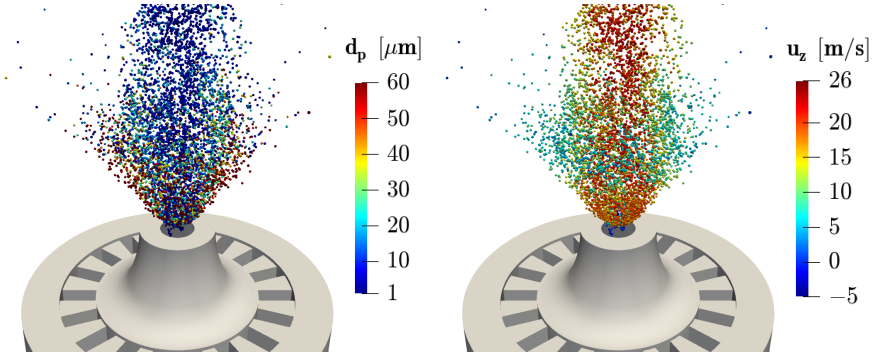

Figure 4.11: 3D view of the simulated hollow-cone spray. Left: spray colored by droplet diameter, right: spray colored by droplet axial velocity.

The droplet distribution according to their size can be seen in Fig. 4.12, where mean diameter is represented at different radial stations. In general, there is a good agreement between the simulation results and experiments.

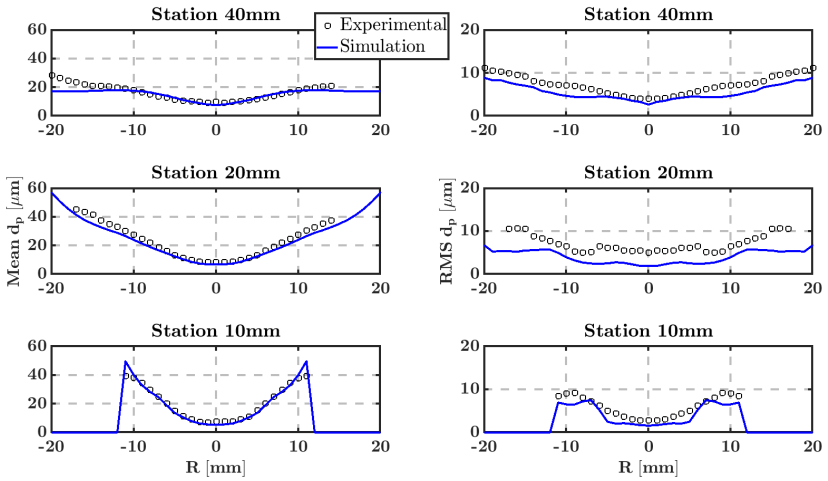

Figure 4.12: Comparison of droplet diameter profiles at different radial stations. Left: mean value, right: RMS value. Blue lines: LES results, circles: experiments.

Fig. 4.13 shows the comparison of axial droplet velocity (mean and RMS) with the measurements. In this case, all droplets are considered to obtain reliable statistics of the liquid phase. Overall, there is good agreement with the experimental data and the droplets statistics are well predicted. Due to the fact that the parameters of the spray model are adjusted to reproduce

the experimental measurements at the nearest region, the simulation results at the station of 10 mm are well captured.

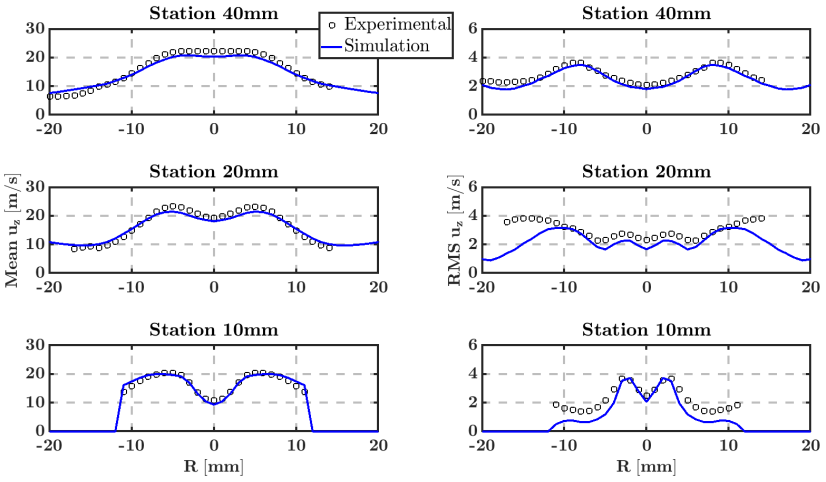

Figure 4.13: Comparison of droplet axial velocity profiles at different radial stations. Left: mean value, right: RMS value. Blue lines: LES results, circles: experiments.

The comparison of radial droplet velocity is shown in Fig. 4.14. The numerical results perfectly fit the experimental measurements for the time-averaged magnitude and the agreement is also good in terms of radial velocity fluctuation. In view of the comparison for the droplet velocity field presented in Fig. 4.13 and 4.14, it can be concluded the calibration of the fuel injection system is suitable for this case.

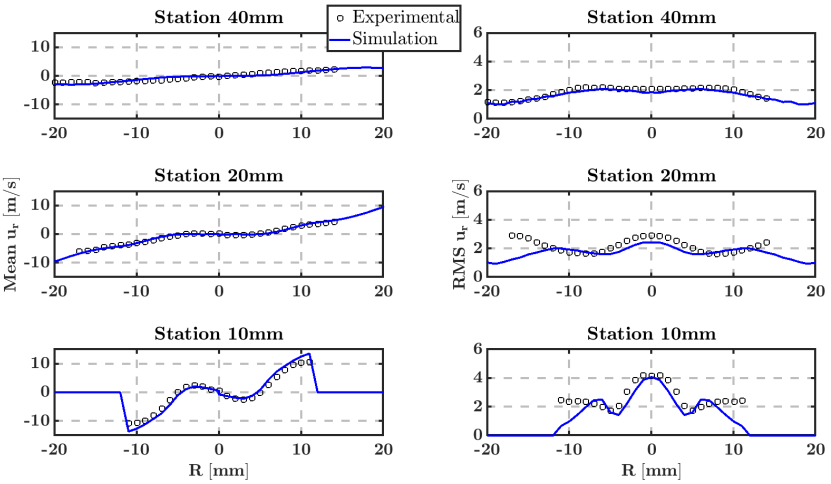

Figure 4.14: Comparison of droplet radial velocity profiles at different radial stations. Left: mean value, right: RMS value. Blue lines: LES results, circles: experiments.

In the previous plots, all droplets were considered for the statistics of axial and radial droplet velocities. In order to understand the kinematic behaviour of the different type of droplets and evaluate the numerical predictions, Fig. 4.15 and 4.16 illustrate the mean and RMS droplet axial velocity conditioned to the droplet size. First, Fig. 4.15 shows the statistics of droplet axial velocity accounting for droplets with diameter between 10 and 20 μm. The behaviour of the small droplets previously described is also observed and quantified here. The small and low inertial droplets are mainly present in the central region of the burner and evidence an axial velocity very similar to that of the main jet. In addition, the agreement between the predicted axial velocity and the experimental measurements is reasonably good. The main discrepancies are found at 10 mm and near the burner axis, where droplets are not detected in simulations and, thus, the velocity is zero.

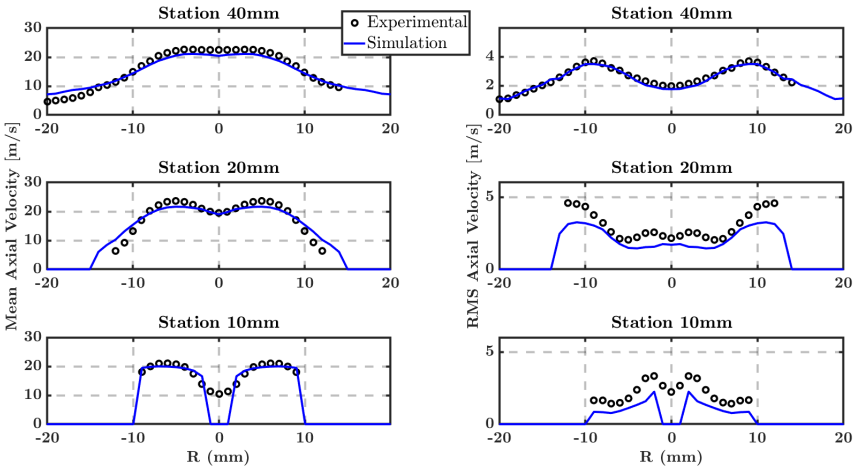

Figure 4.15: Comparison of droplet axial velocity profiles at different radial stations (droplet diameter between 10 and 20 μm). Left: mean value, right: RMS value. Blue lines: LES results, circles: experiments.

Regarding the large droplets, Fig. 4.16 presents the same comparison for droplets between 40 and 50 μm of diameter. In this case, the droplets follow the main spray path (a half injection angle of $\sim$40°) and their axial velocity is significantly reduced downstream. The simulation predicts a slightly higher widening of the droplet trajectory, specially at stations 20 and 40 mm, but the overall agreement in terms of the mean and fluctuating axial velocity of large droplets is also satisfactory.

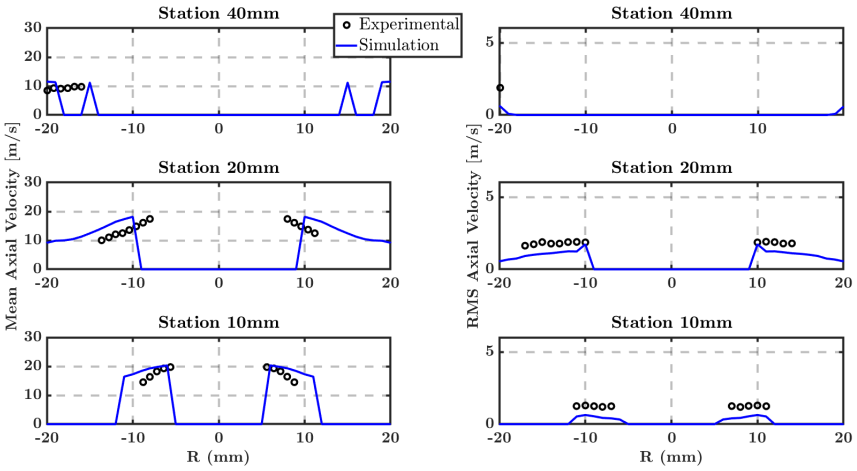

Figure 4.16: Comparison of droplet axial velocity profiles at different radial stations (droplet diameter between 40 and 50 μm). Left: mean value, right: RMS value. Blue lines: LES results, circles: experiments.

Finally, droplet temperature profiles are presented in Fig. 4.17. On the left side, temperature profiles of constant radial coordinate ($R = const$) along the axial distance are presented. On the right side, the usual representation in radial stations ($Z = const$) is shown (note that in this case the stations are different compared to the velocity field, due to the availability of the measured temperature). In view of the results at constant radial positions (left), a good prediction of the droplet temperature is achieved at the burner axis and the cold jet region ($R = 0$ and $R = 5$ mm). The interaction with the flame is initiated at $R = 10$ and is evident at $R = 15$ mm. At this position, an overestimation of the droplet temperature is obtained and LES predicts a faster heating of the droplets at contact with the hot gases of the flame. This behaviour is also evidenced at radial stations (right). The radial profiles and heating-up due to the flame are properly captured by simulations, however, an overprediction of up to ∼25 K is obtained in the flame region. Despite the these discrepancies, the agreement in terms of droplet temperature is considered satisfactory.

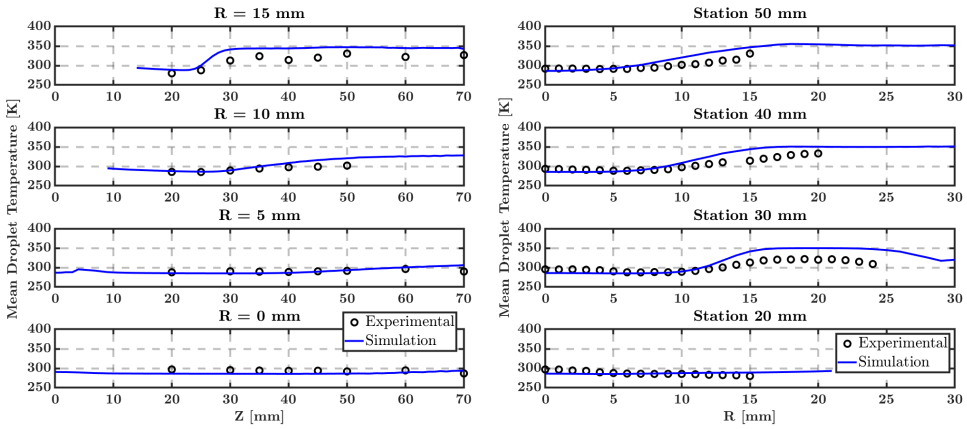

Figure 4.17: Comparison of droplet temperature profiles (all droplets). Left: mean value at constant radial positions, right: mean value at constant axial positions (stations). Blue lines: LES results, circles: experiments.

4.4 Flame structure

In this section, results about the shape of the flame and its thermochemical structure are discussed. Figure 4.18 shows an instantaneous OH mass fraction contour, in which three regions can be clearly seen. Previous experimental studies have already identified the different areas of the flame [5, 11] and the same nomenclature will be followed in this work. The region of the flame closest to the injector, denoted as leading edge (LE) connects the two main reaction zones, namely the inner and outer reaction zones (IRZ and ORZ respectively). The ORZ exhibits a thick non-fluctuating OH layer and the IRZ presents a thinner and strongly wrinkled flame front, due to the turbulent air jet located close to the central axis of the burner. Regarding the combustion regime, the ORZ seems to be a quasi-steady diffusion flame, while the IRZ features a partially premixed flame propagation, as discussed by Shum-Kivan et al. [6].

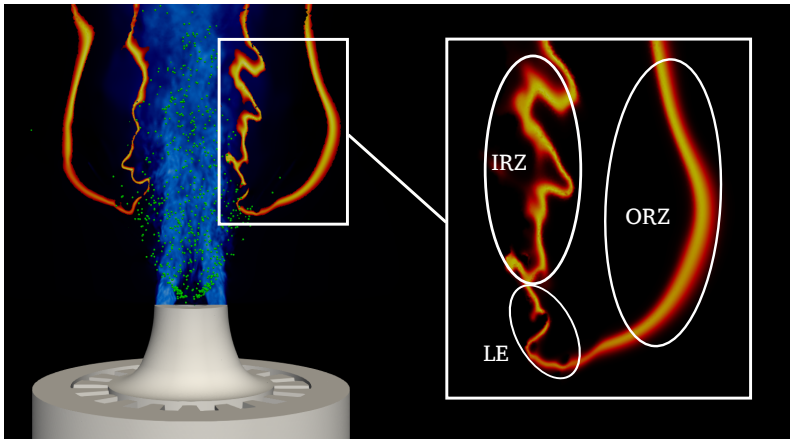

Figure 4.18: Different regions of the flame (LE, IRZ, ORZ) on a global view of the reaction front and flow field (red contours: OH concentration, blue contours: velocity magnitude, green: spray.

On the other hand, dynamics of the droplets and their interaction with the flame were also described in experimental and numerical works [6, 9, 10] and are revised here in light of the ability of unsteady flamelet approach to capture this interaction. Figure 4.18 shows droplets reaching the flame front at the LE, which correspond with the largest diameters due to the fact that they tend to follow the main spray direction, as previously discussed. Although there are many small droplets that follow the central air jet and evaporate in the region between the axis and the IRZ, most of the gaseous fuel comes from the evaporation of the large droplets crossing the reaction front and reaching the inside of the flame, due to the high temperature. Therefore, the maximum mixture fraction values are reached in the region between both IRZ and ORZ and closest to the LE, as shown in the first field of Fig. 4.19. Flow entrainment results in a reduction of the mixture fraction values further downstream. Furthermore, according to [11, 31], inside the flame and close to the ORZ the fuel thermal decomposition and incomplete combustion lead to the appearance of species such as CO, CO_2, H_2O and soot precursors (PAH). This phenomenon is well captured by the simulation, as it is observed in the mean fields of CO, CO_2 and C_2H_2 (which contributes to the formation of soot precursors [32]), presented in Fig. 4.19.

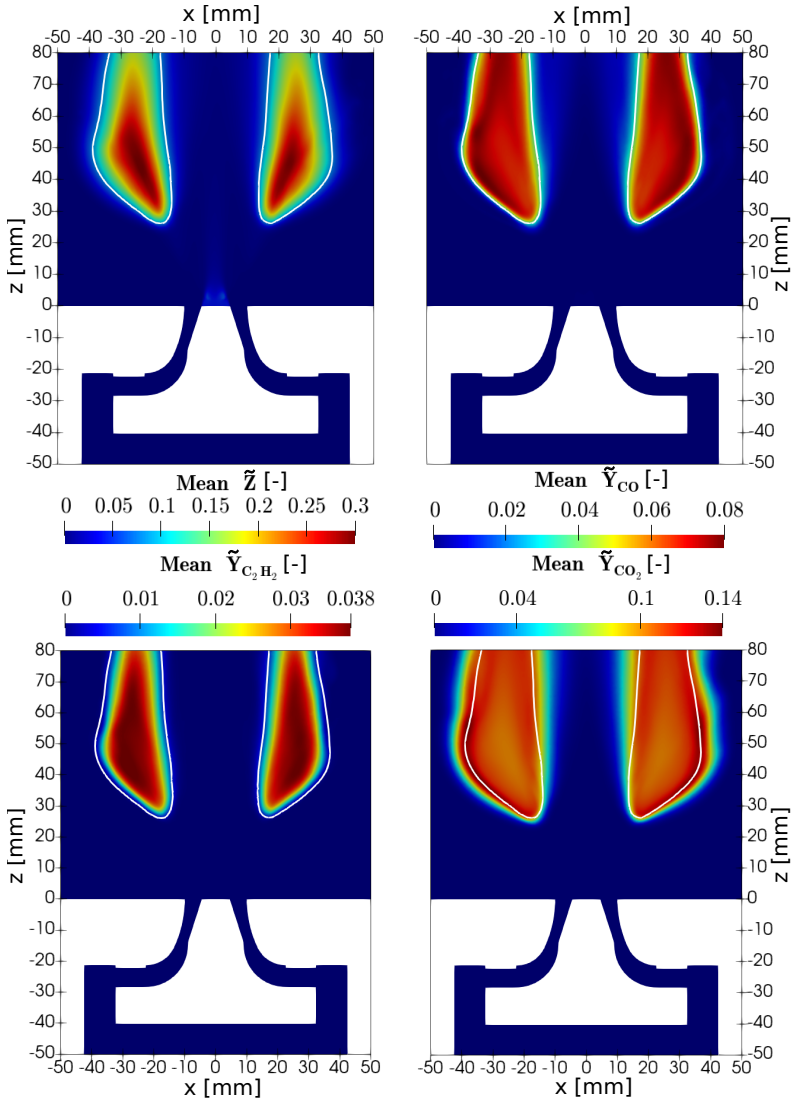

Figure 4.19: Mean contours of mixture fraction (top left), CO mass fraction (top right), C_2H_2 mass fraction (bottom left) and CO_2 mass fraction (bottom right). White line: mean stoichiometric mixture fraction iso-line.

A cut of the instantaneous stoichiometric mixture fraction iso-surface is observed in Fig. 4.20, together with the fuel spray colored by droplet diameter. This representation evidence the differences between the regions of the flame described previously. In contrast with the uniform and homogeneous appearance of the ORZ, the IRZ presents small areas, near the leading edge

of the flame, where the temperature and OH mass fraction decrease locally, while heat release and CH_2O mass fraction reach higher values. This particular behavior in the IRZ is related to the local extinction and re-ignition phenomena due not only to the droplets crossing the reaction front, but also to the interaction between the flame and the turbulent flow [11]. These aspects will be addressed in the next section.

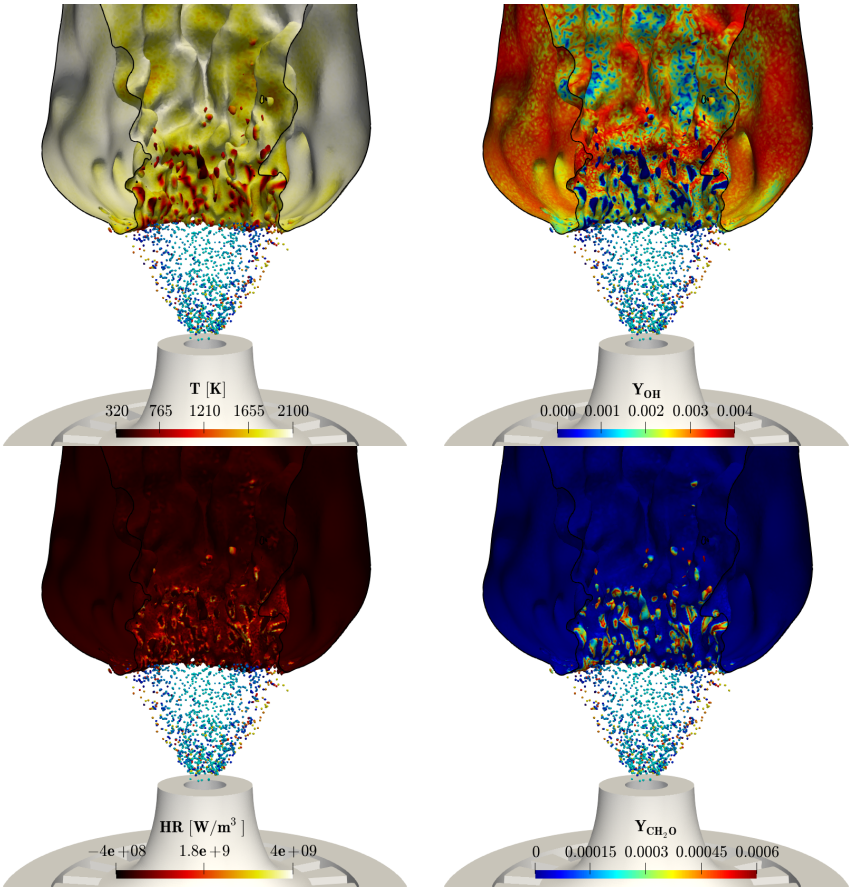

Figure 4.20: Vertical cut of the stoichiometric mixture fraction iso-surface colored by temperature (top left), OH mass fraction (top right), heat release (bottom left) and CH_2O mass fraction (bottom right). Spray droplets colored by diameter.

In order to perform a qualitative comparison of the flame topology, Fig. 4.21 shows mean and instantaneous OH contours from simulation and experimental measurement [11]. The overall shape of the flame can be observed to be well captured by the calculation. The positions of the IRZ and

ORZ at $r \approx 13$ mm and $r \approx 35$ mm, respectively, are correctly predicted. Nevertheless, the shape of the outer flame is slightly different, with a wider radial distance between the IRZ and the ORZ for the calculations. It is important to note that discrepancies in the shape of the ORZ are consistent with those obtained in the radial velocity results for the gas phase at larger distances from the orifice (see Fig. 4.10). However, it is difficult to determine the reason for these differences, since experimental measurements are missing at this radial position and there is a large set of coupled factors affecting the ORZ.

The lift-off length is defined as the maximum value of progress variable gradient in the axial direction following a similar procedure to the experiments [33]. The time-averaged value of simulated lift-off length is approximately 25 mm, while the experimentally observed value is 25 ± 3 mm, so the proposed modelling approach was able to predict the lift-off length on this flame quite accurately. Moreover, despite these simulations have reproduced some oscillations of the lift-off height, this aspect deserves further quantitative evaluation and it is left for future work.

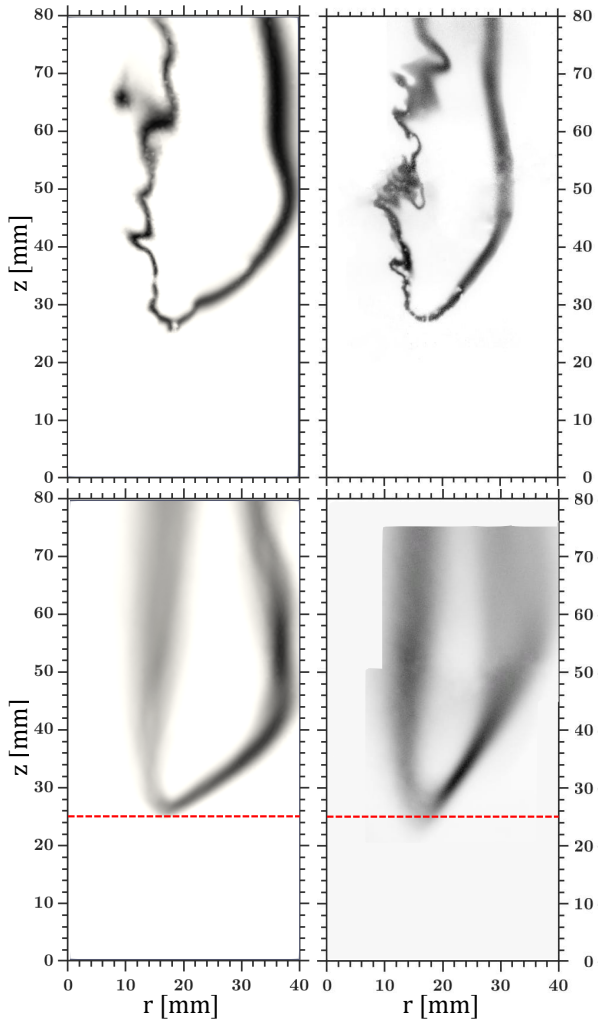

Figure 4.21: Comparison of OH contours. Left: LES results, right: OH-PLIF data from experiments [11]. Top: instantaneous signal, bottom: time-averaged fields. Red dashed line: mean lift-off length value.

4.5 Analysis of local extinction

This section focuses on the analysis of the different mechanisms of extinction that appear in the inner layer of the flame and on the capability of the combustion model to predict them. According to the experimental studies [11], the flame exhibits localized extinction in the IRZ close to the leading edge (LE) and also downstream. Numerical simulations using LES will be used

here to provide further understanding on this phenomena and shed some light in the principal mechanisms governing these effects.

4.5.1 Extinction due to droplet-flame interaction

Experimental observations [11] have shown the flame exhibits transient phenomena with some intermittency on the reacting layer, which is associated to existence of local extinction. Large droplets, which follow the main path of the spray, reach this region and impact the reacting layer causing rapid droplet evaporation and formation of rich pockets that quench the flame front. Figure 4.22 illustrates the extinction events at three different time instants. In the left column, contours of temperature and droplets are represented together, while the evaporation source term $\bar{S}_Z$ is shown on the right. In order to better visualize the position of the flame, a white iso-line representing the stoichiometric mixture fraction is included. An indicator of flame intermittency and localized extinction is the OH concentration, which is shown in Fig. 4.22 by a black line enclosing the regions with OH mass fraction $\widetilde{Y}_{OH}$ higher than 25% of peak values. The plots show a decrease in temperature close to the stoichiometric mixture fraction iso-line when the droplets cross the flame front, which is concurrent with a spatial intermittency in the OH signal. In fact, the contours of evaporation source term evidence high values of $\bar{S}_Z$ located near the extinction regions.

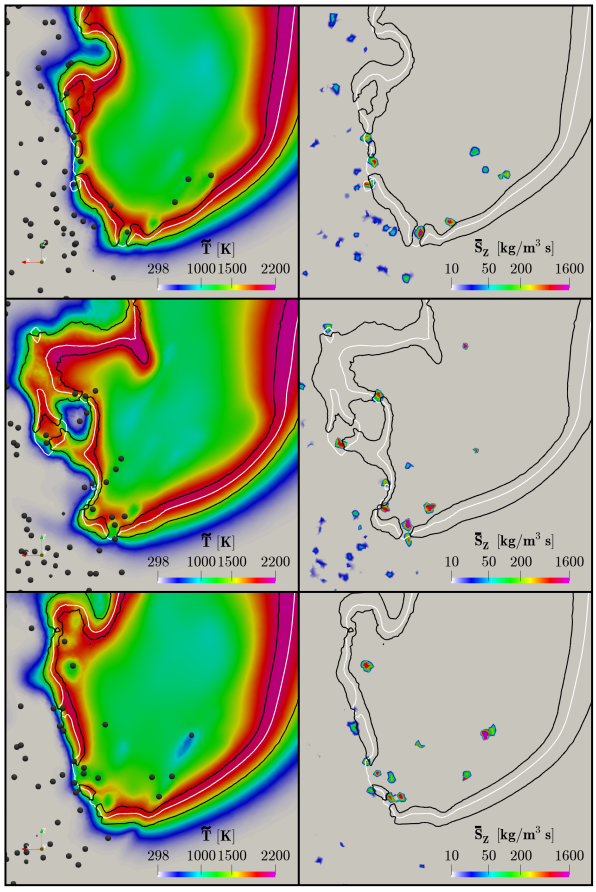

Figure 4.22: Extinction in the leading edge of the flame due to droplet interaction. Contours: temperature (left) and evaporation source term (right). Black line: threshold of 25% peak OH, white line: stoichiometric mixture fraction iso-line. Rows represent different time instants which are not equally time-spaced and illustrate clearly the phenomenon.

The analysis of the extinction by flame-droplet interactions is complemented with the results presented in Fig. 4.23. In this case, the figure shows a scatter plot of temperature and mixture fraction for different points located in the LE of the flame (points considered are located inside the LE region described in Fig. 4.18). The thermochemical variables are recorded within a 15 ms time window with a frequency of 0.05 ms, which correspond to 300 time samples. Points are colored by normalized progress variable $\widetilde{C}$, while solid and dashed lines represent the equilibrium values of the steady flamelets at adiabatic conditions ($\widetilde{\mathcal{H}} = 1$) and at the highest heat loss ($\widetilde{\mathcal{H}} = 0$), respectively.

The blue line represents a steady adiabatic flamelet considering non-zero mixture fraction variance ($Z_v = 0.125$). In this way, it is possible to evaluate quantitatively the phenomenon described in Fig. 4.22. Although temperature dispersion is clearly seen in a wide range of mixture fraction, the most interesting effect is observed near the stoichiometric conditions (vertical dotted line). The dispersion of temperature located in this region evidence that there are points very close to the reaction zone which experience extinction phenomena, showing a decrease in both temperature and normalized progress variable and moving away from chemical equilibrium conditions. Moreover, it is possible to appreciate that the peak in temperature values remains below the line of adiabatic conditions, closer to the maximum heat loss line. In this region, there are a large number of droplets crossing the flame front, evaporating and exchanging heat with the flame, which causes conditions of higher enthalpy losses. Points with higher values of mixture fraction that exceed the laminar adiabatic line are closer to the turbulent curve, since they are located inside the flame, where the mixture fraction variance Z_v reaches high values.

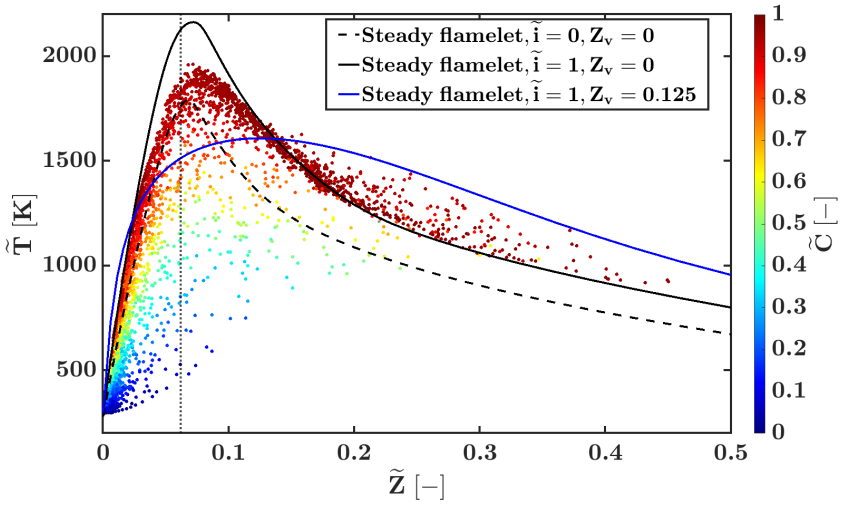

Figure 4.23: Scatter plot of temperature versus mixture fraction. Black dashed line: stoichiometric mixture fraction. Black solid and dashed lines: laminar steady flamelets. Blue solid line: turbulent steady flamelet. Colors: normalized progress variable.

In order to quantify the impact of droplet evaporation on the extinction process, Fig. 4.24 shows the correlation between the different magnitudes characterizing the extinction events. This includes normalized progress variable

$\widetilde{C}$, OH mass fraction $\widetilde{Y}_{OH}$, formaldehyde mass fraction $\widetilde{Y}_{CH_2O}$ and evaporation source term $\bar{S}_Z$. Compared to Fig. 4.23, the mixture fraction of points located near the LE of the flame has been conditioned in this case to a range of 20% around of the stoichiometric value and the evaporation mass rates are discretized in 30 bins. Each bin shows the averaged value of the magnitude and is colored by the standard deviation. Regarding the mixture fraction, the fuel/air concentration in this region fluctuates around the same mean (approximately the stoichiometric value) when the evaporation is low. As the evaporation rate increases, the formation of rich pockets contributes to increase locally the mixture fraction, while the reactivity of the mixture is reduced. Even for low evaporation rates, the normalized progress variable takes values $\widetilde{C} < 0.5$, and keeps reducing as $\bar{S}_Z$ increases. The same behavior is observed for the OH concentration. Due to this distribution of $\widetilde{Z}$ and $\widetilde{C}$, $\widetilde{Y}_{OH}$ is larger when the flame interacts with low concentrations of evaporated fuel. On the other hand, the concentration of CH_2O can be used as an indicator of the extinction events. The concentration of formaldehyde tends to behave opposite to OH, so CH_2O is close to zero with low evaporation rates and increases during extinction and re-ignition events. Furthermore, it is important to highlight that dispersion remains low for high values of $\bar{S}_Z$. When the evaporation rate reaches high values, extinctions are evident and $\widetilde{C}$ and $\widetilde{Y}_{OH}$ remain low or close to zero.

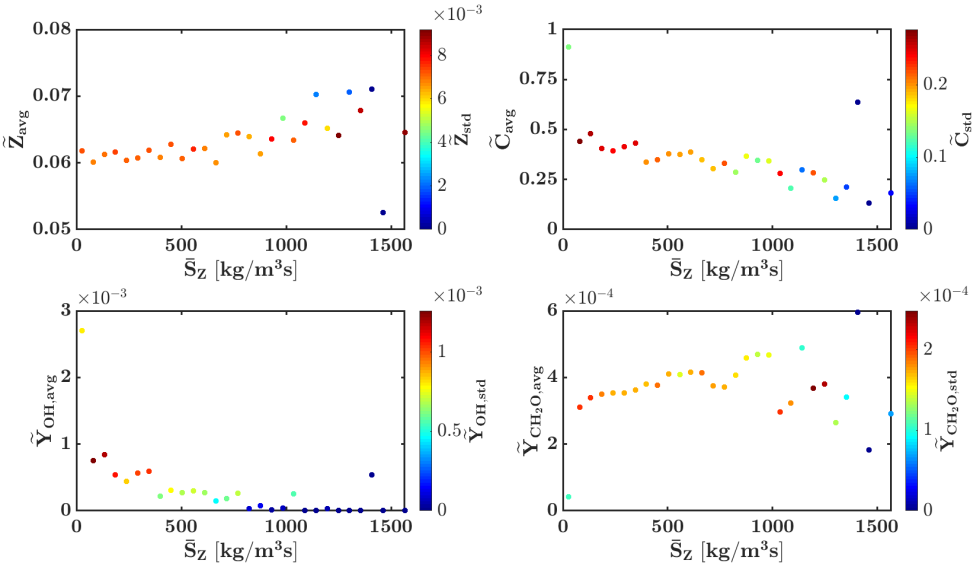

Figure 4.24: Correlation between droplet evaporation source term and mean mixture fraction (top left), normalized progress variable (top right), OH concentration (bottom left) and CH_2O concentration (bottom right). Colors: standard deviation of each magnitude.

4.5.2 Extinction due to turbulence-flame interactions

A second characteristic mechanism of flame front extinction is due to turbulence-flame interactions [11]. This phenomena occurs at axial positions further away from the LE of the flame, downstream in the IRZ, see Fig. 4.18. As described in the previous subsection, these events also exhibit the same features, that is low values of temperature, progress variable and OH concentration with high concentration of CH_2O. In this region, only small droplets that follow the main path of the gas jet evaporate close to the reacting layer and do not alter the flame front. As already described in the experimental work [11], the extinction of the flame in this region is associated to the stretching of the front produced by high levels of strain in the flow field. Figure 4.25 illustrates this event with a temporal sequence of the flame front obtained by LES. The strain is represented by a contour plot of the sum of resolved and subgrid scalar dissipation rates $\widetilde{\chi} = 2\bar{D}\boldsymbol{\nabla}\tilde{Z}\cdot\boldsymbol{\nabla}\tilde{Z} + 2\frac{Z_v}{\tau_{SGS}}$. Black and white isolines are associated with the OH threshold ($\widetilde{Y}_{OH} > 25\%$ of peak OH) and the stoichiometric mixture fraction, respectively. It can be clearly observed that when the scalar dissipation rate reaches high values near the reaction zone, the

flame front becomes thinner and wrinkled until it eventually quenches. This is a slower event than the extinction located at the LE of the flame, where the appearance of high evaporation rates close to the flame front produces its extinction very rapidly. In this case, quenching occurs when the front is affected by high scalar dissipation rate values during certain time. Note that the time window of this temporal sequence corresponds to 1 ms, which is sufficient to find an extinction event associated with strain, since the time scale of this phenomenon is approximately 0.7 ms, as introduced in Section 4.1.2. The current LES is able to reproduce these extinction events and evidence the same quenching features as those observed in the experimental measurements [11].

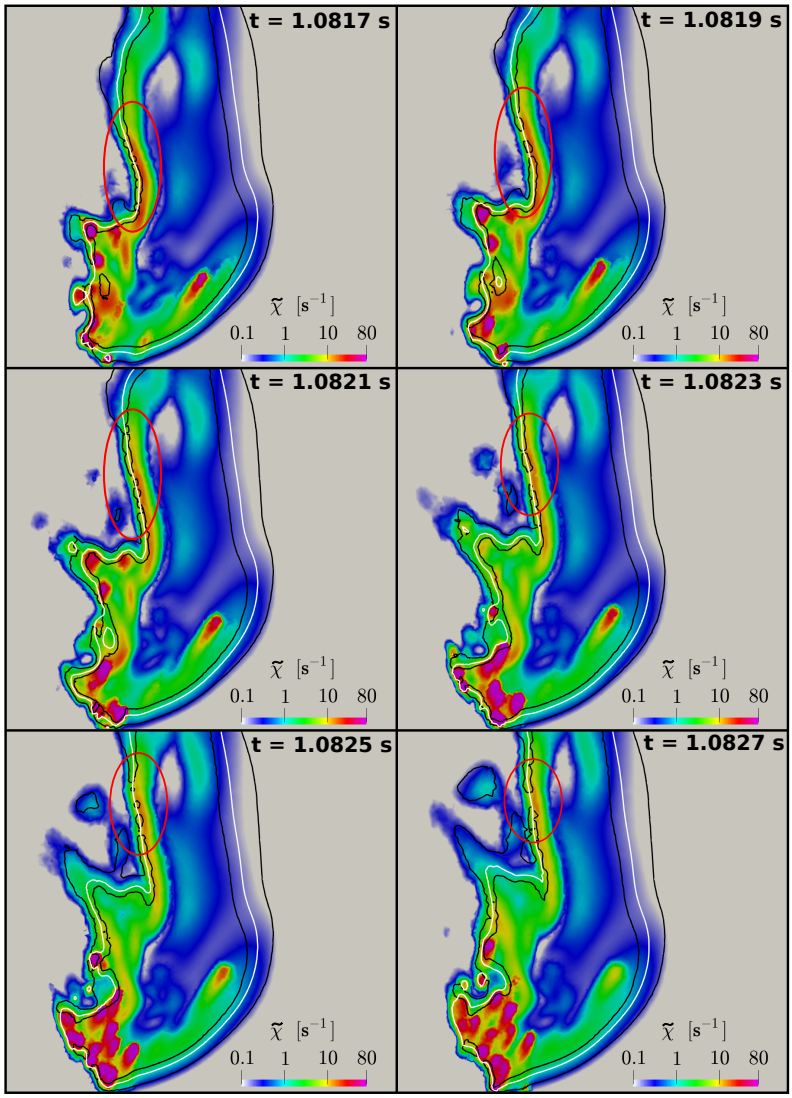

Figure 4.25: Temporal sequence of an extinction event due to strain, where each row represents a different time instant with a time separation of 0.2 ms. Contours: scalar dissipation rate. Black line: threshold of 25% peak OH, white line: stoichiometric mixture fraction iso-line.

In the same way as in the previous section, the analysis is complemented with some scatter plots in order to quantify the extinction phenomenon. Fig. 4.26 shows both $\widetilde{T} - \widetilde{Z}$ and $\widetilde{T} - \widetilde{\chi}$ scattered data for points located in the IRZ (the region affected by extinction due to turbulence-flame interactions). The methodology followed is similar to that of Fig. 4.23. Regarding

the $\widetilde{T} - \widetilde{Z}$ plot (left side), the dispersion of temperature for mixture fraction values ranged between 0 and 0.2 is also evident in this region of the IRZ. Considering the points near the stoichiometric conditions allows to clearly observe the decrease of both temperature and progress variable, as a result of the quenching events. Besides, the temperature peak located at slightly rich mixtures is closer to the adiabatic conditions, compared to the LE region of the flame, see Fig. 4.23. As mentioned above, the evaporation rate is considerably lower in this region, therefore enthalpy losses due to heat transfer between the flame and droplets are also lower. On the other hand, the plot on the right side of Fig. 4.26 shows the scattered data of temperature related to the scalar dissipation rate for points located at the stoichiometric mixture fraction iso-surface within the IRZ. For low values of $\widetilde{\chi}$ ($\widetilde{\chi} < 1\ [s^{-1}]$), all points are present in the region of high temperature, which represent the stable flame conditions. Temperature dispersion appears when $\widetilde{\chi} > 1\ [s^{-1}]$, showing extinction and re-ignition events in a wide range of $\widetilde{\chi}$ values. Note that extinction events appear for $\widetilde{\chi}$ values lower than the quenching scalar dissipation rate for laminar adiabatic steady flamelet ($\chi_{ext,lam} \approx 80\ [s^{-1}]$, see Fig. 4.2b). Thus, it is not necessary to reach this condition in order to find an extinction event, which has already been observed in other turbulent flames and modelling approaches [34, 35].

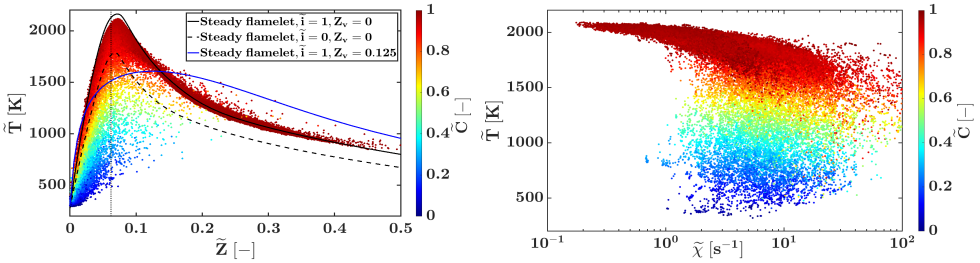

Figure 4.26: Scattered data of temperature versus mixture fraction in the IRZ (left) and of temperature versus scalar dissipation rate for points on the stoichiometric mixture fraction iso-surface (right). Vertical black dashed line: stoichiometric mixture fraction. Black solid lines: laminar steady flamelets. Blue solid line: turbulent steady flamelet. Colors: normalized progress variable.

The same information for OH and CH_2O mass concentration is presented in Fig. 4.27. In this case, points coloured by the normalized progress variable correspond to all the data of the stoichiometric surface within the region of the IRZ affected by strain. The scatter data is recorded during 10 ms, while black squares and error bars indicate the mean value and the standard deviation,

respectively. Due to the fact that there are many points of the flame front burning stable even for high values of $\widetilde{\chi}$, mean $\widetilde{Y}_{OH}$ decreases more slowly with $\widetilde{\chi}$, compared to those of the region affected by droplet evaporation (Fig. 4.24). However, it is important to highlight the level of fluctuations of OH and CH_2O concentrations. The remarkable increase in the fluctuations of these magnitudes with the scalar dissipation rate shows that extinctions generally occur for high $\widetilde{\chi}$ values, in a similar range to that observed for the dispersion of temperature in Fig. 4.26. In addition, the inverse relation between $\widetilde{Y}_{OH}$ and $\widetilde{Y}_{CH_2O}$ can be distinguished again [34], and suggests that formaldehyde can be used as an indicator to predict unsteady combustion phenomena like localized extinction.

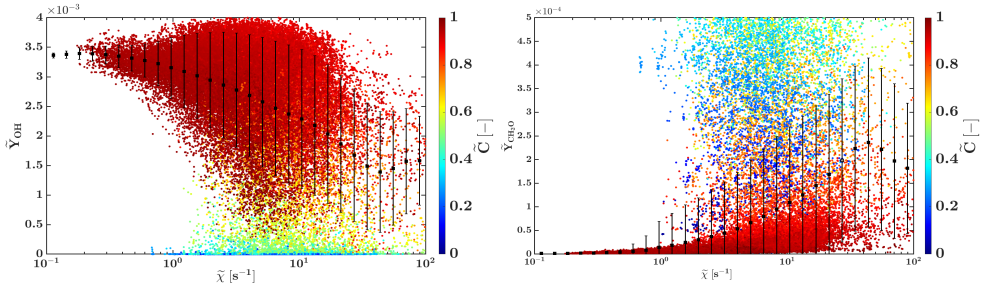

Figure 4.27: Effect of the scalar dissipation rate on OH (left) and CH_2O (right) concentrations. Data collected on the stoichiometric mixture fraction iso-surface between $z = 35$ mm and $z = 60$ mm (region extinguished due to strain). Black squares: mean value, errorbars: standard deviation. Colors: normalized progress variable.

4.6 Summary

In this chapter, the study of flame stabilization and local extinction of a spray flame in an atmospheric non-swirled test rig referred to as the CORIA Rouen Spray Burner has been presented. The present spray flame shows a double reaction front structure, with an outer laminar diffusion flame and an inner wrinkled partially-premixed flame undertaking local extinction. This unsteady phenomenon has been investigated in this work using the Eulerian-Lagrangian modelling framework for gaseous and dispersed phases described in Chapter 3. A first introduction of the experimental rig has been introduced first, followed by the detailed description of the modelling parameters. In this case, large-eddy simulations have been performed with a tabulated chemistry method based on steady and unsteady diffusion flamelets computed at different enthalpy levels in order to account for heat loss during droplet evaporation.

The numerical setup has been also presented together with the characteristics of the reference computational grid, which ensures a good resolution with a reasonable computational cost.

A validation of the numerical simulations is conducted first for the carrier and dispersed phase and good agreement with the experimental data is found for mean and fluctuating quantities. The accuracy on the prediction of droplet velocity components and temperature has led to the conclusion that the calibration of the spray model is adequate for this application. In addition, the present results have been able to predict relevant combustion parameters like the flame shape, the different inner and outer regions of the reacting front and the main combustion species. The lift-off length has been also evaluated and an excellent accuracy has been obtained in comparison to the experimental measurements.

The unsteady behaviour of the flame front already observed in previous experimental works has been also reproduced by LES. Numerical results evidence some intermittency on the OH concentration with the presence of high values of formaldehyde indicating the existence of localized extinction in the leading edge of the flame. A detailed analysis has shown the impact of droplets on the reacting layer and the existence of rich pockets quenching the flame front. Further downstream, it has been shown that when the scalar dissipation rate reaches high values near the reaction zone, the flame front becomes thinner and wrinkled until it eventually quenches. This behaviour has been analyzed by the presence of high values of droplet evaporation source term and scalar dissipation rate, for the first and second extinction event respectively, which lead to a local reduction of the OH concentration and an increase of formaldehyde due to the flame quenching.

In general, the proposed modelling approach has been able not only to reproduce the spray flame characteristics, but the results obtained and presented in this chapter have demonstrated that the applied tabulated chemistry method is capable of capturing the local extinction and re-ignition events occurring in the inner layer of the CRSB.

References

[1] Dryer, Frederick L. "Chemical kinetic and combustion characteristics of transportation fuels". In: *Proceedings of the Combustion Institute* 35.1 (2015), pp. 117–144. DOI: https://doi.org/10.1016/j.proci.2014.09.008.

[2] Giusti, A. and Mastorakos, E. "Turbulent Combustion Modelling and Experiments: Recent Trends and Developments". In: *Flow, Turbulence and Combustion* 103 (2019), pp. 1–18.

[3] Jenny, Patrick, Roekaerts, Dirk, and Beishuizen, Nijso. "Modeling of turbulent dilute spray combustion". In: *Progress in Energy and Combustion Science* 38.6 (2012), pp. 846–887. DOI: 10.1016/j.pecs.2012.07.001.

[4] Measurement, 7th Workshop on and Turbulent Spray Combustion (TCS7), Computation of. In: (2019).

[5] Verdier, Antoine et al. "Experimental study of local flame structures and fuel droplet properties of a spray jet flame". In: *Proceedings of the Combustion Institute* 36.2 (2017), pp. 2595–2602. DOI: 10.1016/j.proci.2016.07.016.

[6] Shum-Kivan, F. et al. "Experimental and numerical analysis of a turbulent spray flame structure". In: *Proceedings of the Combustion Institute* 2 (2017), pp. 2567–2575. DOI: 10.1016/j.proci.2016.06.039.

[7] Jones, William P., Marquis, Andrew J., and Noh, Dongwon. "An investigation of a turbulent spray flame using Large Eddy Simulation with a stochastic breakup model". In: *Combustion and Flame* 186 (2017), pp. 277–298. DOI: 10.1016/j.combustflame.2017.08.019.

[8] Noh, Dongwon, Gallot-Lavallée, Simon, Jones, William P., and Navarro-Martinez, Salvador. "Comparison of droplet evaporation models for a turbulent, non-swirling jet flame with a polydisperse droplet distribution". In: *Combustion and Flame* 194 (2018). DOI: 10.1016/j.combustflame.2018.04.018.

[9] Chatelier, Adrien, Fiorina, Benoît, Moureau, Vincent, and Bertier, Nicolas. "Large Eddy Simulation of a Turbulent Spray Jet Flame Using Filtered Tabulated Chemistry". In: *Journal of Combustion* 2020 (2020). DOI: 10.1155/2020/2764523.

[10] Sitte, Michael Philip and Mastorakos, Epaminondas. "Large Eddy Simulation of a spray jet flame using Doubly Conditional Moment Closure". In: *Combustion and Flame* 199 (2019), pp. 309–323. DOI: 10.1016/J.COMBUSTFLAME.2018.08.026.

[11] Verdier, Antoine et al. "Local extinction mechanisms analysis of spray jet flame using high speed diagnostics". In: *Combustion and Flame* 193 (2018), pp. 440–452. DOI: 10.1016/j.combustflame.2018.03.032.

[12] Oijen, J.A. Van and Goey, L.P.H. De. "Modelling of Premixed Laminar Flames using Flamelet-Generated Manifolds". In: *Combustion Science and Technology* 161.1 (2000), pp. 113–137. DOI: 10.1080/00102200008935814.

[13] Pierce, Charles D. and Moin, Parviz. "Progress-variable approach for large-eddy simulation of non-premixed turbulent combustion". In: *Journal of Fluid Mechanics* 504.504 (2004), pp. 73–97. DOI: 10.1017/S0022112004008213.

[14] Both, A. "RANS-FGM simulation of n-heptane spray flame in OpenFOAM". MA thesis. Delft University of Technology, 2017.

[15] Ma, Likun and Roekaerts, Dirk. "Modeling of spray jet flame under MILD condition with non-adiabatic FGM and a new conditional droplet injection model". In: *Combustion and Flame* 165 (2016), pp. 402–423. DOI: 10.1016/j.combustflame.2015.12.025.

[16] Ihme, Matthias and Pitsch, Heinz. "Prediction of extinction and reignition in nonpremixed turbulent flames using a flamelet/progress variable model. 2. Application in LES of Sandia flames D and E". In: *Combustion and Flame* 155.1-2 (2008), pp. 90–107. DOI: 10.1016/j.combustflame.2008.04.015.

[17] Benajes, J et al. "Large Eddy Simulations of a n-heptane spray flame with local extinction". In: *3rd Edition of the HPC Spanish Combustion Workshop 2021*. 2021.

[18] Benajes, J et al. "Analysis of local extinction of a n-heptane spray flame using large-eddy simulation with tabulated chemistry". In: *Combustion and Flame* 235 (2022), p. 111730.

[19] Cordier, M, Vandel, Alexis, Cabot, G, Renou, B, and Boukhalfa, AM. "Laser-induced spark ignition of premixed confined swirled flames". In: *Combustion Science and Technology* 185.3 (2013), pp. 379–407.

[20] Lu, Tianfeng and Law, Chung K. "Linear time reduction of large kinetic mechanisms with directed relation graph: n-Heptane and iso-octane". In: *Combustion and Flame* 144.1 (2006), pp. 24–36. DOI: https://doi.org/10.1016/j.combustflame.2005.02.015.

[21] Illana, Enric, Mira, Daniel, and Mura, Arnaud. "An extended flame index partitioning for partially premixed combustion". In: *Combustion Theory and Modelling* 25.1 (2021), pp. 121–157. DOI: 10.1080/13647830.2020.1841912.

[22] Liñán, Amable, Martínez-Ruiz, Daniel, Vera, Marcos, and Sánchez, Antonio L. "The large-activation-energy analysis of extinction of counterflow diffusion flames with non-unity Lewis numbers of the fuel". In: *Combustion and Flame* 175 (2017), pp. 91–106. DOI: https://doi.org/10.1016/j.combustflame.2016.06.030.

[23] Ji, Weiqi, Yang, Tianwei, Ren, Zhuyin, and Deng, Sili. "Dependence of kinetic sensitivity direction in premixed flames". In: *Combustion and Flame* 220 (2020), pp. 16–22. DOI: https://doi.org/10.1016/j.combustflame.2020.06.027.

[24] Fiorina, Benoit et al. "Modelling non-adiabatic partially premixed flames using flame-prolongation of ILDM". In: *Combustion Theory and Modelling* 7.3 (2003), p. 449.

[25] Ma, Likun. "Computational modeling of turbulent spray combustion". PhD thesis. Delft University of Technology, 2016.

[26] Marrero Santiago, Javier. "Experimental study of lean aeronautical ignition: impact of critical parameters on the mechanisms acting along the different ignition phases". PhD thesis. Normandie, 2018.

[27] Alessandro, D'Ausilio, Stankovic, Ivana, and Merci, Bart. "LES study of a turbulent spray jet: mesh sensitivity, mesh-parcels interaction and injection methodology". In: *Flow, Turbulence and Combustion* 103 (2019), pp. 537–564.

[28] Pope, S.B. "Ten questions concerning the large-eddy simulation of turbulent flows". In: *New Journal of Physics* 6 (2004). DOI: 10.1088/1367-2630/6/1/035.

[29] Yoshizawa, Akira. "Statistical theory for compressible turbulent shear flows, with the application to subgrid modeling". In: *The Physics of fluids* 29.7 (1986), pp. 2152–2164.

[30] Mira, D. and Jiang, X. "Large-eddy simulations of unsteady hydrogen annular flames". In: *Computers & Fluids* 80 (2013). Selected contributions of the 23rd International Conference on Parallel Fluid Dynamics ParCFD2011, pp. 429–440. DOI: https://doi.org/10.1016/j.compfluid.2012.01.013.

[31] Mulla, Irfan A. and Renou, Bruno. "Simultaneous imaging of soot volume fraction, PAH, and OH in a turbulent n-heptane spray flame". In: *Combustion and Flame* (2019). DOI: 10.1016/j.combustflame.2019.08.012.

[32] Frenklach, Michael, Clary, David W., Gardiner, William C., and Stein, Stephen E. "Detailed kinetic modeling of soot formation in shock-tube pyrolysis of acetylene". In: *Symposium (International) on Combustion* 20.1 (1985). Twentieth Symposium (International) on Combustion, pp. 887–901. DOI: https://doi.org/10.1016/S0082-0784(85)80578-6.

[33] Mulla, Irfan A., Godard, Gilles, Cabot, Gilles, Grisch, Frédéric, and Renou, Bruno. "Quantitative imaging of nitric oxide concentration in a turbulent n-heptane spray flame". In: *Combustion and Flame* 203 (2019), pp. 217–229. DOI: 10.1016/j.combustflame.2019.02.005.

[34] Giusti, A. and Mastorakos, E. "Detailed chemistry LES/CMC simulation of a swirling ethanol spray flame approaching blow-off". In: *Proceedings of the Combustion Institute* 36.2 (2017), pp. 2625–2632. DOI: 10.1016/j.proci.2016.06.035.

[35] Yu, S., Liu, X., Bai, X. S., Elbaz, A. M., and Roberts, W. L. "LES/PDF modeling of swirl-stabilized non-premixed methane/air flames with local extinction and re-ignition". In: *Combustion and Flame* 219 (2020), pp. 102–119. DOI: 10.1016/j.combustflame.2020.05.018.

Chapter 5

Computationally efficient soot modelling on a pressurized gas turbine burner

This chapter presents the analysis of a pressurized ethylene-based model burner using the modelling approach described previously for the characterization of the combustion process and soot prediction. The chosen configuration is the aero-engine model combustor developed at the German Aerospace Center (DLR) by Geigle et al. [1, 2] (referenced as *DLR burner* along this chapter for brevity), which has been widely studied in terms of turbulent combustion and soot formation. It is a pressurized burner featuring a dual swirler configuration for the primary air supply, generating a strong recirculation region inside the combustion chamber. Secondary air is injected downstream, creating a soot oxidation zone typical of the Rich-Burn/Quick-Mix/Lean-Burn (RQL) combustor concept. The relevance of this burner is evidenced by its role as a target case in the ISF Workshop [3] for turbulent flames. This configuration has been selected to evaluate the applicability and prediction capabilities of the efficient coupling between the Discrete Sectional (DSM) method for soot and the Flamelet Generated Manifold (FGM) combustion model within the LES framework described in Chapter 3.

As mentioned in previous chapters, soot modelling remains a challenge and further research is required to develop and employ detailed predictive methods, which consider an adequate description of the soot key kinetic processes

and provide information of particle size distribution and aerosol dynamics, at affordable computational requirements for practical applications. In this burner, different modelling strategies have been used over the last few years to predict soot emissions [3]. In [4–6], semi-empirical two-equation soot models and reduced kinetic mechanism coupled to different turbulent combustion approaches were employed to predict soot quantity. In general, the numerical results were able to qualitatively capture soot distribution although important discrepancies were observed in the soot volume fraction magnitude, depending on the combustion modelling and chemistry description. In addition, these modelling approaches do not account for particle characteristics and size distributions. Simulations with detailed soot chemistry and particle dynamics of this burner were conducted in [7], where the hybrid MoM [8] was coupled to tabulated chemistry. A good qualitative agreement with the experimental data was obtained, but the SVF was strongly overpredicted. A similar soot description was used in [9] showing a fair prediction of the soot field for the reference operating condition of the DLR combustor. Conversely, the soot distribution was not captured for the burner configuration without secondary air injection. In [10] the burner simulation with Split-based Extended Quadrature MoM [11] was able to capture soot field distribution but the magnitude was underestimated by a factor of three. Recently, DSM has been applied to simulate this burner coupled to tabulated [12] and to finite-rate [13] chemistry. Good qualitative and quantitative soot predictions were obtained, though soot oxidation in the outer part of the burner is overestimated, such as in most of the simulations previously discussed. Particle Size Distribution (PSD) information was only provided by [12]. Unfortunately, validation was not possible due to the lack of experimental measurements.

The work presented here is focused on the assessment of the modelling approach proposed by Kalbhor et al. [14, 15] in a realistic application such as the DLR burner, where the trade-off between CPU cost and accuracy is a major concern. The chapter is structured as follows. Section 5.1 introduces the characteristics of the burner, including a description of the experimental test rig, the computational domain, numerical setup and some particularities of combustion and soot models. Results for the baseline configuration of the DLR burner, which includes the secondary dilution air, are presented in Sections 5.2 and 5.3. On the one hand, gas phase results of the reacting flow are presented in Section 5.2, where flow structures and flame characteristics are discussed. On the other hand, Section 5.3 is focused on soot predictions, including the soot field assessment, an analysis of soot formation and particle size distributions. Finally, the operating condition without secondary air injection is evaluated in Section 5.4 and the effect of the dilution air in the reacting

flow and soot distribution is discussed there. The content of this chapter is partially published in [16, 17] and is included in a journal publication which is currently under review.

5.1 Case description

In this section, a general overview of the case studied is presented in terms of burner characteristics and numerical setup. First, a description of the model combustor and experimental rig is introduced. Then, the chemical characteristics of the burner and some details of the general modelling framework described in Chapter 3 are specified for this application. Finally, the computational domain and different grids employed are presented.

5.1.1 Experimental test rig

This work is focused on the study of the pressurized ethylene-based model combustor from DLR. It exhibits features similar to real gas turbine burners and it is representative of the RQL concept. A more detailed description of the experimental setup can be found in the work of Geigle et al. [1, 2].

A sketch of the geometrical burner characteristics is shown in Fig. 5.1. The burner contains a dual radial swirler configuration for the air supply. The inner swirler consists of 8 vanes, while the outer one is composed of 11 ducts. The combustion chamber has a square section of 68 x 68 mm^2 and a height of 120 mm. Up to four quartz windows are arranged on the sides of the chamber ensuring the optical access for measurements. Additional ducts for secondary oxidation air injection are located at the corners of the chamber, 80 mm downstream the chamber inlet plane. Fuel is injected through a concentric ring of 60 equally spaced ports located between the inner and outer air inlets.

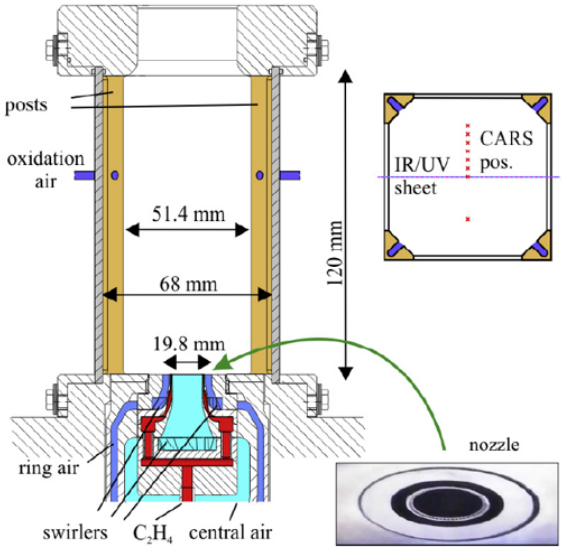

Figure 5.1: Sketch of the DLR-RQL burner experimental setup. Image from [2].

Multiple experimental diagnostics are available for flame characterization and soot formation [1, 2, 18]. Velocity component statistics at different positions inside the combustion chamber were measured using Stereo-Particle Image Velocimetry (Stereo-PIV). Temperature measurements were obtained from Coherent Anti-Stokes Raman scattering (CARS) and OH radical distribution was qualitatively estimated by Laser Induced Fluorescence (LIF). In addition, Planar Laser-Induced Incandescence (LII) was used to measure the soot volume fraction.

The experimental database contains several operating conditions with variations of the operating pressure, primary air and fuel mass flows, primary air and fuel ratios and secondary air mass flow. In this work, two of these operating points are evaluated and a summary of the flame parameters is presented in Tab. 5.1. Op 1 corresponds to the reference operating condition of the DLR burner while the secondary oxidation air is removed in Op 2, modifying the global equivalence ratio. The results presented in this chapter are mainly focused on Op 1 but Op 2 is also analysed in Section 5.4.

5.1.2 Details of the modelling approach

In a similar way to Chapter 4, this section aims to detail some aspects of the general modelling approach described in Chapter 3 that are considered for

	p	ϕ_{global}	Q_a	$Q_{a,ox}$	T_a	Q_f	T_f
Op 1	3	0.86	468.3	187.4	300	39.3	300
Op 2	3	1.2	468.3	0	300	39.3	300

Table 5.1: Flame parameters of the operating conditions evaluated. Pressure, p [bar]*; global equivalence ratio, ϕ_{global}; mass flows for air through burner, Q_a; oxidation air through secondary inlets, $Q_{a,ox}$; fuel, Q_f* [slpm, or standard litre per minute]*; air and fuel temperatures, T_a and T_f* [K].

this application. In this case, the efficient coupling of the FGM combustion model and the CDSM method for soot is employed and the following lines are intended to provide information about the parameters and considerations used for combustion and soot modelling. Note that any details of the modelling approach not specified here are assumed to be the same as described in Chapter 3.

Thermochemical conditions and combustion model

In both operating conditions described in Table 5.1, the burner is pressurized and fuel and air are injected at ambient temperature. Therefore, $p = 3$ bar, $T_{air} = T_{fuel} = 300$ K are considered for the flamelet calculations. The chemistry for ethylene fuel is taken from a 214-species and 1537 reactions kerosene surrogates mechanism [19] including recent developments for PAH soot precursors [20]. This chemical mechanism has been developed within the ESTiMatE European project and has been extensively validated in laminar counterflow diffusion flames [21] (including ethylene and other fuels). As an example of the performance of the mechanism in ethylene flames, Fig. 5.2 shows the soot predictions in a reference counterflow configuration from the literature [22]. The simulation of the 1D flame has been performed using Chem1D [23] with the Discrete Sectional Method for soot outlined in Section 3.3.1. Although the soot number density and particle diameter are underpredicted (specially at $x = -0.5$ mm), the trend is correctly captured and the agreement with the measurements in terms of Soot Volume Fraction is reasonably good.

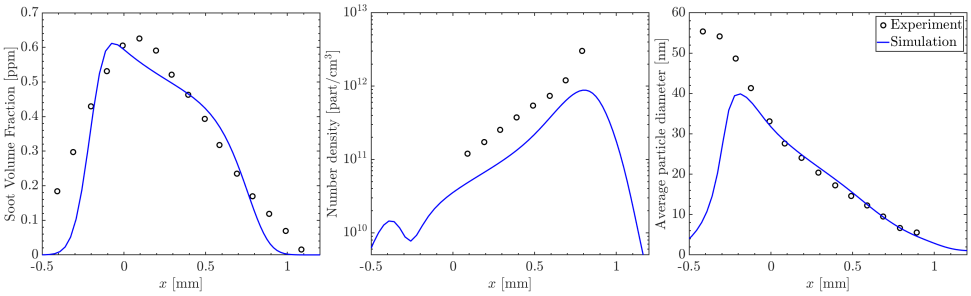

Figure 5.2: Soot predictions on the ethylene counterflow flame from Wang et al. [22] with the Discrete Sectional Method (DSM) using the kerosene surrogates mechanism [20]. Left: Soot Volume Fraction, center: soot number density, right: average particle diameter.

Regarding the flamelet generation, the general strategy described in Chapter 3 and used in the application of Chapter 4 is also employed here. The manifold is composed of different laminar diffusion one-dimensional flames at different strain rates which account for strain effects. Flamelets are tabulated at increasing strains until the extinction point, where an unsteady extinguishing calculation is initiated from this point to the inert conditions as a continuation of the manifold. Despite fuel and air being injected separately, the combustion process in this configuration occurs in partially premixed conditions due to the rapid fuel/air mixing so the tabulation of diffusion or premixed flamelets is an open question. In fact, some authors state that including premixing effects in a manifold composed of non-premixed flames could be relevant for combustion characterization and soot prediction [7]. However, in this burner partial premixing is achieved before the mixture interacts with the reacting layer, and then the flame burns across a wide range of equivalence ratios, even outside the flammability range. Due to such conditions, the tabulation of counterflow diffusion flamelets is employed here. Similar approaches considering diffusion flamelets have been successfully employed in previous works of this burner [7, 9, 24].

In this case, the database also contains non-adiabatic flamelets at different enthalpy levels in order to account for heat losses to the burner walls. The local enthalpy deficit is achieved by the use of a radiative source term in the energy equation, in the same way as described in Chapters 3 and 4. A representation of the manifold is illustrated in Figs. 5.3. The temperature at the stoichiometric point T_{st} is represented as a function of both the strain rate a and stoichiometric scalar dissipation rate χ_{st} for the set of flamelets at different enthalpy levels (represented by the radiative source term Q_{rad}).

Note that the enthalpy deficit slightly affects the extinction point and has a considerable impact at low strain conditions.

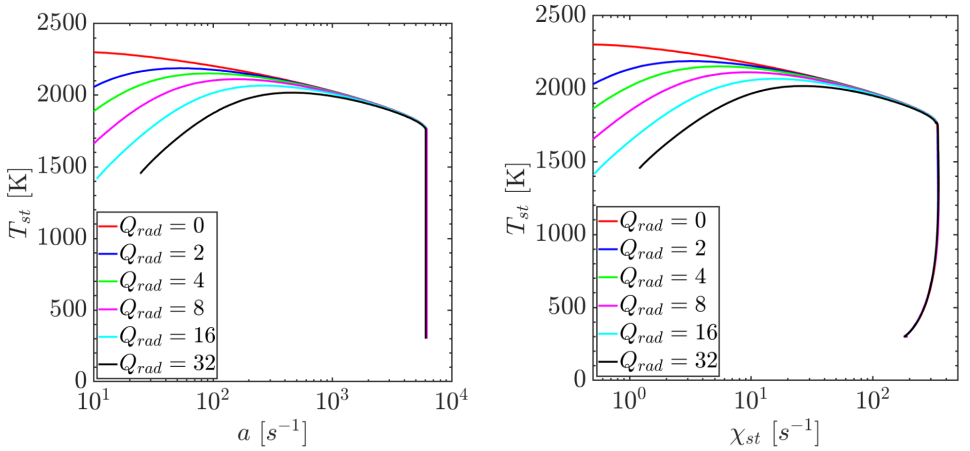

(a) Stoichiometric temperature as function of the strain rate.

(b) Stoichiometric temperature as function of the stoichiometric scalar dissipation rate.

Figure 5.3: S-curve of the counterflow diffusion ethylene flamelets at different enthalpy levels described by the radiation factor Q_{rad}.

In order to have an approximation of the representative flame thickness, temporal and velocity scales of the combustion process in the ethylene flamelets considered, Table 5.2 illustrates the values of the relevant chemical scales using the definitions described in Chapter 2. Note that the first set of definitions are evaluated at the extinction point while the chemical time scale definition of Ihme and Pitsch [25] is obtained with the entire manifold. In these ethylene flames, the extinction strain rate and stoichiometric scalar dissipation rate are considerably high compared to other hydrocarbon fuels, so the obtained characteristic chemical time is really low and the length scale very thin, resulting in a high combustion velocity. Furthermore, it is worth to mention that the mixing time scale at the extinction limit is very similar to the chemical time scale due to the low stoichiometric mixture fraction for this case ($Z_{st} = 0.0637$). The chemical time based on the concept of progress variable is slightly higher ($\tau_c^{\dot{\omega}} \sim \tau_c^{ext,\chi}$), but remains in the same order of magnitude. Therefore, this application is expected to be quite reactive and under the flamelet regime assumption.

The turbulence/chemistry interactions are accounted in the manifold using the presumed PDF integration described in Chapter 3 and the chemical

Counterflow diffusion ehtylene flame at extinction point	
a^{ext}	6160 1/s
χ_{st}^{ext}	337.52 1/s
T_{st}^{ext}	1762.95 K
δ_{diff}^{ext}	0.051 mm
τ_m^{ext}	0.012 ms
$\tau_c^{ext,\chi}$	0.012 ms
$v_c^{ext,\chi}$	3.691 m/s
Manifold of counterflow diffusion flames (Eq. 2.45)	
$\tau_c^{\dot{\omega}}$	0.023 ms
$v_c^{\dot{\omega}}$	2.686 m/s

Table 5.2: Chemical scales ethylene flames.

state is ultimately described by five control variables: $\widetilde{Z}$, Z_v, $\widetilde{Y_c}$, $Y_{c,v}$ and $\widetilde{h}$. Although the consideration of progress variable variance is not common in non-premixed combustion models, it has demonstrated to provide a proper statistical representation of the residual fluctuation of Y_c in burner simulations [26]. The resulting system of equations for this case read as:

$$\frac{\partial \bar{\rho}}{\partial t} + \boldsymbol{\nabla} \cdot (\bar{\rho}\tilde{\boldsymbol{u}}) = 0, \tag{5.1}$$

$$\frac{\partial \bar{\rho}\tilde{\boldsymbol{u}}}{\partial t} + \boldsymbol{\nabla} \cdot (\bar{\rho}\tilde{\boldsymbol{u}}\tilde{\boldsymbol{u}}) = -\boldsymbol{\nabla} \cdot \overline{\tau}_M - \boldsymbol{\nabla}\bar{p} + \boldsymbol{\nabla} \cdot (\bar{\mu}\boldsymbol{\nabla}\tilde{\boldsymbol{u}}), \tag{5.2}$$

$$\frac{\partial \bar{\rho}\tilde{h}}{\partial t} + \boldsymbol{\nabla} \cdot \left(\overline{\rho}\tilde{\boldsymbol{u}}\tilde{h}\right) = -\boldsymbol{\nabla} \cdot \overline{\tau}_h + \boldsymbol{\nabla} \cdot \left(\bar{\rho}\bar{D}\boldsymbol{\nabla}\tilde{h}\right), \tag{5.3}$$

$$\frac{\partial \bar{\rho}\tilde{Z}}{\partial t} + \boldsymbol{\nabla} \cdot \left(\overline{\rho}\tilde{\boldsymbol{u}}\tilde{Z}\right) = -\boldsymbol{\nabla} \cdot \overline{\tau}_Z + \boldsymbol{\nabla} \cdot \left(\bar{\rho}\bar{D}\boldsymbol{\nabla}\tilde{Z}\right), \tag{5.4}$$

$$\frac{\partial \bar{\rho}\tilde{Y}_c}{\partial t} + \boldsymbol{\nabla} \cdot \left(\overline{\rho}\tilde{\boldsymbol{u}}\tilde{Y}_c\right) = -\boldsymbol{\nabla} \cdot \overline{\tau}_{Y_c} + \boldsymbol{\nabla} \cdot \left(\bar{\rho}\bar{D}\boldsymbol{\nabla}\tilde{Y}_c\right) + \overline{\dot{\omega}}_{Y_c}, \tag{5.5}$$

$$\frac{\partial \bar{\rho}Z_v}{\partial t} + \boldsymbol{\nabla} \cdot (\overline{\rho}\tilde{\boldsymbol{u}}Z_v) = -\boldsymbol{\nabla} \cdot \overline{\tau}_{Z_v} + \boldsymbol{\nabla} \cdot \left(\bar{\rho}\bar{D}\boldsymbol{\nabla}Z_v\right) - 2\overline{\tau}_Z \cdot \boldsymbol{\nabla}\tilde{Z} - 2\overline{s}_{\chi_Z}, \tag{5.6}$$

$$\frac{\partial \bar{\rho}Y_{c,v}}{\partial t} + \boldsymbol{\nabla} \cdot (\overline{\rho}\tilde{\boldsymbol{u}}Y_{c,v}) = -\boldsymbol{\nabla} \cdot \overline{\tau}_{Y_{c,v}} + \boldsymbol{\nabla} \cdot \left(\bar{\rho}\bar{D}\boldsymbol{\nabla}Y_{c,v}\right) - 2\overline{\tau}_{Y_c} \cdot \boldsymbol{\nabla}\tilde{Y}_c - 2\overline{s}_{\chi_{Y_c}} + 2\left(\overline{Y_c\dot{\omega}}_{Y_c} - \tilde{Y}_c\overline{\dot{\omega}}_{Y_c}\right). \tag{5.7}$$

All the assumptions and modelling constants previously described are applied here.

The thermochemical table contains 81x7x81x7x6 entries corresponding those five control variables (for clarity, $(n_{\widetilde{Z}}, n_{Z_v}, n_{\widetilde{C}}, n_{C_v}, n_{\widetilde{\mathcal{H}}}) = (81, 7, 81, 7, 6)$, where n_ϕ is the number of points used for the discretization of control variable ϕ). For the progress variable discretization, a power function is used considering an exponent value of 3, while the mixture fraction space is discretized with a non-uniform distribution centered at the stoichiometric point. Mixture fraction and progress variable variances are also discretized with a power function, using a value of 3 for the exponent. The enthalpy level is tabulated for 6 equidistant steps. Note, that the number of these levels is larger than the number of different radiation scalings applied, this approach is chosen because the radiation scaling does not guarantee an equidistant spacing in enthalpy, thus more levels are applied in the table to represent the flamelets in sufficient detail. In this work, two different manifolds are compared: one using non-adiabatic flamelets with the radiative approach (reference) and another using adiabatic flamelets. For the adiabatic manifold, the control variable corresponding to the enthalpy level is simply removed.

For this study, the progress variable is defined by the previously described Eq. 3.18 with six species using $Y_k = \{Y_{CO_2}, Y_{CO}, Y_{H_2}, Y_{H_2O}, Y_{C_2H_2}, Y_{A4}\}$. The contribution of each species to the progress variable Y_k is given by the coefficients $a_k = \{4.0, 1.0, 1.0, 2.0, -1.0, 2000\}$ respectively. The current progress variable definition is defined to facilitate unique mapping of thermochemical variables in the composition space for both combustion chemistry and soot-gas phase chemistry interaction. While the progress variable definition generally includes main combustion products, those species do not have sensitivity to recover slow developing processes like PAH formation or soot. Therefore, additional key species involved in soot inception and growth, such as A4 and C_2H_2, have been incorporated in the progress variable definition to account for the evolution of soot in the manifold space [14]. Note that A4 is a PAH soot precursor with slow formation chemistry that is restricted to low strain rates, and its contribution to the progress variable is selected to improve the sensitivity in the FGM [27]. Nevertheless, since the A4 species is not explicitly transported for the calculation of soot source terms, the accuracy of the current FGM-CDSM framework is not significantly impacted by adding A4 in the progress variable definition.

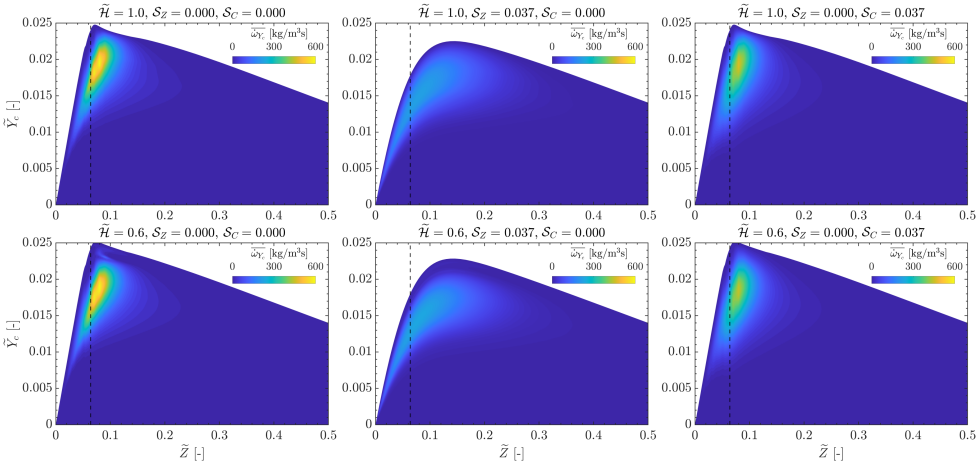

Figure 5.4: Illustration of the non-adiabatic manifold used for the DLR burner case. Effect of scaled enthalpy $\widetilde{\mathcal{H}}$, mixture fraction segregation factor $\mathcal{S}_Z$ and progress variable segregation factor $\mathcal{S}_C$ on the $\widetilde{Z} - \widetilde{Y}_c$ map of the filtered progress variable source term $\overline{\dot{\omega}_{Y_c}}$. Dashed line: stoichiometric mixture fraction.

To illustrate the non-adiabatic manifold, Fig. 5.4 shows the different $\widetilde{Z} - \widetilde{Y_c}$ maps of the filtered progress variable source term $\overline{\dot{\omega}_{Y_c}}$ depending on the values of the scaled enthalpy $\widetilde{\mathcal{H}}$, mixture fraction variance and progress variable variance. Note that variances are represented here by the corresponding segregation factor: $\mathcal{S}_Z = \frac{Z_v}{\widetilde{Z}(1-\widetilde{Z})}$ and $\mathcal{S}_C = \frac{C_v}{\widetilde{C}(1-\widetilde{C})}$. In general, the progress variable source term peak is remarkably modified by variations of the three control variables mentioned. A decrease of the scaled enthalpy does not affect $\overline{\dot{\omega}_{Y_c}}$ peak value, however, the location of the peak is slightly displaced to lower $\widetilde{Y_c}$ values. On the other hand, the effect of mixture fraction and progress variable variances is more relevant, since both considerably reduce the source term peak and distributes the $\overline{\dot{\omega}_{Y_c}}$ magnitude along the respective coordinate. In addition, $\mathcal{S}_Z$ affects the $\widetilde{Y_c}$ profile, reducing and moving its peak to higher mixture fraction values and widening the region of relevant progress variable source terms.

Soot model

The soot modelling approach was fully described in Chapter 3 and only a few details of the configuration and parameters used are provided here.

For this case, 60 original soot sections are considered during the manifold generation, which are grouped into 6 clusters for the efficient application of the

model in the LES framework. This 90% reduction in sectional dimensions provided a speed-up factor of 4.5 in laminar 2-D flames with almost no impact on soot predictions [14], and it has been retained in this application. The original sections are uniformly distributed within the clusters so that each clustered section contains 10 original sections. Table 5.3 summarizes the distribution of soot sections and also provides information about the particle diameter (d_p) range for each cluster, assuming spherical particles and the particle volume distribution specified in Chapter 3 (see Eq. 3.38).

	Range of original sections	Min. d_p	Max. d_p
Cluster 1	Sections: 1 - 10	0.868 nm	4.126 nm
Cluster 2	Sections: 11 - 20	4.126 nm	19.609 nm
Cluster 3	Sections: 21 - 30	19.609 nm	93.184 nm
Cluster 4	Sections: 31 - 40	93.184 nm	442.82 nm
Cluster 5	Sections: 41 - 50	442.82 nm	2104.3 nm
Cluster 6	Sections: 51 - 60	2104.3 nm	10000 nm

Table 5.3: Distribution of soot sections within the clusters for the application of the CDSM approach in the DLR burner.

As mentioned in the description of the modelling approach, soot source terms are integrated with the presumed PDF function in order to account for the effects of sub-grid fluctuations on soot and production and consumption parts are tabulated in the manifold. In this way, the soot source term for each cluster is given by Eq. 3.58, which is repeated here for clarity:

$$\overline{\dot{\omega}}^{c}_{s,j} = \overline{\dot{\omega}}^{c,+}_{s,j} + \overline{\dot{\omega}}^{c,-}_{s,j} \approx \left[\overline{\dot{\omega}}^{c,+}_{s,j}\right]^{\mathrm{tab}} + \widetilde{Y}_{s,j} \left[\frac{\dot{\omega}^{c,-}_{s,j}}{Y_{s,j}}\right]^{\mathrm{tab}} , \tag{5.8}$$

To illustrate the effects of enthalpy levels and control variable variances on the tabulated production and consumption parts of the soot source term, Fig. 5.5 presents the corresponding $\widetilde{Z} - \widetilde{Y_c}$ maps. Note that the production and consumption parts for all clusters are represented in the figure, so that $\overline{\dot{\omega}}^{c,+}_{s} = \sum_{j=1}^{6} \overline{\dot{\omega}}^{c,+}_{s,j}$ and $\overline{\dot{\omega}}^{c,-}_{s}/Y_s = \sum_{j=1}^{6} \overline{\dot{\omega}}^{c,-}_{s,j}/Y_{s,j}$. It is worth mentioning that the difference in the order of magnitude between both terms is associated to the linearization of the consumption part, which is expected to be multiplied by the filtered soot mass fraction $\widetilde{Y}_{s,j}$ during the total source term calculation and, thus, it presents very high negative values.

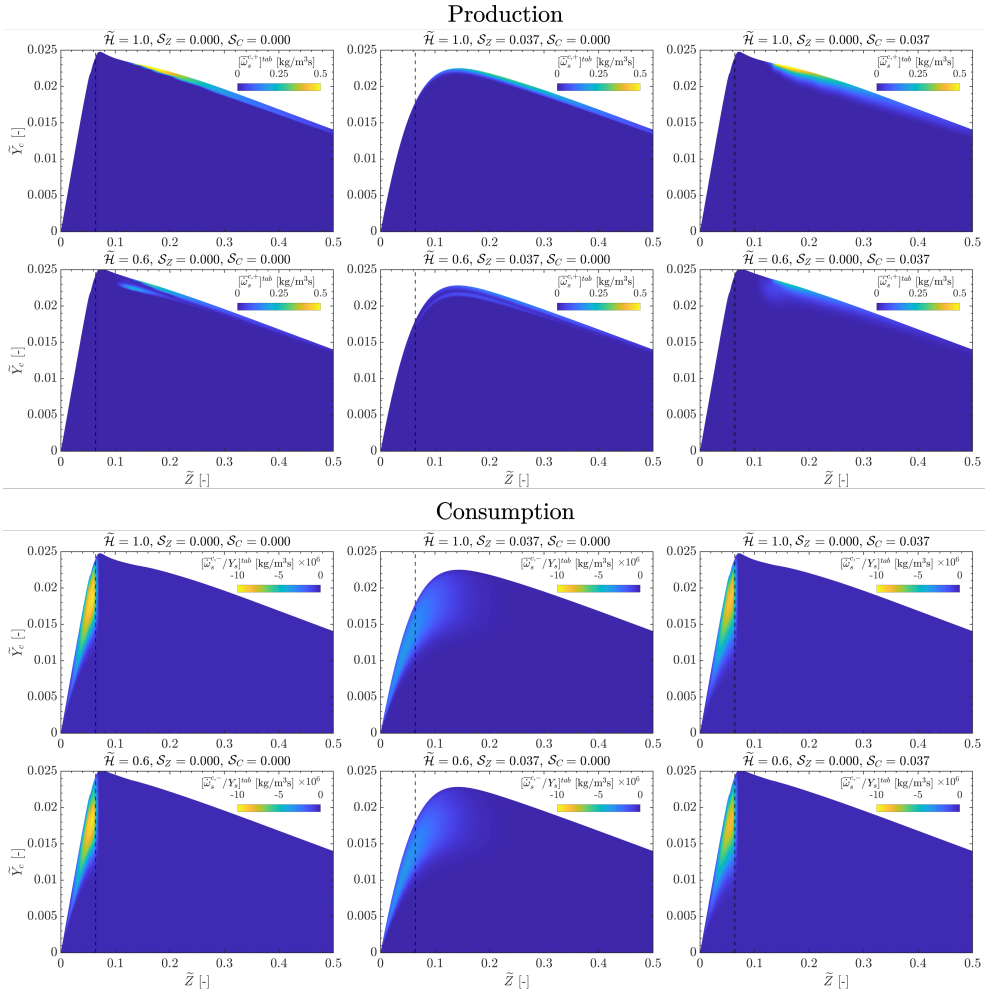

Figure 5.5: Effect of scaled enthalpy $\widetilde{\mathcal{H}}$, mixture fraction segregation factor $\mathcal{S}_Z$ and progress variable segregation factor $\mathcal{S}_C$ on the $\widetilde{Z} - \widetilde{Y}_c$ map of the tabulated production and consumption parts of the soot source term. Top: production term, bottom: consumption term. Dashed line: stoichiometric mixture fraction.

As expected, high soot production terms are found at rich mixtures and close to the maximum progress variable values, which corresponds to low strain rates, while the consumption part is important when approaching to stoichiometric and lean conditions. The influence of scaled enthalpy and mixture fraction and progress variable variances on the soot source term is analogous to that seen for the progress variable source term (Fig. 5.4). The most important effect is the decrease of the production and consumption peak values

when decreasing $\widetilde{\mathcal{H}}$ or increasing $\mathcal{S}_Z$ or $\mathcal{S}_C$. This effect is more clear for soot production but also present for consumption, specially the influence of the mixture fraction segregation factor. Therefore, a mitigation of soot formation and oxidation is expected in the regions where heat losses effects or sub-grid fluctuations are important.

5.1.3 Numerical setup

The computational domain considered for numerical simulations is based on the experimental test rig described in Section 5.1.1. It includes all the different components of the burner: inlet ducts for air and fuel supply, the dual swirler injection system, the combustion chamber and secondary oxidation air ducts, while the fuel injection is modelled as a single continuous nozzle ring with a minimum width of 0.4 mm. Furthermore, the domain includes a cubic volume of side 400 mm at the exit of the burner to reproduce the atmosphere. A representation of the computational domain is illustrated in Fig. 5.6.

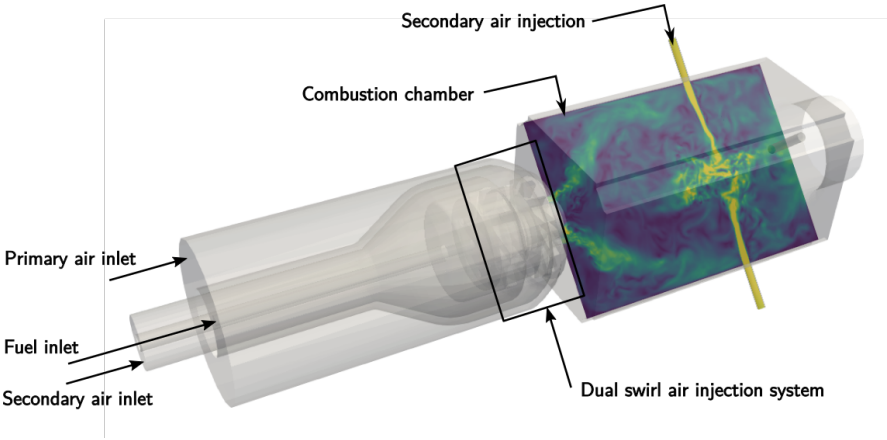

Figure 5.6: Computational domain

Similar meshes of 52M (Op 1) and 48M (Op 2) are used for this geometry with the difference in mesh size is given to the refinement region of the dilution jets. They are composed mainly of tetrahedrons and pyramids with layers of prisms applied in the air and fuel ducts in order to better resolve the boundary layer. Fig. B.1 shows the different meshes used for both Op 1 (left) and Op 2 (right). Information about the filter size $\Delta x = \sqrt[3]{V_{cell}}$ is also provided at the main regions of the combustor. A minimum filter size of 0.15 mm is considered for the refinement of the near mixing region inside the combustion chamber

and 0.025 mm within the fuel injector. In this application, the minimum element size is strongly conditioned by the narrow fuel duct and a very low size is required to properly resolve that region.

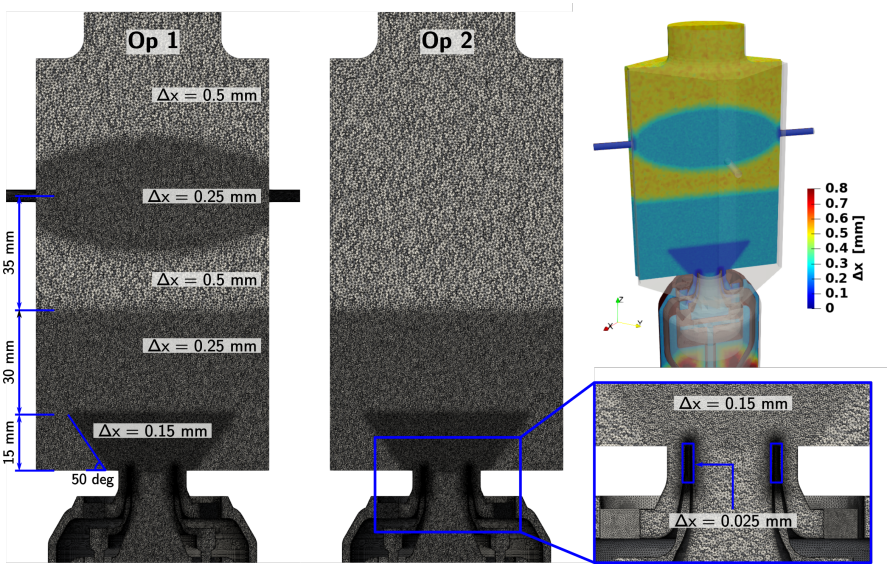

Figure 5.7: Details of the meshes employed for simulations of Op 1 (left) and Op 2 (center). The filter size Δx is specified for each region and represented on the contour of the top right figure.

Constant air and fuel mass flow rates at 300 K are prescribed as inlet conditions. Regarding wall boundary conditions, both non-slip adiabatic and isothermal walls are used. The combustion chamber wall temperature is specified according to the experimental measurements of the quartz windows [28].

In this work, time-averages for flow statistics are collected over approximately 5 flow-through times to allow for the soot to reach steady state. For further details, the effect of the temporal window in velocity, temperature and soot statistics is summarized in Appendix C.

5.2 Gas phase

The gaseous phase results of the DLR combustor are presented in this section. It is important to highlight that most of the results are presented for the reference case: Op 1 with the non-adiabatic modelling approach. However, this approach is compared with the adiabatic manifold for some magnitudes

and fields in order to evaluate the most relevant differences between both strategies. The cases are referenced in legends as Adiabatic and Non-adiabatic and differences in modelling are summarized in Table 5.4.

Case	CC wall boundary conditions	Flamelet database
Adiabatic	Adiabatic walls	Adiabatic manifold
Non-adiabatic	Isothermal walls	Non-adiabatic manifold

Table 5.4: Differences in the modelling approach between adiabatic and non-adiabatic DLR Op1 cases.

The section is structured as follows. First, a brief analysis of the grid quality is addressed by the use of the usual criteria. Subsequently, the structures of the flow field are described and the velocity field is presented and evaluated. Finally, the characteristics of the flame and reacting flow are discussed, including the assessment of the temperature and OH mass fraction field and the analysis of the combustion regime.

5.2.1 Grid quality

In order to evaluate the quality of the reference grid employed, the usual LES quality criteria are applied in this subsection. The analysis is performed for Op 1 of the DLR burner, therefore, the mesh considered is the one previously illustrated in Fig. B.1 left, which was already described in Section 5.1.3.

First, Pope's criterion is applied following the same procedure outlined in Section 4.1.3. The resolved and total turbulent kinetic energy are computed using the approximation of Yoshizawa [29] for the sub-grid scale part. Fig. 5.8 shows the ratio between resolved and total turbulent kinetic energy k_{res}/k in a vertical cut plane of the combustion chamber and at different stations. As illustrated, k_{res}/k satisfies Pope's criterion ($k_{res}/k > 0.8$) in almost the entire combustion chamber and even values very close to unity are reached, indicating that the turbulent kinetic energy is almost completely resolved. Note that the lowest values are reached in the shear layers very close to the injector (5 mm station and $x \sim \pm 10$ mm), where $k_{res}/k \sim 0.9$ is obtained.

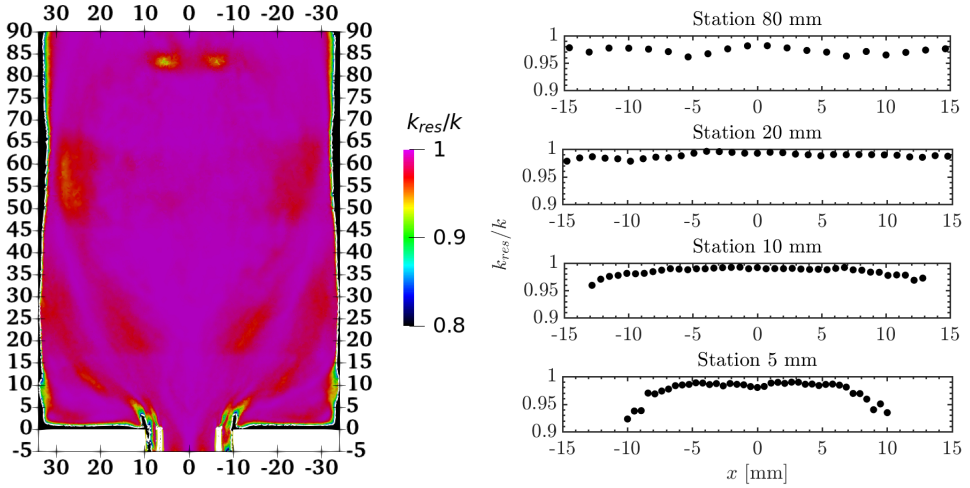

Figure 5.8: Ratio between resolved turbulent kinetic energy k_{res} and total turbulent kinetic energy k. Left: contour in a vertical cut plane of the DLR combustion chamber. White line: $k_{res}/k = 0.8$. Spatial units in mm. Right: turbulent kinetic energy ratio at different stations.

The grid quality is further assessed with the comparison between the filter size and the estimated Kolmogorov scales and with the illustration of the turbulence Reynolds number presented in Fig. 5.9. The turbulent scales have been estimated following the methodology proposed by Both [30] using temporal data at different monitoring points. Close to the injection plane (station 5 mm), the high turbulence intensity due to the swirling flow and evidenced from the high values of Re_t leads to small Kolmogorov scales. In this region, $\Delta x \sim 4\eta$ close to the burner axis and $\Delta x \sim 12\eta$ is reached near the shear layers. The intensity of turbulence vanishes downstream (10 mm), leading to larger Kolmogorov scales and lower $\Delta x/\eta$ ratios. Note that stations 5 and 10 mm corresponds to the first refined region where $\Delta x = 0.15$ mm (see Fig. B.1). Turbulence is even lower at $z = 20$ mm and the filter size is comparable to the Kolmogorov scale across the width of the combustion chamber. The presence of the secondary injection air at 80 mm evidences a new high-turbulence region characterized by a high Reynolds number. In this case, the $\Delta x/\eta$ ratio increases again, but the filter size is comparable, at most, $\sim$10 times the Kolmogorov scale.

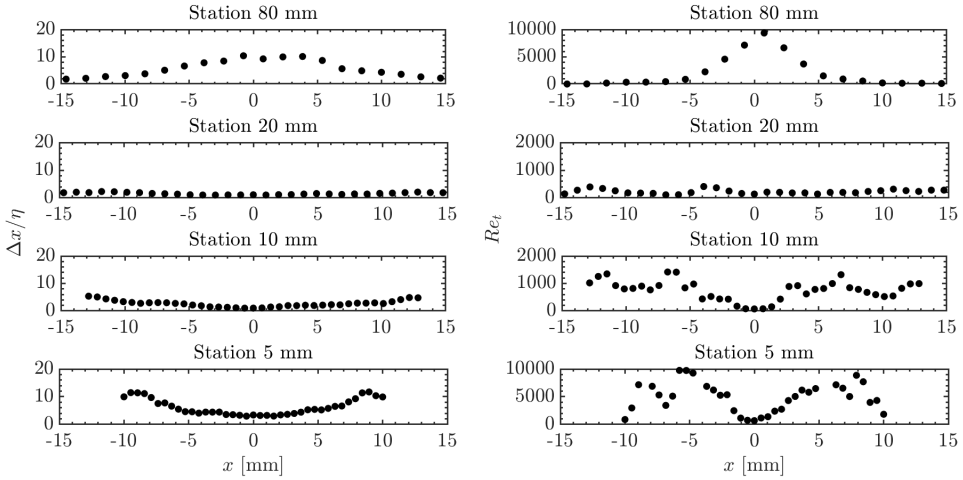

Figure 5.9: Turbulent scales at different stations inside the DLR burner. Left: filter size compared to the Kolmogorov scale $\Delta x/\eta$. Right: Reynolds number based on the turbulence integral scales Re_t.

In view of the these results, an excellent LES resolution is achieved with the reference mesh in the full length and width of the combustion chamber. In fact, a coarser mesh is likely to be sufficient in terms of flow resolution. However, the present mesh is retained in order to correctly solve combustion and soot. Additional results using different grid refinements are included in Appendix B to complement the analysis presented in this section.

5.2.2 Flow field description

Several velocity contours at different cut planes of the combustion chamber are presented in Fig. 5.10 to show a qualitative description of the flow field and turbulent structures. On the left, the instantaneous axial velocity is presented in a vertical cut plane and different axial stations are represented in order to illustrate the location for the comparison with the experimental data. The mean axial velocity field is shown at center with the locations of the main recirculation regions and arrows illustrating the flow motion. On the right, some cross cut planes at different axial positions are presented to observe the swirl motion. At each figure, zero-axial velocity isoline is represented with the white isoline to identify the recirculation regions. In general, the current LES is able to capture the characteristics of the swirling flow in this configuration. A corner recirculation region (CRZ) is located at the outer bottom part of the combustion chamber, close to the air and fuel injection. In

addition, an inner recirculation zone (IRZ) is formed at the central part of the combustor, where axial velocity reaches its maximum negative value. Due to the presence of the secondary oxidation jets, the axial velocity field is strongly affected downstream, at 80 mm in the axial direction, approximately. Part of this secondary air is recirculated, affecting the local mixture field in the combustion region, and contributing to soot oxidation, as will be discussed later. In view of the cross cut planes, the strongest swirl motion is evidenced at the first stations, which are closer to the combustion chamber entry and the swirl injection system. Swirl motion vanishes downstream and its intensity is considerably reduced at $z = 45$ mm. Further downstream, at 80 mm in the axial direction, the cross flow is completely influenced by the presence of the secondary jets, which greatly disrupt the main flow pattern.

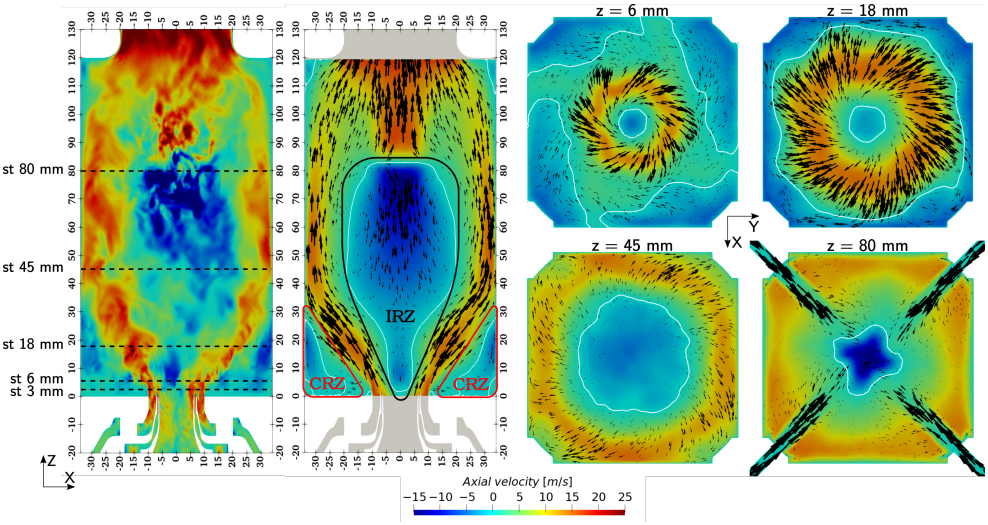

Figure 5.10: From left to right: instantaneous axial velocity contour in the XZ mid plane, time-averaged axial velocity contour in the XZ mid plane, time-averaged axial velocity contour in XY planes along the burner axis. White line: zero axial velocity isoline. Arrows: velocity magnitude. Spatial units in mm.

The instantaneous flow structures can be derived from Fig. 5.11, where instantaneous iso-surfaces of the $\mathcal{Q}$-criterion colored by the instantaneous velocity magnitude are illustrated. The $\mathcal{Q}$-criterion [31] is defined as:

$$\mathcal{Q} = \frac{1}{2}\left(\|\mathbf{\Omega}\|^2 - \|\mathbf{S}\|^2\right) \tag{5.9}$$

It defines an eddy structure as the region where the vorticity ($\mathbf{\Omega}$) magnitude is higher than the strain rate ($\mathbf{S}$) magnitude. Two regions with this small structures are clearly identified in Fig. 5.11. The first one is located at the outlet of the swirl injection system, where high intensity of turbulence is evidenced due to the development of strong shear layers generated by the high velocity swirling flow. Therefore, well-organized vortical structures are formed along this conical shape and disappear in the CRZ and slightly downstream the combustor. However, the small turbulent structures are present again at the axial position of the secondary air injection, due to the interaction and disturbance of the flow coming from the dilution jets.

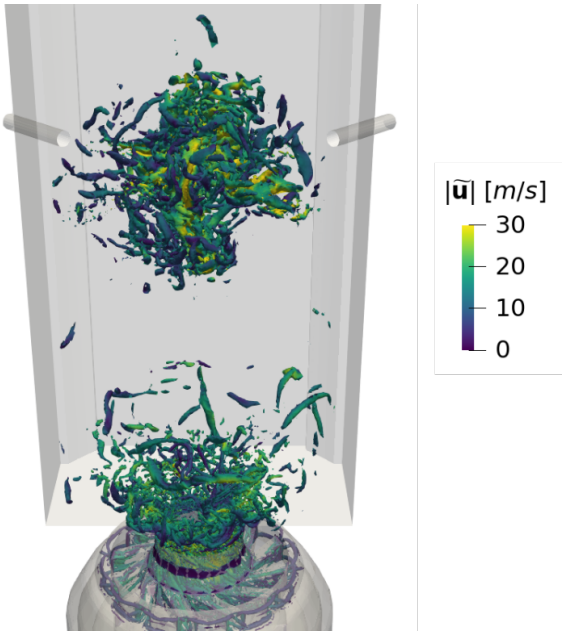

Figure 5.11: Instantaneous $\mathcal{Q}$-criterion iso-surfaces ($\mathcal{Q} = 100000$). Colors: instantaneous velocity magnitude.

In order to quantitatively evaluate the predictions of the velocity field, Fig. 5.12 shows the comparison between the numerical results and experimental data for the time-averaged velocity components and Root Mean Square (RMS) of the fluctuations at the centerline and at different axial stations inside the combustion chamber (see Fig. 5.10 left). At the centerline, two datasets are included concerning the treatment of experimental measurements from PIV: Field of View (FoV) and Sum of Correlation (SoC) data [18]. The recirculation pattern described previously is clearly observed along the burner

axis (see Fig. 5.12a), where axial velocity remains negative until the secondary jets axial position (80 mm). In addition, the widening of swirled jets is properly captured by LES, as it is observed from the axial component at stations presented in Fig. 5.12c. Radial and tangential velocity components are also illustrated in Fig. 5.12e and 5.12g. As for axial velocity, some discrepancies appear at radial positions over ∼10 mm the injector, but the differences vanish downstream. In terms of velocity fluctuations, RMS is also properly captured both at the centerline and at the stations and only small discrepancies are found near the injection plane and close to the location of the dilution air. The overall agreement with the experimental measurements is satisfactory and the velocity field is accurately reproduced by numerical simulations.

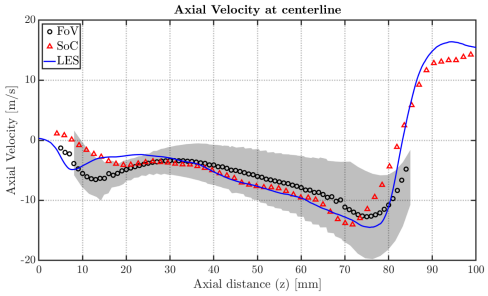

(a) Mean axial velocity at centerline.

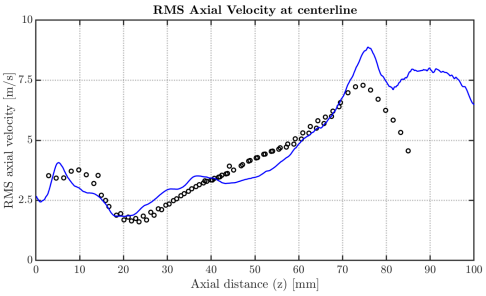

(b) RMS axial velocity at centerline.

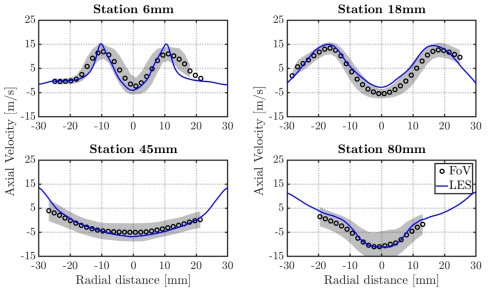

(c) Mean axial velocity at stations.

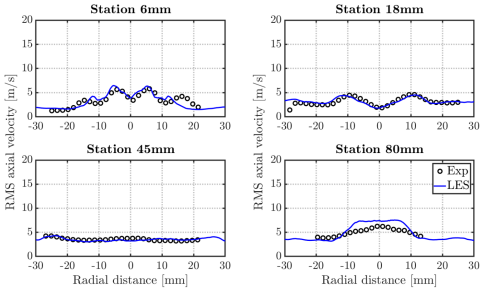

(d) RMS axial velocity at stations.

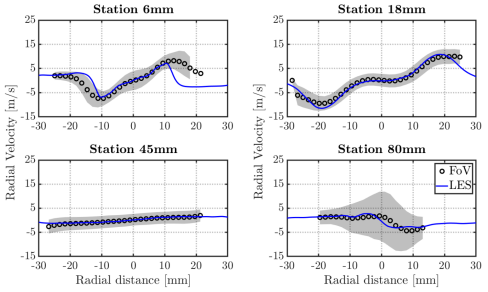

(e) Mean radial velocity at stations.

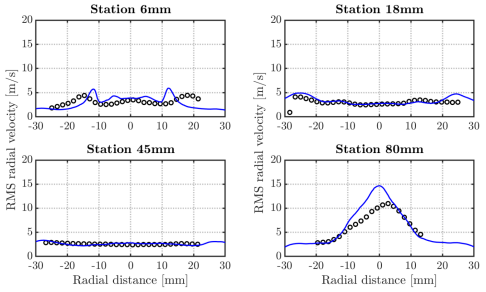

(f) RMS radial velocity at stations.

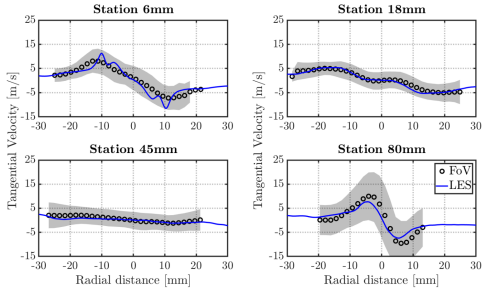

(g) Mean tangential velocity at stations.

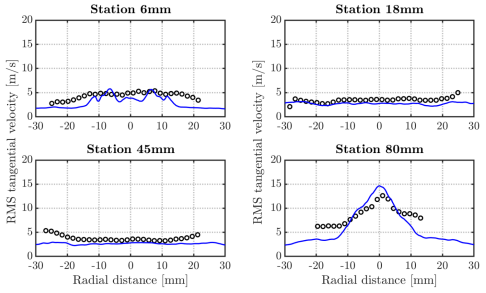

(h) RMS tangential velocity at stations.

Figure 5.12: Comparison between LES results (non-adiabatic case) and experiments of velocity field. Shaded area: RMS velocity fluctuation from experiments.

5.2.3 Flame characteristics

The behaviour of the reacting flow and flame characteristics is studied here. Fig. 5.13 shows several instantaneous contours of representative magnitudes and chemical species in order to illustrate the features of the combustion process in this configuration. The top left and top center figures correspond to the local equivalence ratio and progress variable contours, and represent the two main control variables of the modelling approach (note that the equivalence ratio is illustrated instead of mixture fraction). The local equivalence ratio provide information about the mixing process inside the combustion chamber. Fuel and air are injected through the intermediate narrow ring and the central and outer nozzles, respectively, and they are mixed rapidly. However, the equivalence ratio range is considerably wide even to locations further downstream. Note that variations between $\phi = 0$ and $\phi \sim 3$ are observed even at axial positions corresponding to $z = 25$ mm. In addition, the mixing field in this configuration is characterized by the formation of two rich branches, which evolve following the shear layers and surround the central lean region generated by the dilution air. Progress variable and temperature contours suggest the region where combustion is taking place. The main combustion zone is comprised between $z \sim 10$ mm and $z \sim 25$ mm. In this region, temperature reaches its maximum value close to the stoichiometric condition (white line) and the slightly rich branches, while it is decreased when approaching to both recirculation regions IRZ and CRZ. Due to the swirl motion, the interaction with the IRZ intensified by the secondary jets and the intermittency of the mixing field, the lower limit of this region is characterized by strong fluctuations of temperature and the other magnitudes. Further downstream, the reaction zone progresses close to the combustion chamber walls and the central region of the burner experiments a strong decrease of temperature due to the cold air coming from the dilution jets. On the bottom part, mass fractions of some chemical species are illustrated at the same temporal instant. The contour of OH mass fraction simply supports the previous description of the combustion process, illustrating the peak of this radical in the areas close to the stoichiometric mixture fraction, where is located the reaction zone. Moreover, mass fractions of soot precursors (pyrene and acetylene) are shown in order to have an idea of where soot is expected to be obtained. As it is derived from the mixing field, the location with highest precursor concentrations (both A4 and C_2H_2) corresponds to the rich pockets formed along the branches mentioned above. A more detailed analysis of the presence of these species and soot formation will be addressed in the next sections.

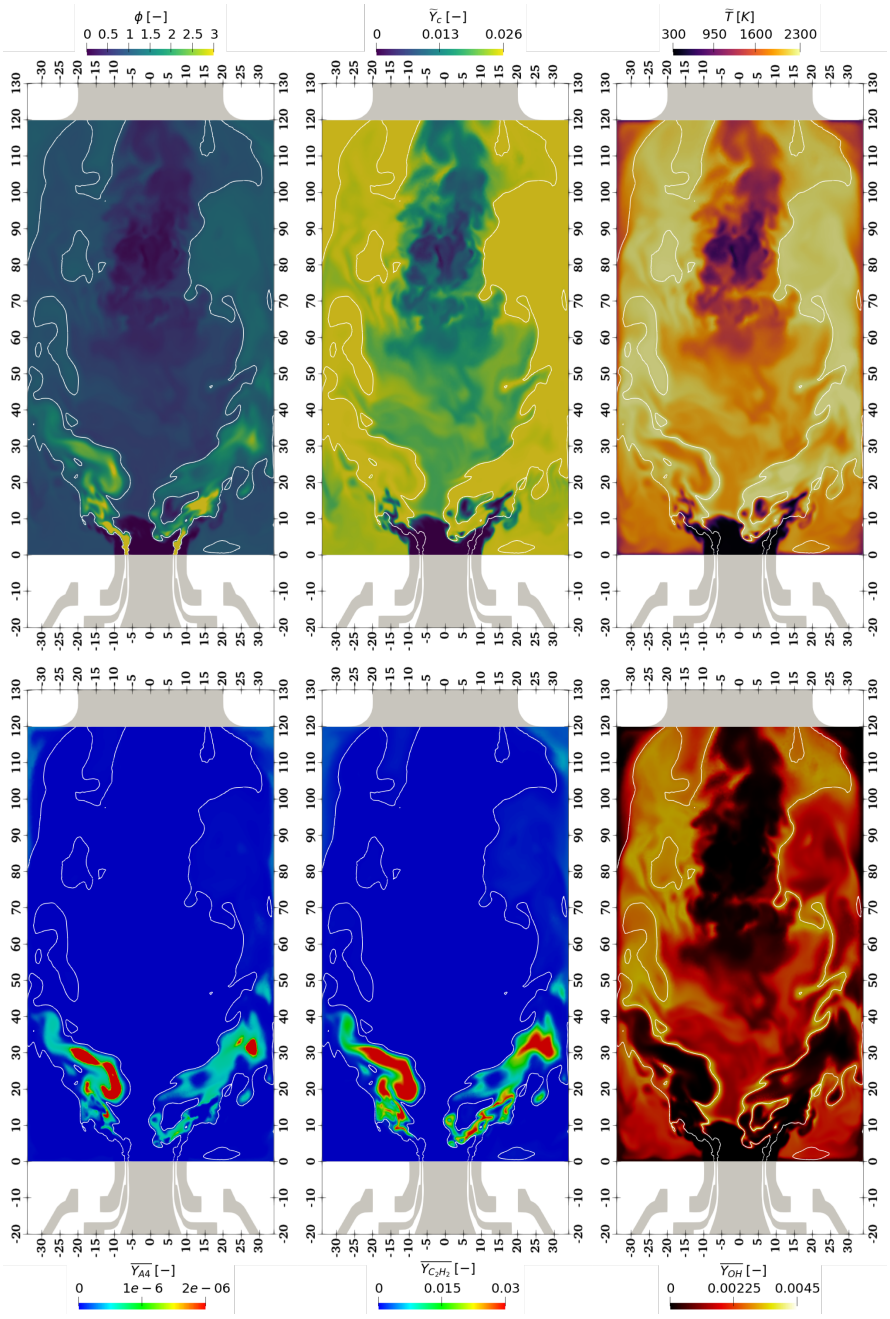

Figure 5.13: Instantaneous fields of various representative magnitudes of the reacting flow in the DLR burner. Top (from left to right): local equivalence ratio, progress variable and temperature. Bottom (from left to right): mass fractions of pyrene (A4), acetylene (C_2H_2) and hydroxyl radical (OH). White line represent the stoichiometric mixture fraction iso-line.

Before the assessment of temperature field, it is worth to compare and evaluate the effect of using an adiabatic or non-adiabatic modelling approach. Fig. 5.14 shows the instantaneous temperature contours for both adiabatic and non-adiabatic numerical results in order to check the effect of including heat losses. In addition, the instantaneous scaled enthalpy contour is presented on the right side to identify the regions more affected by this effect. As observed, the temperature magnitude is quite similar between both approaches in most of the rich region enclosed by the stoichiometric mixture fraction isoline (white) and also in the IRZ. However, the effect of heat losses is particularly noticeable near the combustion chamber walls and in the CRZ. Inside this region, the residence time is higher and the effect of the non-adiabatic walls is more relevant, and lower temperatures are predicted. Note that, in these regions, $\mathcal{H}$ reduces its value significantly and even reaches near-zero values (maximum heat losses) very close to the combustor walls.

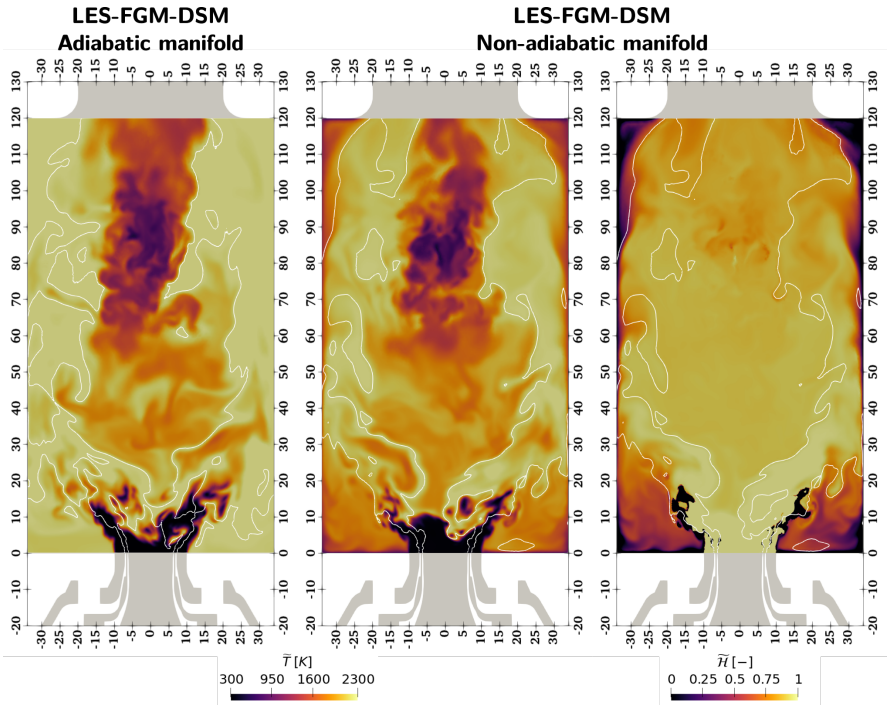

Figure 5.14: Non-adiabatic effects on temperature field. Instantaneous temperature contours of the adiabatic case (left) and non-adiabatic case (center). Instantaneous contour of scaled enthalpy using the non-adiabatic approach.

As for the velocity field, the comparison between LES and experimental data is presented in Fig. 5.15 at different axial stations and centerline. In view

of the results of mean and RMS temperature, a good prediction of the reacting flow is achieved. The strong temperature gradients mentioned before from the instantaneous contours can be observed also here. These temperature variations are located close to the shear layers that separate both recirculation regions. Furthermore, the simulations properly capture the decrease of temperature in the central region due to the cold secondary flow. At further radial positions, which are affected by the CRZ, the agreement with the experimental data is remarkably better when considering the non-adiabatic approach in terms of both mean and RMS temperature. In this region (see 3 mm station), the adiabatic case greatly overpredicts the temperature value when approaching to the combustion chamber walls while the mean and RMS temperature profiles are reliably captured by the non-adiabatic approach. The highest discrepancies are found for temperature RMS at the first axial positions close to the burner axis, where a clear overpredicion is observed. The base of the flame is located there and LES predicts very high temperature fluctuations at this position. Despite of that, the overall agreement in temperature field is satisfactory and the proposed modelling approach based on non-adiabatic counterflow diffusion flamelets seems adequate for this configuration. Notice that this configuration is more consistent with the flow conditions in the burner, where enthalpy is affected by heat loss, and the manifold is able to account for this effect on the reaction rates (see Fig. 5.4).

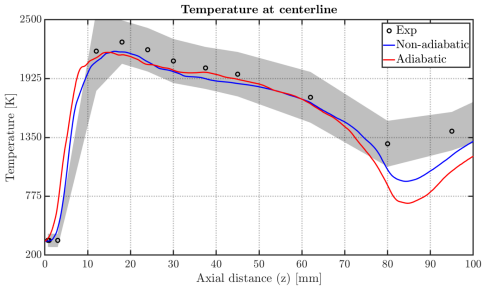

(a) Mean temperature at centerline.

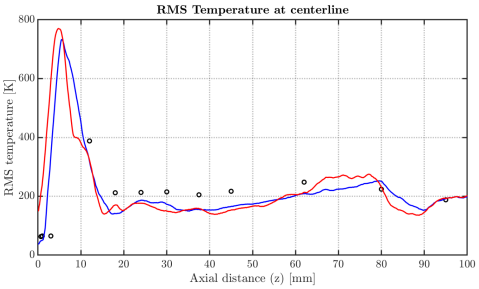

(b) RMS temperature at centerline.

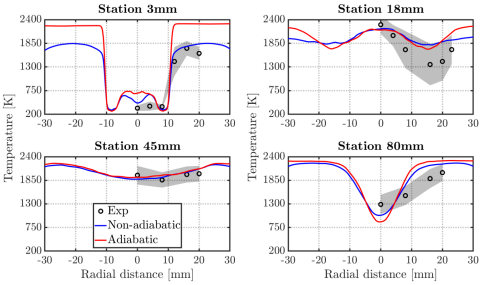

(c) Mean temperature at stations.

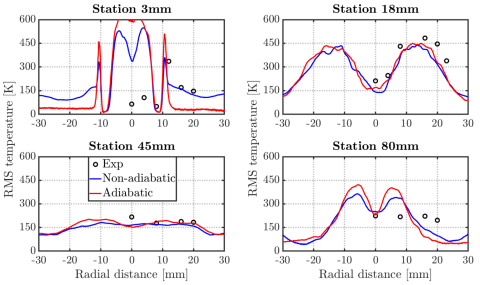

(d) RMS temperature at stations.

Figure 5.15: Comparison between LES results (adiabatic and non-adiabatic) and experiments of temperature field. Shaded area: RMS of the measured temperature.

Fig. 5.16 shows the comparison between the numerical results and the experimental measurements in terms of the hydroxyl radical (OH) mass fraction. Both numerical results considering the adiabatic and non-adiabatic approaches are included. In addition, the instantaneous (top) and time-averaged (bottom) fields are presented. In general, the OH mass fraction distribution and the location of the reaction zone is correctly reproduced by LES. The instantaneous contour evidences the complexity and wrinkling of the reaction front due to the turbulent structures of the swirled flow and the strong fluctuations of the mixing field. On the other hand, a satisfactory qualitative agreement of the mean field is also obtained. It is observed a noticeable improvement when considering heat losses, specially in the CRZ. The adiabatic approach clearly overpredicts the OH mass fraction in this region. The CRZ is characterized by slightly lean conditions and low fluctuations, therefore, the OH mass fraction peak is obtained there if the adiabatic approach is considered. When including heat losses, the CRZ is greatly affected by low enthalpy levels (see Fig. 5.14) and presents a lower reactivity and OH mass fraction magnitude, which is consistent with experiments.

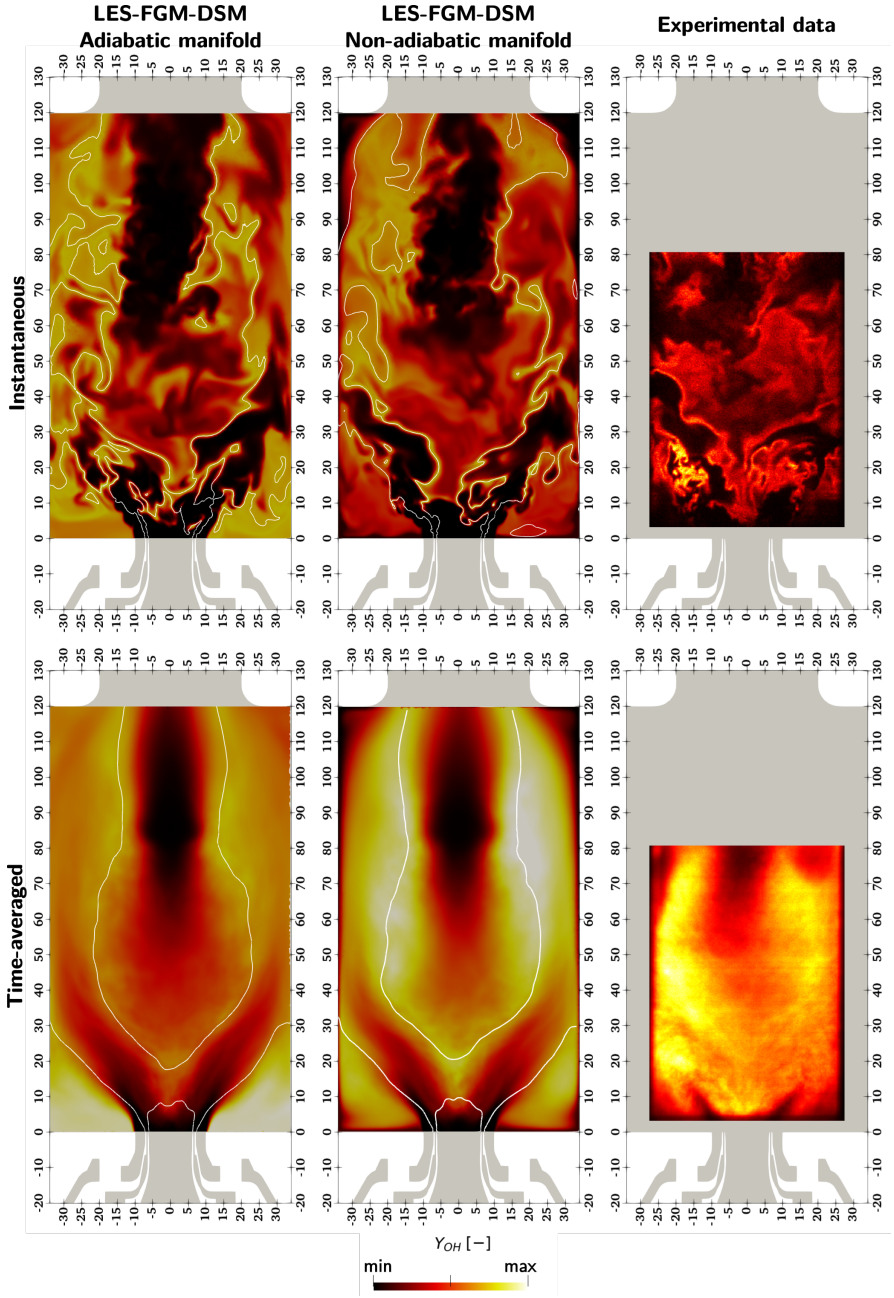

Figure 5.16: Comparison of OH mass fraction between both numerical approaches (adiabatic and non-adiabatic manifolds) and the experimental data. Top: instantaneous OH mass fraction field. Bottom: time-averaged OH mass fraction field. White line: stoichiometric mixture fraction iso-line.

In order to characterize the turbulence/chemistry interactions in the DLR combustor, Fig.5.17 shows the non-dimensional regime diagram for turbulent diffusion flames [32] introduced in Chapter 2. Turbulence scales are extracted at several locations inside the combustion chamber and the turbulent Damköhler Da_t and Reynolds Re_t numbers are computed using the chemical scales presented in Table 5.2. In particular, the Damköhler number is calculated considering the chemical time scale $\tau_c^{ext,\chi} = 0.012$ ms. In addition, the points identified in the diagram are colored by the time-averaged temperature. In this case, chemistry is very fast compared to the characteristic time scale of turbulence, thus, all points are located within the flamelet regime. Even the points located at low temperature regions have a minimum Damköhler number associated to the Kolmogorov scale Da_η of ~ 4.3 so the combustion process is not disturbed by the smallest turbulence scales. Therefore, assuming the flame front structure as a composition of one-dimensional laminar flames seems reasonable and the tabulated flamelet-based modelling approach used is adequate for turbulence combustion modelling in this application.

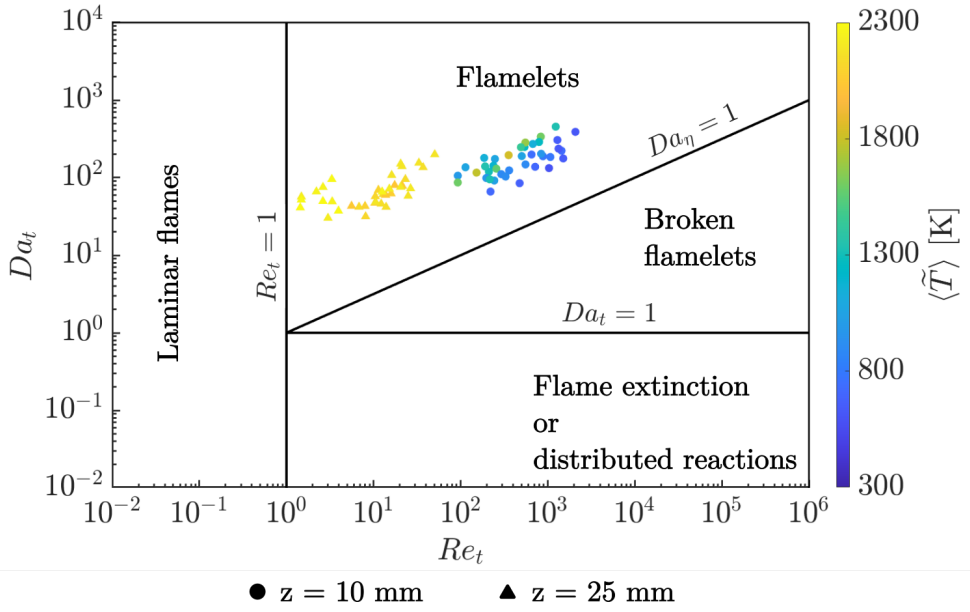

Figure 5.17: Diagram of turbulent non-premixed combustion [32] in the DLR combustor (Op 1). Points located along the combustion chamber width at the specified axial positions z. Color: time-averaged temperature.

Finally, it is worth to evaluate the level of premixing in the DLR combustor by means of an analysis of the local instantaneous flame structure and the

identification of the combustion regimes. In this regard, the flame index (FI) concept was first introduced by Yamashita et al. [33] to identify the combustion modes on the basis of the diffusion fluxes in one-dimensional premixed and diffusion flames. Over the recent years, various definitions derived from the original flame index formulation have been proposed and successfully employed in different combustion problems [34–37]. However, this definition has shown certain limitations in various applications [38, 39], when detailed chemistry effects are taken into account or when tabulated combustion models are used and no information on the reactants is available [40]. Consequently, new flame index formulations are recently proposed to identify combustion regimes under particular conditions or when using specific combustion modelling approaches [40, 41]. In this work, the flame index proposed in [40] is used to identify the combustion regimes in the DLR burner. It is an adequate flame index for combustion models based on flamelet databases, since it is defined by the gradients of mixture fraction and progress variable, which are commonly used for the parametrization of flamelet manifolds. The flame index GI_Z is defined by:

$$GI_Z = \left. \frac{\nabla \widetilde{Z} \nabla \widetilde{Y_c}}{|\nabla \widetilde{Z}||\widetilde{Y_c}|} \right|_{\overline{\dot{\omega}_{Y_c}}>1} \tag{5.10}$$

A conditioning threshold of $\overline{\dot{\omega}_{Y_c}} > 1$ kg/m^{3}s is considered to analyze only the reaction zone, which corresponds to $\sim 1\%$ of $\overline{\dot{\omega}_{Y_c}}_{max}$. According to this definition, $GI_Z = \pm 1$ is obtained in a diffusion combustion mode, where mixture fraction and progress variable gradients are aligned. On the contrary, perpendicular gradients lead to $GI_Z = 0$, which defines the premixed combustion mode. Following the proposal of [40], the discrete volume-weighted flame index is also evaluated in this study in order to estimate the volumetric contribution of the different combustion regimes when the mesh is composed of tetrahedral elements with variations in the cell size. It read as:

$$\zeta_Z = \frac{\sum V_{cell}|_{\overline{\dot{\omega}_{Y_c}}>1, GI_Z}}{\sum V_{cell}|_{\overline{\dot{\omega}_{Y_c}}>1}} \tag{5.11}$$

The instantaneous flame index in the DLR burner is presented in Fig. 5.18. On the left side, the instantaneous contour of GI_Z is illustrated for the entire combustion chamber. A black background is used for the regions outside of

the $\overline{\dot{\omega}_{Y_c}}$ threshold so GI_Z is only computed in the colored area (from blue to magenta). Note that in this case the absolute value of GI_Z is presented (just for clarity in the color scale) so the diffusion combustion mode is defined by abs(GI_Z) = 1 while $GI_Z = 0$ determines the premixed regime. As observed, the instantaneous reacting region is mainly characterized by the diffusion regime. GI_Z takes values very close to 1 in most of the locations of the primary combustion region and further downstream, where excess fuel continues to burn due to the additional dilution air. Only a few small regions of $GI_Z < 1$ are present in the main reaction zone indicating conditions of partially premixed combustion. The volume-weighted flame index is shown on the right side using the instantaneous data of the full combustion chamber (not only the cut plane illustrated on the left contour). Approximately 70% of the reaction zone is characterized by the alignment of mixture fraction and progress variable gradients and, therefore, by the diffusion combustion mode. The remaining ∼30% is distributed between $-1 < GI_Z < 1$ suggesting a partially premixed combustion regime. In view of these results, it is possible to conclude that the combustion process in the DLR burner is mainly controlled by the non-premixed mode and the proposed modelling approach based on diffusion flamelets is thus expected to properly describe the flame structure. Nevertheless, minor premixed zones are found in the main combustion region near the injection system and it would be interesting to evaluate the influence of including premixing effects in the flamelet manifold.

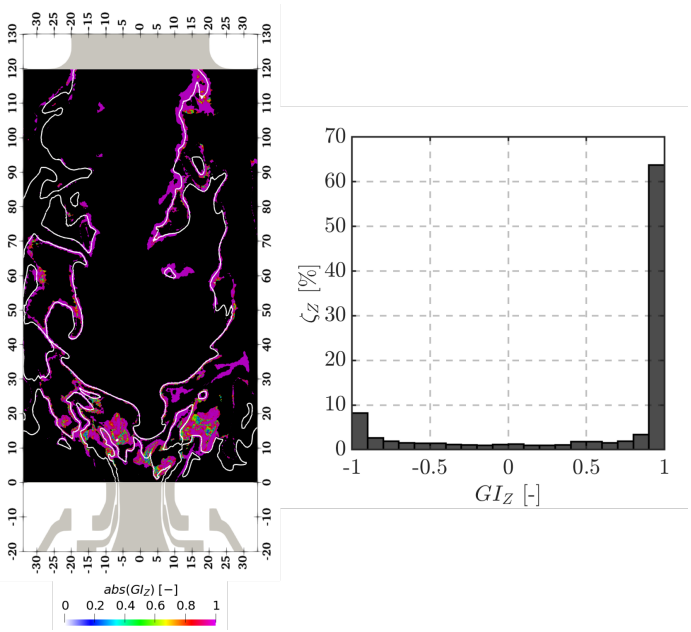

Figure 5.18: Flame index in the DLR combustor. Left: contour of the absolute value of flame index GI_Z conditioned to the progress variable source term. White line: stoichiometric mixture fraction iso-line. Right: discrete volume-weighted flame index ζ_Z conditioned to the progress variable source term.

5.3 Soot predictions

The results presented in the previous section evidence a good reproduction of the reacting flow in the DLR burner and demonstrate that the current modelling approach is sufficiently valid for this application. Therefore, this section is focused on the capabilities of the LES-FGM-CDSM to predict soot formation and oxidation are discussed. It contains the results for soot predictions obtained using the FGM-DSM modelling approach for the DLR burner configuration with secondary oxidation air (Op 1). If not mentioned, the presented results correspond to the non-adiabatic modelling approach, however, the comparison between both approaches will be presented for some magnitudes to evaluate the effect of heat losses on soot formation.

The section is structured as follows. First, the assessment of Soot Volume Fraction (SVF) predictions using LII data from experiments is presented. Then, the soot formation and oxidation processes are analyzed. Finally, Particle Size Distribution (PSD) functions retrieved from the sectional method for soot are discussed.

5.3.1 Soot Volume Fraction assessment

A qualitative comparison of time-averaged SVF fields can be observed in Fig. 5.19, in which the results with and without heat losses are included. For both cases, the spatial localization of soot is correctly predicted, although the onset of soot is located upstream of the experimental data for the adiabatic case, and accuracy is improved when accounting for heat losses. In addition, the lean central region caused by the dilution air is slightly wider in LES using both approaches. As observed, soot is primarily present in the rich branches between the IRZ and the CRZ, and persists downstream in the combustor outer region while it is oxidized in the lean IRZ region due to secondary air injection.

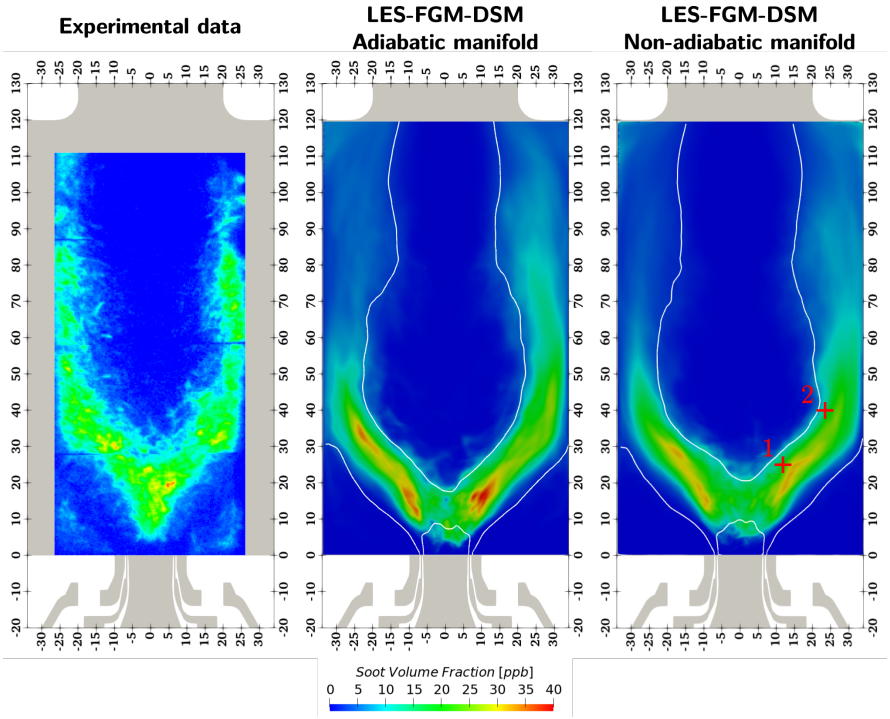

Figure 5.19: Comparison of time-averaged Soot Volume Fraction (SVF) contours (Op 1). White line: stoichiometric mixture fraction. Markers: points for time-averaged PSD computation (5.27). Spatial units in mm.

In order to have a more quantitative evaluation of soot magnitude, SVF profiles at different radial stations are illustrated in Fig. 5.20. Both modelling approaches show a considerably good prediction of SVF magnitude. Nevertheless, the adiabatic case presents a slightly higher overall soot level and an

overestimation of the SVF peak. Taking into account that the soot main location (approximately between $-20 < x < 20$ mm and $10 < z < 25$ mm) is not much affected by the enthalpy loss, a strong variation on the soot field is not expected. In fact, the heat loss effect on SVF is more noticeable where CRZ affects flame temperature and thus precursors and soot chemistry, as shown in SVF profiles at $z = 18$ mm. The impact is limited downstream, where soot regions are subjected to low enthalpy losses. For reference, the regions more affected by heat loss effects may be derived from the temperature field in Fig. 5.14. Furthermore, the decrease on the peak value obtained when including wall heat losses is consistent with the conclusions of previous modelling works in this regard [12, 42, 43]. As previously illustrated in Fig. 5.5, heat losses reduce the magnitude of tabulated soot source terms and thus a decreased soot quantity is expected when this effect is more relevant.

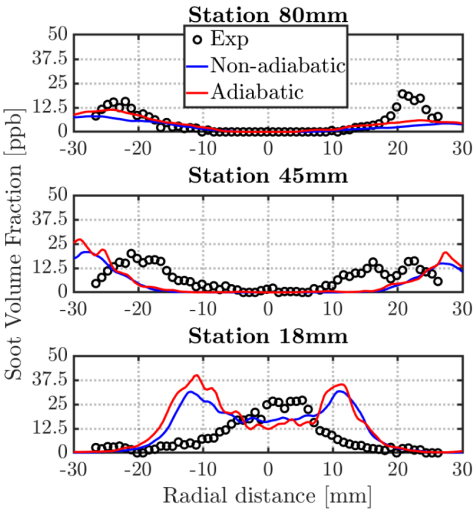

Figure 5.20: Comparison between LES results (adiabatic and non-adiabatic) and experiments (Op 1). Soot Volume Fraction (SVF) at different radial stations.

5.3.2 Analysis of soot formation and oxidation

A detailed analysis of the main mechanisms involved in soot formation and oxidation processes inside the combustor is addressed to evaluate the prediction capabilities of the proposed modelling approach. The results presented in this subsection correspond to the case with secondary air injection using the non-adiabatic manifold, which is taken as a reference. Fig. 5.21 shows scattered plots of mixture fraction ($\widetilde{Z}$) and temperature ($\widetilde{T}$), colored by SVF

(left) and the total soot source term $\overline{\dot{\omega}}_s^c$ (center). Note that the total soot source term corresponds to the sum of the source terms for clustered sections, according to Eq. 5.8, $\overline{\dot{\omega}}_s^c = \sum_{j=1}^{n_c} \overline{\dot{\omega}}_{s,j}^c$. Additionally, solid colored lines are overlapped on the plots representing different regions of the burner (R1 the near nozzle mixing layer region; R2 the rich outer branches; R3 the IRZ), which are depicted in Fig. 5.21 (right). The scattered data is obtained from the instantaneous results in five different time instants including points inside the full combustion chamber with normalized enthalpy higher than 0.5 ($\tilde{\mathcal{H}} > 0.5$) to avoid locations very close to the combustion chamber walls. Solid lines enclose the cloud of points associated with each region and they are conditioned to high scaled progress variable values ($\widetilde{C} > 0.8$), in order to avoid non-representative conditions for the soot analysis. As previously described in the SVF comparison, the highest soot quantity is mainly found in the mixture fraction rich side ($0.1 < \widetilde{Z} < 0.2$) and high temperature ($\widetilde{T} > 1500K$). This location is mainly covered by R1 and to a lesser extent by R2, where the reactivity and rich mixture lead to high temperature and soot precursors concentrations. In view of the center plot of Fig. 5.21, this $\widetilde{Z}$ range corresponds to the highest positive source terms values and, thus, the main soot production region. When $\widetilde{Z}$ approaches the stoichiometric condition (values below 0.1), $\overline{\dot{\omega}}_s^c$ reaches highly negative values and soot consumption eventually becomes predominant. Furthermore, contour lines make it possible to distinguish different states in each of the analyzed regions of the burner. R1 clearly evidences a wider range of thermochemical states from lean and low-temperature conditions due to the proximity to the injection system and the CRZ, to high-temperature rich regions characterized by soot production. R2 is more enclosed in high-temperature zones and a limited range of mixture fraction, where both soot production and consumption are present. Finally, R3, primarily corresponding to the IRZ, is extended to the lower temperature and lean conditions (and strong soot consumption) due to the secondary oxidation air.

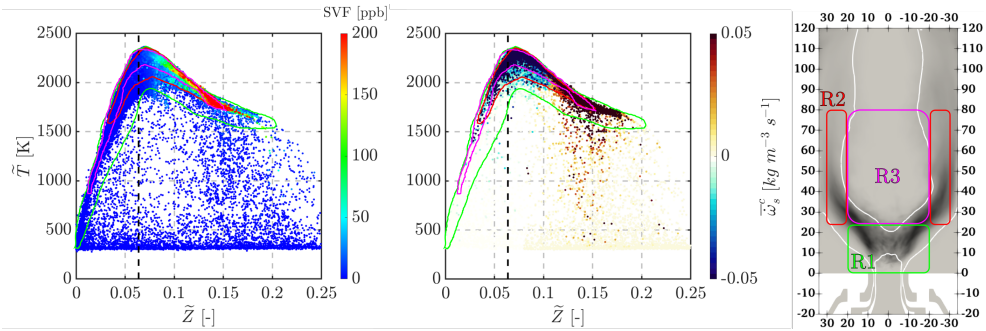

Figure 5.21: Scattered plots of mixture fraction ($\widetilde{Z}$) and temperature ($\widetilde{T}$) with solid lines representing different regions of the burner. Left: scatter data colored by SVF. Center: scatter data colored by total soot source term ($\overline{\dot{\omega}}_s^c$). Right: schematic of the analyzed regions (color: time-averaged SVF).

The soot formation processes and variety of thermochemical conditions in each region may be further analyzed by means of Fig. 5.22. In this figure, scattered plots of the main control variables ($\widetilde{Z}$ and $\widetilde{Y_c}$) colored by the joint-PDF of $\widetilde{Z}$-$\widetilde{Y_c}$ are illustrated for each region. A black contour line is also included, representing the boundary line that encloses the cloud of points with a significant soot production rate ($\overline{\dot{\omega}}_s^c > 0.05$ kg/m^{3}s), in order to identify the presence in the soot formation area. Note that in this case the data is not conditioned to the scaled progress variable $\widetilde{C}$.

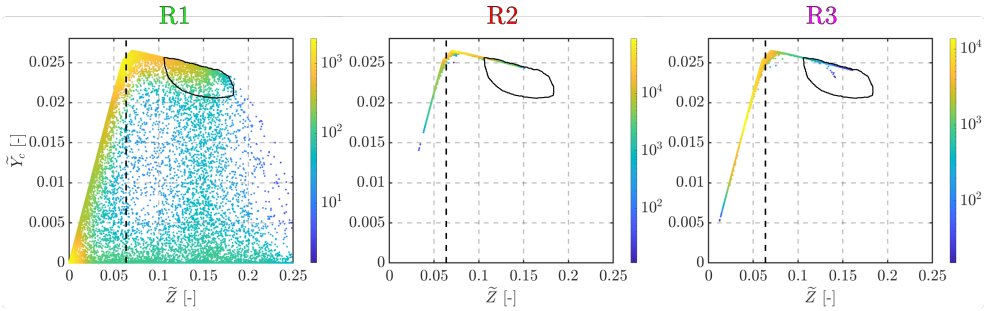

Figure 5.22: Scattered plots of mixture fraction and progress variable from instantaneous LES results. Colors: joint-PDF of $\widetilde{Z}$-$\widetilde{Y_c}$. Black line: isoline of $\overline{\dot{\omega}}_s^c = 0.05$ kg/m^{3}s.

A strong fluctuation in R1, especially in terms of $\widetilde{Y_c}$, compared to the other regions is evidenced due to the multiple states present in this zone. Despite the most probable states being lean inert and slightly rich reacting conditions, a high probability of soot formation conditions is also observed for R1. On

the other hand, R2 presents the highest probability in regions between soot formation and oxidation, consequently, soot is not completely oxidized and is transported and remains downstream. Finally, R3 is mainly located in lean conditions with strong soot oxidation term, therefore, a close to zero SVF value is observed.

In view of the most probable states derived from the joint-PDF in R1, an intermittent behaviour of soot formation is suggested. Note that, although there is a high probability of finding suitable conditions for soot formation, it is even more common to find thermochemical states close to the stoichiometric, lean or inert conditions. In order to properly illustrate soot intermittency, Fig. 5.23 shows the scatter data of mixture fraction and SVF colored by the joint-PDF of $\widetilde{Z}$-SVF. As observed, although very high SVF values are present within the range of $0.1 < \widetilde{Z} < 0.15$, they are very rarely found, and the soot quantity is more likely to be low. In fact, the most probable situation is to find a very low (even close to zero) SVF magnitude and significant soot peaks are eventually observed if proper flow and mixing conditions for soot production are satisfied.

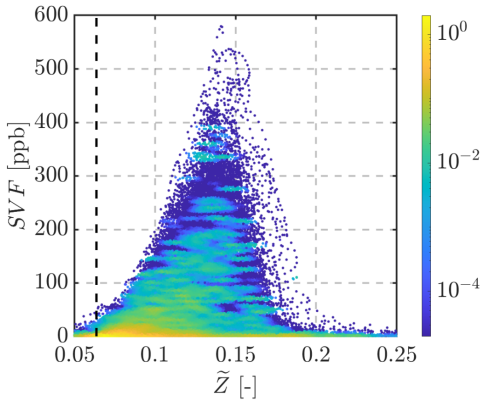

Figure 5.23: Scattered plot of mixture fraction and SVF from instantaneous LES results. Color: joint-PDF of $\widetilde{Z}$-SVF.

Due to the unsteady behaviour of the swirled flow and the intermittency on the soot generation, it is interesting to analyze the time evolution of certain quantities to better understand the soot formation and oxidation processes. Therefore, instantaneous contours of pyrene (A4), acetylene (C_2H_2), SVF and the total soot source term ($\overline{\dot{\omega}}_s^c$) are represented at three time instants in Fig. 5.24. The stoichiometric mixture fraction isoline is shown in white while the black line represents different soot source terms depending

on the contour: 20% of the maximum nucleation source term (A4 mass fraction field), 20% of the maximum surface growth source term (C_2H_2 mass fraction field) and total soot source term equal to $-0.005\ kg\,m^{-3}s^{-1}$ (SVF field). This particular temporal sequence clearly illustrates a complete soot formation event located along the right rich branch inside the combustor (red box in Fig. 5.24). The event starts with the formation of a rich-burned gas (RBG) pocket in the central near-nozzle region. Along the time sequence, this pocket grows in size, and high concentrations of pyrene and acetylene are found inside ($x \sim 5$ mm and $z \sim 15$ mm). Consequently, soot inception and growth processes (black lines) are observed, which lead to a high positive total soot source term value and an increase in the SVF level (represented in the fourth and third rows, respectively). It is interesting to observe that A4 and C_2H_2 mass fraction peak values (and therefore nucleation and surface growth processes) are confined to the closer rich pockets, however, a higher C_2H_2 concentration is observed downstream and soot growth is still present along the slightly rich branches. Regarding the soot production sequences, note that the last two temporal frames ($t = 1$ and $t = 1.5$ ms) show the start of a new RBG pocket and soot formation event in the left branch (magenta box in Fig. 5.24, at $x \sim -10$ mm and $z \sim 15$ mm).

On the other hand, soot oxidation events can be appreciated at the locations closer to the stoichiometric mixture line. In Fig. 5.24, several oxidation sequences are clearly observed downstream at both branches (yellow boxes). Soot is formed, transported downstream and eventually approaches the IRZ, where lean-burned gas (LBG) with high OH concentrations is found. In this regions, high negative soot source terms are present and SVF decreases because of the fresh air coming from the secondary injection. The unsteady motion of RBG and LBG regions close to the injection nozzle is related to the flow dynamics induced by the secondary air injection and these intermittent soot formation events reproduced by LES were experimentally observed by Stöhr et al. [44] and Litvinov et al. [45].

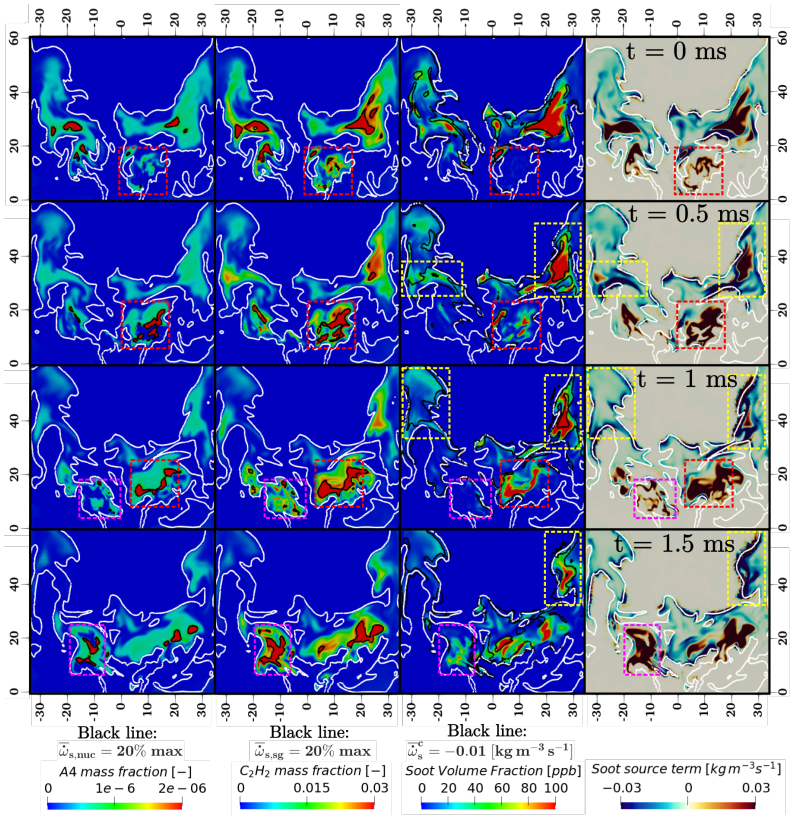

Figure 5.24: Temporal sequence of A4 mass fraction, C_2H_2 mass fraction, SVF and soot source term contours. White line: stoichiometric mixture fraction isoline. Black lines: isolines of soot source terms. Spatial units in mm.

To illustrate the contributions of the soot subprocesses considered in the sectional modelling approach, time-averaged contours of the different source terms are presented in Fig. 5.25. In view of the magnitude of the source terms, soot production is mainly dominated by surface growth based on acetylene. In fact, soot surface growth magnitude is approximately one order of magnitude higher than the rest of the subprocesses. Regarding the spatial distribution, the most intense production (nucleation, PAH condensation and surface growth) terms are located at the main soot formation region described in previous figures, since the presence of A4, C_2H_2 and soot is quite important. It is worth mentioning that surface growth seems to be present in a slightly extended area, while nucleation and condensation are confined in the rich region close to the injection plane. A similar source term distribution inside the combustion chamber and trend for the different subprocesses can

be observed in the works of Tardelli et al. [24] and Chong et al. [9] for the same combustor.

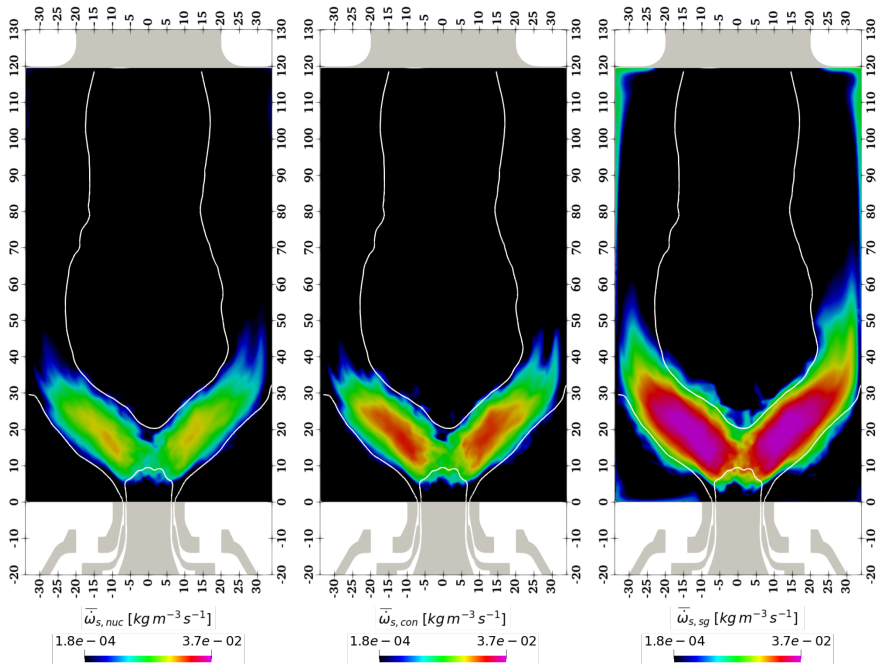

Figure 5.25: Time-averaged contours of soot production source terms by subprocess (Op 1). White line: stoichiometric mixture fraction isoline. Legend in log scale. Spatial units in mm.

Finally, mass fractions and source terms of the different soot clusters considered in the modelling approach (review Table 5.3 for information of soot clusters) are presented in Fig. 5.26 to evaluate the mass contribution and formation/consumption of soot sections. Due to the low soot mass of the fifth and sixth clusters, only the first four clusters are included for analysis. In view of the soot cluster mass fractions (top row), the main soot mass contribution corresponds to the third and fourth clusters. In fact, the mass contribution is increasing with each consecutive cluster. Furthermore, it is possible to observe that clusters number 1 and 2 are only present in the main soot formation region while soot growth along the rich branches leads to the presence of higher clusters (3 and 4) further downstream. Indeed, at the furthest axial positions ($z > 60$ mm) the soot mass contribution is primary due to the fourth cluster. Soot source terms represented at the bottom row give information of production and consumption of each cluster. It is important to highlight that the

analysis of the soot source term for clusters could be confusing. As opposed to the total soot source term seen above, production and consumption of each cluster are affected by intersectional dynamics. For instance, a negative value of the source term of an intermediate cluster represents not only the oxidation of that cluster and reduction of particle size, but also the growth in size and its consequent transition to the next higher section. However, it is possible to clearly observe some differences between formation and consumption of the different clusters. The primary soot region (rich branches up to $z \sim 40$ mm) shows a similar behaviour for all clusters, characterized by the eventual mass production and consumption of each of them. In the rich pockets, soot mass is produced for each cluster from the previous one and consumed as it grows into even larger clusters. The high soot mass quantity of cluster 3 and 4 downstream makes them prone to oxidation when approaching to the stoichiometric condition and more intense consumption source terms appear in this region.

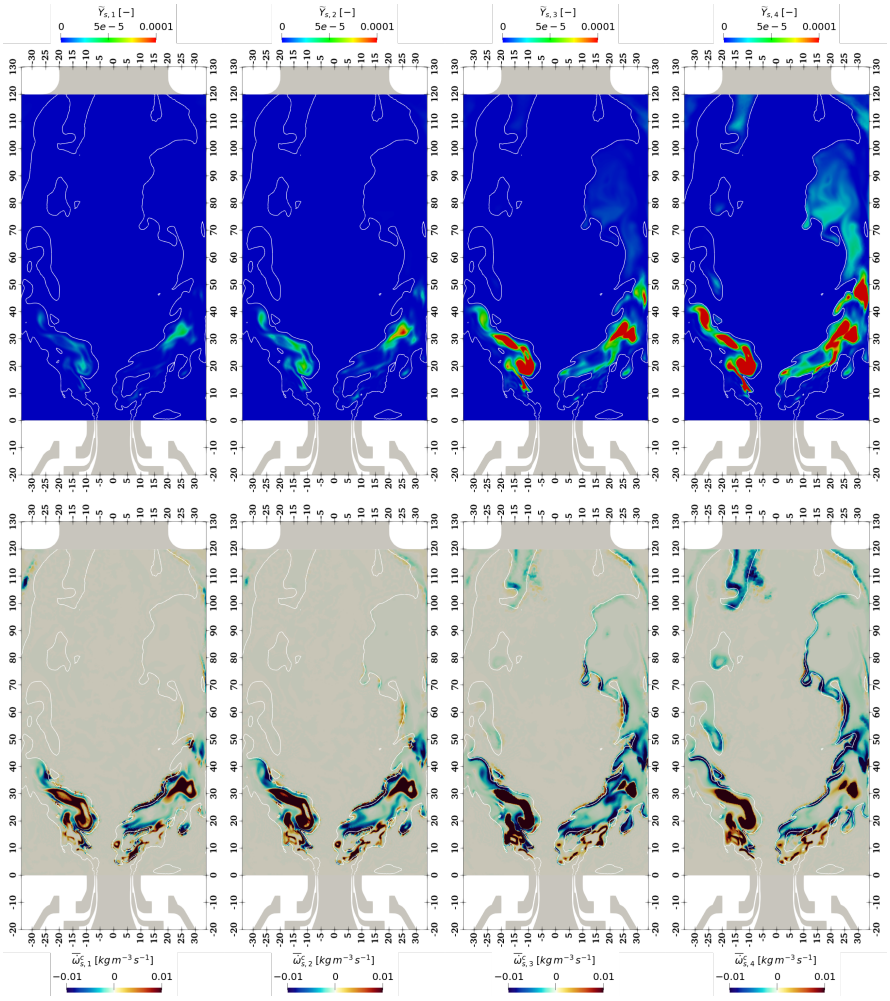

Figure 5.26: Soot mass fractions and source terms for the first four clusters considered in the CDSM modelling approach. Top: cluster mass fractions. Bottom: soot source term of clusters.

5.3.3 Particle Sizes Distribution

Since the sectional method evaluated in this work provides information about particulate sizes, the Particle Size Distribution function (PSDF) has been computed at different locations inside the combustion chamber. For the analysis of size distributions, both temporal and spatial averaging of the function have been considered, using the original sections re-constructed from the different clusters (see Eq. 3.59 for additional details).

To evaluate the time evolution of the particle size distribution at specific coordinates, instantaneous and time-averaged PSDF are presented in Fig. 5.27. Two particular positions are selected for the analysis, whose location inside the combustion chamber can be observed in Fig. 5.19 (red markers). Point 1 ($x = 12$, $z = 25$ mm) is located near the main soot formation region while point 2 ($x = 24$, $z = 40$ mm) is found slightly downstream, following one of the rich branches. At each point, flow variables and soot clusters have been recorded during ∼4 ms of physical time. Regarding Fig. 5.27, the instantaneous (colored solid lines) and time-averaged (black dashed line) PSDF are presented on the left side. On the right-hand side, the time-evolution of filtered mixture fraction ($\widetilde{Z}$) and instantaneous Soot Volume Fraction are recorded over the same time window as for the PSD computation. In any case, colors represent the instantaneous SVF. In view of the obtained PSDF, the point located close to the main soot formation region (1) reaches a higher mixture fraction value and, therefore, evidences a higher overall SVF magnitude. Although the relationship between SVF and mixture fraction is not instantaneous due to the delay induced by the transport equations for soot clusters, it is possible to observe how the amount of soot eventually increases when reaching high mixture fraction levels ($\widetilde{Z} > 0.1$ approximately). Consequently, size distributions at this point evidence a high particle number that decreases at time instants when mixture fraction and soot quantity are slightly reduced. The second location (point 2) suggests a local fuel-air ratio closer to the stoichiometric conditions ($\widetilde{Z}$ fluctuates around 0.08). In this case, soot is more affected by consumption processes and the SVF magnitude is generally lower. Therefore, the instantaneous function covers a lower range of particle number and the PSDF shape is slightly modified showing a strong reduction in the number of particles with small sizes.

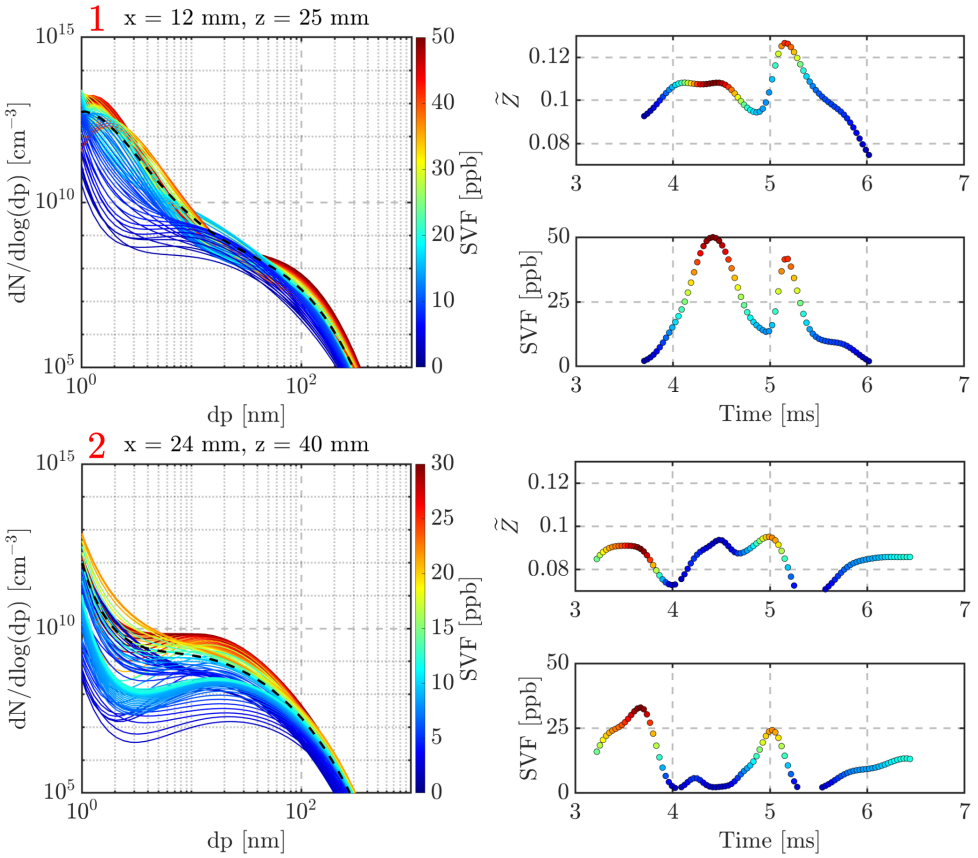

Figure 5.27: Instantaneous and time-averaged PSD results (Op1) at two different locations inside the combustion chamber (see markers in Fig. 5.19). Left: instantaneous (solid lines) and time-averaged (black dashed line) PSDF. Right: time-evolution of mixture fraction ($\widetilde{Z}$) and SVF. Colors: instantaneous SVF magnitude.

Due to the dependency of the size distribution to the local mixture level observed in Fig. 5.27, it is interesting to perform a spatial averaging of the PSDF considering a certain amount of points conditioned to the mixture fraction, as presented in Fig. 5.28. A vertical cut plane of the burner colored by the total soot source term ($\overline{\dot{\omega}}_s^c$) is shown on the left side to illustrate the different regions considered for the spatial average of the PSDF. Green and white lines represent the $\widetilde{Z} = 0.1$ and $\widetilde{Z} = Z_{st}$ isolines, respectively. Therefore, the green line encloses the primary soot production area while oxidation is mainly present in the region between the green and white lines (i.e. in the slightly rich zone near stoichiometric conditions, where soot is still present and oxidation is possible). The spatially averaged PSD functions in the two

previously described regions are presented in the central plot. The solid line indicates the averaged PSDF in the richer region, where the domination of soot formation processes leads to a higher number of small particles and to a more almost uni-modal like PSDF shape. On the contrary, the PSDF computed in the zone closer to Z_{st} (dashed line) evidences an overall decrease in the number of particles of all sizes, strongly affecting the smallest diameters (up to 10 nm, approximately) which are easier to oxidize. In order to have a better understanding of the PSD transition when approaching to the stoichiometric region, the plot on the right side presents the spatially averaged PSDF including points conditioned to a more bounded $\widetilde{Z}$ values, from $\widetilde{Z} > 0.1$ to $\widetilde{Z} = Z_{st}$ (red to black). Thus, when the local mixture level moves from the richer soot formation region to lean conditions, the number of particles slowly decreases and the PSD shape transitions to a more bi-modal like distribution. Due to the strong oxidation along the Z_{st} iso-surface, soot is completely consumed in the lean regions (e.g. the IRZ in this configuration) and the PSDF is not relevant there.

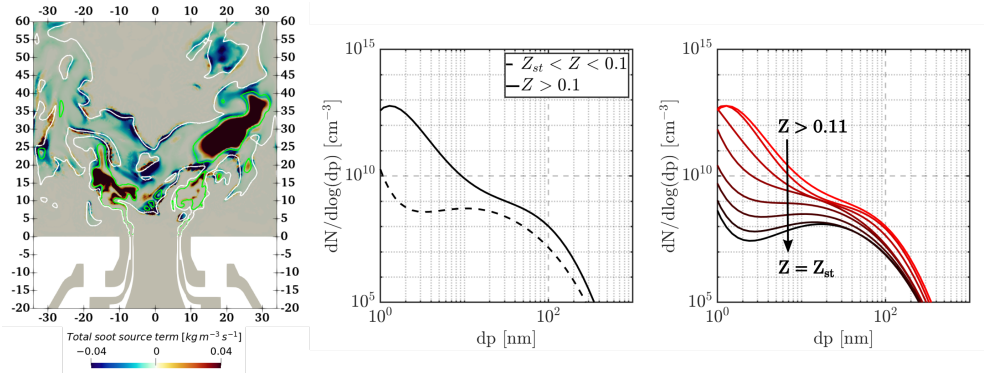

Figure 5.28: Spatial-averaged PSD results (Op1). Left: contour of total soot source term in a vertical cut plane. Green line: $Z = 0.1$ isoline, white line: $Z = Z_{st}$ isoline. Center: PSDF in two regions depending on Z. Right: evolution of the PSDF from very rich conditions to Z_{st}.

5.4 Effect of secondary oxidation air

This section is focused on the results of the second operating condition specified in Table 5.1. It corresponds to the DLR burner configuration without secondary air injection so the effects of excluding the dilution air are evaluated here in terms of combustion and soot formation and growth.

The section is structured in a similar way as for Op 1. A description of gas phase and the combustion process is addressed first, followed by soot predictions, analysis and discussion of particle size distributions. Due to the fact that both burner configurations share some characteristics of the reacting flow (e.g. the soot formation region is indeed very similar), the complete analysis of certain magnitudes and processes addressed in the previous sections is not included here and only a general overview of the results and the evaluation of the LES-FGM-CDSM modelling approach for this configuration is given. Note that the non-adiabatic modelling approach is retained here and the results presented in this section correspond to that case.

5.4.1 Gas phase description

First, the general flow field is compared between both operating conditions in Fig. 5.29. Mean axial velocity contours are illustrated with arrows representing the velocity magnitude. Indeed, the flow pattern in both cases is quite similar. The recirculation regions previously observed (IRZ, CRZ) are also present in Op 2. Flow structures in the first part of the combustor ($z < 30$ mm) are almost identical in both configuration while some differences are present downstream due to the influence of the secondary air. Recirculation in the IRZ is noticeably less intense in Op 2, showing reduced negative axial velocity values in this region. In addition, flow disturbance at $z = 80$ mm is completely removed and the axial velocity at the combustion chamber exit is considerably decreased due to the absence of the secondary pushing air.

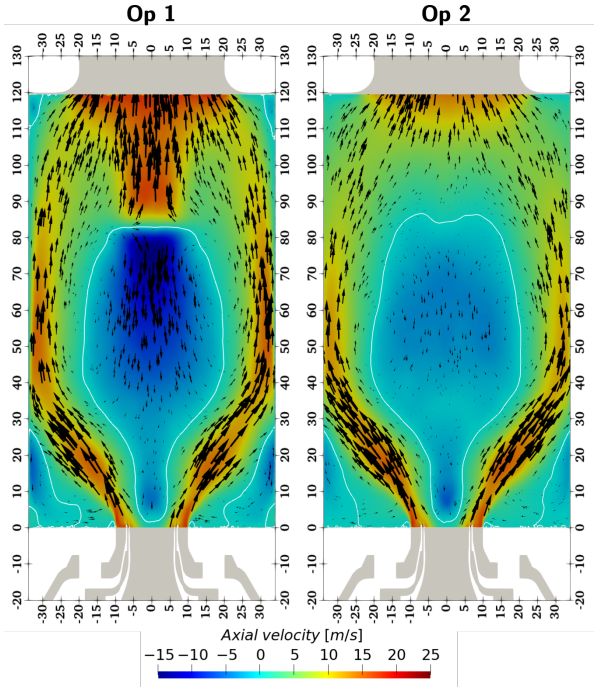

Figure 5.29: Comparison of the flow field between Op 1 (left) and Op 2 (right). Contours of time-averaged axial velocity for both cases. Arrows represent the velocity magnitude. White line: zero axial velocity iso-line. Spatial units in mm.

Similarly to the previous configuration, the velocity field assessment is presented in Fig. 5.30. In this case, only the time-averaged velocity components are shown at centerline and different stations. At centerline, the comparison with Op 1 is included in order to illustrate the main differences in terms of axial velocity. In general, the agreement with the experimental data is quite good and simulations are able to capture correctly the radial profiles of the different mean velocity components. The main discrepancies are found at centerline, where the numerical results show a slight overprediction of the axial velocity (or underprediction of recirculation). It is possible to observe in Fig. 5.30a the differences between Op 1 and Op 2 mentioned above. The recirculation region is similar at the first axial positions but the effect of the secondary injection is evident close to $z = 80$ mm, inducing a strong recirculation nearby and higher axial velocities downstream, close to the exit nozzle.

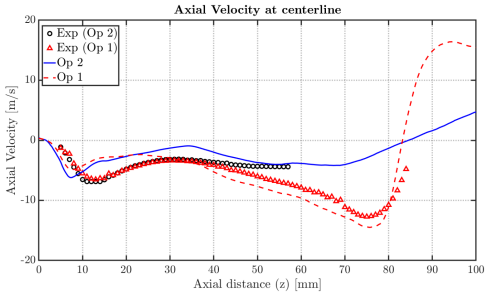

(a) Mean axial velocity at centerline.

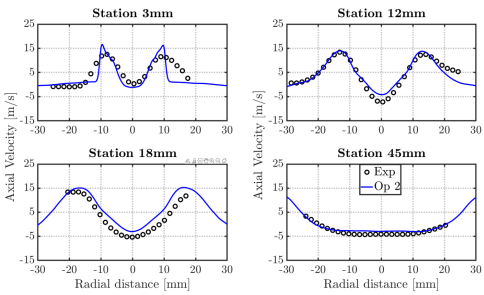

(b) Mean axial velocity at stations.

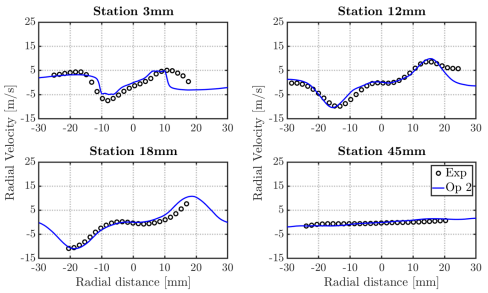

(c) Mean radial velocity at stations.

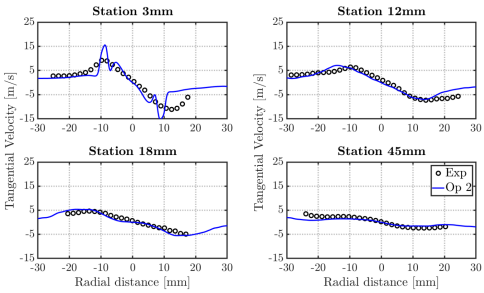

(d) Mean tangential velocity at stations.

Figure 5.30: Comparison between LES results and experiments of velocity field (Op 2). Red line and markers: results for Op 1.

The characteristics of the combustion process can be observed by means of the instantaneous contours presented in Fig. 5.31. The same magnitudes as in Fig. 5.13 are shown here for the configuration without dilution air. It is evident that the mixing field and combustion process is considerably different in this operating condition. In view of the equivalence ratio contour, fuel and air mixing in the near-injection region is performed in a similar way as Op 1, but the equivalence ratio field downstream is completely different due to the absence of secondary air. The second part of the combustion chamber is characterized by a quasi-homogeneous fuel-air mixture, corresponding to the operating equivalence ratio condition ($\phi \sim 1.2$). Progress variable and temperature fields are also affected downstream. In this case, important temperature gradients are found in the first axial locations of the combustor, between the CRZ and the shear layers and close to the walls, but the IRZ is not showing the previously observed decrease on temperature. In view of the mixing and temperature fields, the behaviour of species mass fractions is as expected. The richer central region leads to a higher concentration of soot precursors (A4, C_2H_2) downstream and the position of the stoichiometric mixture fraction iso-

line results in a location of the peak OH mass fraction (and thus the reaction zone) between the CRZ and the main shear layers.

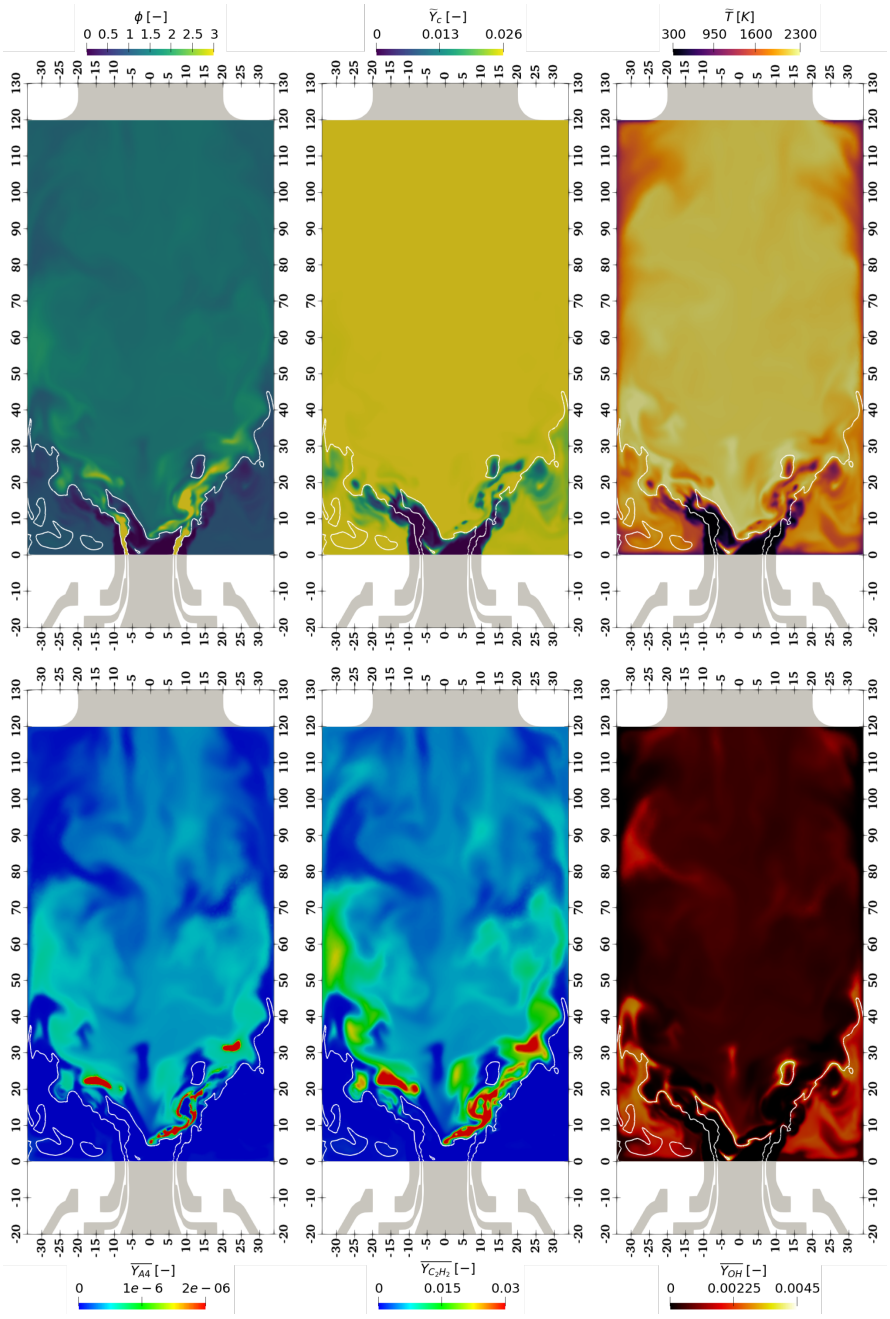

Figure 5.31: Instantaneous fields of various representative magnitudes of the reacting flow in the DLR burner (Op 2). Top (from left to right): local equivalence ratio, progress variable and temperature. Bottom (from left to right): mass fractions of pyrene (A4), acetylene (C_2H_2) and hydroxyl radical (OH). White line represent the stoichiometric mixture fraction iso-line.

The temperature field comparison between LES results and experimental data at centerline and several stations is illustrated in Fig. 5.32. In this case, the results for Op 1 using the non-adiabatic approach are included to quantitatively evaluate the main differences between both operating conditions. Regarding the results at centerline, a slight overprediction of the temperature value is obtained for Op 2 at most of the axial positions, however, the temperature values are within the experimental uncertainty on the reacting layers and the overall trend of the temperature field is well captured. The modification of the temperature distribution along the burner axis in this configuration is evidenced here. Due to the fact that cold air from the secondary injection is not included, In Op 2, temperature increases at the closest axial locations because of the primary reactive region and remains uniform further downstream due to the absence of cold air from the secondary injection. Radial profiles evidence also the slight temperature overprediction downstream, however, a satisfying agreement is also obtained. When approaching to the combustion chamber walls, temperature profiles of both configurations become similar and simulations for Op 2 achieve as good agreement as that obtained for Op 1. In particular, in the near-nozzle region (3 mm station) and inside the CRZ, the temperature profile is accurately predicted also in this case.

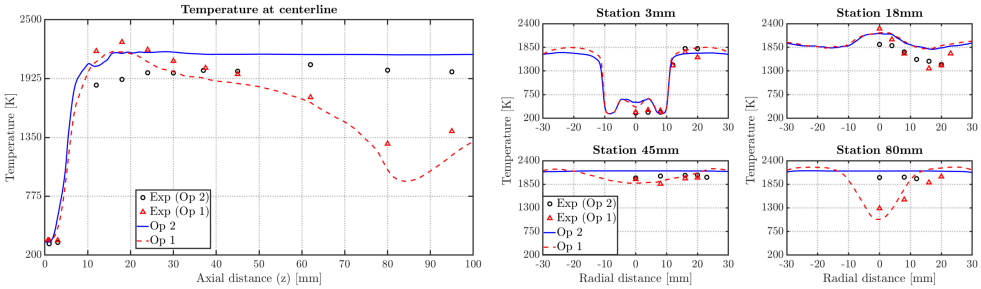

(a) Mean temperature at centerline. *(b) Mean temperature at stations.*

Figure 5.32: Comparison between LES results (Op 1: red, Op 2: blue) and experiments of temperature field.

Finally, Fig. 5.33 shows the comparison between LES and experiments of the OH mass fraction field for the current configuration. As for the previous OH mass fraction comparison, instantaneous and time-averaged contours are included. As mentioned above, removing the secondary air jets leads to a reaction zone exclusively confined to the first part of the combustor and fuel burns in a kind of cone-shaped flame. Strong OH mass fraction fluctuations are only present close to the injection, where the swirl motion induces a high

intensity of turbulence. In fact, this operating condition presents an almost non-fluctuating behaviour downstream because the flow is not disrupted by the additional jets. Only a slight overprediction of the OH mass fraction is obtained in the CRZ, but the overall agreement with the experimental data is quite good and LES is able to capture the flame region also in this case.

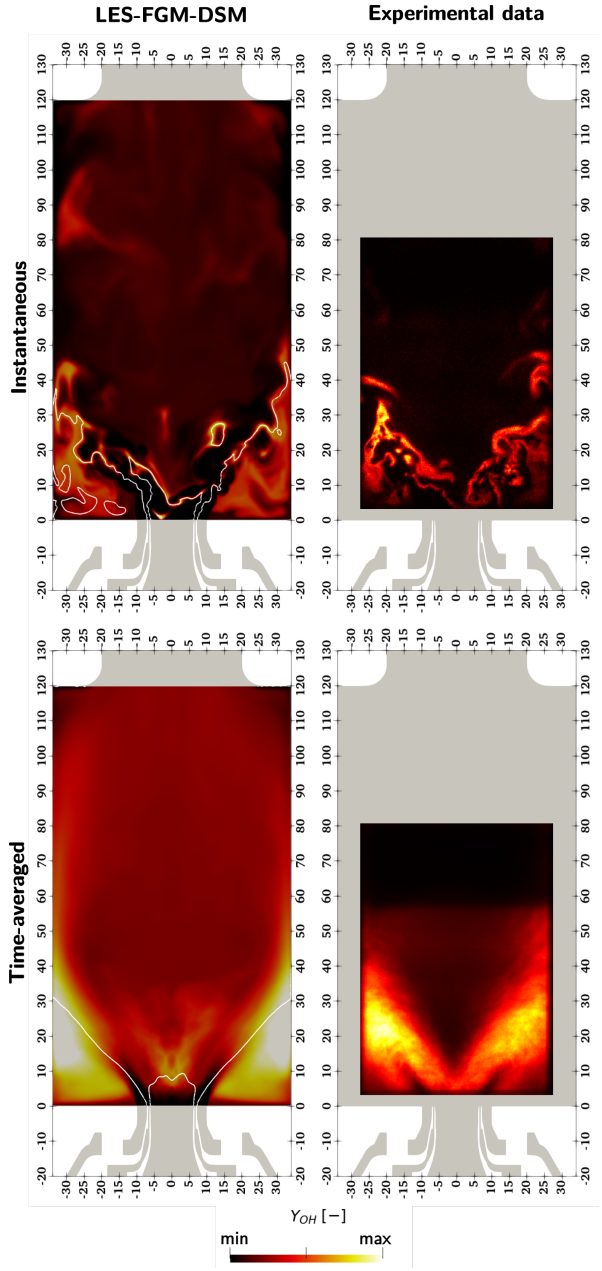

Figure 5.33: Comparison of OH mass fraction between numerical results (Op 2) and the experimental data. Top: instantaneous OH mass fraction field. Bottom: time-averaged OH mass fraction field. White line: stoichiometric mixture fraction iso-line.

5.4.2 Soot predictions

This subsection aims to summarize the soot predictions obtained for Op 2 and first the assessment of the Soot Volume Fraction field is presented. The numerical SVF contour is compared with the experimental measurements in Fig. 5.34 and Fig. 5.35 presents a comparison at three different axial stations. In general, a good qualitative agreement is achieved and soot distribution inside the combustor is well captured. In this case, the main soot formation phenomena take place at the rich branches following the swirled flow pattern closer to the combustion chamber entry, in a similar way to Op 1. A different soot field is observed downstream due to the absence of secondary air jets, which inhibits the oxidation process. In this case, soot generated in the main branches is transported and diluted inside the IRZ, therefore, an almost constant SVF level is observed in this region and further downstream positions. To illustrate this behaviour, Fig. 5.36 shows the nucleation, condensation and surface growth source terms for this case. As indicated, the soot production zone is quite similar regardless the secondary oxidation air (note that the scale for soot source terms is the same as in Fig. 5.25). The main difference can be observed in the nucleation process, which faintly extends over the whole combustion chamber. In spite of that, the soot main formation is still confined in the closer rich branches and soot distribution in the IRZ is controlled by transport due to the flow structures created by the swirling inlet stream pattern in the burner.

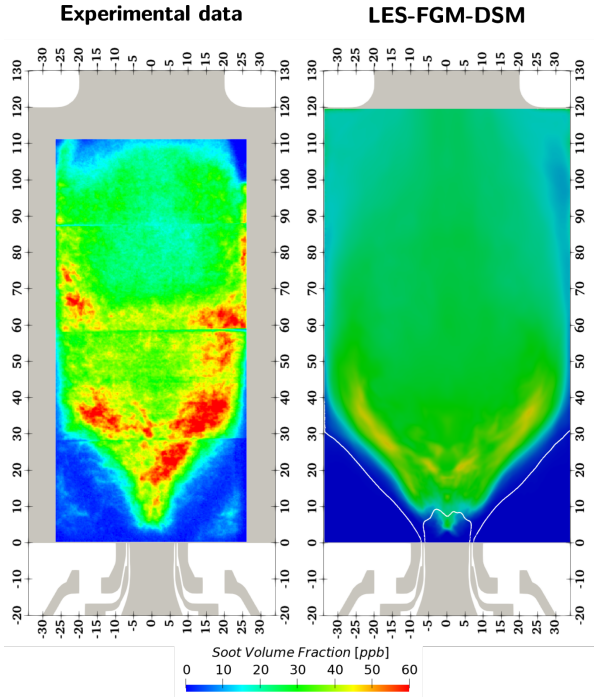

Figure 5.34: Comparison of time-averaged Soot Volume Fraction (SVF) contours (Op 2). White line: stoichiometric mixture fraction. Spatial units in mm.

As plotted in Fig. 5.35, the order of magnitude of SVF and radial profiles are correctly predicted and the agreement with the experimental data is satisfactory. Nevertheless, an underestimation of the SVF peak value (∼50 ppb in LES, ∼100 ppb in experiments) and the overall magnitude is obtained in the first mid part of the burner, as seen at 18 and 45 mm stations. A better agreement is achieved further downstream, where the soot level slightly decreases close to the axis. There are not many previous investigations on numerical modelling that include this operating condition, and the few works that analyze it show notable discrepancies in terms of soot quantity prediction. Chong et al. [46] properly captured the soot formation region in the branches, but almost no soot is predicted in the IRZ using two MoM variants. When using a two-equations semi-empirical model, soot was mainly present in the IRZ but SVF was strongly overestimated. On the other hand, Grader et al. [13] obtained good results for this configuration in terms of soot volume fraction peak value using a sectional approach. However, soot quantity in the IRZ was also underpredicted. In this work, despite the slight underestimation mentioned above, the proposed modelling approach is able to reliably capture the SVF in the shear layers and the recirculation zone.

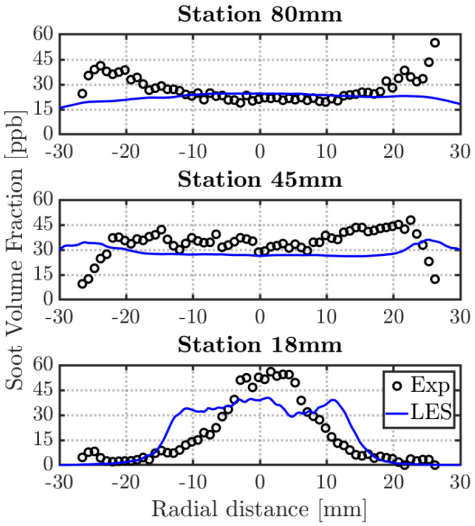

Figure 5.35: Comparison between LES results and experiments (Op 2). Soot Volume Fraction (SVF) at different radial stations.

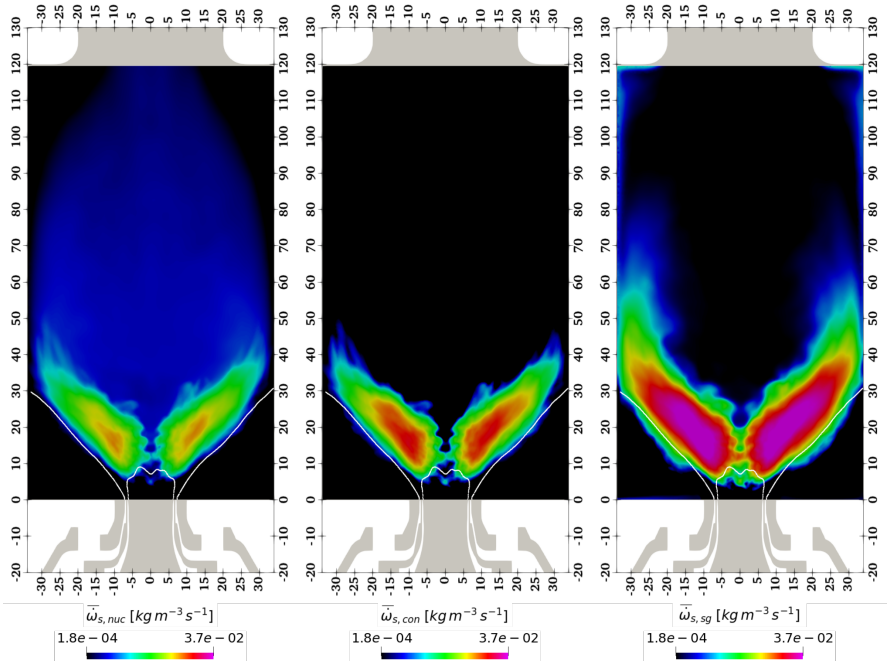

Figure 5.36: Time-averaged contours of soot production source terms by subprocess. White line: stoichiometric mixture fraction isoline. Legend in log scale. Spatial units in mm.

To understand the mass contribution and soot distribution between the different sections used, Fig. 5.37 illustrates soot mass fractions and source terms for clusters in this configuration. In terms of cluster contribution to the total soot mass, the conclusions are quite similar as for Op 1: soot mass is primary composed of clusters with high volume particles (3 and 4). On the other hand, the distribution of soot sections in the inner region is considerably different, as expected from the SVF distribution presented above. In this case, mass of clusters with small sizes is mainly found along the cone-shaped region corresponding to the shear layers while the IRZ exclusively contains mass of big clusters. Indeed, the formation/consumption of clusters derived from the source terms supports this distribution. The different clustered sections are generated and grow into larger and larger clusters along the rich branches and the mass of the large sections formed at the end of the process is transported and diluted towards the IRZ. The strong consumption observed for the first clusters is a combination of oxidation (when approaching to the stoichiometric mixture condition) and growth to a larger size. Note that consumption of cluster number 4 is very low due to the absence of lean zones that reduce their size (in comparison to Op 1) and the inability to grow towards the last sections (the tabulated source terms for clusters 5 and 6 is too low and they are not generated even in the flamelets).

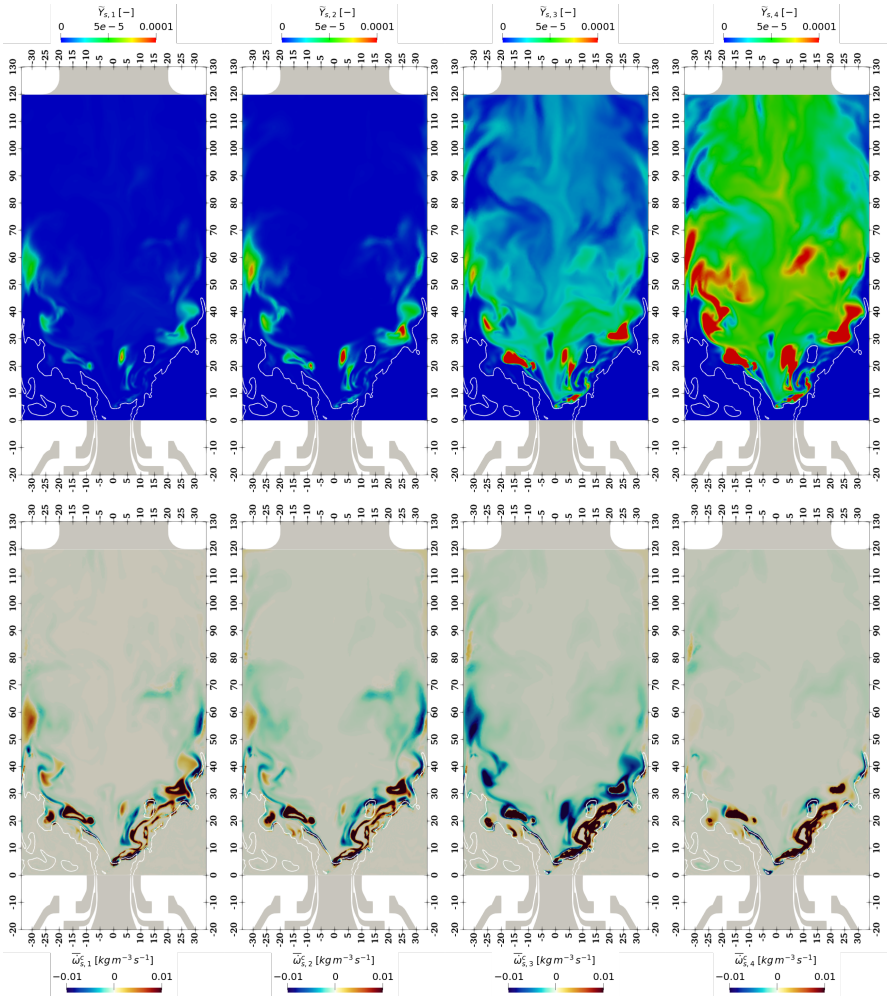

Figure 5.37: Soot mass fractions and source terms for the first four clusters considered in the CDSM modelling approach (Op 2). Top: cluster mass fractions. Bottom: soot source term of clusters.

Finally, PSD are also recovered for this configuration. The results are shown in Fig. 5.38 in a similar way to the previous case. On the left, a vertical cut plane of the burner is illustrated, colored by the total soot source term. The spatially averaged PSD functions are represented in the plot at the right side. For the PSDF averaging, two different regions are considered: the rich primary soot production zone ($Z > 0.1$) and a region located within the IRZ (see left contour). In this configuration, the absence of secondary air jets leads to a different soot level in the IRZ so it is interesting to evaluate

the size distribution in this region. The PSDF obtained at the richer region is similar to the previous case in terms of both the number of particles and shape. As previously mentioned, the soot production zone is almost unaffected by the secondary air and the IRZ in this case is characterized by neither soot production nor oxidation, only transport and dilution (it is observed in the left contour of Fig. 5.38 from the near-zero value of the total soot source term in the IRZ). Therefore, the resulting PSDF has a slightly lower number of particles due to the dilution and low oxidation along the main branches so the size distribution is almost unchanged inside this zone.

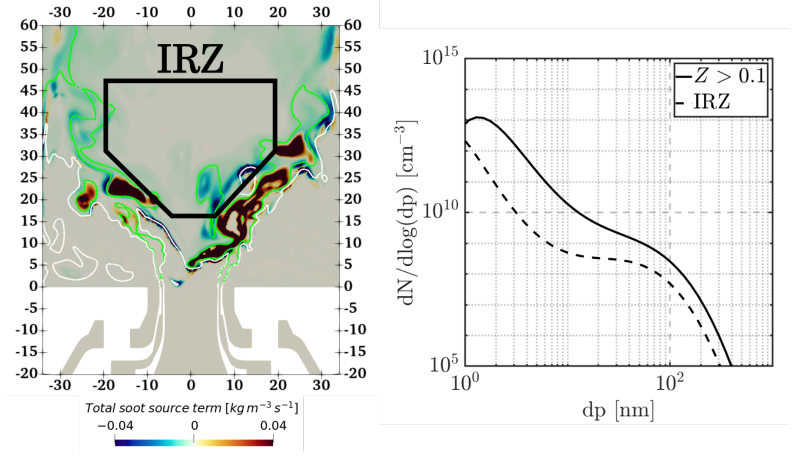

Figure 5.38: Spatial-averaged PSD results (Op 2). Left: contour of total soot source term in a vertical cut plane. Green line: $Z = 0.1$ isoline, white line: $Z = Z_{st}$ iso-line. Right: spatial averaging of PSDF in two regions: rich region ($Z > 0.1$) and IRZ.

5.5 Summary

The pressurized ethylene-based model burner investigated at DLR has been studied during this chapter in terms of combustion and soot formation and oxidation. This burner features a dual swirler configuration for the primary air supply and includes secondary dilution jets inside the combustion chamber, showing reacting flow characteristics representative of the RQL combustor technology. In this work, Large-eddy simulations of the DLR burner have been conduced to assess the coupling approach between flamelet generated manifold (FGM) chemistry and discrete sectional method (DSM) based soot model presented in Chapter 3 (referred as FGM-CDSM). For the computationally efficient application of DSM in LES, soot source terms are tabulated

in the FGM and filtered transport equations are solved for the soot mass fraction in a few clustered sections by assuming the preservation of soot particle size distribution within the clusters. As an introduction of the chapter, the particularities of the modelling approach have been presented first, together with the description of the experimental rig, the numerical setup and the computational grids used. In the present study, the baseline operating condition with secondary air injection has been taken as a reference and the analysis of the reacting flow and soot formation has been focused on this configuration. However, the burner configuration without dilution air has been also analyzed in order to evaluate the effects of the secondary injection in the reacting flow field and soot.

First, flow structures in the DLR combustor configuration with secondary jets have been presented and LES has demonstrated to reliably reproduce the different recirculation regions and features of the swirling flow. Furthermore, the assessment of the velocity field has been conducted, showing a really good agreement with PIV measurements in terms of both mean velocity components and fluctuations. Subsequently, an analysis of combustion and flame characteristics has been addressed. The predicted mixing, temperature and relevant species mass fraction fields illustrates the complexity of the reacting flow inside the DLR burner due to the flow pattern. Combustion is stabilized in the near-nozzle region where the high turbulence intensity leads to a strongly wrinkled reacting front. Downstream, the combustion process progresses following the main axial flow close to the chamber walls and the flame parameters are greatly affected by the cold air coming from the secondary injection. A detailed comparison between the numerical results and the experimental data has been presented for temperature and OH mass fraction fields. In this case, adiabatic and non-adiabatic modelling approaches have been considered in order to check the influence of heat losses. Both fields are satisfactorily predicted by LES and the agreement with experiments is noticeably better when considering the non-adiabatic approach, specially in the corner recirculation region. Finally, a brief analysis of the turbulent combustion regimes has been performed. The $Da_t - Re_t$ diagram for turbulent diffusion flames showed that most of the locations inside the combustion chamber present a really high turbulent Damkhöler number due to the fast chemistry and the flamelet assumption seems reasonable in this application. In addition, premixed and non-premixed combustion modes have been characterized using a flame index definition based on the mixture fraction and progress variable gradients. The DLR burner evidenced a diffusion-dominated combustion regime with minor premixing effects located in the main combustion region close to the chamber entry.

Soot predictions have been presented for the baseline configuration and the capabilities of the FGM-CDSM approach to reproduce soot formation and oxidation in the DLR combustor have been evaluated. The Soot Volume Fraction (SVF) field has been compared with the experimental measurements, showing a satisfactory agreement in both SVF distribution and magnitude. Moreover, the results evidence a noticeable improvement when considering heat losses in the flamelet manifold. The analysis of the instantaneous evolution of soot magnitude, precursors and source terms has shown that the present approach is able to reproduce the soot formation and oxidation processes in this burner. Simulations evidence the production of soot in the intermittent rich pockets located along the main branches close to the shear layers, where high concentrations of soot precursors lead to positive source terms. Oxidation is also captured downstream, where soot is completely consumed when approaching to the lean region generated by the dilution air. Soot analysis is concluded by the evaluation of the temporal and spatial averaged Particle Size Distribution (PSD) reconstructed from the soot sections of the DSM. The behaviour of the PSD function evidences a strong dependency on the local mixture fraction level. In the main soot formation region, where the mixture fraction reaches considerably high values, the PSDF presents a uni-modal like distribution. When approaching to the stoichiometric condition, the PSDF is influenced by soot oxidation and its shape transitions to a bi-modal distribution due to the strong consumption of small particles.

Finally, the configuration without secondary air has been evaluated. Despite the absence of the secondary injection, flow structures are quite similar in both configurations and only the previously disturbed central region is different here. However, the combustion process is noticeably affected and the temperature and species fields indicate a different behaviour downstream. In this configuration, the assessment of velocity, temperature and OH mass fraction fields has been also conducted, showing a really satisfactory agreement with the experiments. Soot predictions have been also presented and an accurate prediction of the SVF field has been obtained in this case. Only a slight underprediction of the SVF peak value could be observed but the overall distribution and magnitude are properly captured, specially in the central region of the combustor, where higher discrepancies were found in previous numerical works. The analysis of the PSDF has evidenced the effect of the secondary air in the size distribution. In this case, a similar PSD shape has been obtained both in the main soot formation region and in the inner recirculation zone, since soot is mainly affected by transport and dilution, not oxidation.

To conclude, the DLR model combustor studied in this chapter has made it possible to evaluate the capabilities of the LES-FGM-CDSM modelling ap-

proach introduced in Chapter 3 to reproduce the reacting flow characteristics and predict soot formation in a turbulent flame application. In general, the proposed modelling framework is capable of qualitatively and quantitatively predicting the soot field and the production and oxidation processes inside the burner for both operating conditions considered with a reasonable computational cost. Furthermore, the analysis of soot particle size distribution has demonstrated that the present approach is able to predict different PSD shapes depending on temporal and spatial variations of the soot formation and oxidation events.

References

[1] Geigle, Klaus Peter, Hadef, Redjem, and Meier, Wolfgang. "Soot Formation and Flame Characterization of an Aero-Engine Model Combustor Burning Ethylene at Elevated Pressure". In: *Journal of Engineering for Gas Turbines and Power* 136.2 (2014). DOI: 10.1115/1.4025374.

[2] Geigle, Klaus Peter, Köhler, Markus, O'Loughlin, William, and Meier, Wolfgang. "Investigation of soot formation in pressurized swirl flames by laser measurements of temperature, flame structures and soot concentrations". In: *Proceedings of the Combustion Institute* 35.3 (2015), pp. 3373–3380. DOI: https://doi.org/10.1016/j.proci.2014.05.135.

[3] *International Sooting Flame workshop*. URL: https://www.adelaide.edu.au/cet/isfworkshop/.

[4] Franzelli, B., Riber, E., Cuenot, B., and Ihme, M. "Numerical modeling of soot production in aero-engine combustors using large eddy simulations". In: *Proceedings of the ASME Turbo Expo* 4B (2015). DOI: 10.1115/GT201543630.

[5] Eberle, Christian, Gerlinger, Peter, Geigle, Klaus Peter, and Aigner, Manfred. "Toward finite-rate chemistry large-eddy simulations of sooting swirl flames". In: *Combustion Science and Technology* 190.7 (2018), pp. 1194–1217. DOI: 10.1080/00102202.2018.1443444.

[6] Felden, Anne, Riber, Eleonore, and Cuenot, Benedicte. "Impact of direct integration of Analytically Reduced Chemistry in LES of a sooting swirled non-premixed combustor". In: *Combustion and Flame* 191 (2018), pp. 270–286. DOI: 10.1016/J.COMBUSTFLAME.2018.01.005.

[7] Wick, Achim, Priesack, Frederic, and Pitsch, Heinz. "Large-Eddy Simulation and Detailed Modeling of Soot Evolution in a Model Aero Engine Combustor". In: Turbo Expo: Power for Land, Sea, and Air. 2017. DOI: 10.1115/gt2017-63293.

[8] Mueller, M. E., Blanquart, G., and Pitsch, H. "Hybrid Method of Moments for modeling soot formation and growth". In: *Combustion and Flame* 156.6 (2009), pp. 1143–1155. DOI: 10.1016/J.COMBUSTFLAME.2009.01.025.

[9] Chong, Shao Teng et al. "Large eddy simulation of pressure and dilution-jet effects on soot formation in a model aircraft swirl combustor". In: *Combustion and Flame* 192 (2018), pp. 452–472. DOI: 10.1016/j.combustflame.2018.02.021.

[10] Çokuslu, Ömer Hakkı, Hasse, Christian, Geigle, Klaus Peter, and Ferraro, Federica. "Soot prediction in a Model Aero-Engine Combustor using a Quadrature-based method of moments". In: *AIAA Science and Technology Forum and Exposition, AIAA SciTech Forum 2022* (2022), pp. 1–12. DOI: 10.2514/6.2022-1446.

[11] Salenbauch, Steffen, Hasse, Christian, Vanni, Marco, and Marchisio, Daniele L. "A numerically robust method of moments with number density function reconstruction and its application to soot formation, growth and oxidation". In: *Journal of Aerosol Science* 128 (2019), pp. 34–49. DOI: https://doi.org/10.1016/j.jaerosci.2018.11.009.

[12] Rodrigues, Pedro. "Modélisation multiphysique de flammes turbulentes suitées avec la prise en compte des transferts radiatifs et des transferts de chaleur pariétaux." PhD thesis. Université Paris-Saclay (ComUE), 2018.

[13] Grader, Martin, Eberle, Christian, Gerlinger, Peter, and Aigner, Manfred. "LES of a Pressurized, Sooting Aero-Engine Model Combustor at Different Equivalence Ratios With a Sectional Approach for PAHs and Soot". In: Turbo Expo: Power for Land, Sea, and Air. 2018. DOI: 10.1115/gt2018-75254.

[14] Kalbhor, Abhijit, Mira, Daniel, and Oijen, Jeroen van. "A computationally efficient approach for soot modeling with the discrete sectional method and FGM chemistry". In: *Combustion and Flame* 255 (2023), p. 112868.

[15] Kalbhor, Abhijit, Mira, Daniel, and Oijen Jeroen A., van. "Computationally efficient integration of a sectional soot model with FGM chemistry". In: 18th International Conference on Numerical Combustion ; Conference date: 08-05-2022 Through 11-05-2022. 2022.

[16] García-Oliver, José M, Pastor Enguídanos, José Manuel, Olmeda-Ramiro, Iván, Both, A, and Mira, D. "Combustion modeling in a pressurized gas turbine burner using Large-Eddy Simulations". In: *Proceedings 12CNIT 2022* (2022), pp. 690–699.

[17] García-Oliver, José M et al. "LES of a pressurized sooting RQL-like combustor with a computationally efficient discrete method coupled to tabulated chemistry". In: *11th European Combustion Meeting ECM2023*. 2023.

[18] Geigle, Klaus Peter, Hadef, Redjem, Stöhr, Michael, and Meier, Wolfgang. "Flow field characterization of pressurized sooting swirl flames and relation to soot distributions". In: *Proceedings of the Combustion Institute* 36.3 (2017), pp. 3917–3924. DOI: https://doi.org/10.1016/j.proci.2016.09.024.

[19] Kathrotia, Trupti, Oßwald, Patrick, Naumann, Clemens, Richter, Sandra, and Köhler, Markus. "Combustion kinetics of alternative jet fuels, Part-II: Reaction model for fuel surrogate". In: *Fuel* 302 (2021), p. 120736. DOI: https://doi.org/10.1016/j.fuel.2021.120736.

[20] Ramirez-Hernandez, Astrid, Kathrotia, Trupti, Methling, Torsten, Braun-Unkhoff, Marina, and Riedel, Uwe. "Reaction Model Development of Selected Aromatics as Relevant Molecules of a Kerosene Surrogate-The Importance of m-Xylene Within the Combustion of 1,3,5-Trimethylbenzene". In: *Journal of Engineering for Gas Turbines and Power* 144.2 (2021). DOI: https://doi.org/10.1115/1.4052206.

[21] University of Stuttgart, ESTiMatE project. *D2.1 Detailed reaction mechanism including PAHs, and soot.* Tech. rep. 2021.

[22] Wang, Yu, Raj, Abhijeet, and Chung, Suk Ho. "Soot modeling of counterflow diffusion flames of ethylene-based binary mixture fuels". In: *Combustion and Flame* 162.3 (2015), pp. 586–596.

[23] CHEM1D. *A one dimensional flame code. Eindhoven University of Technology.* 2002.

[24] Tardelli, Livia, Franzelli, Benedetta, Rodrigues, Pedro, and Darabiha, Nasser. "Impact of the Reaction Mechanism Model on Soot Growth and Oxidation in Laminar and Turbulent Flames". In: *Turbo Expo: Power for Land, Sea, and Air.* Vol. 58615. American Society of Mechanical Engineers. 2019, V04AT04A055.

[25] Ihme, Matthias and Pitsch, Heinz. "Prediction of extinction and reignition in nonpremixed turbulent flames using a flamelet/progress variable model. 2. Application in LES of Sandia flames D and E". In: *Combustion and Flame* 155.1-2 (2008), pp. 90–107. DOI: 10.1016/j.combustflame.2008.04.015.

[26] See, Yee Chee and Ihme, Matthias. "Large eddy simulation of a partially-premixed gas turbine model combustor". In: *Proceedings of the Combustion Institute* 35.2 (2015), pp. 1225–1234. DOI: https://doi.org/10.1016/j.proci.2014.08.006.

[27] Kalbhor, Abhijit and Oijen, Jeroen van. "An assessment of the sectional soot model and FGM tabulated chemistry coupling in laminar flame simulations". In: *Combustion and Flame* 229 (2021), p. 111381. DOI: 10.1016/j.combustflame.2021.02.027.

[28] Nau, Patrick, Yin, Zhiyao, Geigle, Klaus Peter, and Meier, Wolfgang. "Wall temperature measurements at elevated pressures and high temperatures in sooting flames in a gas turbine model combustor". In: *Applied Physics B: Lasers and Optics* 123.12 (2017), pp. 1–8. DOI: 10.1007/s00340-017-6856-y.

[29] Yoshizawa, Akira. "Statistical theory for compressible turbulent shear flows, with the application to subgrid modeling". In: *The Physics of fluids* 29.7 (1986), pp. 2152–2164.

[30] Both, Ambrus. "High-fidelity numerical simulations of reacting flows with tabulated chemistry". PhD thesis. Universitat Politècnica de Catalunya, 2023.

[31] Jeong, Jinhee and Hussain, Fazle. "On the identification of a vortex". In: *Journal of fluid mechanics* 285 (1995), pp. 69–94.

[32] Balakrishnan, G and Williams, FA. "Turbulent combustion regimes for hypersonic propulsion employing hydrogen-air diffusion flames". In: *Journal of Propulsion and Power* 10.3 (1994), pp. 434–437.

[33] Yamashita, H, Shimada, M, and Takeno, T. "A numerical study on flame stability at the transition point of jet diffusion flames". In: *Symposium (international) on combustion*. Vol. 26. 1. Elsevier. 1996, pp. 27–34.

[34] Buttay, R, Gomet, L, Lehnasch, G, and Mura, A. "Highly resolved numerical simulation of combustion downstream of a rocket engine igniter". In: *Shock Waves* 27 (2017), pp. 655–674.

[35] Zhao, Song, Bouali, Zakaria, and Mura, Arnaud. "Computational investigation of weakly turbulent flame kernel growths in iso-octane droplet clouds in CVC conditions". In: *Flow, Turbulence and Combustion* 104 (2020), pp. 139–177.

[36] Lignell, David O, Chen, Jacqueline H, and Schmutz, Hans A. "Effects of Damköhler number on flame extinction and reignition in turbulent non-premixed flames using DNS". In: *Combustion and Flame* 158.5 (2011), pp. 949–963.

[37] Abdelsamie, Abouelmagd and Thévenin, Dominique. "Direct numerical simulation of spray evaporation and autoignition in a temporally-evolving jet". In: *Proceedings of the Combustion Institute* 36.2 (2017), pp. 2493–2502.

[38] Fiorina, Benoit, Gicquel, O, Vervisch, L, Carpentier, S, and Darabiha, N. "Approximating the chemical structure of partially premixed and diffusion counterflow flames using FPI flamelet tabulation". In: *Combustion and flame* 140.3 (2005), pp. 147–160.

[39] Knudsen, E and Pitsch, H. "A general flamelet transformation useful for distinguishing between premixed and non-premixed modes of combustion". In: *Combustion and flame* 156.3 (2009), pp. 678–696.

[40] Lamouroux, Jean, Ihme, Matthias, Fiorina, Benoit, and Gicquel, Olivier. "Tabulated chemistry approach for diluted combustion regimes with internal recirculation and heat losses". In: *Combustion and flame* 161.8 (2014), pp. 2120–2136.

[41] Illana, Enric, Mira, Daniel, and Mura, Arnaud. "An extended flame index partitioning for partially premixed combustion". In: *Combustion Theory and Modelling* 25.1 (2021), pp. 121–157.

[42] Mehta, RS, Haworth, Daniel Connell, and Modest, MF. "Composition PDF/photon Monte Carlo modeling of moderately sooting turbulent jet flames". In: *Combustion and Flame* 157.5 (2010), pp. 982–994.

[43] Reddy, Manedhar, De, Ashoke, and Yadav, Rakesh. "Effect of precursors and radiation on soot formation in turbulent diffusion flame". In: *Fuel* 148 (2015), pp. 58–72.

[44] Stöhr, M. et al. "Time-resolved study of transient soot formation in an aero-engine model combustor at elevated pressure". In: *Proceedings of the Combustion Institute* 37.4 (2019), pp. 5421–5428. DOI: https://doi.org/10.1016/j.proci.2018.05.122.

[45] Litvinov, Ivan et al. "Time-resolved study of mixing and reaction in an aero-engine model combustor at increased pressure". In: *Combustion and Flame* 231 (2021), p. 111474. DOI: https://doi.org/10.1016/j.combustflame.2021.111474.

[46] Chong, Shao Teng, Raman, Venkat, Mueller, Michael E., Selvaraj, Prabhu, and Im, Hong G. "Effect of soot model, moment method, and chemical kinetics on soot formation in a model aircraft combustor". In: *Proceedings of the Combustion Institute* 37.1 (2019), pp. 1065–1074. DOI: https://doi.org/10.1016/j.proci.2018.06.093.

Chapter 6

Conclusions and future works

This final chapter aims to summarize all the work carried out during the present dissertation, as well as presenting the main conclusions and achievements obtained. First, the objectives defined initially are reviewed and the main tasks presented in each chapter and the most relevant findings are summarized in order to evaluate the fulfillment of the different goals. Finally, the main uncovered questions of this work are discussed to propose new possible research directions or future investigations on combustion and pollutant emissions modelling in aeronautical applications.

6.1 Conclusions

Turbulent combustion remains a topic of particular interest with regard to the transport sector and, in particular, the aviation industry. The environmental impact of greenhouse gases as well as the harmful health effects of pollutant emissions have prompted the study of combustion systems and the search for ever cleaner propulsion plants. In this context, numerical simulations arise as an excellent alternative for the analysis of the reacting flow and further understanding of the processes leading to pollutant generation. More specifically, high-fidelity large-eddy simulations (LES) provide a valuable predictive tool for the study of complex physical and chemical phenomena characteristic of advanced combustion systems. In the present thesis, the assessment of a complete modelling framework for turbulent combustion which accounts for multiphase flow and soot prediction has been presented in different cases based

on gas turbine applications. The present modelling approach, implemented in the multi-physics simulation code Alya, has been evaluated using high-fidelity LES in the context of high-performance computing (HPC) systems. Three main objectives were initially defined to guide the tasks carried out in this work:

- The consolidation of a computational methodology for the study of combustion and soot formation in representative aeronautical burners using high-fidelity LES with tabulated chemistry methods, in order to maintain affordable computational cost for realistic applications.
- The study of liquid fuel combustion in a reference spray flame application.
- The analysis of the reacting flow and soot formation and oxidation in a representative aeronautical combustor.

The tasks carried out in pursuit of these objectives, as well as the main conclusions extracted, are summarized below.

In view of the set of tasks presented in the previous chapters, it can be concluded that the present thesis has served to define a general working methodology for combustion modelling and soot prediction in aeronautical applications. Two relevant case studies have been selected and have been simulated with a flexible numerical modelling framework adaptable to the complex processes expected to be studied in each of the applications. The use of HPC systems to perform high fidelity LES has allowed to evaluate realistic configurations, including all the geometrical elements of the burners in order to perform detailed analysis and obtain state-of-the-art results.

The general modelling framework based on a flexible tabulated chemistry approach was presented in Chapter 3. In this regard, a flamelet-based turbulent combustion model (based on the well-known FGM model) was introduced coupled to a Lagrangian approach for multi-phase flows and a Discrete Sectional Method for soot prediction. This work has made it possible to evaluate this modelling approach and to test its validity in predicting and studying several representative phenomena of gas turbine combustion systems. The present framework has demonstrated its capabilities to model complex flow structures typical of swirled burner configurations, the interaction between liquid fuel droplets and the flame front, local extinction phenomena or soot formation and oxidation processes, as well as soot particle size distributions. In addition, the proposed modelling strategy based on the tabulation of steady

counterflow diffusion flamelets and the unsteady extinguishing continuation of the manifold has proven to be valid in the burner configurations studied, providing a good accuracy in the reacting flow predictions and correctly representing the flame structure.

In Chapter 4, large-eddy simulations of a reference spray flame have been performed using the previously mentioned modelling framework, which considers a Eulerian-Lagrangian description of the two-phase flow. A Lagrangian Particle Tracking approach has been used to evaluate the characteristics of the dispersed phase with two-way coupling with the carrier phase. For turbulent combustion modelling, a tabulated chemistry approach has been considered, based on the tabulation of steady and unsteady extinguishing diffusion flamelets at different enthalpy levels to account for heat loss during droplet evaporation. The selected configuration corresponds to the Coria-Rouen Spray Burner (CRSB), which has been consolidated as a reference case for turbulent combustion of sprays and has been used in this thesis to study the characteristics of the spray-flame, droplet-flame interactions and local extinction. The most relevant conclusions extracted from this work are summarized in the next paragraphs:

- The Eulerian-Lagrangian modelling approach has shown excellent capabilities to capture the flow field, the spray and the relevant combustion parameters. An assessment of the predictions of the liquid phase and flow characteristics have been conducted and good agreement with the experimental measurements was achieved for droplet and gas velocities and fluctuations. The numerical results were able to predict the flame topology and identify the different regions of the flame. In particular, the numerical results successfully predicted the flame lift-off-length and the wrinkled shape and position of the inner flame.

- In addition to the validation, the most innovative part of the work presented in Chapter 4 is the study and characterization of the extinction phenomena occurring in different regions of the spray flame. This analysis has evidenced that the proposed modelling framework is able to reproduce the transient extinction events in the inner reaction zone of the flame and can be used to investigate flame extinction and re-ignition in combustion problems. In this case, the flame exhibits localized extinction in the inner reaction zone close to the leading edge due to the interaction of the droplets with the flame front, while extinction events also occur further downstream in the inner region due to the high turbulence level.

- Close to the injector and near the leading edge, the simulations show a strong interaction between droplets and the flame front, which is also confirmed by the experimental results. The flame front shows some intermittency on the OH concentration with the presence of high values of CH_2O indicating the existence of localized extinction. The analysis of the evaporation source term evidences the relationship between the formation of fuel rich pockets and the quenching process. Calculation results show a decrease in temperature close to the stoichiometric mixture fraction contours when the droplets cross the flame front, coinciding with a spatial intermittency in the OH signal, which correspond to locations of high evaporation rates.

- A similar behaviour is found downstream in the inner region of the flame. In this case, the extinction of the flame is associated to the stretching of the reacting front produced by high levels of turbulence in the flow field. In this study, this interaction has been quantified in terms of the scalar dissipation rate along with OH and CH_2O concentrations. It was shown that when the scalar dissipation rate reaches high values near the reaction zone, the flame front becomes thinner and wrinkled until it eventually quenches. Quenching was shown to occur when the front is affected by high scalar dissipation rates during certain time. This process is characterized by larger time-scales than the extinction by droplet-flame interactions.

- The similarity of the resulting OH and CH_2O concentration during the two types of extinction events suggests that CH_2O can be used as an indicator to predict unsteady combustion phenomena such as localized extinction.

Chapter 5 was focused mainly on soot predictions in a representative aero-engine model combustor. The main contribution of this work consist on the assessment of a detailed method for soot prediction in a reference case of turbulent flames. In addition, a computationally efficient implementation of the soot model within the LES framework has allowed to analyze soot formation in the complex geometry of a complete burner configuration. For this purpose, the DLR pressurized burner has been selected for the study, which includes additional ducts downstream the combustion chamber for secondary air injection, features the usual characteristics of the RQL combustor concept and is a reference case for soot analysis. In this work, both configurations with and without dilution air have been considered for the analysis.

The proposed general modelling approach has been employed using a tabulated chemistry method for turbulent combustion based on diffusion flamelets at different strain rates and enthalpy levels coupled to a Discrete Sectional Method for soot modelling using clustered sections (CDSM) and tabulated soot source terms in the FGM manifold. The main findings and conclusions obtained in this study are synthesised below:

- The swirled flow characteristics, complex turbulent structures and recirculations regions inside the RQL-like burner have been properly captured by LES. The assessment of the gas phase has evidenced a really good agreement with the experimental measurements in terms of both velocity and temperature fields. Adiabatic and non-adiabatic modelling approaches have been tested and relevant discrepancies have found on the prediction of the temperature field and combustion characteristics. The non-adiabatic approach has demonstrated a noticeable improvement for capturing the temperature profiles and OH mass fraction field specially in the corner recirculation region, where the residence time is higher and the effects of heat losses to the walls are more important.

- Turbulent combustion scales and regimes have been estimated for this application. The identification of different points inside the combustion chamber on the typical $Da_t - Re_t$ diagram for turbulent diffusion flames has evidenced the suitability of the tabulated flamelet-based combustion model, showing really high turbulent Damkhöler numbers at any location corresponding to the flamelet regime. In addition, an adequate flame index definition has been employed to identify the combustion modes, indicating a non-premixed controlled combustion regime in most of the combustion chamber. However, minor premixed zones were found in the main combustion region and it would be interesting to extend the modelling approach in order to include premixing effects.

- A detailed analysis of soot production has been performed on the baseline configuration with secondary oxidation air. First, soot results have been evaluated and compared with experiments, showing good predictions of soot distribution in the combustion chamber and a satisfactory agreement on the Soot Volume Fraction magnitude. Regarding the effect of heat losses, relevant discrepancies in results have been found when considering a non-adiabatic approach, obtaining a slightly better agreement in SVF fields. Furthermore, the present modelling approach has been able to reproduce the transient soot processes and dynamics, reliably capturing the different regions where soot is formed and oxidized.

The analysis of the different soot source term contributions reveals that soot production in the DLR burner is primarily controlled by surface growth, which occurs at the near-nozzle rich pockets and persists downstream surrounding the lean inner recirculation region affected by the secondary air.

- Particle Size Distributions have been obtained with the results provided by the clustered sectional soot model. The analysis covers both the temporal evolution of the local PSDF and the spatial-averaged function. In general, an almost uni-modal PSD shape is obtained where the mixture fraction magnitude is high (over $\sim$0.1) and, thus, SVF soot production is important. Moreover, the model is able to capture the decrease in the number of particles, especially for small sizes, when the local fuel-air ratio approaches to the stoichiometric conditions and the PSDF evolves towards a bi-modal shape. It is worth to mention that the clustered sectional approach is able to predict different PSDF shapes according to spatial and temporal variations of soot clusters. Unfortunately, PSD results have not been validated due to the unavailability of their measurement data.

- Finally, the effect of excluding the secondary oxidation air has been evaluated by analyzing the corresponding numerical results. This configuration has shown a similar flow pattern than the baseline operating condition, however, the flame shape and combustion characteristics is quite different downstream due to the absence of dilution air. In general, a good agreement with the measured data has been obtained in terms of velocity, temperature and OH mass fraction fields. Soot predictions have been also analyzed in this configuration and a satisfactory agreement has been obtained in the SVF field. Although a slight underprediction of the peak SVF level has been observed, the overall distribution and magnitude have been correctly predicted, specially downstream in the central region. The present modelling approach has demonstrated to accurately predict the soot amount and distribution in both burner configurations (i.e. with and without dilution air), which has been a challenge for previous modelling strategies used in the literature, especially with regard to soot prediction in the configuration without secondary oxidation air. PSD functions have been also recovered for this case and compared with the previous operating condition. While size distributions are quite similar in the main soot formation region for both cases, the IRZ evidences a slightly different PSDF. Due to the absence of the secondary

jets, the central zone of the burner is not affected by soot formation or consumption and the PSDF is slightly modified by soot dilution.

6.2 Future works

In general, the main objectives proposed in Chapter 1 have been covered with the different tasks presented in this document. Nevertheless, there remain some open questions and opportunities for improvement from this research work. The possible future investigations and research guidelines are summarized in this section.

Regarding the modelling approach for turbulent combustion and soot prediction, it would be interesting to evaluate additional strategies or take into account different considerations.

- The proposed tabulated chemistry modelling approach has demonstrated to perform really well in gas turbine applications and the presented analysis and results obtained confirm this. However, this tabulated framework does not consider multi-regime effects and could be insufficient for partially premixed combustion systems. Therefore, it would be appropriate to evaluate the tabulation of premixed flamelets, or extend the modelling framework to flamelet manifolds which contain premixed and non-premixed effects [1, 2]. On the other hand, the strategy followed for the flamelet tabulation only considers the steady state of the one-dimensional flames and the unsteady behaviour of the extinguishing branch at the extinction strain rate. Re-ignition or extinction from the S-curve (at intermediate strains) are not included in the manifold and, therefore, possible thermochemical states that may be relevant to re-ignition processes or soot formation in flames are not considered. The evaluation of tabulated chemistry methods which include unsteady flamelets at different strain rates in the composition of the manifold (for instance, UFPV-like models [3]) could be adequate for further analyze these phenomena.

- The accuracy of the FGM-CDSM modelling approach for soot prediction could be further improved and there are still some tasks to be addressed in order to further evaluate its performance. On the one hand, it would be interesting to evaluate the sensitivity of soot predictions with the CDSM to some parameters. For instance, the effect of the number of clusters has been evaluated for laminar flames in terms of accuracy and

computational cost, but it has not been checked in turbulent cases. On the other hand, the limitations of the modelling approach highlight the need to investigate and explore other modelling strategies. For example, the clustering strategy may lead to loss of information as to how the different mechanisms of soot formation and oxidation affect the soot sections. In this regard, revising the strategy or developing better post-processing tools could allow for more detailed analysis. In addition, the linearization of soot consumption in the computation of soot source terms is considered in the present approach and the accuracy of the CDSM model could be further improved by considering more complex non-linear effects of the soot production and consumption rates.

Some additional tasks may be carried out with regard to the validation of the proposed modelling approach in different turbulent flames.

- In the context of turbulent flames, soot investigations from both a numerical and an experimental point of view have commonly been carried out in jet flame configurations or model burners operating with gaseous fuels (such as the DLR burner presented in Chapter 5). However, since fuel is generally injected in the liquid phase in many practical applications, the analysis of soot formation may be extended to spray flames. An additional task derived from this work could be the evaluation of the soot modelling approach employed in Chapter 5 in an experimentally tested reacting spray jet or liquid-fueled swirl-stabilized flame [4–7]. Indeed, soot measurements of the CRSB have been recently published [8] and Chapter 4 may be extended to soot predictions and analysis.

- In view of the results presented in Chapter 5, the LES-FGM-CDSM modelling approach has demonstrated its capabilities of recovering the PSD function. In addition, the sectional method has been able to provide different PSDF shapes depending on the soot processes taking place in the combustion chamber, thus allowing a detailed analysis. Nevertheless, the absence of experimental measurements on the DLR combustor has made it impossible to validate the PSD predictions. A final step in the assessment of the soot modelling approach would be the comparison of the particle distributions with experimental measurements available in the literature for turbulent flames.

References

[1] Knudsen, E and Pitsch, H. “Capabilities and limitations of multi-regime flamelet combustion models”. In: *Combustion and Flame* 159.1 (2012), pp. 242–264.

[2] Illana, Enric, Mira, Daniel, and Mura, Arnaud. “An extended flame index partitioning for partially premixed combustion”. In: *Combustion Theory and Modelling* 25.1 (2021), pp. 121–157.

[3] Pitsch, Heinz and Ihme, Matthias. “An unsteady/flamelet progress variable method for LES of nonpremixed turbulent combustion”. In: *43rd AIAA Aerospace Sciences Meeting and Exhibit*. 2005, p. 557.

[4] Inagaki, Kazuhisa, Takasu, Semon, and Nakakita, Kiyomi. “In-cylinder quantitative soot concentration measurement by laser-induced incandescence”. In: *SAE transactions* (1999), pp. 574–586.

[5] Skeen, Scott A et al. “A progress review on soot experiments and modeling in the engine combustion network (ECN)”. In: *SAE International Journal of Engines* 9.2 (2016), pp. 883–898.

[6] Meyer, Terrence R, Roy, Sukesh, Belovich, Vincent M, Corporan, Edwin, and Gord, James R. “Simultaneous planar laser-induced incandescence, OH planar laser-induced fluorescence, and droplet Mie scattering in swirl-stabilized spray flames”. In: *Applied optics* 44.3 (2005), pp. 445–454.

[7] Wang, Lu-Yin, Bauer, Cody K, and Gülder, Ömer L. “Soot and flow field in turbulent swirl-stabilized spray flames of Jet A-1 in a model combustor”. In: *Proceedings of the Combustion Institute* 37.4 (2019), pp. 5437–5444.

[8] Mulla, Irfan A and Renou, Bruno. “Simultaneous imaging of soot volume fraction, PAH, and OH in a turbulent n-heptane spray flame”. In: *Combustion and Flame* 209 (2019), pp. 452–466.

Appendices

Appendix A

Effect of the computational grid in the CRSB

Besides the grid assessment presented in Section 4.1.3 based on the usual LES quality criteria, the numerical results using the reference mesh for the CRSB and a finer mesh are presented in this appendix. First, Fig. A.1 illustrates both computational grids, colored by the filter size Δx (being $\Delta x = \sqrt[3]{V_{cell}}$). Note that the 20M element mesh is the reference mesh introduced in Section 4.1.3 and used for the analysis presented in Chapter 4. A finer mesh containing around 79M of elements has been also evaluated in order to check grid convergence. The first refinement is applied to the near-nozzle region, which includes the nozzle ducts, the close injection zone, the leading edge of the flame and the first part of the inner reacting front (named as R1 in the figure). In this region, the filter size is refined from 0.2 mm in the reference grid to 0.12 mm in the fine grid. The second region (R2) comprises almost the entire flame, which includes the inner and outer flame fronts up to ∼70 mm downstream. In this case, the filter size evolves from 0.4 mm to 0.2 mm.

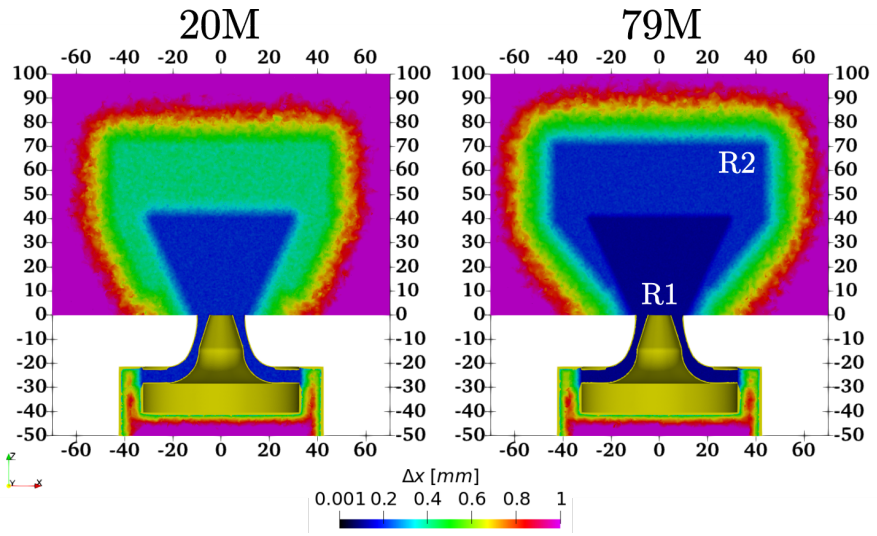

Figure A.1: Different meshes evaluated in the CRSB. Color: filter size Δx.

The velocity field is presented in Fig. A.2 for the different computational grids. Due to the availability of the experimental results, the velocity profiles at the same stations selected in Section 4.2 are also illustrated here. In addition, the axial velocity at centerline is compared between both numerical cases to check the evolution at the burner axis. In general, no relevant discrepancies are observed in the results for the different meshes and both mean and RMS values are predicted with a similar accuracy. Very slight discrepancies can be found for the fluctuating magnitude at 40 mm station and high radial positions (R $\sim$ 15 mm) but overall, the grid refinement has almost no effect on the velocity statistics.

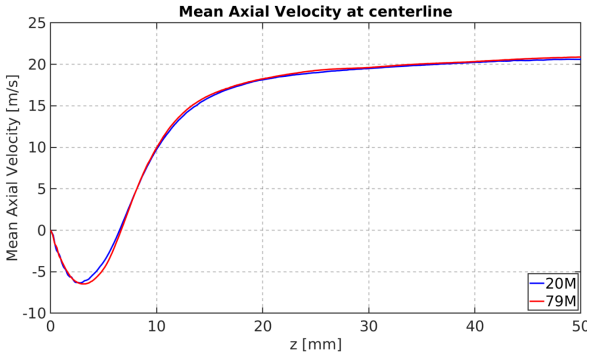

(a) Mean axial velocity at centerline.

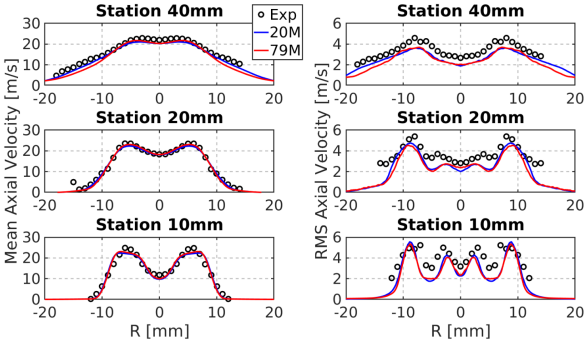

(b) Axial velocity at stations.

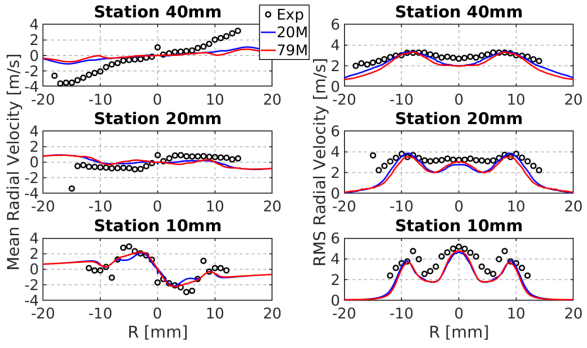

(c) Radial velocity at stations.

Figure A.2: Comparison of velocity field in the CRSB. Lines: LES with different computational grids. Symbols: experiments.

Appendix B

Effect of the computational grid in the DLR burner

The grid quality analysis performed in Section 5.2.1 is complemented in this appendix with the numerical results of the flow in the DLR burner using meshes with different refinements. Fig. B.1 shows the three grids evaluated, being the 53M element mesh the reference grid employed during the analysis performed in Chapter 5. Note that the grid assessment is only applied to the configuration with secondary oxidation air (Op 1). A coarser mesh has been evaluated which is composed of ∼14M elements. In terms of the refinement regions, it is quite similar to the reference mesh and the only difference lies in the element size in all zones, which has been doubled compared to the reference values. It is worth mentioning that the element size in the fuel injection nozzle has not been modified due to the narrowness of the duct. Although Section 5.2.1 in Chapter 5 evidences a very good flow resolution for the reference mesh (in terms of Pope's criterion and the comparison between the filter size and Kolmogorov scales), a finer grid is also evaluated in order to check the effect on the predictive capabilities of the combustion model. This mesh contains up to 80M elements and the refinement affects primarily to three regions. First, the injection zone and the main combustion region is further refined. On the one hand, a very fine refinement (up to $\Delta x \sim 0.075$ mm) is applied to the shear layers, where fuel is mixed with the air coming from the primary and secondary ducts of the swirled injection system. On the other hand, the refinement cone already present in the reference mesh ($\Delta x \sim 0.15$

mm) is extended downstream, in order to fully cover the main combustion region. The second refinement is applied downstream the combustion chamber in order to homogenise the element size. Therefore, a constant filter size of $\sim$0.25 mm is specified up to $z \sim 100$ mm.

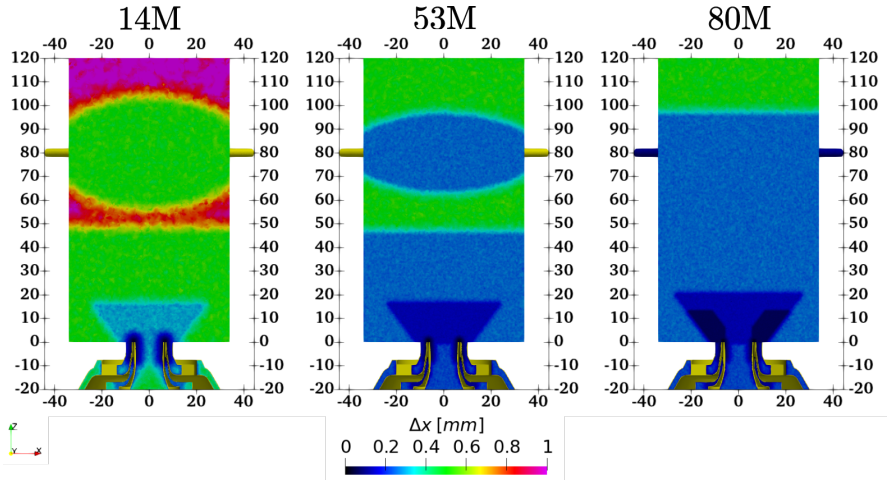

Figure B.1: Different meshes evaluated in the DLR burner. Color: filter size Δx.

Fig. B.2 illustrates the comparison between both meshes and the experiments in terms of velocity components. In general, the three computational grids provide very similar statistics for the three components. Notable discrepancies are found at the 80 mm station, where the secondary jets induce high flow disruption. In this region, the fine mesh (80M) seems to provide slightly better results, specially for the velocity fluctuation. In addition, the coarse mesh (14M) is not able to capture the near-nozzle profiles with the same accuracy (see 6 mm station). With this grid, a slightly narrower swirled jet is obtained compared to the experiments and to the 53M and 80M element meshes.

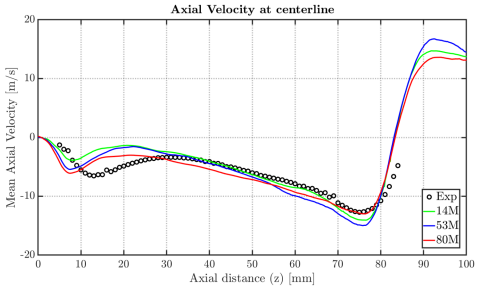

(a) Mean axial velocity at centerline.

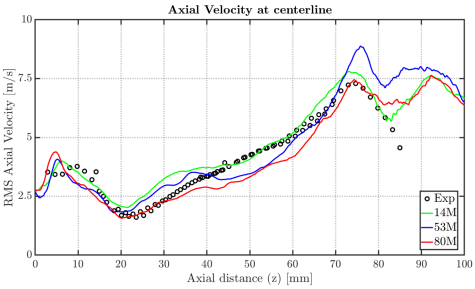

(b) RMS axial velocity at centerline.

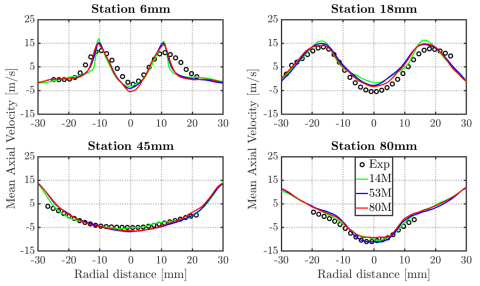

(c) Mean axial velocity at stations.

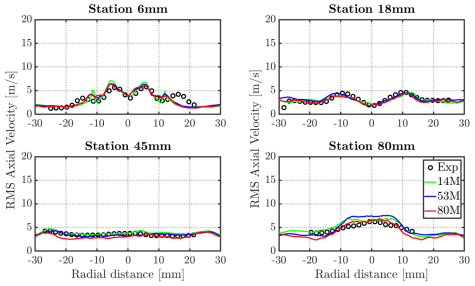

(d) RMS axial velocity at stations.

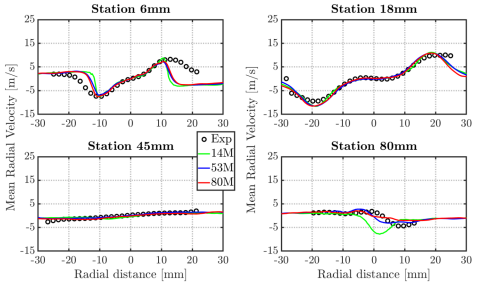

(e) Mean radial velocity at stations.

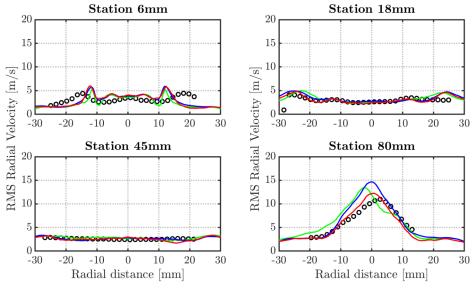

(f) RMS radial velocity at stations.

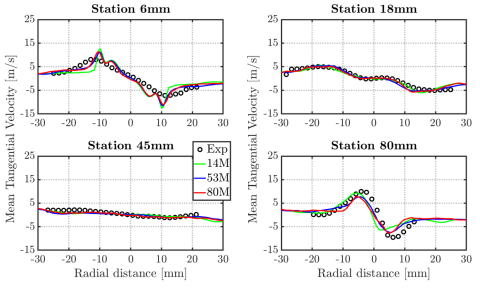

(g) Mean tangential velocity at stations.

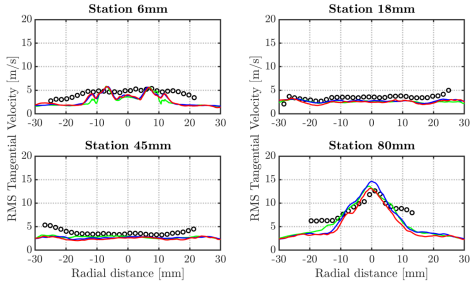

(h) RMS tangential velocity at stations.

Figure B.2: Comparison of velocity components in the DLR burner. Lines: LES with different computational grids. Symbols: experiments.

Temperature field and statistics are presented in Fig. B.3 and similar conclusions can be extracted. Although the discrepancies between numerical grids are higher in temperature statistics compared to the velocity field, all cases provide quite similar profiles and statistics are accurately predicted. In view of these results and the slightly higher discrepancies of the coarse mesh close to the combustion chamber entry, the 53M element grid has been retained for the analysis.

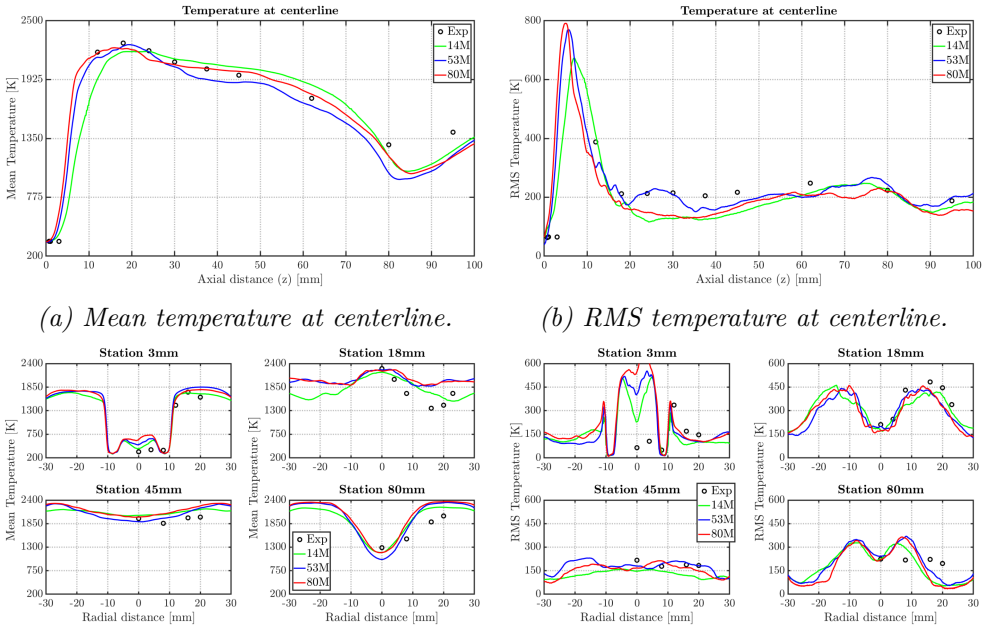

(a) Mean temperature at centerline. *(b) RMS temperature at centerline.*

(c) Mean temperature at stations. *(d) RMS temperature at stations.*

Figure B.3: Comparison of temperature field in the DLR burner. Lines: LES with different computational grids. Symbols: experiments.

Appendix C

Temporal statistics in the DLR burner

In this appendix, additional results of the DLR burner are presented considering different time windows for the temporal statistics. In order to achieve the convergence of velocity, temperature and soot field statistics, three temporal windows have been considered, which are summarized in Table C.1. Note that each case is characterized by the total averaging time and its equivalence in flow-through times. In the DLR burner, one flow-through time is approximately 23 ms, which has been estimated computing the averaged axial velocity integrated over the full combustion chamber volume. Besides the temporal averaging, two perpendicular planes (XZ and YZ planes, see the reference system in Fig. 5.10) have been considered for computing the final statistics.

Case ID	Averaging time	Flow-through times
2FT	46 ms	2
4FT	90 ms	4
5FT	115 ms	5

Table C.1: Summary of the time windows considered for temporal statistics.

Velocity and temperature profiles at stations are shown in Fig. C.1. As observed, the temporal windows considered for the analysis have no effect on velocity and temperature statistics. Even the lowest averaging time, corre-

sponding to two flow-through times, is sufficient to obtain good gas phase statistics.

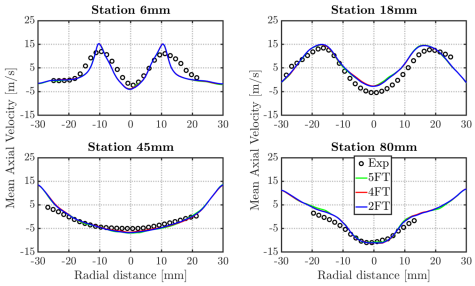

(a) Mean axial velocity at stations.

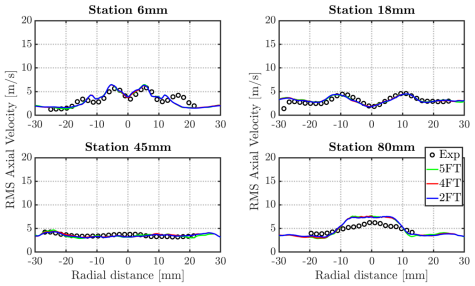

(b) RMS axial velocity at stations.

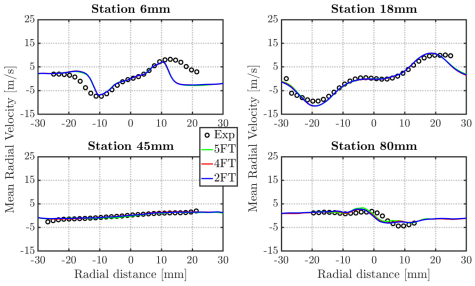

(c) Mean radial velocity at stations.

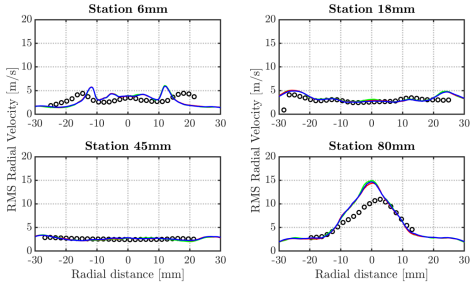

(d) RMS radial velocity at stations.

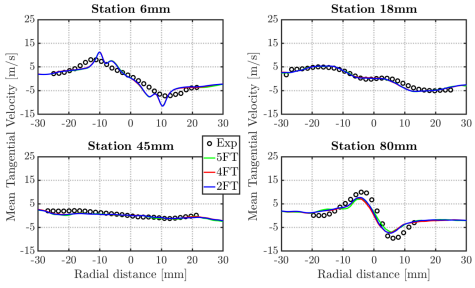

(e) Mean tangential velocity at stations.

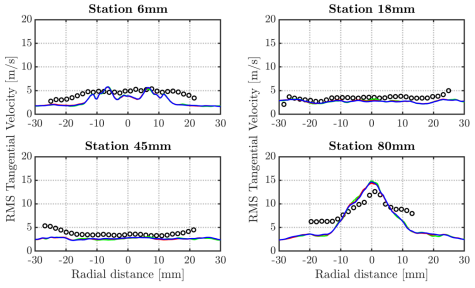

(f) RMS tangential velocity at stations.

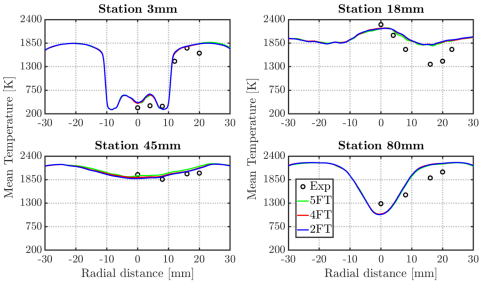

(g) Mean temperature at stations.

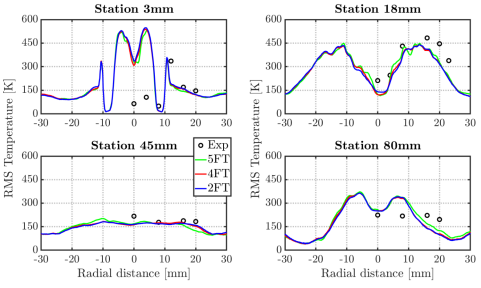

(h) RMS temperature at stations.

Figure C.1: Velocity and temperature fields at stations in the DLR burner. Lines: LES with different averaging time. Symbols: experiments.

However, a more relevant effect of the averaging time is observed when comparing the mean SVF field at stations, which is illustrated in Fig. C.2. As appreciated at stations 18 and 45 mm, the SVF field becomes more symmetric when increasing the temporal window. 2FT provides a considerably more asymmetric soot profile compared with 4FT, which is further improved by 5FT. Furthermore, increasing the averaging time also affects the SVF peak at the region close to the onset of soot (see 6 mm station) and 5FT case provides a slightly better agreement with experiments. Therefore, although the gas-phase is completely converged even for shorter time windows, an averaging time equivalent to 5 flow-through times has been retained in order to properly capture soot statistics.

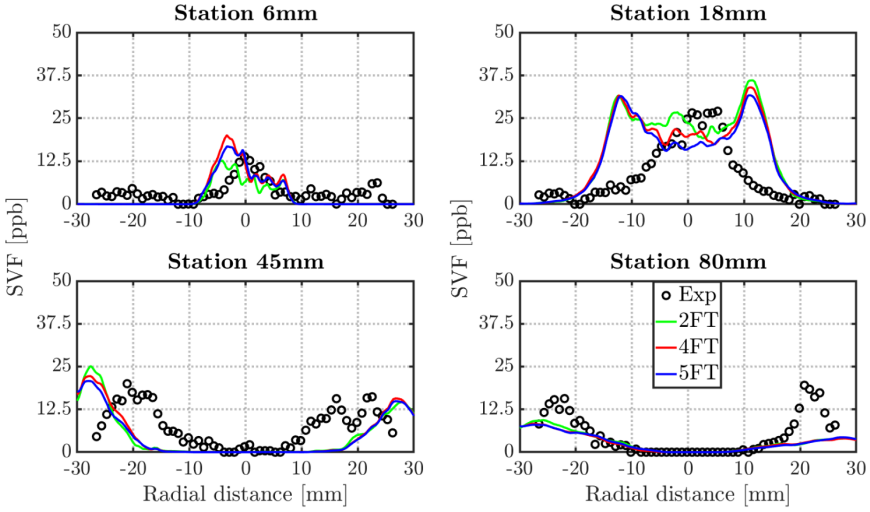

Figure C.2: SVF field at stations in the DLR burner. Lines: LES with different averaging time. Symbols: experiments.

Global Bibliography

Abdel-Gayed, RG, Bradley, Derek, and Lung, FK-K. "Combustion regimes and the straining of turbulent premixed flames". In: *Combustion and Flame* 76.2 (1989), pp. 213–218 (cited on page 41).

Abdelsamie, Abouelmagd and Thévenin, Dominique. "Direct numerical simulation of spray evaporation and autoignition in a temporally-evolving jet". In: *Proceedings of the Combustion Institute* 36.2 (2017), pp. 2493–2502 (cited on page 189).

Abramzon, B and Sirignano, W A. "Droplet vaporization model for spray combustion calculations". In: *International journal of heat and mass transfer* 32.9 (1989), pp. 1605–1618 (cited on page 106).

ACARE. *Strategic Research and Innovation Agenda, The goals of Flightpath 2050.* 2017 (cited on page 4).

Adams, Nikolaus A and Soltz, S. "Deconvolution methods for subgrid-scale approximation in large-eddy simulation". In: *Modern simulation strategies for turbulent flow.* RT Edwards, Inc, 2001 (cited on page 35).

Alessandro, D'Ausilio, Stankovic, Ivana, and Merci, Bart. "LES study of a turbulent spray jet: mesh sensitivity, mesh-parcels interaction and injection methodology". In: *Flow, Turbulence and Combustion* 103 (2019), pp. 537–564 (cited on page 128).

Alkabie, HS, Andrews, GE, and Ahmad, NT. "Lean low NOx primary zones using radial swirlers". In: *Turbo Expo: Power for Land, Sea, and Air.* Vol. 79207. American Society of Mechanical Engineers. 1988, V003T06A027 (cited on page 8).

Anderson, RD, Herman, AS, Tomlinson, JG, Vaught, JM, and Verdouw, AJ. *Pollution Reduction Technology Program, Turboprop Engines, Phase 1.* Tech. rep. 1976 (cited on page 5).

Angelberger, Christian, Veynante, Denis P., Egolfopoulos, Fokion N., and Poinsot, Thierry. "Large eddy simulations of combustion instabilities in premixed flames". In: 1999 (cited on page 49).

Appel, Jörg, Bockhorn, Henning, and Frenklach, Michael. "Kinetic modeling of soot formation with detailed chemistry and physics: laminar premixed flames of C2 hydrocarbons". In: *Combustion and Flame* 121.1-2 (2000), pp. 122–136 (cited on page 100).

Applied Computational Fluid Dynamics. *DNS, LES and URANS.* Youtube. 2020. URL: https://www.youtube.com/watch?v=6wEgC5H9yLg&ab_channel=AppliedComputationalFluidDynamics (cited on page 29).

Attili, Antonio, Bisetti, Fabrizio, Mueller, Michael E., and Pitsch, Heinz. "Damköhler number effects on soot formation and growth in turbulent non-premixed flames". In: *Proceedings of the Combustion Institute* 35.2 (2015), pp. 1215–1223. DOI: https://doi.org/10.1016/j.proci.2014.05.084 (cited on page 57).

Aubagnac-Karkar, Damien, El Bakali, Abderrahman, and Desgroux, Pascale. "Soot particles inception and PAH condensation modelling applied in a soot model utilizing a sectional method". In: *Combustion and Flame* 189 (2018), pp. 190–206. DOI: https://doi.org/10.1016/j.combustflame.2017.10.027 (cited on page 53).

Bagchi, Prosenjit and Balachandar, S. "Response of the wake of an isolated particle to an isotropic turbulent flow". In: *Journal of Fluid Mechanics* 518 (2004), pp. 95–123 (cited on page 62).

Bahr, DWand and Gleason, CC. *Experimental clean combustor program, phase 1.* Tech. rep. 1975 (cited on page 7).

Balakrishnan, G and Williams, FA. "Turbulent combustion regimes for hypersonic propulsion employing hydrogen-air diffusion flames". In: *Journal of Propulsion and Power* 10.3 (1994), pp. 434–437 (cited on page 188).

Balthasar, M and Kraft, M. "A stochastic approach to calculate the particle size distribution function of soot particles in laminar premixed flames". In: *Combustion and Flame* 133.3 (2003), pp. 289–298. DOI: https://doi.org/10.1016/S0010-2180(03)00003-8 (cited on page 55).

Banchelli, Fabio, Garcia-Gasulla, Marta, Houzeaux, Guillaume, and Mantovani, Filippo. "Benchmarking of state-of-the-art HPC Clusters with a Production CFD Code". In: *Proceedings of the Platform for Advanced Scientific Computing Conference*. 2020, pp. 1–11 (cited on page 81).

Banchelli, Fabio et al. "A portable coding strategy to exploit vectorization on combustion simulations". In: *arXiv preprint arXiv:2210.11917* (2022) (cited on page 81).

Bao, Hesheng, Kalbhor, Abhijit, Maes, Noud, Somers, Bart, and Van Oijen, Jeroen. "Investigation of soot formation in n-dodecane spray flames using LES and a discrete sectional method". In: *Proceedings of the Combustion Institute* 39.2 (2023), pp. 2587–2597 (cited on page 82).

Bardina, Jorge, Ferziger, J, and Reynolds, WC. "Improved subgrid-scale models for large-eddy simulation". In: *13th fluid and plasmadynamics conference*. 1980, p. 1357 (cited on page 34).

Barré, David et al. "Flame propagation in aeronautical swirled multi-burners: Experimental and numerical investigation". In: *Combustion and Flame* 161.9 (2014), pp. 2387–2405 (cited on page 10).

Bayoro, F, Habachi, C, and Daniel, E. "Numerical and physical basis of an Eulerian multi-phase flow model for the simulation of the liquid injection in internal combustion engines". In: *Proceedings of the ILASS Europe Conference, Paper*. 2008, pp. 2–5 (cited on page 62).

Belmar Gil, Mario. "Computational study on the non-reacting flow in Lean Direct Injection gas turbine combustors through Eulerian-Lagrangian Large-Eddy Simulations". PhD thesis. Universitat Politècnica de València, 2021 (cited on page 8).

Benajes, J et al. "Large Eddy Simulations of a n-heptane spray flame with local extinction". In: *3rd Edition of the HPC Spanish Combustion Workshop 2021*. 2021 (cited on page 119).

Benajes, J et al. "Analysis of local extinction of a n-heptane spray flame using large-eddy simulation with tabulated chemistry". In: *Combustion and Flame* 235 (2022), p. 111730 (cited on pages 81, 119).

Bilger, R. W. "Conditional moment closure for turbulent reacting flow". In: *Physics of Fluids A: Fluid Dynamics* 5.2 (1993), pp. 436–444. DOI: 10.1063/1.858867 (cited on page 50).

Blanquart, G. and Pitsch, H. "Analyzing the effects of temperature on soot formation with a joint volume-surface-hydrogen model". In: *Combustion and Flame* 156.8 (2009), pp. 1614–1626. DOI: https://doi.org/10.1016/j.combustflame.2009.04.010 (cited on page 54).

Borghi, R. “On the structure and morphology of turbulent premixed flames”. In: *Recent Advances in the Aerospace Sciences: In Honor of Luigi Crocco on His Seventy-fifth Birthday*. Springer, 1985, pp. 117–138 (cited on page 41).

Borrell, Ricard et al. “Parallel mesh partitioning based on space filling curves”. In: *Computers & Fluids* 173 (2018), pp. 264–272 (cited on page 81).

Borrell, Ricard et al. “Heterogeneous CPU/GPU co-execution of CFD simulations on the POWER9 architecture: Application to airplane aerodynamics”. In: *Future Generation Computer Systems* 107 (2020), pp. 31–48 (cited on page 81).

Both, A. “RANS-FGM simulation of n-heptane spray flame in OpenFOAM”. MA thesis. Delft University of Technology, 2017 (cited on pages 118, 121, 129).

Both, Ambrus. “High-fidelity numerical simulations of reacting flows with tabulated chemistry”. PhD thesis. Universitat Politècnica de Catalunya, 2023 (cited on pages 59, 82, 83, 86, 87, 93, 106, 176).

Both, Ambrus, Lehmkuhl, Oriol, Mira, D, and Ortega, Marc. “Low-dissipation finite element strategy for low Mach number reacting flows”. In: *Computers & Fluids* 200 (2020), p. 104436 (cited on pages 85, 86, 94).

Both, Ambrus, Mira Martínez, Daniel, and Lehmkuhl Barba, Oriol. “Assessment of tabulated chemistry models for the les of a model aero-engine combustor”. In: *Proceedings of Global Power and Propulsion Society, GPPS Chania22, 18th-20th September, 2022*. Global Power and Propulsion Society (GPPS). 2022 (cited on page 81).

BP. *Statistical Review of World Energy*. 2020 (cited on page 1).

Brown, Peter N, Byrne, George D, and Hindmarsh, Alan C. “VODE: A variable-coefficient ODE solver”. In: *SIAM journal on scientific and statistical computing* 10.5 (1989), pp. 1038–1051 (cited on page 46).

Bruce, TW, Davis, FG, Kuhn, TE, and Mongia, HC. *Pollution Reduction Technology Program for Small Jet Aircraft Engines, Phase 2*. Tech. rep. 1978 (cited on pages 5, 7).

Buckmaster, John D. *The mathematics of combustion*. SIAM, 1985 (cited on page 48).

Burton, Tristan M and Eaton, John K. “Fully resolved simulations of particle-turbulence interaction”. In: *Journal of Fluid Mechanics* 545 (2005), pp. 67–111 (cited on page 62).

Butler, T.D. and O'Rourke, P.J. "A numerical method for two dimensional unsteady reacting flows". In: *Symposium (International) on Combustion* 16.1 (1977), pp. 1503–1515. DOI: https://doi.org/10.1016/S0082-0784(77)80432-3 (cited on page 49).

Buttay, R, Gomet, L, Lehnasch, G, and Mura, A. "Highly resolved numerical simulation of combustion downstream of a rocket engine igniter". In: *Shock Waves* 27 (2017), pp. 655–674 (cited on page 189).

Calcote, H.F. "Mechanisms of soot nucleation in flames—A critical review". In: *Combustion and Flame* 42 (1981), pp. 215–242. DOI: https://doi.org/10.1016/0010-2180(81)90159-0 (cited on page 53).

Calmet, Hadrien et al. "Computational modelling of an aerosol extraction device for use in COVID-19 surgical tracheotomy". In: *Journal of Aerosol Science* 159 (2022), p. 105848 (cited on page 81).

Chatelier, Adrien, Fiorina, Benoît, Moureau, Vincent, and Bertier, Nicolas. "Large Eddy Simulation of a Turbulent Spray Jet Flame Using Filtered Tabulated Chemistry". In: *Journal of Combustion* 2020 (2020). DOI: 10.1155/2020/2764523 (cited on pages 118, 121, 142).

CHEM1D. *A one dimensional flame code. Eindhoven University of Technology.* 2002 (cited on pages 88, 165).

Chiang, CH, Raju, MS, and Sirignano, WA. "Numerical analysis of convecting, vaporizing fuel droplet with variable properties". In: *International journal of heat and mass transfer* 35.5 (1992), pp. 1307–1324 (cited on page 59).

Chong, Shao Teng, Raman, Venkat, Mueller, Michael E., Selvaraj, Prabhu, and Im, Hong G. "Effect of soot model, moment method, and chemical kinetics on soot formation in a model aircraft combustor". In: *Proceedings of the Combustion Institute* 37.1 (2019), pp. 1065–1074. DOI: https://doi.org/10.1016/j.proci.2018.06.093 (cited on page 214).

Chong, Shao Teng et al. "Large eddy simulation of pressure and dilution-jet effects on soot formation in a model aircraft swirl combustor". In: *Combustion and Flame* 192 (2018), pp. 452–472. DOI: 10.1016/j.combustflame.2018.02.021 (cited on pages 162, 166, 199).

Christo, Farid C, Masri, Assaad R, Nebot, Eduardo Mario, and Pope, Stephen B. "An integrated PDF/neural network approach for simulating turbulent reacting systems". In: *Symposium (International) on Combustion.* Vol. 26. 1. Elsevier. 1996, pp. 43–48 (cited on page 47).

Clark, Robert A, Ferziger, Joel H, and Reynolds, William Craig. "Evaluation of subgrid-scale models using an accurately simulated turbulent flow". In: *Journal of fluid mechanics* 91.1 (1979), pp. 1–16 (cited on page 35).

Çokuslu, Ömer Hakkı, Hasse, Christian, Geigle, Klaus Peter, and Ferraro, Federica. "Soot prediction in a Model Aero-Engine Combustor using a Quadrature-based method of moments". In: *AIAA Science and Technology Forum and Exposition, AIAA SciTech Forum 2022* (2022), pp. 1–12. DOI: 10.2514/6.2022-1446 (cited on page 162).

Colin, O., Ducros, F., Veynante, D., and Poinsot, T. "A thickened flame model for large eddy simulations of turbulent premixed combustion". In: *Physics of Fluids* 12.7 (2000), pp. 1843–1863. DOI: 10.1063/1.870436 (cited on page 49).

Cordier, M, Vandel, Alexis, Cabot, G, Renou, B, and Boukhalfa, AM. "Laser-induced spark ignition of premixed confined swirled flames". In: *Combustion Science and Technology* 185.3 (2013), pp. 379–407 (cited on page 119).

D'Anna, A. and Kent, J.H. "A model of particulate and species formation applied to laminar, nonpremixed flames for three aliphatic-hydrocarbon fuels". In: *Combustion and Flame* 152.4 (2008), pp. 573–587. DOI: https://doi.org/10.1016/j.combustflame.2007.08.003 (cited on page 56).

De Villiers, E, Gosman, AD, and Weller, HG. "Large eddy simulation of primary diesel spray atomization". In: *SAE transactions* (2004), pp. 193–206 (cited on page 60).

Deardorff, JW. "The use of subgrid transport equations in a three-dimensional model of atmospheric turbulence". In: (1973) (cited on page 35).

Delhaye, S., Somers, L.M.T., van Oijen, J.A., and de Goey, L.P.H. "Incorporating unsteady flow-effects beyond the extinction limit in flamelet-generated manifolds". In: *Proceedings of the Combustion Institute* 32.1 (2009), pp. 1051–1058. DOI: https://doi.org/10.1016/j.proci.2008.06.111 (cited on page 89).

Dellinger, Nicolas, Bertier, Nicolas, Dupoirieux, Francis, and Legros, Guillaume. "Hybrid Eulerian-Lagrangian method for soot modelling applied to ethylene-air premixed flames". In: *Energy* 194 (2020), p. 116858. DOI: https://doi.org/10.1016/j.energy.2019.116858 (cited on page 56).

Desantes, JM et al. "LES Eulerian diffuse-interface modeling of fuel dense sprays near-and far-field". In: *International Journal of Multiphase Flow* 127 (2020), p. 103272 (cited on page 61).

Dhanuka, Sulabh K, Temme, Jacob E, and Driscoll, James F. "Unsteady aspects of lean premixed prevaporized gas turbine combustors: flame-flame interactions". In: *Journal of Propulsion and Power* 27.3 (2011), pp. 631–641 (cited on page 8).

Domingo, P., Vervisch, L., and Veynante, D. "Large-eddy simulation of a lifted methane jet flame in a vitiated coflow". In: *Combustion and Flame* 152.3 (2008), pp. 415–432. DOI: http://dx.doi.org/10.1016/j.combustflame.2007.09.002 (cited on pages 85, 92, 94).

Donini, A, M. Bastiaans, RJ, Van Oijen, JA, and H. de Goey, LP. "A 5-D implementation of FGM for the large eddy simulation of a stratified swirled flame with heat loss in a gas turbine combustor". In: *Flow, turbulence and combustion* 98 (2017), pp. 887–922 (cited on page 10).

Drew, Donald A and Passman, Stephen L. *Theory of multicomponent fluids*. Vol. 135. Springer Science & Business Media, 2006 (cited on page 62).

Dryer, Frederick L. "Chemical kinetic and combustion characteristics of transportation fuels". In: *Proceedings of the Combustion Institute* 35.1 (2015), pp. 117–144. DOI: https://doi.org/10.1016/j.proci.2014.09.008 (cited on page 117).

Dukowicz, John K. "A particle-fluid numerical model for liquid sprays". In: *Journal of computational Physics* 35.2 (1980), pp. 229–253 (cited on page 62).

EASA. *European Aviation Environmental Report 2022*. 2022 (cited on page 3).

Eaves, Nick A., Dworkin, Seth B., and Thomson, Murray J. "Assessing relative contributions of PAHs to soot mass by reversible heterogeneous nucleation and condensation". In: *Proceedings of the Combustion Institute* 36.1 (2017), pp. 935–945. DOI: https://doi.org/10.1016/j.proci.2016.06.051 (cited on page 53).

Eberle, Christian, Gerlinger, Peter, Geigle, Klaus Peter, and Aigner, Manfred. "Toward finite-rate chemistry large-eddy simulations of sooting swirl flames". In: *Combustion Science and Technology* 190.7 (2018), pp. 1194–1217. DOI: 10.1080/00102202.2018.1443444 (cited on page 162).

Echekki, Tarek and Mastorakos, Epaminondas. "Turbulent combustion modeling: Advances, new trends and perspectives". In: (2010) (cited on pages 28, 29, 45, 46, 50, 51).

Eisenklam, Paul, Arunachalam, SA, and Weston, JA. "Evaporation rates and drag resistance of burning drops". In: *Symposium (International) on combustion*. Vol. 11. 1. Elsevier. 1967, pp. 715–728 (cited on page 59).

Enright, Douglas, Fedkiw, Ronald, Ferziger, Joel, and Mitchell, Ian. "A hybrid particle level set method for improved interface capturing". In: *Journal of Computational physics* 183.1 (2002), pp. 83–116 (cited on page 61).

Ern, Alexandre and Giovangigli, Vincent. *Multicomponent transport algorithms*. Vol. 24. Springer Science & Business Media, 1994 (cited on page 23).

European Environment Agency. *EEA Report: Healthy environment, healthy lives: how the environment influences health and well-being in Europe*. 2020 (cited on page 3).

European Environment Agency. *Air pollution: how it affects our health*. 2021 (cited on page 1).

Faeth, GM. "Spray combustion phenomena". In: *Symposium (international) on combustion*. Vol. 26. 1. Elsevier. 1996, pp. 1593–1612 (cited on page 60).

Felden, Anne, Riber, Eleonore, and Cuenot, Benedicte. "Impact of direct integration of Analytically Reduced Chemistry in LES of a sooting swirled non-premixed combustor". In: *Combustion and Flame* 191 (2018), pp. 270–286. DOI: 10.1016/J.COMBUSTFLAME.2018.01.005 (cited on page 162).

Fiorina, Benoit, Gicquel, O, Vervisch, L, Carpentier, S, and Darabiha, N. "Approximating the chemical structure of partially premixed and diffusion counterflow flames using FPI flamelet tabulation". In: *Combustion and flame* 140.3 (2005), pp. 147–160 (cited on page 189).

Fiorina, Benoit et al. "Modelling non-adiabatic partially premixed flames using flame-prolongation of ILDM". In: *Combustion Theory and Modelling* 7.3 (2003), p. 449 (cited on pages 47, 123).

Foust, Michael, Thomsen, Doug, Stickles, Richard, Cooper, Clayton, and Dodds, Will. "Development of the GE aviation low emissions TAPS combustor for next generation aircraft engines". In: *50th AIAA aerospace sciences meeting including the new horizons forum and aerospace exposition*. 2012, p. 936 (cited on pages 7, 8).

Fox, R.O., Laurent, F., and Massot, M. "Numerical simulation of spray coalescence in an Eulerian framework: Direct quadrature method of moments and multi-fluid method". In: *Journal of Computational Physics* 227.6 (2008), pp. 3058–3088. DOI: https://doi.org/10.1016/j.jcp.2007.10.028 (cited on page 63).

Franzelli, B, Vié, A, Boileau, M, Fiorina, B, and Darabiha, N. "Large eddy simulation of swirled spray flame using detailed and tabulated chemical descriptions". In: *Flow, Turbulence and Combustion* 98 (2017), pp. 633–661 (cited on page 86).

Franzelli, B., Riber, E., Cuenot, B., and Ihme, M. “Numerical modeling of soot production in aero-engine combustors using large eddy simulations”. In: *Proceedings of the ASME Turbo Expo* 4B (2015). DOI: 10.1115/GT201543630 (cited on page 162).

Franzelli, B., Vié, A., and Darabiha, N. “A three-equation model for the prediction of soot emissions in LES of gas turbines”. In: *Proceedings of the Combustion Institute* (2018). DOI: 10.1016/J.PROCI.2018.05.061 (cited on page 55).

Frenklach, Michael. “On surface growth mechanism of soot particles”. In: *Symposium (International) on Combustion* 26.2 (1996), pp. 2285–2293. DOI: https://doi.org/10.1016/S0082-0784(96)80056-7 (cited on page 100).

Frenklach, Michael. “Method of moments with interpolative closure”. In: *Chemical Engineering Science* 57.12 (2002). Population balance modelling of particulate systems, pp. 2229–2239. DOI: https://doi.org/10.1016/S0009-2509(02)00113-6 (cited on page 55).

Frenklach, Michael. “Method of moments with interpolative closure”. In: *Chemical Engineering Science* 57.12 (2002). Population balance modelling of particulate systems, pp. 2229–2239. DOI: https://doi.org/10.1016/S0009-2509(02)00113-6 (cited on page 95).

Frenklach, Michael. “Reaction mechanism of soot formation in flames”. In: *Phys. Chem. Chem. Phys.* 4 (2002). DOI: 10.1039/B110045A (cited on pages 52, 53).

Frenklach, Michael, Clary, David W., Gardiner, William C., and Stein, Stephen E. “Detailed kinetic modeling of soot formation in shock-tube pyrolysis of acetylene”. In: *Symposium (International) on Combustion* 20.1 (1985). Twentieth Symposium (International) on Combustion, pp. 887–901. DOI: https://doi.org/10.1016/S0082-0784(85)80578-6 (cited on page 142).

Frenklach, Michael and Harris, Stephen J. “Aerosol dynamics modeling using the method of moments”. In: *Journal of Colloid and Interface Science* 118.1 (1987), pp. 252–261. DOI: https://doi.org/10.1016/0021-9797(87)90454-1 (cited on page 55).

Frenklach, Michael and Wang, Hai. “Detailed modeling of soot particle nucleation and growth”. In: *Symposium (International) on Combustion*. Vol. 23. 1. Elsevier. 1991, pp. 1559–1566 (cited on pages 52, 53, 55, 99).

Frenklach, Michael and Wang, Hai. "Detailed Mechanism and Modeling of Soot Particle Formation". In: *Soot Formation in Combustion: Mechanisms and Models*. Ed. by Henning Bockhorn. Berlin, Heidelberg: Springer Berlin Heidelberg, 1994, pp. 165–192. DOI: 10.1007/978-3-642-85167-4_10 (cited on pages 52, 53, 55).

Friendlander, S.K. *Smoke, Dust and Haze: Fundamentals of Aerosol Dynamics*. Oxford University Press, New York, USA, 2000 (cited on page 96).

Gallen, Lucien, Felden, Anne, Riber, Eleonore, and Cuenot, Bénédicte. "Lagrangian tracking of soot particles in LES of gas turbines". In: *Proceedings of the Combustion Institute* 37.4 (2019), pp. 5429–5436. DOI: https://doi.org/10.1016/j.proci.2018.06.013 (cited on page 56).

Gao, Feng and O'Brien, Edward E. "A large-eddy simulation scheme for turbulent reacting flows". In: *Physics of Fluids A: Fluid Dynamics* 5.6 (1993), pp. 1282–1284. DOI: 10.1063/1.858617 (cited on page 49).

García-Oliver, José M, Pastor Enguídanos, José Manuel, Olmeda-Ramiro, Iván, Both, A, and Mira, D. "Combustion modeling in a pressurized gas turbine burner using Large-Eddy Simulations". In: *Proceedings 12CNIT 2022* (2022), pp. 690–699 (cited on page 163).

García-Oliver, José M et al. "LES of a pressurized sooting RQL-like combustor with a computationally efficient discrete method coupled to tabulated chemistry". In: *11th European Combustion Meeting ECM2023*. 2023 (cited on page 163).

Ge, Haiwen et al. "Laser-Based Experimental and Monte Carlo PDF Numerical Investigation of an Ethanol/Air Spray Flame". In: *Combustion Science and Technology - COMBUST SCI TECHNOL* 180 (2008), pp. 1529–1547. DOI: 10.1080/00102200802125693 (cited on page 63).

Geigle, Klaus Peter, Hadef, Redjem, and Meier, Wolfgang. "Soot Formation and Flame Characterization of an Aero-Engine Model Combustor Burning Ethylene at Elevated Pressure". In: *Journal of Engineering for Gas Turbines and Power* 136.2 (2014). DOI: 10.1115/1.4025374 (cited on pages 161, 163, 164).

Geigle, Klaus Peter, Hadef, Redjem, Stöhr, Michael, and Meier, Wolfgang. "Flow field characterization of pressurized sooting swirl flames and relation to soot distributions". In: *Proceedings of the Combustion Institute* 36.3 (2017), pp. 3917–3924. DOI: https://doi.org/10.1016/j.proci.2016.09.024 (cited on pages 164, 179).

Geigle, Klaus Peter, Köhler, Markus, O'Loughlin, William, and Meier, Wolfgang. "Investigation of soot formation in pressurized swirl flames by laser measurements of temperature, flame structures and soot concentrations". In: *Proceedings of the Combustion Institute* 35.3 (2015), pp. 3373–3380. DOI: https://doi.org/10.1016/j.proci.2014.05.135 (cited on pages 161, 163, 164).

Geigle, Klaus Peter, Zerbs, Jochen, Köhler, Markus, Stöhr, Michael, and Meier, Wolfgang. "Experimental analysis of soot formation and oxidation in a gas turbine model combustor using laser diagnostics". In: *Journal of engineering for gas turbines and power* 133.12 (2011) (cited on page 10).

Gelbard, Fred, Tambour, Yoram, and Seinfeld, John H. "Sectional representations for simulating aerosol dynamics". In: *Journal of Colloid and Interface Science* 76.2 (1980), pp. 541–556 (cited on pages 56, 95).

Germano, Massimo. "Turbulence: the filtering approach". In: *Journal of Fluid Mechanics* 238 (1992), pp. 325–336 (cited on page 30).

Germano, Massimo, Piomelli, Ugo, Moin, Parviz, and Cabot, William H. "A dynamic subgrid-scale eddy viscosity model". In: *Physics of Fluids A: Fluid Dynamics* 3.7 (1991), pp. 1760–1765 (cited on page 34).

Gicquel, L.Y.M., Staffelbach, G., and Poinsot, T. "Large Eddy Simulations of gaseous flames in gas turbine combustion chambers". In: *Progress in Energy and Combustion Science* 38.6 (2012), pp. 782–817. DOI: https://doi.org/10.1016/j.pecs.2012.04.004 (cited on pages 46–48).

Gicquel, Laurent YM, Givi, P, Jaberi, FA, and Pope, SB. "Velocity filtered density function for large eddy simulation of turbulent flows". In: *Physics of Fluids* 14.3 (2002), pp. 1196–1213 (cited on page 35).

Giusti, A. and Mastorakos, E. "Detailed chemistry LES/CMC simulation of a swirling ethanol spray flame approaching blow-off". In: *Proceedings of the Combustion Institute* 36.2 (2017), pp. 2625–2632. DOI: 10.1016/j.proci.2016.06.035 (cited on pages 154, 155).

Giusti, A. and Mastorakos, E. "Turbulent Combustion Modelling and Experiments: Recent Trends and Developments". In: *Flow, Turbulence and Combustion* 103 (2019), pp. 1–18 (cited on pages 117, 118).

Giusti, Andrea, Kotzagianni, Maria, and Mastorakos, Epaminondas. "LES/CMC simulations of swirl-stabilised ethanol spray flames approaching blow-off". In: *Flow, turbulence and combustion* 97 (2016), pp. 1165–1184 (cited on page 86).

Goey, LPH de, Oijen, JA van, Bongers, H, and Groot, GRA. "New flamelet based reduction methods: the bridge between chemical reduction techniques and flamelet methods". In: *European Combustion Meeting, Orléans (France)*. 2003 (cited on page 47).

Gövert, Simon, Mira, Daniel, Kok, Jacobus BW, Vázquez, Mariano, and Houzeaux, Guillaume. "Turbulent combustion modelling of a confined premixed methane/air jet flame using tabulated chemistry". In: *Energy procedia* 66 (2015), pp. 313–316 (cited on page 10).

Gövert, Simon, Mira, Daniel, Kok, Jim BW, Vázquez, Mariano, and Houzeaux, Guillaume. "The effect of partial premixing and heat loss on the reacting flow field prediction of a swirl stabilized gas turbine model combustor". In: *Flow, turbulence and combustion* 100 (2018), pp. 503–534 (cited on page 10).

Gövert, Simon et al. "Heat loss prediction of a confined premixed jet flame using a conjugate heat transfer approach". In: *International Journal of Heat and Mass Transfer* 107 (2017), pp. 882–894 (cited on page 81).

Grader, Martin, Eberle, Christian, Gerlinger, Peter, and Aigner, Manfred. "LES of a Pressurized, Sooting Aero-Engine Model Combustor at Different Equivalence Ratios With a Sectional Approach for PAHs and Soot". In: Turbo Expo: Power for Land, Sea, and Air. 2018. DOI: 10.1115/gt2018-75254 (cited on pages 162, 214).

Guellouh, Noureddine, Szamosi, Zoltán, and Siménfalvi, Zoltán. "Combustors with low emission levels for aero gas turbine engines". In: *International Journal of Engineering and Management Sciences* 4.1 (2019), pp. 503–514 (cited on page 7).

Guillamet, Gerard et al. "Application of the partial Dirichlet-Neumann contact algorithm to simulate low-velocity impact events on composite structures". In: *Composites Part A: Applied Science and Manufacturing* 167 (2023), p. 107424 (cited on page 81).

Harris, Stephen J. and Weiner, Anita M. "Surface Growth of Soot Particles in Premixed Ethylene/Air Flames". In: *Combustion Science and Technology* 31.3-4 (1983), pp. 155–167. DOI: 10.1080/00102208308923637 (cited on page 53).

Hasse, Christian. "Scale-resolving simulations in engine combustion process design based on a systematic approach for model development". In: *International Journal of Engine Research* 17.1 (2016), pp. 44–62 (cited on page 10).

Haynes, B.S. and Wagner, H.Gg. "Soot formation". In: *Progress in Energy and Combustion Science* 7.4 (1981), pp. 229–273. DOI: https://doi.org/10.1016/0360-1285(81)90001-0 (cited on pages 53, 54).

He, Z. Y., Zhou, Kun, Xiao, Ming, and Wei, F. "Simulation of Soot Size Distribution in a Counterflow Flame". In: *International Journal of Chemical Reactor Engineering* 13 (2015), pp. 101–95 (cited on page 88).

Healy, DP and Young, JB. "Full Lagrangian methods for calculating particle concentration fields in dilute gas-particle flows". In: *Proceedings of the Royal Society A: Mathematical, Physical and Engineering Sciences* 461.2059 (2005), pp. 2197–2225 (cited on page 63).

Herrmann, Marcus. "A Eulerian level set/vortex sheet method for two-phase interface dynamics". In: *Journal of Computational Physics* 203.2 (2005), pp. 539–571 (cited on pages 60, 61).

Hoerlle, Cristian A. and Pereira, Fernando M. "Effects of CO2 addition on soot formation of ethylene non-premixed flames under oxygen enriched atmospheres". In: *Combustion and Flame* 203 (2019), pp. 407–423. DOI: 10.1016/J.COMBUSTFLAME.2019.02.016 (cited on pages 95, 100, 104).

Homann, K.H. and Wagner, H.Gg. "Some new aspects of the mechanism of carbon formation in premixed flames". In: *Symposium (International) on Combustion* 11.1 (1967), pp. 371–379. DOI: https://doi.org/10.1016/S0082-0784(67)80161-9 (cited on page 54).

Houzeaux, Guillaume et al. "Dynamic load balance applied to particle transport in fluids". In: *International Journal of Computational Fluid Dynamics* 30.6 (2016), pp. 408–418 (cited on pages 81, 105).

Houzeaux, Guillaume et al. "Dynamic resource allocation for efficient parallel CFD simulations". In: *Computers & Fluids* 245 (2022), p. 105577 (cited on page 81).

Huo, Hongfa, Wang, Xingjian, and Yang, Vigor. "A general study of counterflow diffusion flames at subcritical and supercritical conditions: Oxygen/hydrogen mixtures". In: *Combustion and flame* 161.12 (2014), pp. 3040–3050 (cited on page 40).

Hwang, J.Y. and Chung, S.H. "Growth of soot particles in counterflow diffusion flames of ethylene". In: *Combustion and Flame* 125.1 (2001), pp. 752–762. DOI: https://doi.org/10.1016/S0010-2180(00)00234-0 (cited on page 54).

Ihme, Matthias and Pitsch, Heinz. "Prediction of extinction and reignition in nonpremixed turbulent flames using a flamelet/progress variable model. 2. Application in LES of Sandia flames D and E". In: *Combustion and Flame* 155.1-2 (2008), pp. 90–107. DOI: 10.1016/j.combustflame.2008.04.015 (cited on pages 43, 93, 103, 119, 167).

Illana, Enric, Mira, Daniel, and Mura, Arnaud. "An extended flame index partitioning for partially premixed combustion". In: *Combustion Theory and Modelling* 25.1 (2021), pp. 121–157. DOI: 10.1080/13647830.2020.1841912 (cited on page 121).

Illana, Enric, Mira, Daniel, and Mura, Arnaud. "An extended flame index partitioning for partially premixed combustion". In: *Combustion Theory and Modelling* 25.1 (2021), pp. 121–157 (cited on pages 45, 189, 233).

Inagaki, Kazuhisa, Takasu, Semon, and Nakakita, Kiyomi. "In-cylinder quantitative soot concentration measurement by laser-induced incandescence". In: *SAE transactions* (1999), pp. 574–586 (cited on page 234).

Intergovernmental Panel on Climate Change. *Climate Change 2021 The Physical Science Basis*. 2021 (cited on page 3).

International Energy Agency. *CO2 Emissions in 2022*. 2021 (cited on page 3).

International Energy Agency. *Key World Energy Statistics 2021*. 2021 (cited on pages 1, 2).

International Energy Agency. *Transport – analysis*. 2022 (cited on page 3).

International Sooting Flame workshop. URL: https://www.adelaide.edu.au/cet/isfworkshop/ (cited on pages 161, 162).

Janus, B, Dreizler, A, and Janicka, J. "Experiments on swirl stabilized nonpremixed natural gas flames in a model gasturbine combustor". In: *Proceedings of the Combustion Institute* 31.2 (2007), pp. 3091–3098 (cited on page 10).

Jeffers, James and Reinders, James. *Intel Xeon Phi coprocessor high performance programming*. Newnes, 2013 (cited on page 10).

Jenny, Patrick, Roekaerts, Dirk, and Beishuizen, Nijso. "Modeling of turbulent dilute spray combustion". In: *Progress in Energy and Combustion Science* 38.6 (2012), pp. 846–887 (cited on pages 58, 59, 62).

Jenny, Patrick, Roekaerts, Dirk, and Beishuizen, Nijso. "Modeling of turbulent dilute spray combustion". In: *Progress in Energy and Combustion Science* 38.6 (2012), pp. 846–887. DOI: 10.1016/j.pecs.2012.07.001 (cited on pages 84, 104, 105, 117).

Jeong, Jinhee and Hussain, Fazle. "On the identification of a vortex". In: *Journal of fluid mechanics* 285 (1995), pp. 69–94 (cited on page 178).

Ji, Weiqi, Yang, Tianwei, Ren, Zhuyin, and Deng, Sili. "Dependence of kinetic sensitivity direction in premixed flames". In: *Combustion and Flame* 220 (2020), pp. 16–22. DOI: https://doi.org/10.1016/j.combustflame.2020.06.027 (cited on page 121).

Jiang, Xi, Siamas, GA, Jagus, K, and Karayiannis, TG. "Physical modelling and advanced simulations of gas–liquid two-phase jet flows in atomization and sprays". In: *Progress in energy and combustion science* 36.2 (2010), pp. 131–167 (cited on page 59).

Jones, William P., Marquis, Andrew J., and Noh, Dongwon. "An investigation of a turbulent spray flame using Large Eddy Simulation with a stochastic breakup model". In: *Combustion and Flame* 186 (2017), pp. 277–298. DOI: 10.1016/j.combustflame.2017.08.019 (cited on page 117).

Kalbhor, Abhijit. "Model development and numerical investigation of soot formation in combustion". PhD thesis. Eindhoven University of Technology, 2023 (cited on pages 56, 82, 95, 96, 99, 101, 102).

Kalbhor, Abhijit, Mira, Daniel, and Oijen, Jeroen van. "A computationally efficient approach for soot modeling with the discrete sectional method and FGM chemistry". In: *Combustion and Flame* 255 (2023), p. 112868 (cited on pages 82, 95, 101, 103, 162, 169, 171).

Kalbhor, Abhijit, Mira, Daniel, and Oijen Jeroen A., van. "Computationally efficient integration of a sectional soot model with FGM chemistry". In: 18th International Conference on Numerical Combustion ; Conference date: 08-05-2022 Through 11-05-2022. 2022 (cited on page 162).

Kalbhor, Abhijit and Oijen, Jeroen van. "An assessment of the sectional soot model and FGM tabulated chemistry coupling in laminar flame simulations". In: *Combustion and Flame* 229 (2021), p. 111381. DOI: 10.1016/j.combustflame.2021.02.027 (cited on pages 103, 169).

Kathrotia, Trupti, Oßwald, Patrick, Naumann, Clemens, Richter, Sandra, and Köhler, Markus. "Combustion kinetics of alternative jet fuels, Part-II: Reaction model for fuel surrogate". In: *Fuel* 302 (2021), p. 120736. DOI: https://doi.org/10.1016/j.fuel.2021.120736 (cited on page 165).

Kee, Robert J, Dixon-Lewis, Graham, Warnatz, Jürgen, Coltrin, Michael E, and Miller, James A. "A Fortran computer code package for the evaluation of gas-phase multicomponent transport properties". In: *Sandia National Laboratories Report SAND86-8246* 13 (1986), pp. 80401–1887 (cited on page 23).

Kemenov, Konstantin A, Wang, Haifeng, and Pope, Stephen B. "Modelling effects of subgrid-scale mixture fraction variance in LES of a piloted diffusion flame". In: *Combustion Theory and Modelling* 16.4 (2012), pp. 611–638 (cited on page 94).

Kennedy, Ian M., Kollmann, Wolfgang, and Chen, J.-Y. "A model for soot formation in a laminar diffusion flame". In: *Combustion and Flame* 81.1 (1990), pp. 73–85. DOI: https://doi.org/10.1016/0010-2180(90)90071-X (cited on page 54).

Kerstein, Alan R. "One-dimensional turbulence: A new approach to high-fidelity subgrid closure of turbulent flow simulations". In: *Computer Physics Communications* 148.1 (2002), pp. 1–16 (cited on page 35).

Kerstein, Alan R. "A Linear- Eddy Model of Turbulent Scalar Transport and Mixing". In: *Combustion Science and Technology* 60.4-6 (1988), pp. 391–421. DOI: 10.1080/00102208808923995 (cited on pages 35, 50).

Klimenko, A Yu. "Multicomponent diffusion of various admixtures in turbulent flow". In: *Fluid dynamics.* 25.3 (1990), pp. 327–334. DOI: 10.1007/BF01049811 (cited on page 50).

Klimenko, A.Y. and Bilger, R.W. "Conditional moment closure for turbulent combustion". In: *Progress in Energy and Combustion Science* 25.6 (1999), pp. 595–687. DOI: https://doi.org/10.1016/S0360-1285(99)00006-4 (cited on page 50).

Knudsen, E and Pitsch, H. "A general flamelet transformation useful for distinguishing between premixed and non-premixed modes of combustion". In: *Combustion and flame* 156.3 (2009), pp. 678–696 (cited on page 189).

Knudsen, E and Pitsch, H. "Capabilities and limitations of multi-regime flamelet combustion models". In: *Combustion and Flame* 159.1 (2012), pp. 242–264 (cited on page 233).

Kolmogorov, Andrei Nikolaevich, Levin, V., Hunt, Julian Charles Roland, Phillips, Owen Martin, and Williams, David. "Dissipation of energy in the locally isotropic turbulence". In: *Proceedings of the Royal Society of London. Series A: Mathematical and Physical Sciences* 434.1890 (1991), pp. 15–17. DOI: 10.1098/rspa.1991.0076 (cited on page 27).

Kolmogorov, Andrei Nikolaevich, Levin, V., Hunt, Julian Charles Roland, Phillips, Owen Martin, and Williams, David. "The local structure of turbulence in incompressible viscous fluid for very large Reynolds numbers". In: *Proceedings of the Royal Society of London. Series A: Mathematical and Physical Sciences* 434.1890 (1991), pp. 9–13. DOI: 10.1098/rspa.1991.0075 (cited on page 27).

Kors, Eugene and Collin, Dominique. "Perspective on 25 Years of European Aircraft Noise Reduction Technology Efforts and Shift Towards Global Research Aimed at Quieter Air Transport". In: *Aviation Noise Impact Management: Technologies, Regulations, and Societal Well-being in Europe*. Springer International Publishing Cham, 2022, pp. 57–116 (cited on page 5).

Kronenburg, A. "Spray Combustion–A Fresh Perspective". In: *Proc. Aust. Combust. Symp., Sydney: University of Sydney*. 2007 (cited on pages 59, 61, 63).

Kuentzmann, Paul. *Report of the independent experts to CAEP/8 on the second NOx review and the establishment of medium and long term technology goals for NOx*. Vol. 9953. International Civil Aviation Organization, 2010 (cited on page 8).

Kumar, Sanjeev and Ramkrishna, D. "On the solution of population balance equations by discretization—I. A fixed pivot technique". In: *Chemical Engineering Science* 51.8 (1996), pp. 1311–1332 (cited on page 100).

Kuo, Kenneth K. "Principles of combustion". In: (1986) (cited on pages 24, 49).

Lam, Sau-Hai and Goussis, Dimitris A. "Understanding complex chemical kinetics with computational singular perturbation". In: *Symposium (International) on Combustion*. Vol. 22. 1. Elsevier. 1989, pp. 931–941 (cited on page 46).

Lamouroux, Jean, Ihme, Matthias, Fiorina, Benoit, and Gicquel, Olivier. "Tabulated chemistry approach for diluted combustion regimes with internal recirculation and heat losses". In: *Combustion and flame* 161.8 (2014), pp. 2120–2136 (cited on page 189).

Laurent, Frédérique and Massot, Marc. "Multi-fluid Modeling of Laminar Poly-dispersed Spray Flames: Origin, Assumptions and Comparison of the Sectional and Sampling Methods". In: *Combustion Theory and Modelling* 5 (2001). DOI: 10.1088/1364-7830/5/4/303 (cited on page 63).

Laurent, Frédérique, Massot, Marc, and Villedieu, Philippe. "Eulerian multi-fluid modeling for the numerical simulation of coalescence in polydisperse dense liquid sprays". In: *Journal of Computational Physics* 194.2 (2004), pp. 505–543. DOI: https://doi.org/10.1016/j.jcp.2003.08.026 (cited on page 63).

Lee, David S et al. "The contribution of global aviation to anthropogenic climate forcing for 2000 to 2018". In: *Atmospheric Environment* 244 (2021), p. 117834 (cited on page 3).

Lefebvre, Arthur H and Ballal, Dilip R. *Gas turbine combustion: alternative fuels and emissions*. CRC press, 2010 (cited on pages 4, 9).

Lefebvre, Arthur H and McDonell, Vincent G. *Atomization and sprays*. CRC press, 2017 (cited on page 58).

Leung, K.M., Lindstedt, R.P., and Jones, W.P. "A simplified reaction mechanism for soot formation in nonpremixed flames". In: *Combustion and Flame* 87.3 (1991), pp. 289–305. DOI: https://doi.org/10.1016/0010-2180(91)90114-Q (cited on page 55).

Lignell, David O, Chen, Jacqueline H, and Schmutz, Hans A. "Effects of Damköhler number on flame extinction and reignition in turbulent nonpremixed flames using DNS". In: *Combustion and Flame* 158.5 (2011), pp. 949–963 (cited on page 189).

Lilly, Douglas K. "The representation of small-scale turbulence in numerical simulation experiments". In: *Proc. IBM Sci. Comput. Symp. on Environmental Science*. 1967, pp. 195–210 (cited on page 85).

Liñán, Amable, Martínez-Ruiz, Daniel, Vera, Marcos, and Sánchez, Antonio L. "The large-activation-energy analysis of extinction of counterflow diffusion flames with non-unity Lewis numbers of the fuel". In: *Combustion and Flame* 175 (2017), pp. 91–106. DOI: https://doi.org/10.1016/j.combustflame.2016.06.030 (cited on page 121).

Linassier, Guillaume et al. "Application of numerical simulations to predict aircraft combustor ignition". In: *Comptes Rendus Mécanique* 341.1-2 (2013), pp. 201–210 (cited on page 10).

Lindstedt, Peter R. "Simplified Soot Nucleation and Surface Growth Steps for Non-Premixed Flames". In: *Soot Formation in Combustion: Mechanisms and Models*. Ed. by Henning Bockhorn. Berlin, Heidelberg: Springer Berlin Heidelberg, 1994, pp. 417–441. DOI: 10.1007/978-3-642-85167-4_24 (cited on page 55).

Litvinov, Ivan et al. "Time-resolved study of mixing and reaction in an aero-engine model combustor at increased pressure". In: *Combustion and Flame* 231 (2021), p. 111474. DOI: https://doi.org/10.1016/j.combustflame.2021.111474 (cited on page 197).

Liu, Yize et al. "Review of modern low emissions combustion technologies for aero gas turbine engines". In: *Progress in Aerospace Sciences* 94 (2017), pp. 12–45 (cited on pages 6–8).

Lodato, Guido, Domingo, Pascale, and Vervisch, Luc. "Three-dimensional boundary conditions for direct and large-eddy simulation of compressible viscous flows". In: *Journal of computational physics* 227.10 (2008), pp. 5105–5143 (cited on page 35).

Lu, Tianfeng and Law, Chung K. "Linear time reduction of large kinetic mechanisms with directed relation graph: n-Heptane and iso-octane". In: *Combustion and Flame* 144.1 (2006), pp. 24–36. DOI: https://doi.org/10.1016/j.combustflame.2005.02.015 (cited on page 121).

Ma, Likun. "Computational modeling of turbulent spray combustion". PhD thesis. Delft University of Technology, 2016 (cited on page 124).

Ma, Likun and Roekaerts, Dirk. "Modeling of spray jet flame under MILD condition with non-adiabatic FGM and a new conditional droplet injection model". In: *Combustion and Flame* 165 (2016), pp. 402–423. DOI: 10.1016/j.combustflame.2015.12.025 (cited on pages 118, 119, 126).

Ma, Likun and Roekaerts, Dirk. "Numerical study of the multi-flame structure in spray combustion". In: *Proceedings of the Combustion Institute* 36 (2017), pp. 2603–2613. DOI: 10.1016/j.proci.2016.06.015 (cited on page 105).

Maas, Ulrich and Pope, Stephen B. "Implementation of simplified chemical kinetics based on intrinsic low-dimensional manifolds". In: *Symposium (International) on Combustion*. Vol. 24. 1. Elsevier. 1992, pp. 103–112 (cited on page 46).

Maas, Ulrich and Pope, Stephen B. "Simplifying chemical kinetics: intrinsic low-dimensional manifolds in composition space". In: *Combustion and flame* 88.3-4 (1992), pp. 239–264 (cited on page 46).

Madden, Paul. "CAEP combustion technology review process and CAEP NOx goals". In: *CAEP Publication: Fergus Falls, MN, USA* (2014) (cited on page 6).

Mallard, ELCH and Le Chatelier, H. "Combustion of explosive gas mixtures". In: *Ann Mine* 8 (1883), p. 274 (cited on page 37).

Marble, FE and Broadwell, JE. "The coherent flame model of non-premixed turbulent combustion". In: *Project Squid TRW-9-PU, Project Squid Headquarters, Chaffee Hall, Purdue University* (1977) (cited on page 48).

Marchal, Caroline. "Modelisation de La Formation et de l'oxydation Des Suies Dans Un Moteur Automobile". PhD thesis. Université d'Orléans, 2008 (cited on pages 52, 53).

Marchisio, Daniele L. and Fox, Rodney O. "Solution of population balance equations using the direct quadrature method of moments". In: *Journal of Aerosol Science* 36.1 (2005), pp. 43–73. DOI: https://doi.org/10.1016/j.jaerosci.2004.07.009 (cited on page 63).

Marrero Santiago, Javier. "Experimental study of lean aeronautical ignition: impact of critical parameters on the mechanisms acting along the different ignition phases". PhD thesis. Normandie, 2018 (cited on page 126).

Matarrese, R., Castoldi, L., and Lietti, L. "Oxidation of model soot by NO2 and O2 in the presence of water vapor". In: *Chemical Engineering Science* 173 (2017), pp. 560–569. DOI: https://doi.org/10.1016/j.ces.2017.08.017 (cited on page 54).

Mauss, Fabian, Schäfer, Thomas, and Bockhorn, Henning. "Inception and growth of soot particles in dependence on the surrounding gas phase". In: *Combustion and Flame* 99.3 (1994). 25th Symposium (International) on Combustion Papers, pp. 697–705. DOI: https://doi.org/10.1016/0010-2180(94)90064-7 (cited on page 54).

McDonell, V. G. and Samuelsen, G. S. "An Experimental Data Base for the Computational Fluid Dynamics of Reacting and Nonreacting Methanol Sprays". In: *Journal of Fluids Engineering* 117.1 (1995), pp. 145–153. DOI: 10.1115/1.2816804 (cited on page 63).

McMurthy, Patrick A., Menon, Suresh, and Kerstein, Alan R. "A linear eddy sub-grid model for turbulent reacting flows: Application to hydrogen-AIR combustion". In: *Symposium (International) on Combustion* 24.1 (1992). Twenty-Fourth Symposium on Combustion, pp. 271–278. DOI: https://doi.org/10.1016/S0082-0784(06)80036-6 (cited on page 50).

Measurement, 7th Workshop on and Turbulent Spray Combustion (TCS7), Computation of. In: (2019) (cited on pages 117, 120).

Mehta, RS, Haworth, Daniel Connell, and Modest, MF. "Composition PDF/photon Monte Carlo modeling of moderately sooting turbulent jet flames". In: *Combustion and Flame* 157.5 (2010), pp. 982–994 (cited on page 193).

Merci, Bart, Roekaerts, Dirk, and Sadiki, Amsini. *Experiments and numerical simulations of diluted spray turbulent combustion*. Springer, 2011 (cited on pages 59, 60, 63).

Meyer, Terrence R, Roy, Sukesh, Belovich, Vincent M, Corporan, Edwin, and Gord, James R. "Simultaneous planar laser-induced incandescence, OH planar laser-induced fluorescence, and droplet Mie scattering in swirl-stabilized spray flames". In: *Applied optics* 44.3 (2005), pp. 445–454 (cited on page 234).

Mira, D et al. "Numerical characterization of a premixed hydrogen flame under conditions close to flashback". In: *Flow, Turbulence and Combustion* 104 (2020), pp. 479–507 (cited on pages 81, 85).

Mira, D. and Jiang, X. "Large-eddy simulations of unsteady hydrogen annular flames". In: *Computers & Fluids* 80 (2013). Selected contributions of the 23rd International Conference on Parallel Fluid Dynamics ParCFD2011, pp. 429–440. DOI: https://doi.org/10.1016/j.compfluid.2012.01.013 (cited on page 133).

Mira, Daniel, Pérez-Sánchez, Eduardo J, Borrell, Ricard, and Houzeaux, Guillaume. "HPC-enabling technologies for high-fidelity combustion simulations". In: *Proceedings of the Combustion Institute* (2022) (cited on page 10).

Mira, Daniel et al. "Heat transfer effects on a fully premixed methane impinging flame". In: *Flow, Turbulence and Combustion* 97 (2016), pp. 339–361 (cited on page 81).

Mira, Daniel et al. "LES study on spray combustion with renewable fuels under ECN spray-A conditions". In: *Internal Combustion Engine Division Fall Technical Conference*. Vol. 85512. American Society of Mechanical Engineers. 2021, V001T06A004 (cited on page 81).

Misra, Ashish and Pullin, Dale I. "A vortex-based subgrid stress model for large-eddy simulation". In: *Physics of Fluids* 9.8 (1997), pp. 2443–2454 (cited on page 35).

Mitra, Tirthankar, Zhang, Tongfeng, Sediako, Anton D., and Thomson, Murray J. "Understanding the formation and growth of polycyclic aromatic hydrocarbons (PAHs) and young soot from n-dodecane in a sooting laminar coflow diffusion flame". In: *Combustion and Flame* 202 (2019), pp. 33–42. DOI: https://doi.org/10.1016/j.combustflame.2018.12.010 (cited on page 53).

Moin, Parviz, Squires, Kyle, Cabot, W, and Lee, Sangsan. "A dynamic subgrid-scale model for compressible turbulence and scalar transport". In: *Physics of Fluids A: Fluid Dynamics* 3.11 (1991), pp. 2746–2757 (cited on page 34).

Mongia, HC and Dodds, WGAE. "Low emissions propulsion engine combustor technology evolution past, present and future". In: *24th Congress of International Council of the Aeronautical Sciences, Yokohama, Japan, Aug.* 2004, pp. 2004–609 (cited on page 5).

Mosier, SA and Pierce, RM. "Advanced Combustor Systems for Stationary Gas Turbine Engines, Phase I. Review and Preliminary Evaluation, Volume I". In: *contract* (1980), pp. 68–02 (cited on page 6).

Moss, J.B., Stewart, C.D., and Syed, K.J. "Flowfield modelling of soot formation at elevated pressure". In: *Symposium (International) on Combustion* 22.1 (1989), pp. 413–423. DOI: https://doi.org/10.1016/S0082-0784(89)80048-7 (cited on page 54).

Mueller, M. E., Blanquart, G., and Pitsch, H. "Hybrid Method of Moments for modeling soot formation and growth". In: *Combustion and Flame* 156.6 (2009), pp. 1143–1155. DOI: 10.1016/J.COMBUSTFLAME.2009.01.025 (cited on page 162).

Mueller, M.E., Blanquart, G., and Pitsch, H. "Hybrid Method of Moments for modeling soot formation and growth". In: *Combustion and Flame* 156.6 (2009), pp. 1143–1155. DOI: https://doi.org/10.1016/j.combustflame.2009.01.025 (cited on page 55).

Mueller, Michael E and Pitsch, Heinz. "LES model for sooting turbulent nonpremixed flames". In: *Combustion and Flame* 159.6 (2012), pp. 2166–2180 (cited on page 103).

Mueller, Michael E. and Pitsch, Heinz. "LES model for sooting turbulent nonpremixed flames". In: *Combustion and Flame* 159.6 (2012), pp. 2166–2180. DOI: https://doi.org/10.1016/j.combustflame.2012.02.001 (cited on pages 55, 57).

Mulla, Irfan A and Renou, Bruno. "Simultaneous imaging of soot volume fraction, PAH, and OH in a turbulent n-heptane spray flame". In: *Combustion and Flame* 209 (2019), pp. 452–466 (cited on page 234).

Mulla, Irfan A., Godard, Gilles, Cabot, Gilles, Grisch, Frédéric, and Renou, Bruno. "Quantitative imaging of nitric oxide concentration in a turbulent n-heptane spray flame". In: *Combustion and Flame* 203 (2019), pp. 217–229. DOI: 10.1016/j.combustflame.2019.02.005 (cited on page 145).

Mulla, Irfan A. and Renou, Bruno. "Simultaneous imaging of soot volume fraction, PAH, and OH in a turbulent n-heptane spray flame". In: *Combustion and Flame* (2019). DOI: 10.1016/j.combustflame.2019.08.012 (cited on page 142).

Nau, Patrick, Yin, Zhiyao, Geigle, Klaus Peter, and Meier, Wolfgang. "Wall temperature measurements at elevated pressures and high temperatures in sooting flames in a gas turbine model combustor". In: *Applied Physics B: Lasers and Optics* 123.12 (2017), pp. 1–8. DOI: 10.1007/s00340-017-6856-y (cited on page 174).

Netzell, Karl, Lehtiniemi, Harry, and Mauss, Fabian. "Calculating the soot particle size distribution function in turbulent diffusion flames using a sectional method". In: *Proceedings of the Combustion Institute* 31.1 (2007), pp. 667–674 (cited on pages 56, 95, 97).

Nicoud, Franck and Ducros, Frédéric. "Subgrid-scale stress modelling based on the square of the velocity gradient tensor". In: *Flow, turbulence and Combustion* 62.3 (1999), pp. 183–200 (cited on page 33).

Nicoud, Franck, Toda, Hubert Baya, Cabrit, Olivier, Bose, Sanjeeb, and Lee, Jungil. "Using singular values to build a subgrid-scale model for large eddy simulations". In: *Physics of fluids* 23.8 (2011) (cited on page 34).

Noh, Dongwon, Gallot-Lavallée, Simon, Jones, William P., and Navarro-Martinez, Salvador. "Comparison of droplet evaporation models for a turbulent, non-swirling jet flame with a polydisperse droplet distribution". In: *Combustion and Flame* 194 (2018). DOI: 10.1016/j.combustflame.2018.04.018 (cited on page 118).

O'Brien, E. E. "The probability density function (pdf) approach to reacting turbulent flows". In: *Turbulent Reacting Flows*. Ed. by Paul A. Libby and Forman A. Williams. Berlin, Heidelberg: Springer Berlin Heidelberg, 1980, pp. 185–218. DOI: 10.1007/3540101926_11 (cited on page 50).

O'Rourke, Peter J and Amsden, Anthony A. *The TAB method for numerical calculation of spray droplet breakup*. Tech. rep. SAE technical paper, 1987 (cited on page 59).

Oijen, J.A. Van and Goey, L.P.H. De. "Modelling of Premixed Laminar Flames using Flamelet-Generated Manifolds". In: *Combustion Science and Technology* 161.1 (2000), pp. 113–137. DOI: 10.1080/00102200008935814 (cited on pages 47, 87, 118).

Ong, Jiun Cai, Pang, Kar Mun, Walther, Jens Honore, Ho, Jee-Hou, and Ng, Hoon Kiat. "Evaluation of a Lagrangian Soot Tracking Method for the prediction of primary soot particle size under engine-like conditions". In: *Journal of Aerosol Science* 115 (2018), pp. 70–95. DOI: https://doi.org/10.1016/j.jaerosci.2017.10.013 (cited on page 56).

Oyarzun, Guillermo, Mira, Daniel, and Houzeaux, Guillaume. "Performance assessment of cuda and openacc in large scale combustion simulations". In: *arXiv preprint arXiv:2107.11541* (2021) (cited on page 81).

Patterson, Mark A and Reitz, Rolf D. "Modeling the effects of fuel spray characteristics on diesel engine combustion and emission". In: *SAE transactions* (1998), pp. 27–43 (cited on page 59).

Peters, N. "Multiscale combustion and turbulence". In: *Proceedings of the Combustion Institute* 32.1 (2009), pp. 1–25 (cited on page 21).

Peters, N. "Laminar diffusion flamelet models in non-premixed turbulent combustion". In: *Progress in Energy and Combustion Science* 10.3 (1984), pp. 319–339. DOI: https://doi.org/10.1016/0360-1285(84)90114-X (cited on page 87).

Peters, Norbert. *Turbulent combustion*. Cambridge university press, 2000 (cited on pages 22, 41, 43, 51).

Petzold, Linda R. *Description of DASSL: a differential/algebraic system solver*. Tech. rep. Sandia National Labs., Livermore, CA (USA), 1982 (cited on page 46).

Pierce, Charles D and Moin, Parviz. "A dynamic model for subgrid-scale variance and dissipation rate of a conserved scalar". In: *Physics of Fluids* 10.12 (1998), pp. 3041–3044 (cited on page 34).

Pierce, Charles D. and Moin, Parviz. "Progress-variable approach for large-eddy simulation of non-premixed turbulent combustion". In: *Journal of Fluid Mechanics* 504.504 (2004), pp. 73–97. DOI: 10.1017/S0022112004008213 (cited on pages 47, 118).

Pitsch, Heinz, Cha, Chong M., and Fedotov, Sergei. "Flamelet modelling of non-premixed turbulent combustion with local extinction and re-ignition". In: *Combustion Theory and Modelling* 7.2 (2003), pp. 317–332. DOI: 10.1088/1364-7830/7/2/306 (cited on page 93).

Pitsch, Heinz and Ihme, Matthias. "An unsteady/flamelet progress variable method for LES of nonpremixed turbulent combustion". In: *43rd AIAA Aerospace Sciences Meeting and Exhibit*. 2005, p. 557 (cited on page 233).

Poinsot, Thierry and Veynante, Denis. *Theoretical and numerical combustion*. RT Edwards, Inc., 2005 (cited on pages 22–24, 29, 33, 38, 43, 49, 51, 84).

Pomraning, Eric and Rutland, Christopher J. "Dynamic one-equation nonviscosity large-eddy simulation model". In: *AIAA journal* 40.4 (2002), pp. 689–701 (cited on page 34).

Pope, S.B. "PDF methods for turbulent reactive flows". In: *Progress in Energy and Combustion Science* 11.2 (1985), pp. 119–192. DOI: https://doi.org/10.1016/0360-1285(85)90002-4 (cited on page 50).

Pope, S.B. "Ten questions concerning the large-eddy simulation of turbulent flows". In: *New Journal of Physics* 6 (2004). DOI: 10.1088/1367-2630/6/1/035 (cited on page 131).

Pope, SB. "The evolution of surfaces in turbulence". In: *International journal of engineering science* 26.5 (1988), pp. 445–469 (cited on page 48).

Pope, Stephen B. "Computationally efficient implementation of combustion chemistry using in situ adaptive tabulation". In: (1997) (cited on page 47).

Pope, Stephen B. *Turbulent flows*. Cambridge university press, 2000 (cited on pages 22, 28, 29, 50).

Ramaekers, WJS. "Development of flamelet generated manifolds for partially-premixed flame simulations". PhD thesis. 2011 (cited on page 87).

Ramirez-Hernandez, Astrid, Kathrotia, Trupti, Methling, Torsten, Braun-Unkhoff, Marina, and Riedel, Uwe. "Reaction Model Development of Selected Aromatics as Relevant Molecules of a Kerosene Surrogate-The Importance of m-Xylene Within the Combustion of 1,3,5-Trimethylbenzene". In: *Journal of Engineering for Gas Turbines and Power* 144.2 (2021). DOI: https://doi.org/10.1115/1.4052206 (cited on pages 165, 166).

Ranz, W E and Marshall, W R. "Evaporation from drops: Part 1". In: *Chem. eng. prog* 48.3 (1952), pp. 141–146 (cited on page 106).

Reddy, Manedhar, De, Ashoke, and Yadav, Rakesh. "Effect of precursors and radiation on soot formation in turbulent diffusion flame". In: *Fuel* 148 (2015), pp. 58–72 (cited on page 193).

Reitz, Rolf D. "Mechanism of breakup of round liquid jets". In: *Encyclopedia of fluid mechanics* 10 (1986) (cited on page 59).

Richardson, Lewis F. *Weather prediction by numerical process*. University Press, 1922 (cited on page 26).

Richter, Henning and Howard, Jack B. "Formation of polycyclic aromatic hydrocarbons and their growth to soot—a review of chemical reaction pathways". In: *Progress in Energy and Combustion science* 26.4-6 (2000), pp. 565–608 (cited on pages 20, 56).

Rittler, Andreas, Proch, Fabian, and Kempf, Andreas M. "LES of the Sydney piloted spray flame series with the PFGM/ATF approach and different sub-filter models". In: *Combustion and Flame* 162.4 (2015), pp. 1575–1598 (cited on page 86).

Roberts, R, Peduzzi, A, and Vitti, GE. *Experimental clean combustor program, phase 1.* Tech. rep. 1975 (cited on page 5).

Rodrigues, P., Franzelli, B., Vicquelin, R., Gicquel, O., and Darabiha, N. "Coupling an LES approach and a soot sectional model for the study of sooting turbulent non-premixed flames". In: *Combustion and Flame* 190 (2018), pp. 477–499 (cited on pages 56, 57, 102).

Rodrigues, Pedro. "Modélisation multiphysique de flammes turbulentes suitées avec la prise en compte des transferts radiatifs et des transferts de chaleur pariétaux." PhD thesis. Université Paris-Saclay (ComUE), 2018 (cited on pages 162, 193).

Roth, P., Brandt, O., and Von Gersum, S. "High temperature oxidation of suspended soot particles verified by CO and CO2 measurements". In: *Symposium (International) on Combustion* 23.1 (1991). Twenty-Third Symposium (International) on Combustion, pp. 1485–1491. DOI: https://doi.org/10.1016/S0082-0784(06)80417-0 (cited on page 54).

Roy, Somesh Prasad. *Aerosol-dynamics-based soot modeling of flames.* The Pennsylvania State University, 2014 (cited on pages 97, 99).

Rusell, P., Beal, G., and Hinton, B. "Low NOx heavy fuel combustor concept program". In: *NASA Technical Report* (1981) (cited on page 8).

Saggese, Chiara et al. "Kinetic modeling of particle size distribution of soot in a premixed burner-stabilized stagnation ethylene flame". In: *Combustion and Flame* 162.9 (2015), pp. 3356–3369. DOI: https://doi.org/10.1016/j.combustflame.2015.06.002 (cited on page 56).

Saini, Subhash et al. "Early multi-node performance evaluation of a knights corner (KNC) based NASA supercomputer". In: *2015 IEEE International Parallel and Distributed Processing Symposium Workshop.* IEEE. 2015, pp. 57–67 (cited on page 10).

Salenbauch, Steffen, Hasse, Christian, Vanni, Marco, and Marchisio, Daniele L. "A numerically robust method of moments with number density function reconstruction and its application to soot formation, growth and oxidation". In: *Journal of Aerosol Science* 128 (2019), pp. 34–49. DOI: https://doi.org/10.1016/j.jaerosci.2018.11.009 (cited on page 162).

Samuelsen, GS, Brouwer, J, Vardakas, MA, and Holdeman, JD. "Experimental and modeling investigation of the effect of air preheat on the formation of NO x in an RQL combustor". In: *Heat and Mass Transfer* 49 (2013), pp. 219–231 (cited on page 6).

Samuelsen, Scott. "Rich burn, quick-mix, lean burn (RQL) combustor". In: *The Gas Turbine Handbook* (2006), pp. 227–233 (cited on pages 6, 7).

Sanjosé, M et al. "Fuel injection model for Euler–Euler and Euler–Lagrange large-eddy simulations of an evaporating spray inside an aeronautical combustor". In: *International Journal of Multiphase Flow* 37.5 (2011), pp. 514–529 (cited on page 61).

Sazhin, S S, Shchepakina, E, and Sobolev, V. "Modelling of sprays: recent results and future challenges". In: *Journal of Physics: Conference Series* 1096.1 (2018), p. 012052. DOI: 10.1088/1742-6596/1096/1/012052 (cited on page 63).

Sazhin, Sergei S. "Modelling of fuel droplet heating and evaporation: Recent results and unsolved problems". In: *Fuel* 196 (2017), pp. 69–101 (cited on page 59).

Schechter, Robert S. *Transport Phenomena (Bird, R. Byron; Stewart, Warren E.; Lightfoot, Edwin N.)* 1961 (cited on page 105).

Schiller, Links. "A drag coefficient correlation". In: *Zeit. Ver. Deutsch. Ing.* 77 (1933), pp. 318–320 (cited on page 59).

Schmidt, David P et al. "Pressure-swirl atomization in the near field". In: *SAE transactions* (1999), pp. 471–484 (cited on page 59).

Schuetz, Charles A. and Frenklach, Michael. "Nucleation of soot: Molecular dynamics simulations of pyrene dimerization". In: *Proceedings of the Combustion Institute* 29.2 (2002), pp. 2307–2314. DOI: https://doi.org/10.1016/S1540-7489(02)80281-4 (cited on page 53).

Scotti, Alberto and Meneveau, Charles. "Fractal model for coarse-grained nonlinear partial differential equations". In: *Physical review letters* 78.5 (1997), p. 867 (cited on page 35).

See, Yee Chee and Ihme, Matthias. "Large eddy simulation of a partially-premixed gas turbine model combustor". In: *Proceedings of the Combustion Institute* 35.2 (2015), pp. 1225–1234. DOI: https://doi.org/10.1016/j.proci.2014.08.006 (cited on page 168).

Sernenov, N. "Thermal theory of combustion and explosion. III. Theory of normal flame propagation". In: *Prog. Phys, Sci., USSR* 24 (1940), pp. 433–486 (cited on page 37).

Sheikhi, MRH, Drozda, TG, Givi, P, Jaberi, FA, and Pope, SB. "Large eddy simulation of a turbulent nonpremixed piloted methane jet flame (Sandia Flame D)". In: *Proceedings of the Combustion Institute* 30.1 (2005), pp. 549–556 (cited on page 35).

Sheikhi, MRH, Givi, P, and Pope, SB. "Velocity-scalar filtered mass density function for large eddy simulation of turbulent reacting flows". In: *Physics of fluids* 19.9 (2007) (cited on page 35).

Shum-Kivan, F. et al. "Experimental and numerical analysis of a turbulent spray flame structure". In: *Proceedings of the Combustion Institute* 2 (2017), pp. 2567–2575. DOI: 10.1016/j.proci.2016.06.039 (cited on pages 117, 118, 120, 135, 141, 142).

Singh, Jasdeep, Balthasar, Michael, Kraft, Markus, and Wagner, Wolfgang. "Stochastic modeling of soot particle size and age distributions in laminar premixed flames". In: *Proceedings of the Combustion Institute* 30.1 (2005), pp. 1457–1465. DOI: https://doi.org/10.1016/j.proci.2004.08.120 (cited on page 55).

Sirignano, Mariano, Kent, John, and D'Anna, Andrea. "Further experimental and modelling evidences of soot fragmentation in flames". In: *Proceedings of the Combustion Institute* 35.2 (2015), pp. 1779–1786. DOI: https://doi.org/10.1016/j.proci.2014.05.010 (cited on page 54).

Sitte, Michael Philip and Mastorakos, Epaminondas. "Large Eddy Simulation of a spray jet flame using Doubly Conditional Moment Closure". In: *Combustion and Flame* 199 (2019), pp. 309–323. DOI: 10.1016/J.COMBUSTFLAME.2018.08.026 (cited on pages 118, 121, 142).

Skeen, Scott A et al. "A progress review on soot experiments and modeling in the engine combustion network (ECN)". In: *SAE International Journal of Engines* 9.2 (2016), pp. 883–898 (cited on page 234).

Slotnick, Jeffrey P et al. *CFD vision 2030 study: a path to revolutionary computational aerosciences*. Tech. rep. 2014 (cited on page 10).

Smagorinsky, Joseph. "General circulation experiments with the primitive equations: I. The basic experiment". In: *Monthly weather review* 91.3 (1963), pp. 99–164 (cited on pages 33, 85).

Smiljanovski, V, Moser, V, and Klein, Rupert. "A capturing-tracking hybrid scheme for deflagration discontinuities". In: *Combustion Theory and Modelling* 1.2 (1997), p. 183 (cited on page 48).

Smith, Thomas and Menon, Suresh. "Model simulations of freely propagating turbulent premixed flames". In: *Symposium (International) on Combustion* 26.1 (1996), pp. 299–306. DOI: https://doi.org/10.1016/S0082-0784(96)80229-3 (cited on page 50).

Smooke, Mitchell D. *Reduced kinetic mechanisms and asymptotic approximations for methane-air flames: a topical volume*. Springer, 1991 (cited on page 23).

Stickles, R and Barrett, J. *TAPS II combustor final report*. Tech. rep. 2013 (cited on page 8).

Stöhr, M. et al. "Time-resolved study of transient soot formation in an aero-engine model combustor at elevated pressure". In: *Proceedings of the Combustion Institute* 37.4 (2019), pp. 5421–5428. DOI: https://doi.org/10.1016/j.proci.2018.05.122 (cited on page 197).

Sussman, Mark and Fatemi, Emad. "An efficient, interface-preserving level set redistancing algorithm and its application to interfacial incompressible fluid flow". In: *SIAM Journal on scientific computing* 20.4 (1999), pp. 1165–1191 (cited on page 61).

Tambour, Yoram. "A Lagrangian sectional approach for simulating droplet size distribution of vaporizing fuel sprays in a turbulent jet". In: *Combustion and Flame* 60.1 (1985), pp. 15–28. DOI: https://doi.org/10.1016/0010-2180(85)90115-4 (cited on page 63).

Tardelli, Livia, Franzelli, Benedetta, Rodrigues, Pedro, and Darabiha, Nasser. "Impact of the Reaction Mechanism Model on Soot Growth and Oxidation in Laminar and Turbulent Flames". In: *Turbo Expo: Power for Land, Sea, and Air*. Vol. 58615. American Society of Mechanical Engineers. 2019, V04AT04A055 (cited on pages 166, 199).

Tennekes, Hendrik and Lumley, John L. *A first course in turbulence*. The MIT Press, 1972 (cited on page 28).

Toda, H Baya, Truffin, Karine, and Nicoud, Franck. "Is the dynamic procedure appropriate for all SGS models". In: *V european conference on computational fluid dynamics, ECCOMAS, Lisbon, Portugal*. 2010, pp. 14–17 (cited on page 34).

Tonse, Shaheen R, Moriarty, Nigel W, Brown, Nancy J, and Frenklach, Michael. "PRISM: Piecewise reusable implementation of solution mapping. An economical strategy for chemical kinetics". In: *Israel Journal of Chemistry* 39.1 (1999), pp. 97–106 (cited on page 47).

Tseng, L-K, Ruff, GA, and Faeth, Gerard M. "Effects of gas density on the structure of liquid jets in still gases". In: *AIAA journal* 30.6 (1992), pp. 1537–1544 (cited on page 60).

Turon, A, González, EV, Sarrado, C, Guillamet, G, and Maimí, P. "Accurate simulation of delamination under mixed-mode loading using a cohesive model with a mode-dependent penalty stiffness". In: *Composite Structures* 184 (2018), pp. 506–511 (cited on page 81).

Tyliszczak, Artur, Cavaliere, Davide E, and Mastorakos, Epaminondas. "LES/CMC of blow-off in a liquid fueled swirl burner". In: *Flow, Turbulence and Combustion* 92 (2014), pp. 237–267 (cited on page 86).

U.S. Energy Information Administration. *September 2022 Monthly Energy Review*. 2022 (cited on page 4).

United Nations Framework Convention on Climate Change. *Paris Agreement: UN Climate Conference*. 2015 (cited on page 4).

University of Stuttgart, ESTiMatE project. *D2.1 Detailed reaction mechanism including PAHs, and soot*. Tech. rep. 2021 (cited on page 165).

Vallet, Ariane, Burluka, AA, and Borghi, R. "Development of a eulerian model for the" atomization" of a liquid jet". In: *Atomization and sprays* 11.6 (2001), pp. 619–642 (cited on page 61).

Vazquez, M. et al. "Multiphysics engineering simulation toward exascale". In: *J. Comput. Sci.* 14 (2016), pp. 15–27 (cited on page 81).

Verdier, Antoine et al. "Experimental study of local flame structures and fuel droplet properties of a spray jet flame". In: *Proceedings of the Combustion Institute* 36.2 (2017), pp. 2595–2602. DOI: 10.1016/j.proci.2016.07.016 (cited on pages 117, 119, 120, 141).

Verdier, Antoine et al. "Local extinction mechanisms analysis of spray jet flame using high speed diagnostics". In: *Combustion and Flame* 193 (2018), pp. 440–452. DOI: 10.1016/j.combustflame.2018.03.032 (cited on pages 118, 120, 141, 142, 144, 146, 147, 151, 152).

Versteeg, Henk Kaarle and Malalasekera, Weeratunge. *An introduction to computational fluid dynamics: the finite volume method*. Pearson education, 2007 (cited on page 10).

Veynante, Denis and Vervisch, Luc. "Turbulent combustion modeling". In: *Progress in energy and combustion science* 28.3 (2002), pp. 193–266 (cited on pages 10, 35, 45, 46, 48–51).

Vié, Aymeric, Jay, Stéphane, Cuenot, Bénédicte, and Massot, Marc. "Accounting for polydispersion in the eulerian large eddy simulation of the two-phase flow in an aeronautical-type burner". In: *Flow, turbulence and combustion* 90 (2013), pp. 545–581 (cited on page 61).

Vreman, AW. "An eddy-viscosity subgrid-scale model for turbulent shear flow: Algebraic theory and applications". In: *Physics of fluids* 16.10 (2004), pp. 3670–3681 (cited on pages 34, 84, 85).

Vujanović, Milan, Edelbauer, Wilfried, Berg, Eberhard von, Tatschl, Reinhard, and Duić, Neven. "Enhancement and validation of an Eulerian-Eulerian approach for diesel sprays". In: *Proceedings of the ILASS Europe Conference, Paper*. 2008, pp. 2–4 (cited on page 62).

Wang, Hu et al. "A comparison study on the combustion and sooting characteristics of base engine oil and n-dodecane in laminar diffusion flames". In: *Applied Thermal Engineering* 158 (2019), p. 113812. DOI: https://doi.org/10.1016/j.applthermaleng.2019.113812 (cited on page 53).

Wang, Lu-Yin, Bauer, Cody K, and Gülder, Ömer L. "Soot and flow field in turbulent swirl-stabilized spray flames of Jet A-1 in a model combustor". In: *Proceedings of the Combustion Institute* 37.4 (2019), pp. 5437–5444 (cited on page 234).

Wang, Yu and Chung, Suk Ho. "Soot formation in laminar counterflow flames". In: *Progress in Energy and Combustion Science* 74 (2019), pp. 152–238. DOI: https://doi.org/10.1016/j.pecs.2019.05.003 (cited on page 52).

Wang, Yu, Raj, Abhijeet, and Chung, Suk Ho. "Soot modeling of counterflow diffusion flames of ethylene-based binary mixture fuels". In: *Combustion and Flame* 162.3 (2015), pp. 586–596. DOI: https://doi.org/10.1016/j.combustflame.2014.08.016 (cited on page 54).

Wang, Yu, Raj, Abhijeet, and Chung, Suk Ho. "Soot modeling of counterflow diffusion flames of ethylene-based binary mixture fuels". In: *Combustion and Flame* 162.3 (2015), pp. 586–596 (cited on pages 165, 166).

Wang, Zhinuo J et al. "Human biventricular electromechanical simulations on the progression of electrocardiographic and mechanical abnormalities in post-myocardial infarction". In: *EP Europace* 23 (2021), pp. i143–i152 (cited on page 81).

Weigand, Peter, Meier, Wolfgang, Duan, Xu Ru, Stricker, Winfried, and Aigner, Manfred. "Investigations of swirl flames in a gas turbine model combustor: I. Flow field, structures, temperature, and species distributions". In: *Combustion and flame* 144.1-2 (2006), pp. 205–224 (cited on page 10).

Weller, H.G., Marooney, C.J., and Gosman, A.D. "A new spectral method for calculation of the time-varying area of a laminar flame in homogeneous turbulence". In: *Symposium (International) on Combustion* 23.1 (1991). Twenty-Third Symposium (International) on Combustion, pp. 629–636. DOI: https://doi.org/10.1016/S0082-0784(06)80310-3 (cited on page 48).

Weller, Henry G. "The Development of a New Flame Area Combustion Model Using Conditional Averaging". In: 1993 (cited on page 48).

Wick, Achim, Priesack, Frederic, and Pitsch, Heinz. "Large-Eddy Simulation and Detailed Modeling of Soot Evolution in a Model Aero Engine Combustor". In: Turbo Expo: Power for Land, Sea, and Air. 2017. DOI: 10.1115/gt2017-63293 (cited on pages 162, 166).

Williams, Forman A. *Combustion Theory: The fundamental theory of chemically reacting flow systems*. CRC Press, 1965 (cited on pages 22, 44, 49, 63).

Xuan, Y. and Blanquart, G. "Effects of aromatic chemistry-turbulence interactions on soot formation in a turbulent non-premixed flame". In: *Proceedings of the Combustion Institute* 35.2 (2015), pp. 1911–1919. DOI: https://doi.org/10.1016/j.proci.2014.06.138 (cited on page 57).

Yamashita, H, Shimada, M, and Takeno, T. "A numerical study on flame stability at the transition point of jet diffusion flames". In: *Symposium (international) on combustion*. Vol. 26. 1. Elsevier. 1996, pp. 27–34 (cited on page 189).

Yang, Suo, Lew, Jeffry K., and Mueller, Michael E. "Large Eddy Simulation of soot evolution in turbulent reacting flows: Presumed subfilter PDF model for soot–turbulence–chemistry interactions". In: *Combustion and Flame* 209 (2019), pp. 200–213. DOI: https://doi.org/10.1016/j.combustflame.2019.07.040 (cited on page 57).

Yin, Feijia and Rao, A Gangoli. "Performance analysis of an aero engine with inter-stage turbine burner". In: *The Aeronautical Journal* 121.1245 (2017), pp. 1605–1626 (cited on page 4).

Yoshizawa, Akira. "Statistical theory for compressible turbulent shear flows, with the application to subgrid modeling". In: *The Physics of fluids* 29.7 (1986), pp. 2152–2164 (cited on pages 131, 175).

You, Donghyun and Moin, Parviz. "A dynamic global-coefficient subgrid-scale eddy-viscosity model for large-eddy simulation in complex geometries". In: *Physics of Fluids* 19.6 (2007) (cited on page 34).

Yu, Han, Zhu, Pengfei, Suo, Jianqin, and Zheng, Longxi. "Investigation of discharge coefficients for single element lean direct injection modules". In: *Energies* 11.6 (2018), p. 1603 (cited on page 9).

Yu, S., Liu, X., Bai, X. S., Elbaz, A. M., and Roberts, W. L. "LES/PDF modeling of swirl-stabilized non-premixed methane/air flames with local extinction and re-ignition". In: *Combustion and Flame* 219 (2020), pp. 102–119. DOI: 10.1016/j.combustflame.2020.05.018 (cited on page 154).

Yuen, M. C. and Chen, L. W. "On drag of evaporating liquid droplets". In: *Combustion Science and Technology* 14.4-6 (1976), pp. 147–154. DOI: 10.1080/00102207608547524 (cited on page 106).

Zang, Yan, Street, Robert L, and Koseff, Jeffrey R. "A dynamic mixed subgrid-scale model and its application to turbulent recirculating flows". In: *Physics of Fluids A: Fluid Dynamics* 5.12 (1993), pp. 3186–3196 (cited on page 35).

Zhang, Qingan. "Detailed modeling of soot formation/oxidation in laminar coflow diffusion flames". PhD thesis. University of Toronto, 2009 (cited on page 56).

Zhao, Song, Bouali, Zakaria, and Mura, Arnaud. "Computational investigation of weakly turbulent flame kernel growths in iso-octane droplet clouds in CVC conditions". In: *Flow, Turbulence and Combustion* 104 (2020), pp. 139–177 (cited on page 189).

Zoby, MRG, Navarro-Martinez, S, Kronenburg, A, and Marquis, AJ. "Evaporation rates of droplet arrays in turbulent reacting flows". In: *Proceedings of the Combustion Institute* 33.2 (2011), pp. 2117–2125 (cited on page 62).